SINTEF
PROCEEDINGS
4

Selected papers from the 10th Trondheim Conference on CO_2 Capture, Transport and Storage

TCCS-10

SINTEF Proceedings

Editors:
Nils A. Røkke and Hanna Knuutila

TCCS–10
CO_2 Capture, Transport and Storage
Trondheim 17th–19th June 2019

Selected papers

SINTEF Academic Press

SINTEF Proceedings no 4
Editors: Nils A. Røkke (SINTEF) and Hanna Knuutila (NTNU)
TCCS–10
CO_2 Capture, Transport and Storage. Trondheim 17th–19th June 2019
Selected papers from the 10th International Trondheim CCS Conference

Keywords:
CCS – Carbon Capture, Transport and Storage, CO_2 Capture, CO_2 Transport, CO_2 Storage, CO_2 Utilization, Pre-combustion capture, Post-combustion capture, Oxy-fuel capture, CCS and hydrogen, CO_2 positive solutions, International R&D activities, Whole system issues, Novel CCS technologies, Public Acceptance, Communication, Policy, Business models

Cover illustration: SINTEF Energy

ISSN 2387-4295 (online)
ISBN 978-82-536-1646-9 (pdf)

SINTEF Academic Press
Address: Børrestuveien 3
PO Box 124 Blindern
N-0314 OSLO
Tel: +47 40 00 51 00

www.sintef.no/community
www.sintefbok.no

SINTEF Proceedings
SINTEF Proceedings is a serial publication for peer-reviewed conference proceedings on a variety of scientific topics.
The processes of peer-reviewing of papers published in SINTEF Proceedings are administered by the conference organizers and proceedings editors. Detailed procedures will vary according to custom and practice in each scientific community.

Preface

These proceedings contain selected papers from the 10th International Trondheim CCS Conference (TCCS-10), held in Trondheim, Norway, on June 17th-19th 2019.

The bi-annual Trondheim CCS Conference is a leading scientific CCS technology conference. Since its inception in 2003, the Conference has developed to become a globally important meeting place for over 400 CCS experts. The Conference typically has 150 oral presentations, five or six parallel sessions, over 100 posters and world leading keynote speakers.

The authors had an opportunity to submit a full manuscript and ten full manuscripts are presented in these proceedings after peer review by two experts.

The organizing committee would like to thank everyone who has helped with review of manuscripts, authors who presented their work during the conference and the authors who have submitted a full manuscript.

We are also grateful for the support from the conference sponsors.

Nils A. Røkke and Hanna Knuutila

Conference sponsors

Contents

INVESTIGATION OF CORROSION-RELATED FAILURE OF REBOILER AT TECHNOLOGY CENTRE MONGSTAD

A. Palencsár[1*], R. Nyborg[1], N. Enaasen Flø[2], F. Iversen[2], B. Deleneuville[2], M. Bonis[3], V. Gregoire[4]

[1] Institute for Energy Technology, Kjeller, Norway

[2] Technology Centre Mongstad, Norway

[3] Total SA, France

[4] Equinor ASA, Norway

* Corresponding author e-mail: attila.palencsar@ife.no

Abstract

Technology Centre Mongstad (TCM) has experienced in 2017 a corrosion-related failure in a stripper reboiler of an amine unit, during a series of long-term test campaigns 2017-2018 for CO_2 capture using monoethanolamine (MEA). The failure affected the heat exchanger plates within the reboiler, made of 316L stainless steel.

A thorough investigation has been initiated in collaboration with Institute for Energy Technology (IFE), Equinor and Total to evaluate the key factors responsible for the damage and the mechanisms leading to the failure of heat exchanger plates. A two-phase approach was adopted. In the first phase the aim was to make a complete evaluation of all circumstances, outline the most plausible hypotheses for the cause of the damage, design and define a sensible scope for a detailed experimental laboratory study allowing to assess the factors contributing to the corrosion issues. The second phase is to encompass the experimental study to either confirm or refute the starting hypotheses.

This contribution presents a detailed account of the relevant findings, the reasoning and the outline of the planned laboratory investigations. On the other hand, the results of the experimental study itself are not part of this paper.

Keywords: *Post-Combustion Capture, MEA, Corrosion, Erosion, Oxygen Scavenger, Potassium Bisulfite*

1. Introduction

Technology Centre Mongstad (TCM) is the world's largest test facility where various technologies for CO_2 capture are assessed and qualified since its completion in 2012. The site is equipped with two distinct units, a proprietary Chilled Ammonia Process (CAP) plant and a highly flexible amine plant on which this paper focuses. The plant is currently owned by Gassnova, Equinor, Total and Shell.

In 2017, TCM started a long-term testing with MEA solvent through a series of test campaigns, to generate useful knowledge and information to be used to reduce the cost, the technical, environmental and financial risks of commercial scale deployment of post-combustion CO_2 capture. Some test activities were also conducted over longer periods in parallel to the abovementioned test series, one being material testing and corrosion monitoring for assessment of suitable materials for the post-combustion CO_2 capture process with MEA solvent. In July 2017, a corrosion-related failure occurred in a stripper reboiler of the amine plant, that affected the heat exchanger plates within the reboiler, made of 316L stainless steel. The operations of the amine plant over the experimental campaign yielded a complex scenario of varying conditions (i.a. flue gas type, solvent composition) over a long period of time, making it a difficult task to identify the key factor(s) responsible for developing the failure, since both corrosion and erosion contributions could be plausible but without any factor appearing as an obvious and certain cause [2], [3].

In addition to the practical value of finding the causes for the damage, the importance of gaining a more fundamental understanding of the possible processes involved was recognized. It was therefore important that the failure assessment includes both a thorough study of the available information of relevance as well as validation by laboratory experiments.

A task force with TCM, Equinor and Total, as TCM owners, performed a complete evaluation of all circumstances leading to the failure, in order to identify the most plausible mechanisms and define working hypotheses to be verified experimentally.

In this context, TCM and their partners Equinor and Total have initiated a collaboration with Institute for Energy Technology (IFE) with the following objectives:

a) To review the study performed to evaluate the circumstances of the failure

b) To agree on the selection of the most plausible mechanisms for the failure and the working hypotheses to be verified experimentally

c) To define a sensible scope for a detailed experimental laboratory study allowing to assess the factors contributing to the corrosion issues

d) Perform the tests and assess whether the experimental results confirm or refute the hypotheses

A two-phase approach has been adopted, where evaluation, defining the hypotheses and scope would constitute the first phase whereas the second stage would consist of the experimental work and assessment of the results.

This paper is concerned with the first stage of this study, the experimental work will be reported separately in due course.

2. Evaluation of plant data

2.1. The amine plant and operational conditions

A simplified process flow diagram of the TCM amine plant is illustrated in Figure 1. The adjacent Mongstad refinery provides the flue gases for testing CO_2 capture, i.e. flue gas from the Combined Heat and Power (CHP) plant at 3.6-4 % CO_2, and flue gas originating from the Residual Fluidized Catalytic Cracker (RFCC) unit at 13-14 % CO_2. The typical gas compositions are also shown in Table 1. TCM has the flexibility to enrich the CHP flue gas by recycling captured CO_2 or to dilute the RFCC flue gas with air to adjust the CO_2 content.

Once the flue gas enters the TCM test site it is conditioned and saturated with water in a Direct Contact Cooler (DCC). The RFCC flue gas is also passed through a highly effective Brownian Diffusion (BD) filter in order to remove aerosols and catalyst particles. Conditioned flue gas enters the bottom of the absorber where it is contacted with amine solvent as gas and solvent flow counter-currently through three sections of structured packing (12, 18 or 24 meters at TCM discretion). CO_2 in the flue gas reacts with the amine to become chemically bound in the solvent. The rich solvent is pumped through the lean/rich cross heat exchanger for pre-heating by hot lean solvent before it enters the stripper section. TCM amine plant is equipped with two strippers, one for operation with low CO_2 content (CHP stripper) or higher CO_2 content (RFCC stripper). Additional heat is supplied by steam to the stripper reboiler in order to reverse the absorption reactions and release CO_2 from the solvent. The regenerated lean solvent leaving the stripper is cooled down in the lean/rich cross heat exchanger and lean cooler, before it is recirculated back to the absorber. The depleted flue gas leaves the top of the absorber after being conditioned in one or two absorber water wash sections, while CO_2 product gas is released to the atmosphere through the stripper water wash and stripper overhead condenser system, as illustrated in Figure 1.

The feed gas type and corresponding CO_2 and O_2 concentrations for the entire test period (2017-2018) are shown in Figure 2, whereas the operating temperatures are plotted in Figure 3. Oxygen scavenger (potassium bisulfite) has been injected in the early periods of the campaign (see Figure 4).

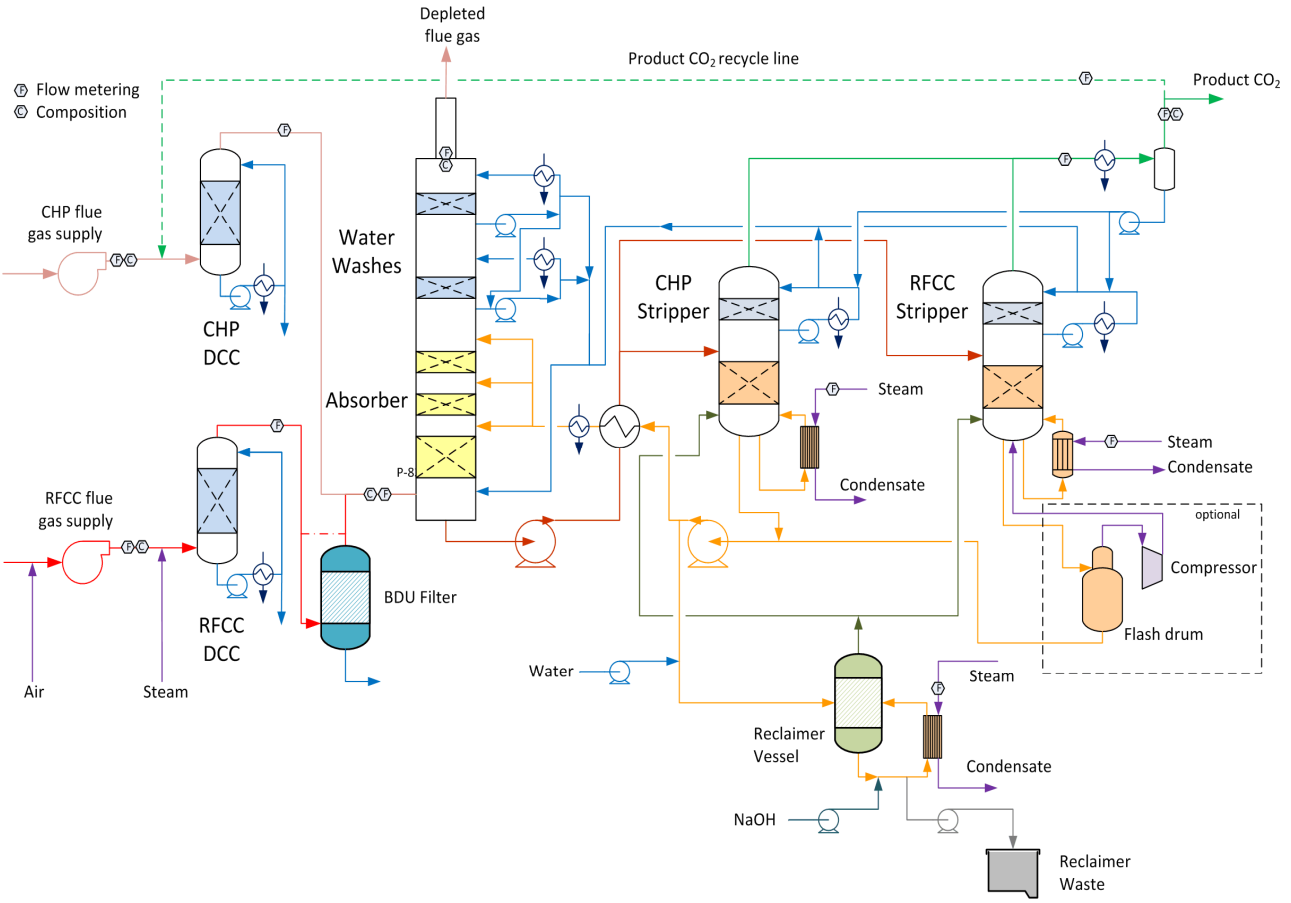

Figure 1: Simplified process diagram of the TCM amine plant (from [1])

Table 1: Typical flue gas compositions (adapted from [1])

Gas composition	Conditioned CHP gas	Conditioned RFCC gas
N_2 (mole%)	73 - 79	73 - 79
O_2 (mole%)	13 - 14	3 - 8
CO_2 (mole%)	3.6 – 4.0	13.0 – 14.5
H_2O (mole%)	Saturated	Saturated
SO_2 (ppmv)	<0.3	<5
NO_x (ppmv)	<5	100
NH_3 (ppmv)	<5	<1
CO (ppmv)		<10
Particles (parts/cm^3)		0.3-0.8×10^6

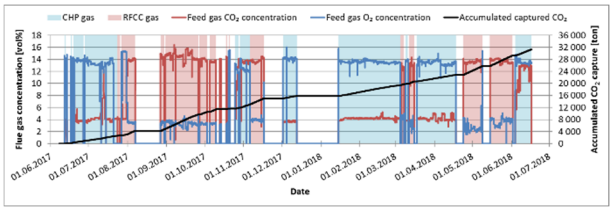

Figure 2. Flue gas sources and corresponding CO_2 and O_2 concentrations throughout the MEA test period (adapted from [1]).

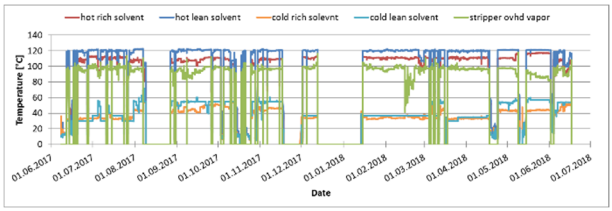

Figure 3. Operating temperatures throughout the MEA test period (adapted from [1]).

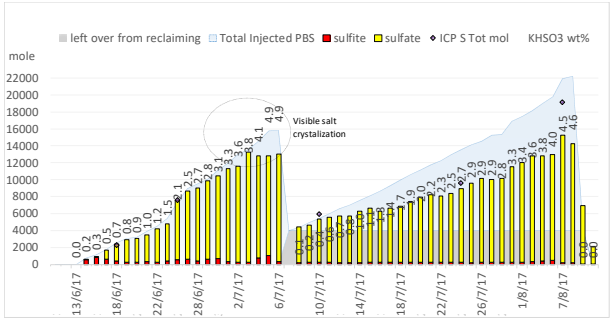

Figure 4. Accumulation of various species related to oxygen scavenger injection

2.2. Relevant findings

Examination of the reboiler after it was taken out of service revealed that the failure consisted in two holes on the heat exchanger plates built in AISI 316L stainless steel. It was observed that plate thickness in the affected area was reduced by about 200-250 µm as shown in Figure 5; the failure might thus have resulted from a corrosion/erosion origin in the context of apparently increased general corrosion.

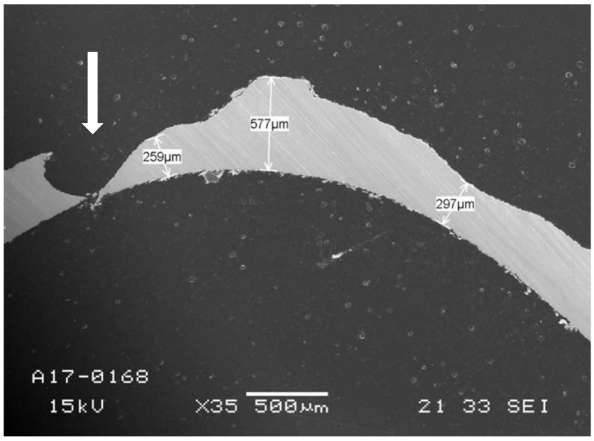

Figure 5. Cross-section SEM image of the reboiler plate region around the leak indicated by the arrow; original thickness 600 µm (adapted from [1]).

Plant inspections did not reveal any sign of corrosion elsewhere in the plant. However, a red/brown layer believed to be corrosion product deposits originating from the CHP reboiler was observed on surfaces exposed to the solvent, e.g. solvent piping and material test racks, process valves, CHP stripper and internals and CHP reboiler.

The period of oxygen scavenger injection (see Figure 4) appears to be closely related to the corrosion issues leading to the failure of the reboiler. The evolution of the chemical composition of the solvent within the scavenger injection period is highly relevant in this context. Rapid changes in metallic cation concentration (iron, nickel, chromium and molybdenum see Figure 6) were clear indications of on-going corrosion at that time, as well as likely precipitation of iron-based products, as observations previously suggested.

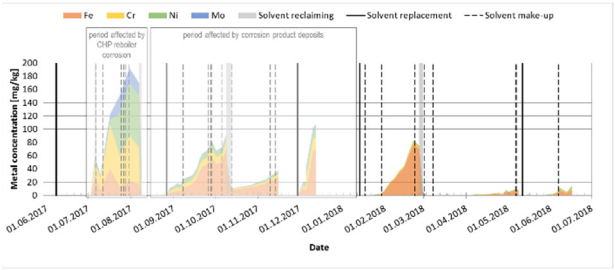

Figure 6. Metal cation concentrations during the MEA test campaigns (adapted from [1]).

Precipitation of solids (sulfates) has also been observed in the period of scavenger injection, this is suspected to have caused local flow restrictions that may have been a relevant factor supporting a flow enhanced damage, possibly in combination with the corrugated shape of the plates.

As part of a material selection assessment [1] corrosion coupons of different metals (including 316L stainless steel, bent) were placed in key locations within the solvent circuit. In each location there were two coupon racks positioned towards the top (upper) and bottom (lower) of the pipe. Analysis of these coupons also provided additional useful feed-back on the possible origins of the corrosion failure.

Among all corrosion coupons locations (hot and cold lean solvent, hot and cold rich solvent, stripper overhead) the 316L stainless steel specimens only showed signs of corrosion in the hot rich solvent (see Table 2). No corrosion was observed on stainless steel coupons exposed to the hot lean solvent. The carbon steel specimens were completely corroded in several locations, indicating generally high intrinsic corrosivity of the solvent.

Table 2. Corrosion rate of carbon steel (CS235) and stainless steel (SS 316L) coupons based on 7420 hours exposure to solvent (from [1])

Location	Steel type	Corrosion rate (mm/y)	
		upper	lower
Hot lean solvent	CS235	>5.91	>5.95
	SS 316L	0.00	0.00
Hot rich solvent	CS235	>6.46	>6.33
	SS 316L	0.02	0.08
Cold lean solvent	CS235	1.62	1.56
	SS 316L	0.00	0.00
Cold rich solvent	CS235	>3.24	>3.25
	SS 316L	0.00	0.00
Stripper overhead	CS235	0.00	0.00
	SS 316L	0.00	0.00

The solvent composition and temperature conditions in this location have similarities with the region where the corrosion damage occurred. This suggests that elevated temperature and the solvent composition (either or both) may be related to increased general corrosion rate. The conditions in the hot rich solvent coupon rack location alone, however, did not cause corrosion of unacceptable severity. Other factors must have contributed to the corrosion of the reboiler plates. Flashing of CO_2, expected to occur in the reboiler, is likely such a factor.

It is notable that within the same specimen location (hot rich solvent) the bent stainless steel coupons had quite different corrosion behavior and appearance depending on their position (see Table 2, Figure 7; for more details see Flø et al [1]):

- the lower bent coupon had higher corrosion rate
- stainless steel coupons in the lower position showed a red coloration (identified as iron oxides)
- not all coupons from the same rack (or position) displayed the colored layer (bent stainless steel in the upper position did not, while other coupons in the upper position did; photos not shown)

These observations may suggest that:

- bent shape may have played a role (strain or flow related)
- the red-brown deposit layer may not have played a significant role (some coupons with deposits did not corrode)

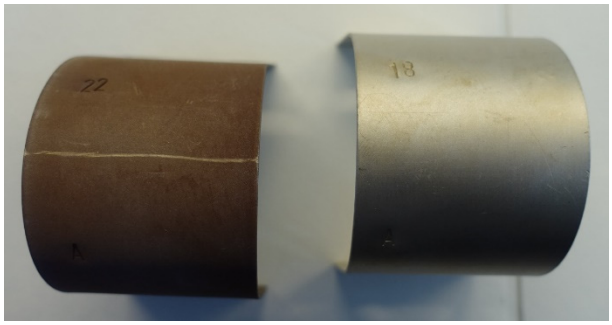

Figure 7. Appearance of bent stainless steel coupons after exposure in the hot rich solvent location. Coupon from the lower position on the left (adapted from [1]).

Solids precipitating (sulfates) in the period of scavenger injection did not appear to affect the corrosion coupons considerably. Deposition within the reboiler plates causing local flow restrictions, however, may be a relevant factor.

An important detail of the reboiler plates is their corrugated shape. The flow regime is expected to be different in the space between the plates and this shape may provide locations for impingement to occur. This may be a relevant factor both in the presence of abrasive particles (erosion) and in their absence.

2.3. Main hypotheses and scope of experimental work

From a detailed consideration of the collected data, two distinct scenarios and a combination of the two have been explicitly considered when forming the main hypotheses to guide the planning of the experimental testing.

1. Erosion. This hypothesis considers that erosion is both necessary and sufficient to cause the failure, the corrosivity aspect being irrelevant for this scenario. Erosion can remove the passive film from the stainless steel surface and even the regular operation conditions may have been corrosive enough to attack the unprotected stainless steel. In principle erosion could be severe enough to abrade the steel as well, not only the passive film.

2. Enhanced corrosivity. According to this hypothesis the specific chemistry in the scavenger period can cause depassivation and sustain a considerably high corrosion rate, probably in combination with some depassivating effect of the amine or its degradation products. The erosion aspect would be in practice irrelevant in the context of this scenario.

3. Erosion and enhanced corrosivity. Erosion could remove passivity, but regular conditions would not be enough to prevent rapid repassivation to sustain corrosion. The specific chemistry in the scavenger period could sustain corrosion in the absence of a passive film but would not be able to depassivate the surface. Enhanced corrosivity could depassivate and maintain a certain corrosion rate, but not high enough to lead to rapid failure.

The main working hypotheses delineated above form the basis for defining the scope of the experimental validation work, as outlined in the diagram below.

Precipitation of solids has been observed, yet there is a lack of information about its nature and properties. Verifying the precipitation and characterization of the solids are therefore considered an important part of the scope.

More specific aspects are discussed within the Experimental approach section.

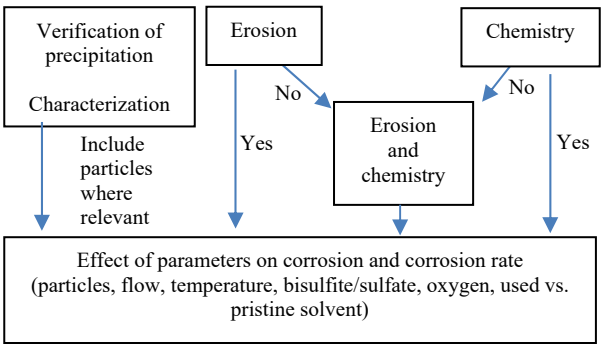

5. Experimental approach

5.1. Apparatus

It is important at the outset to distinguish between two possible modes of operation when it comes to experimental design. The real-life conditions in the region of the reboiler where the failure has occurred are thought to be represented by a transition between partly stripped rich solvent and lean solvent. It is a dynamic scenario where the system may not reach thermodynamic equilibrium within the residence time of the solvent flowing through. Studying such a system experimentally can be done in two ways:

- dynamic (flowing type) experiments mimicking closely the plant process (including continuous feeding and removal of solvent); this type of experiments may be a better representation of the conditions in the reboiler, but those specific conditions would at the same time be difficult to assess due to continuous transitions.
- static (batch type) experimental series where one set of conditions is implemented, variations are studied by parametric studies (test matrix); for this approach thermodynamic equilibrium can be reached, the conditions are known with higher level of certainty, making correlations between parameters and results more robust. The static mode is preferred for most of the planned experiments.

The experimental setup is to be built around a closed autoclave that can be operated under the desired pressure and temperature conditions. The setup is designed to be modular, allowing for both flowing and batch type of experiments.

A key consideration of the test setup was that it should be flexible enough to allow specimens to be exposed to a combination of the key factors (temperature, pressure, flow, action of suspended solids, specific chemical environments) and ideally allow in situ electrochemical measurements to be carried out. A glass reactor allows visual observation of precipitation and efficient suspension of solid particles.

Figure 8 presents a graphical representation of the envisioned test autoclave setup, where two types of specimens can be exposed, possibly in all experiments:

- impeller blade specimen: mounted in special holders that allow rectangular specimens to be affixed to the end of a rotator shaft. The specimen will act as impeller blade which will provide enhanced flow, shear, entrainment of suspended solids and possibly entrainment of bubbles. The specimen will be electrically isolated from any metallic parts (e.g. the shaft itself) to avoid galvanic coupling
- stationary specimens placed to receive impinging flow from the impeller; outfitted with electrical connections for electrochemical measurements

Figure 8. Sketch of the reactor with specimens placed as both impeller blades and stationary

5.2. Test conditions

The “history” of the solvent may render its chemical composition greatly different from pristine solvent. Comparison of the stainless steel behavior in clean and

used solvent from TCM may reveal whether these differences have a detrimental effect on the passivity of the steel or may affect other aspects (e.g. solubility and precipitation). It is therefore envisioned that experiments will include both pristine and used solvent.

The majority of the experiments will fall within a parametric study performed in batch mode. The test system will reach equilibrium within the timeframe of the experiments, yet can initially undergo transitions, e.g. when starting with rich solvent and driving the conditions toward lean or an intermediate state of the solvent. An advantage implied is that the thermodynamic (and, to a certain extent redox) behavior of the solvent system can be predicted, helping technical planning and execution of the tests as well as interpretation of the results.

The key parameters considered/studied to be included within the scope of the experimental work are listed below:

Temperature: in the range relevant to rich-lean transition (around 120 °C), extensions to lower and higher values for sensitivity.

Solvent and CO_2 loading: both pristine and used solvents to be included, both rich and lean may be relevant starting solutions. Aspects of chemical composition related to solvent history (i.a. degradation products) are implicit.

Oxygen and scavenger: these species are of special relevance and the impact of their reaction product (sulfate) as well as the excess of one species over the other is to be included

To gain a better understanding of how environmental parameters will affect the studied system of equilibria, a series of scenarios have been preliminarily modelled using the OLI Studio software where the composition and speciation as a function of temperature at a given total pressure were predicted.

CO_2 loading of lean solvent

It is envisioned that initial loading of pristine lean solvent shall be performed by continuous purging with pure CO_2 at low temperature and ambient pressure. Model calculations presented here are based on 30 mass% MEA and the reaction below. Dissolution of CO_2 into the aqueous phase is also accounted for. Reaction kinetics are not considered. The case presented here as an example models the CO_2 loading process at 40 °C.

$$2\ MEA + CO_2 \leftrightarrow MEA\text{-}COO^- + MEAH^+$$

To be noted that used lean solvent will likely not be completely stripped of CO_2. It is expected, however, that reloading by this procedure would yield the same final conditions as loading of pristine lean solvent.

Figure 9 shows the distribution of species during the loading process modelled at 40 °C.

Up to an uptake of ca. 0.4 mol CO_2 / mol MEA all added CO_2 is predicted to be bound by the solvent (see Figure 9). As more CO_2 gas is purged through the solvent, the bound fraction continues to increase while some of the CO_2 is being retained as dissolved CO_2 (see lower panel in the same figure). After ca. 0.6 mol CO_2 / mol MEA has been added, the dissolved CO_2 will reach saturation and all further addition will escape into the gas phase while the speciation appears to remain constant. This gives a predictable and reproducible state with a constant chemical composition. Performing the loading process at lower temperatures will ensure that the composition will not be significantly altered by e.g. evaporation, resulting in good consistency.

Should it be considered necessary to perform experiments starting with a particular loading level, it can be achieved by mixing the loaded stock with pristine lean solvent in the required proportion.

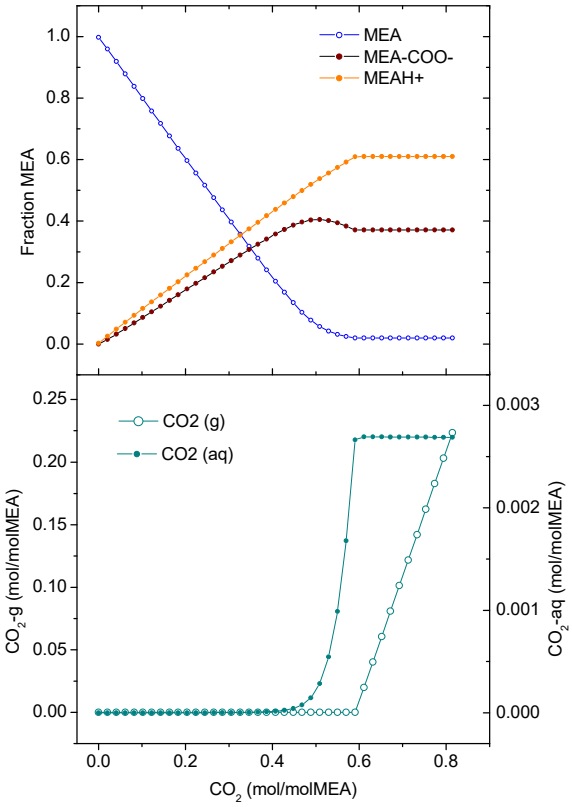

Figure 9. Plot of the evolution of selected species during loading of MEA by purging with pure CO_2 at 40 °C and ambient pressure

Isobaric heating of rich test solutions

It is expected that during temperature ramping the solution composition will show a transient, reaching the new equilibrium after some time at the target temperature depending on the kinetics of the processes involved. This implies that testing in a closed reactor at fixed conditions (batch testing) will give results where equilibrium can be assumed to have been established within the timeframe of the experiment. In a continuous flow system, in contrast, a continuous transition may be envisioned (rich solvent continuously fed, lean solvent removed, flashing of CO_2).

To understand the behavior of the test solutions upon heating to a high target temperature, the process was modelled using the OLI Studio software starting with a fully loaded rich solvent (generated as described in the previous section and ramping the temperature from 40 °C to 120 °C while maintaining the reactor vessel pressure at 2 bar.

As shown in Figure 10, increasing the temperature leads to the gradual reversal of the loading process, releasing more and more CO_2. It is to be noted that for each given temperature a new equilibrium state can be reached characterized by a distinct distribution of species. Evidently, care must be taken to release the gas-phase CO_2 to avoid excessive pressure buildup in the vessel. To illustrate this, the bubble point of three solutions was plotted in Figure 11 as the temperature was raised to 120 °C as follows:

- Solvent loaded with CO_2 at 40 °C and ambient pressure (as described in section 0)
- Solvent at equilibrium at 80 °C and 2 bar
- Solvent at equilibrium at 110 °C and 2 bar

While it is not expected that the pressure would rise to the bubble point value (since there is always a gas pocket present in the reactor), considerable pressure can build up if the released CO_2 is not vented.

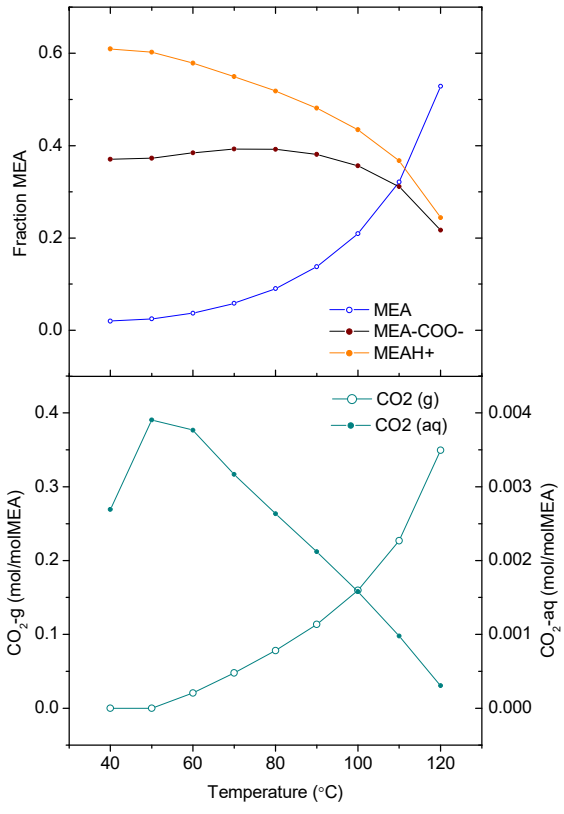

Figure 10. Plot of the evolution of selected species as a result of increasing the temperature of a solution prepared as described in the text

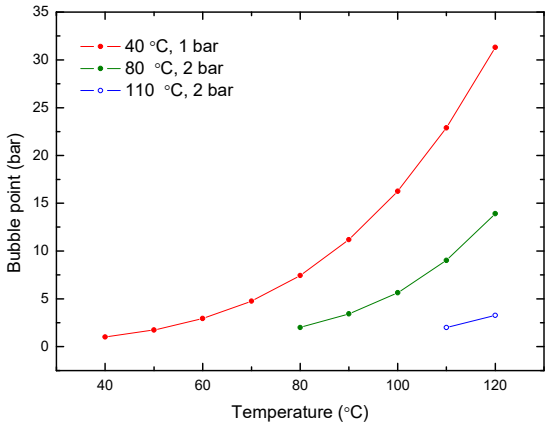

Figure 11. Plots of the bubble point as a function of increasing temperature for three different starting solutions

Addition of oxygen and oxygen scavenger

The modelling results indicate that addition of $KHSO_3$ as oxygen scavenger is expected to affect the speciation in the solution as it will lower the pH. Shown in Figure 12 are results of model calculations for various concentrations of added potassium bisulphite. The reaction with dissolved O_2 was taken into account in these calculations. It is predicted that the equilibrium composition of the test solutions will change as a function of the added scavenger concentration for any given temperature. In other words, for a given test temperature and pressure the composition will be different in the presence and the absence of the oxygen scavenger.

Starting solutions will be prepared by first adding the prescribed quantity of $KHSO_3$ to the lean solvent, followed by purging the solution with air until the scavenger-oxygen reaction is complete, to yield the desired level of sulphate in solution. This will be performed at low temperature to avoid excessive evaporation and have an increased O_2 solubility. The solvent will then be loaded with CO_2; this process is expected to effectively purge out excess dissolved O_2.

For experiments with excess bisulphite it can be dosed as desired to the resulting enriched solvent.

For experiments with excess O_2 the solution can be purged with air or a gas mixture at low temperature to yield the desired dissolved O_2 concentration at equilibrium while avoiding removal of bound CO_2. Dissolved oxygen will not remain constant during testing; flashing of CO_2 upon heating may remove dissolved O_2. If it is desirable to maintain O_2 in solution purging with air or gas mixture can be applied during tests as well.

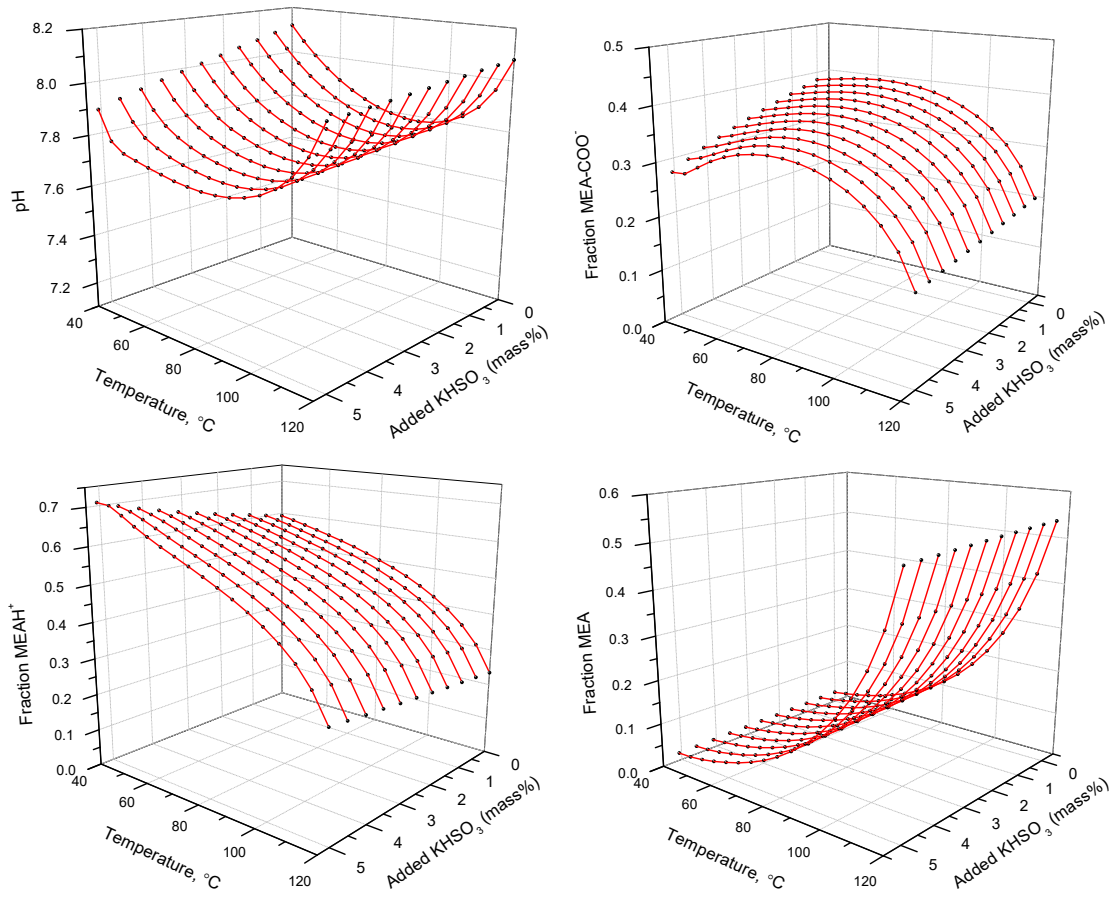

Figure 12. Plots of the pH and concentration of selected species at equilibrium as a function of temperature and added oxygen scavenger

5.3. Abrasive solids

Should precipitation studies result in a reproducible way to generate solids in situ, it shall be implemented for the tests involving an erosion aspect. If in situ generation of particles is not successful, erosion-corrosion tests can be performed using inert solids, e.g. silica (sand) particles. These may be expected to be harder and more abrasive than precipitating particles.

6. Way forward

The outlined experimental work (Phase 2 of this collaborative effort) will be carried out as a systematic parametric study at the IFE laboratories closely coordinated with TCM, Total and Equinor. The effects of erosion and corrosion (as well as synergies thereof) will be distinguished by means of judicious testing of the main hypotheses, i.e. within the scopes they define, as described in Section 2.3; experiments targeting a given hypothesis will be carried out with focus on the particularities related to that hypothesis (erosion – suspended solids, enhanced corrosion – chemical composition, etc.). It is expected that the majority of experiments will be carried out in batch mode, with selected conditions tested in flowing mode as well. The actual test matrices are to be adapted constantly as needed in view of the obtained results. The results, interpretations and conclusions regarding the working hypotheses will be reported in a separate publication.

Acknowledgements

The authors wish to thank TCM, Total and Equinor for the collaboration and the permission to publish this material

References

[1] Enaasen Flø, N., Faramarzi, L., Iversen, F., Romslo Kleppe, E., Graver, B., Nornes Bryntesen, H. and Johnsen, K., Assessment of Material Selection for the CO2 Absorption Process with Aqueous MEA Solution based on Results from Corrosion Monitoring at Technology Centre Mongstad, 14th International Conference on Greenhouse Gas Control Technologies, GHGT-14, Melbourne, Australia (2018)

[2] Addington, C. F. and Hendrix, D. E., Aggressive Corrosion of 316 Stainless Steel in an Amine Unit: Causes and Cures, CORROSION 2000, paper no. NACE-00698, NACE International, 2000

[3] Kittel, J. and Gonzalez, S., Corrosion in CO2 Post-Combustion Capture with Alkanolamines – A Review, Oil & Gas Science and Technology – Rev. IFP Energies nouvelles, Vol. 69 (2014), No. 5, pp. 915-929

DEVELOPMENT OF SILICA SODALITE WITH ENHANCED POROSITY VIA TOPOTACTIC SYNTHESIS FOR PRE COMBUSTION CO_2 CAPTURE

C-I. Eden, N. Ntombela, M.O. Daramola*

School of Chemical and Metallurgical Engineering, Faculty of Engineering and the Built Environment, University of the Witwatersrand, Johannesburg, South Africa

* Corresponding author e-mail: michael.daramola@wits.ac.za

Abstract

Topotactic conversion of layered silicates is reported to yield sodalite with enhanced frameworks, chemical compositions and predictable outcomes. Traditional hydrothermal synthesis results in sodalite with occluded matter preventing the effective use of sodalite cages for adsorption and separation applications. However, the reproducibility of high quality silica sodalite depends on obtaining optimized synthesis conditions and investigating the effect these conditions is essential. A 2^3 factorial design was employed to investigate the effect of process variables (acid strength, acid treatment time and calcination temperature) on the quality of silica sodalite produced via topotactic conversion in this study. XRD, SEM and Nitrogen physisorption at 77K were used for physio-chemical characterization of the sodalite samples. The produced sodalite crystals were used in membrane synthesis, and the membrane was tested for $CO_2/H_2/N_2$ separation. Sodalite of desirable crystallinity and plate-like morphology was produced with surface area and porosity of 79.44m^2/g and 0.081cm^3/g, respectively. An incomplete transformation of sodalite at low acid concentration and treatment time was experienced. A significant improvement on surface area and pore volume was reported on all samples as compared to that of the hydroxy sodalite. Analysis of the regression model obtained from the experimental data indicates acid treatment time as an insignificant variable. The preliminary investigation of the application for membrane synthesis indicates enhanced porosity of the HSOD improved the membrane H_2 permeance by 178%.

Keywords: *Silica sodalite, Topotactic conversion, Response surface methodology*

1. Introduction

Increasing levels of anthropogenic CO_2 have been noted as a major cause for environmental climate change. The most effective means for remediation focuses on point-source emission such as power plants [1]. The majority of the world's energy production comes from the combustion of fossil fuels, and an example of a system employed to achieve this is the Natural Gas Combined Cycle (NGCC) or Integrated Gasification Combined Cycle (IGCC) which result in large volumes of CO_2 emissions [2]. The depletion of fossil fuels and the increasing energy demand have led to a global movement towards high energy efficiency of industrial processes and the capture of point-source CO_2 emissions [3, 4]. Carbon capture from power generation is possible through three ways; pre-combustion, post combustion and oxy-fuel combustion capture. Pre-combustion carbon capture is typically favoured in coal burning IGCC power generation due to the high concentration of CO_2 in the flue gas (>20%) which improves the sorption efficiency and increases the heating value of the hydrogen fuel stream [5, 6]. For these reason a large amount of research has gone into the separation of CO_2 from gases such as H_2 and CH_4.

Traditional large scale CO_2 separation methods such as pressure-swing adsorption and cryogenic distillation are preferred due to their reliable nature, superior separation and low capital costs but are highly energy intensive and utilize environmentally damaging chemicals [7, 8]. Membrane systems provide an alternative with low energy intensity, operating and capital costs as well as high flux [9]. However, the high temperature and steam utilized in coal gasification means that membranes used for in pre-combustion CO_2 capture need to be thermally and hydro-thermally stable, with good separation performance to make them an economically feasible alternative to traditional methods [9, 10]. Polymeric membranes form the majority of membranes current used in industry, however these membranes can be brittle and exhibit an undesirable trade-off between permeability and selectivity [7]. Mixed matrix membranes (MMM) combine the high selectivity and easily processable nature of polymers with inorganic materials such as zeolites, and are being intensively investigated for gas separations [1, 11-13]. One candidate material employed in membrane development and applicable in pre-combustion CO_2 capture is hydroxy sodalite [14, 13].

Hydroxy sodalite is a common zeolite with cage structures consisting of 4 and 6 ring sodalite cages with pores of approximately 2.2 Å [15-17]. Sodalite has shown promise in membrane applications due to its low framework density and small cage apertures (0.265 nm) which could effectively separate small atoms such as hydrogen (0.289 nm) from carbon dioxide (0.33 nm) [12, 13]. Synthetic sodalite fabricated via the hydrothermal method typically contain less occluded water but large

volumes of occluded organic matter from solvents and structure directing agents (SDA) used during synthesis as well as small molecules such as hydrogen and helium which block pores and prevent the effective use of the sodalite cages [9, 14]. Removing these occluded materials from the cage via dehydration or calcination at high temperatures (> 450°C) collapses the cage, rendering the sodalite ineffective [14, 18, 19]

Topotactic conversion is a relatively new synthesis method that enables the production of zeolite structures with unique new chemical frameworks, compositions and morphologies [20]. In the past decade a number of zeolites have been successfully fabricated from layered silicates using the topotactic conversion process, some of these include MWW, RUB-24 and RUB-41 [21, 22]. Sodalite formed through this method report the absence of occluded matter and increased porosity [15].

Moteki et al. [15] noted that that acid treatment with small carboxylic acids would shorten the interlayer distance and translate the layers in a parallel direction to facilitate guest exchange and produce pure silica sodalite. However, the samples produced after calcination were amorphous. This was attributed to differences in the interlayer environments caused by the gradual elimination of organic guest species. Moteki et al [19] went on to further understand the conversion process by investigating the effect of the length of the alkyl chain, the strength of the acid and the acid treatment time. Good crystallinity was observed for samples treated with acetic or propionic acid in concentrations from 3 to 9 M, with samples treated with propionic acid displaying the highest crystallinity. While those treated with formic or butyric acid resulted in amorphous products after calcination. The use of 1M propionic acid resulted in low crystallinity which was attributed to poor ion exchange and non-uniform interlayer distances. The crystallinity of the samples increased with increasing acid treatment time from 10 seconds to 10 minutes, no further improvements for samples treated up to 3 hours were recorded but residual TMA+ cations were noted in samples treated for less than 3 hours. In spite of inconsistencies in the results, Moteki and his associates concluded that effective synthesis of pure silica sodalite through topotactic conversion is realizable [19].

Koike et al. [20] proposed a stepwise method including intercalation of N-methylformamide (NMF) into the acid treated RUB-15 before calcination for the synthesis of silica sodalite. Furthermore, the authors use both HCl and acetic acid to treat the RUB-15. All samples prepared using HCl were reported to be amorphous after calcination while plate-like sodalite was successfully synthesized with acetic acid (6M). In addition, the role of the NMF was suggested to be similar to that of the SDA, but yielded an inferior quality of sodalite to those produced hydrothermally.

Evidently, previous studies have shown inconsistencies in the synthesis of silica sodalite produced via topotactic conversion thereby diminishing its reproducibility. Furthermore, the influence of synthesis conditions is shown to be a major hurdle. In depth understanding of the influence of synthesis conditions would be paramount to developing a robust technique for the reproducible synthesis of silica sodalite via topotactic conversion. This study investigated the effect of synthesis conditions on the textural and morphological quality of silica sodalite produced in order to optimize the pore volume of the synthesized sodalite. A preliminary investigation on the application of the produced crystals in membrane synthesis and application was carried out as well.

2. Experimental

2.1 Materials

Tetra-ethoxysilane (TEOS, reagent grade 98%, Sigma-Aldrich, South Africa), tetrametyl ammonium hydroxide (TMAOH, 25wt.% in water, Sigma-Aldrich, South Africa) and acetone (Sigma-Aldrich, South Africa) were used for the synthesis of RUB-15. Propionic acid (>99.5wt.%, Sigma-Aldrich, South Africa) was used for the acid treatment of RUB-15 in the synthesis of silica sodalite. Sodium metasilicate (Sigma-Aldrich, South Africa), sodium hydroxide pellets (Sigma-Aldrich, South Africa) and anhydrous sodium aluminate (Sigma-Aldrich, South Africa) was used for the production of hydroxy sodalite (HSOD) for comparison. Membranes were prepared from polysulfone (PSf, beads (transparent), Sigma-Aldrich, South Africa) and N,N-Dimethylacetamide (>99.9%, Sigma-Aldrich, South Africa). Pure gas cylinders were purchased from Afrox, South Africa (N_2, H_2, CO_2, >99.9%).

2.2 Synthesis methods

The procedure stipulated by Moteki et al. was used for the synthesis of RUB-15 [19]. TEOS and TMAOH were combined in a 1:1 molar ratio and stirred for 24 hours to homogenize. The solution was then placed in a Teflon autoclave and heated at 413 K for 7 days. RUB-15 was recovered as a white waxy substance, which was washed with acetone, separated by centrifugation and dried overnight at 333 K in a convection oven to yield a white powder.

The obtained RUB-15 (0.1 g) was dispersed in propionic acid (30 ml) of varying concentrations (1-5 M) and stirred at 900 rpm for various time periods (10-180 minutes). The solution was separated by centrifugation, washed repeatedly with deionized water and dried in a convection oven overnight at 333 K. The samples were then calcined for 5 hours at temperatures between 1073 and 1173 K.

HSOD crystals were synthesized by hydrothermal synthesis using sodium metasilicate, sodium hydroxide pellets, anhydrous sodium aluminate, and deionized water as described by Daramola et al. [14].

2.3 Characterization of synthesized particles

Powder X-ray diffraction (XRD) patterns were performed on both the precursor RUB-15 layers as well as the calcined sodalite using a Bruker D2 XRD with CuKα radiation (λ = 1.54060 Å) to analyze the crystalline and amorphous nature of the sodalite. Scanning electron microscopy (SEM) was conducted on a Carl Zeiss sigma field emission scanning electron microscope equipped with Oxford X-act EDS detector to examine the surface morphology and elemental composition of the samples.

Single point Brunauer-Emmett-Teller (BET) analysis was conducted from the results of Nitrogen Physisorption at 77 K, to determine the surface area (SA) and pore volume (PV) and pore size (PS) of the sodalite samples.

2.4 Experimental design

A statistical approach using response surface methodology was employed to investigate the effect of synthesis variables on sodalite quality. A 2^3 full factorial design was utilized to reduce the number of experimental runs as opposed to traditional design methods as well as to account for the main and interactive effects of the variables. Design Expert v.11 Software (Stat-Ease, USA, 2018) and Matlab software (2016) was used to statistically analyse the experimental data. The 2^3 factorial design was implemented to investigate 3 factors at 2 levels producing a minimum of 8 runs. Three factors were considered; acid concentration (A), acid treatment time (B) and calcination temperature (C). The 2 levels and the mid-level (also referred to as the center point) utilized for each factor as tabulated in the experimental design scheme (Table 1).

Table 1: Experimental Design Scheme

Run	Coded Values			Actual values		
	A	B	C	A	B	C
	M	minutes	K	M	minutes	K
SSOD 1	1	1	-1	5	180	1073
SSOD 2	-1	1	-1	1	180	1073
SSOD 3	1	-1	-1	5	10	1073
SSOD 4	-1	-1	-1	1	10	1073
SSOD 5	1	1	1	5	180	1173
SSOD 6	-1	1	1	1	180	1173
SSOD 7	1	-1	1	5	10	1173
SSOD 8	-1	-1	1	1	10	1173
SSOD 9	0	0	0	3	95	1123

A) Acid concentration; B) Acid treatment time; C) Calcination temperature

The center point was included in the study to improve statistical significance and aid in exploring the curvature effect in the design space [23]. Due to limited resources a single replicate was utilized preventing the estimation of pure error. It was assumed that the system was dominated by the main effects and low-order interactions, following the effect sparsity principle [24].

2.5. Model Formulation

A general regression model was assumed (Equation 1) and the experimental data was utilized to determine the best model. Design Expert v.11 Software (Stat-Ease, USA, 2018) and Matlab Software (2016) were used to investigate ten candidate models.

$$y = \beta_0 + \beta_a A + \beta_b B + \beta_c C + \beta_{ab} AB + \beta_{bc} BC + \beta_{ac} AC + \beta_{abc} ABC \pm \epsilon \quad \text{Equation 1}$$

In Equation 1, y represents the system response (pore volume), β_o the intercept of the regression line, $\beta_{a,b,c}$ the regression coefficients for the respective synthesis variables A (acid concentration), B (acid treatment time) and C (calcination temperature), with ϵ being the mean square error.

An ANOVA test was performed on each candidate model and the P values (within 95% confidence interval) for each model term and the model as a whole was assessed to determine significance. Lacks of fit tests of the suggested model were also calculated within a 95% confidence interval, the coefficient of determination (R^2), the adjusted R^2 as well as the mean square error were evaluated to produce the suggested model.

2.6. Membrane synthesis and single gas permeation tests

Membrane synthesis followed the phase inversion technique as documented elsehwere [18]. To fabricate the membranes, individual measurements of SSOD (0 and 5 wt. %) as well as HSOD (5 wt. %) were mixed with 20 ml of N,N Dimethylacetamide for 3 hours before 5 g polysulfone was added and stirred for a further 24 hours. The mixture solution was repeatedly ulltra-sonicated and mixed to ensure a homogeneous mixture. The solution was cast into a thin film membrane using a "doctor" blade and a glass plate. Membranes were immediately submerged in deionized water and soaked for 24 hours. The membranes were then oven dried at 333 K for 2 hours. Membrane thickness (l) was measured using a digital outside micrometre (InSize, 3109-25A).

The single gas permeation tests were carried out using pure component of N_2, H_2, and CO_2 in a custom-built separation rig using a membrane area (A) of 9.6 cm^2. The feed upstream pressure was set to 1 bar_g at ambient conditions (temperature = 298K). The pure gas permeability (P) was calculated following Equation 2 in Barrer (1 Barrer = 1×10^{-10} cm^3(SPT).cm/cm^2.s.cmHg) [9, 12]. The volumetric gas flowrate (Q) and transmembrane pressure (Δp) were measured from the rig. Dividing permeability by membrane thickness yields the membrane permeance. Measurements were converted to SI units
(1 Barrer = 3.35×10^{-16} mol.m/m^2.s.Pa).

$$P = \frac{l\,Q}{A\,\Delta p}\,\frac{273.15}{T} \quad \text{Equation 2}$$

From the individual permeability, the ideal selectivity (α) for gas A over gas B was calculated using Equation 3.

$$\alpha_{A/B} = \frac{P_A}{P_B} \quad \text{Equation 3}$$

3. Results and discussion

3.1. Physio-chemical characterization

3.1.1. Crystallinity and morphology

The RUB-15 synthesized displayed some of the characteristic peaks shown in literature such as the peaks at 2θ= 15° and 22° (Figure 1) [25, 26, 15]. However, the strongest characteristic peak at 2θ = 6.3° is not present in the XRD pattern. A significant amount of noise is present and the low crystallinity suggests a high volume of intercalated TMA^+ cations [19]. The SEM images of the RUB-15 depict the plate-like morphology of similarly sized and shaped plates, superposed onto one another in agreement with Moteki et al [19].

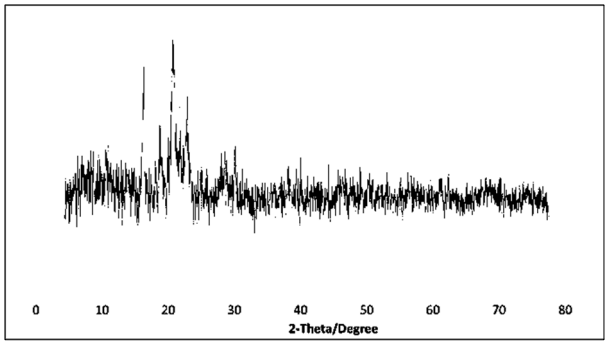

Figure 1: XRD pattern for synthesized RUB-15.

The HSOD synthesized hydrothermally for comparison shows correctly positioned XRD diffraction peaks and good crystallinity (Figure 2) in line with the work conducted by Daramola, et al and the IZA simulated octahydrate standard [14, 27]. In comparison to the sodalite synthesized via topotactic conversion the HSOD displays higher crystallinity and a greater number of the characteristic peaks.

The samples prepared from the propionic acid treatment and calcination of synthesized RUB-15 displayed XRD patterns (Figure 2) with two of the characteristic peaks of the IZA SOD standard, specifically at 2θ= 12.2° and 21.2° [27]. All of the samples display a large volume of noise and an amorphous hump indicating incomplete transformation of the crystalline phase due to the formation of intra-layer Si-O-Si bridges [28]. Considering the poor crystallinity of the synthesized RUB-15 precursor, poor crystallinity is expected in the produced sodalite samples. Silica sodalite sample 4 (SSOD4) was initially dominated by noise and impurities (as seen by the background pattern) but when repeated displayed the significant peaks at low intensities and a smooth pattern as shown in Figure 2. This clearly highlights an inconsistency in reproducibility. The intensity of diffraction peaks was seen to decrease with increasing sample number and a tradeoff between the second peak (2θ = 21.2°) and hump intensity was evident in the remaining samples. This may be attributed to incorrect layer translation with lower acid strength and treatment time [15].

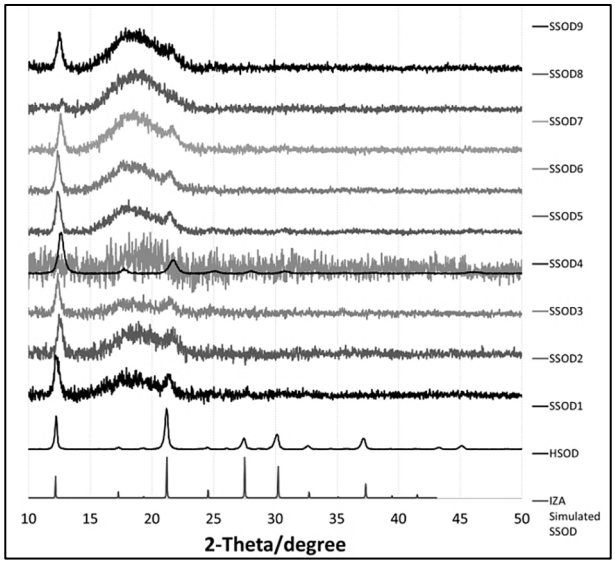

Figure 2: XRD pattern for sodalite samples (SSOD Run 1-9, RUB-15, HSOD and the IZA simulated sodalite standard)

SEM images of the synthesized HSOD show spherical morphology consisting of agglomerated rod-like structures (Figure 3b). SSOD2 and SSOD3 were determined to be of the closest morphology to RUB-15 (Figure 3c and 3d), showing plate-like morphology of larger, irregular sized plates with curled edges superposed on one another. This is similar but not identical to that of RUB-15 which depicts the layering of smaller plates (Figure 3a). This is attributed to inconsistencies in the thickness of the plates resulting in thinner plates becoming more wrinkled and curled during the condensation process [28]. SEM imaging on SSOD 4-9 produced a plate like morphology and varying degrees of curling which can be seen in the supplementary data.

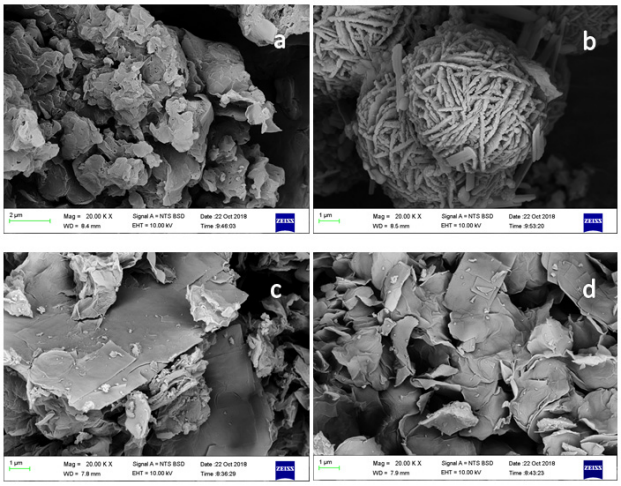

Figure 3: SEM imagines of a) RUB-15; b) HSOD; c) SSOD2; d) SSOD3

3.1.2. Textural properties

The pore volume produced from Brunauer-Emmett-Teller (BET) analysis results were used as the model response [29]; the determined model was then utilized to define optimum synthesis parameters in order to maximize the response.

HSOD was synthesized to form a baseline for comparing the sodalite surface area and pore volume. The HSOD surface area (SA) and pore volume (PV) were 2.35m^2/g and 0.012cm^3/g, respectively. SSOD 2 displayed the highest surface area and pore volume, with suitable XRD results and SEM images. Moteki and associates [19] concluded that at low acid concentrations poor crystallinity was produced, presumably due to a low degree of ion exchange, yet in this study SSOD2 synthesized at low acid concentration, low acid treatment time and low calcination temperature yielded the greatest surface area and pore volume. BET results for SSOD2 yielded a surface area and pore volume of 79.44m^2/g and 0.081cm^3/g, respectively. All samples showed increased surface area and pore volume with decreased pore size, relative to HSOD (Table 3). SSOD 2 and 3 were identified to be of the best quality despite conflicting acid concentrations.

Significant reductions in pore size of the synthesized sodalite nanoparticles as compared to hydroxy sodalite

were also observed. The synthesized silica sodalite nanoparticles are characterized as mesoporous with pore diameters between 2-50 nm. The small porosity could be instrumental to separating small molecules such as H_2 H_2O and NH_3 from bigger molecules.

Table 2: BET results for synthesized samples

Run	BET Results			Relative to HSOD		
	SA	*PV*	*PS*	*SA*	*PV*	*PS*
	m^2/g	cm^3/g	*nm*	m^2/g	cm^3/g	*nm*
SSOD1	42.91	0.065	6.09	18.29	5.49	0.30
SSOD2	79.44	0.081	4.08	33.87	6.81	0.20
SSOD3	70.54	0.072	4.07	30.07	6.03	0.20
SSOD4	43.61	0.064	5.87	18.59	5.37	0.29
SSOD5	18.85	0.046	9.81	8.04	3.89	0.48
SSOD6	26.02	0.052	7.96	11.09	4.35	0.39
SSOD7	23.38	0.051	8.76	9.97	4.30	0.43
SSOD8	42.27	0.064	6.06	18.02	5.38	0.30
SSOD9	21.74	0.049	8.97	9.27	4.10	0.44
HSOD	2.35	0.012	20.29	1.00	1.00	1.00

3.2. Pore volume regression model

Response surface methodology was utilized to better understand the main and interactive effects of the topotactic synthesis variables on the porosity of the sodalite produced. The half-normal (Figure 4a) and Pareto Plots (Figure 4b) were evaluated to determine the significant factors. Factor C- temperature and Factor A- acid concentration fall to the right of the half-normal plot and were recommended as key factors. Factor C- temperature has a much greater standardized effect and this can be seen in the Pareto plot where only factor C- temperature is likely to be a significant model term.

Multiple candidate models (linear, 2 and 3 factor interaction, quadratic) were examined for the best fit to experimental data using regression analysis. The majority of these models produced good regression coefficients but high P values leading to an insignificant model. In all candidate models factor B- acid treatment time had an exceptionally high P value and was determined to have close to no effect on the response, for this reason it was removed from the model equation and should not be considered a critical synthesis parameter for future work. This result is corroborated by the report of Moteki et al, where no difference in sodalite crystallinity for samples treated for 10 minutes as opposed to those treated for 3 hours was reported [19].

A model utilizing factors A and C was adopted as the best fit to experimental data, displaying high regression with sufficiently low p-value. The empirical model suggested to relate synthesis variables to pore volume is expressed in Equation 4.

$$PV = 0.2599 - 1.64X10^{-3}A - 1.72X10^{-4}C \pm 2.98X10^{-5}$$ Equation 4

ANOVA analysis of the suggested model revealed a significant model of a sufficiently low probability value of 0.0428 (P <0.05) within a 95% confidence interval. While good correlation between the experimental values and the regression model as stated by the coefficient of determination (R^2) of 0.7164 was observed, this value is not as close to 1 as desired. This indicates 28.36% of the total variation was unexplained by the suggested model as can be seen from the spread of points from the regression line on the graph of experimental and predicted values in Figure 4c.The greater the F value for each term, the greater the effect that variable will have on the response [30].

Factor C was concluded to be a significant model term with a p-value of 0.021 (p < 0.0500) and F value of 8.4 indicating a significant contribution to the response. An adequate precision value of 5.127 was calculated. This represents the signal to noise ratio. As the value is above 4, the signal was determined to be of adequate strength to navigate the design space (Table 4). A low coefficient of variance (C.V. %) indicates the good reliability and high precision in the suggested model, the calculated value of 12.12 % shows adequate reliability and precision. The graph of internally studentized residuals (Figure 4d) confirms the independence assumption and exhibits random scatter. All points fall within the limits and the absence of clustered data confirms satisfactory fit of the proposed model.

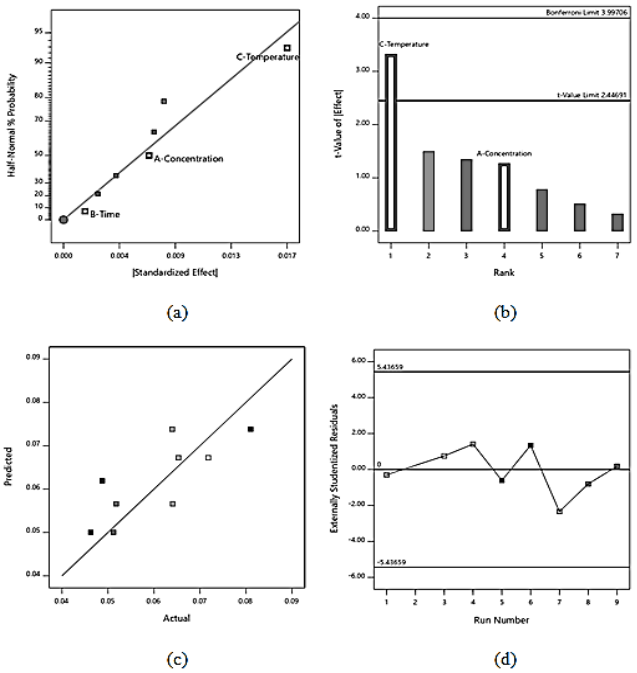

Figure 4: a) Half-normal; b) Pareto chart; c) Predicted versus actual values; d) Residual versus run plot

Table 3: Analysis of variance for main effects of the variables

Source	Sum of squares	df	Mean	F-value	p-value
Model	67.8×105	2	33.9×105	6.315	0.043
A	8.63×105	1	8.63×105	1.609	0.261
C	59.1×105	1	59.1×105	11.020	0.021
Curvature	0.000154	1	1.54×105	2.8687	0.151
Residual	0.000268	5	5.36×105		

Cor Total	0.0011	8			

Table 4: Statistical parameters

Std. Dev.	0.007	R^2	0.716
Mean	0.060	Adjusted R^2	0.603
C.V. %	12.115	Adeq Precision	5.128

The 3-D response surfaces and 2-D Contours visually describe the effects of the independent variables and their interactions on the response. The curvature of the system was found to be insignificant in the ANOVA analysis however, removing this term renders the model insignificant. The lack of curvature in the design space can be seen by the straight contour lines in Figure 5b. Lower acid strength and lower calcination temperature can be seen to produce greater pore volume of the nanoparticles. It could be speculated that lower acid strength correlates to a lower degree of ion exchange and the inhibition of well-ordered silicate layers, thereby resulting in poor crystallinity [19]. Thus it could be explained that the high surface area and pore volume produced is as a result of high degree of ion exchange between interlayer TMA^+ and H^+ cations leading to the rapid formation of Si-OH bonds with greater removal of TMA^+ cations, resulting in enhanced cage dimensions [19]. Lower calcination temperature is favourable for increased porosity as decomposition of interlayer propionic acid is limited (>873 K). Complete removal of organic matter at higher temperatures through the small sodalite cage aperture could result in the collapse of the cage structures and reduced porosity [31].

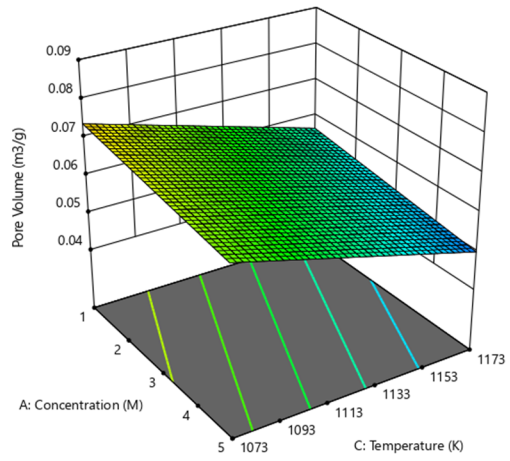

(a)

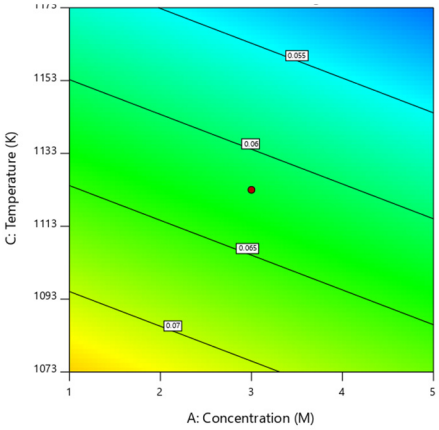

(b)

Figure 5: (a) 3-D response surface and (b) 2-D contour diagram showing the interaction between acid strength (A) and calcination temperature (C) at (B = 95 min)

3.3. Model validation

Synthesis variables were tested for reproducibility and model confirmation (Table 5). New RUB-15 was synthesized following the same procedure and found to have a higher crystallinity than that initially reported in this study. While this facilitated greater crystallinity in the product, the pore volume of the produced sodalite samples exhibited a large error in relation to the model predicted values. This highlights problems with reproducibility of the process and the modeling of synthesis factors due to the 2-stage synthesis; synthesis of RUB-15 and conversion to SSOD.

Table 5: Model validation

A	B	C	Experimental (cm^3/g)	Predicted (cm^3/g)	Error (%)
1	180	1173	0.043	0.057	32.56
5	180	1173	0.061	0.050	18.03

Optimization was conducted maximizing surface area and pore volume and minimize pore size while keeping the synthesis parameters within the upper and lower limits. An optimal surface area, pore volume and pore size of 56.72 m^2/g, 0.074 cm^3/g and 0.5026 nm respectively were proposed at 1M, 95 minutes and 1073 K. Low calcination temperatures were desirable to maximize both surface area and pore volume.

4. Membrane synthesis and single gas permeation tests

A preliminary study was conducted to investigate the synthesis and performance of mixed matrix membrane obtained using the SSOD (SSOD infused PSf membranes). The synthesized SSOD (5 wt. %) and HSOD (5 wt. %) were infused into polysulfone (PSf) and tested for the separation of H_2/CO_2. These membranes displayed an asymmetric morphology common to polysulfone (SEM images are not shown in this article) [32, 18]. Results of single gas permeation reveal that addition of SSOD with enhanced porosity displayed H_2 permeance of 178% higher than that of a PSf membrane infused with HSOD (see Table 6). This permeance is in

slightly lower than that reported for other zeolite/polysulfone membranes [33, 34]. The addition of the sodalite particles lowered the membrane selectivity compared to the pure PSF membrane however; the higher porosity SSOD yielded lower ideal selectivity (1.06) than that of the HSOD (1.32). This was attributed to membrane defects and high particle agglomeration of the SSOD. The selectivity displayed by the membranes falls within the range of pure gas selectivity reported in literature (0.083-4.64) [35, 36]. This is encouraging but further studies and mixed gas separations are required to improve on the separation performance of the membranes.

Table 6: Preliminary pure gas permeation results at 1 barg and 298 K

MMM	Pure Gas Permeance ($\times 10^{-9}$ mol/m^2.s.Pa)			Perm-Selectivity		
	H_2	N_2	CO_2	H_2/CO_2	H_2/N_2	N_2/CO_2
PSf	2.73	1.98	1.97	1.38	1.38	1.00
HSOD (5%)	7.31	5.84	5.55	1.32	1.25	1.05
SSOD (5%)	7.60	7.34	7.16	1.06	1.03	1.03

5. Conclusion

Silica sodalite, with enhanced porosity, has been synthesized via topotactic conversion. A 2^3 full factorial design with "a center" was employed to optimize synthesis factors; acid strength, treatment time and calcination temperature. All sodalite samples showed some degree of amorphorization. SSOD 2 displayed the best surface area, pore volume and pore size, which was of the samples produced showed improved surface area and pore volume relative to HSOD. It was assumed that the system was dominated by the main effects and low-order interactions, following the effect sparsity principle [24]. A 1st order regression model was developed utilizing Design Expert v.11, the model produced showed good correlation to the model with a R^2 of 0.716. Calcination temperature was shown to be the only statistically significant model term, decreasing the temperature was found to improve the sodalite pore volume. Acid treatment time was found to have no effect on the response and the effect of acid strength was also insignificant. Optimum parameters were proposed at 1M, 95 minutes and 1073 K. Further study is required to determine optimal variable conditions that yield high quality sodalite with the desired morphology with improved reproducibility. Furthermore, the membranes produced using the porosity-enhanced sodalite displayed comparative H_2/CO_2 separation performance with literature. Further research and development (R&D) is necessary to optimize the synthesis and performance of the membrane in order to produce a competitive membrane-based technology for pre-combustion CO_2 capture.

6. Acknowledgements

CL Eden is grateful to Air Products, South Africa for financial support in this work.

References

[1] C. Scholes, K. Smith, S. Kentish and G. Stevens, "CO2 capture from pre-combustion processes- Strategies for membrane gas separation," *Intarnational Journal of Greenhouse Gas Control,* vol. 4, pp. 739-755, 2010.

[2] D. Jansen, M. Gazzani, G. Manzolini and E. Van Dijk, "Pre-combustion CO2 capture," *International Journal of Greenhouse Gas Control,* vol. 40, pp. 167-187, 2015.

[3] Earth Life Africa Johannesburg, "Climate change, developement and energy problems in SOuth Africa: Another world is possible," OxFam International, Johannesburg, 2009.

[4] K. Lane, IEA Energy Efficiency 2018 and World Energy Outlook 2018, Brussels: International Energy Agency, 2018.

[5] D. Leung, G. Caramanna and M. Mercedes Maroto-Valer, "An overview of current status of carbon dioxide capture and storage technologies," *Renewable and Sustainable Energy Reviews,* vol. 39, pp. 426-443, 2014.

[6] N. M. Anwar, A. Fayyaz, N. F. Sohail, M. F. Khokhar, M. Khokhar, W. D. Khan, K. Rasool, M. Rehan and A. S. Nizami, "CO2 capture and storage: A way forward for sustainable environment," *Journal of Environmental Management,* vol. 226, pp. 131-144, 2018.

[7] [7] Y. Huang, R. W. Baker and L. M. Vane, "Low-Energy Distillation-Membrane Separation Process," *Industrial & Engineering Chemistry Research,* vol. 49, pp. 3760-3768, 2010.

[8] C. Gouedard, D. Picq, F. Launay and P. L. Carrette, "Amine degradation in CO2 capture I. A review," *International journal of greenhouse gas control,* vol. 10, pp. 244-270, 2012.

[9] A. Basu, J. Akhtar, M. Rahman and M. Islam, "A review of separation of gasses using membrane systems," *Petroleum Science and Technology,* vol. 22, p. 1343, 2004.

[10] B. Smith, M. Loganathan and M. Shantha, "A review of the water-gas shift reaction kinetics," *International journal of chemical reactor engineering,* vol. 8, no. Review R4, 2010.

[11] N. Kosinov, J. Gascon, F. Kapteijn and E. Hensen, "Recent developments in zeolite membranes for gas separation," *Journal of membrane science,* vol. 499, pp. 65-79, 2016.

[12] J. Ahn, W.-J. Chung, I. Pinnau and M. D. Guiver, "Polysulfone/silica nanoparticle mixed-matrix membranes for gas separation," *Journal of membrane science,* vol. 314, pp. 123-133, 2008.

[13] M. Daramola, O. Oloye and A. Yaya, "Nanocomposite sodalite/ceramic membrane for pre-combustion CO2 capture: synthesis and morphological characterization," *International journal of coal science & technology,* vol. 4, no. 1, pp. 60-66, 2017.

[14] M. Daramola, A. Dinat and S. Hasrod, "Synthesis and Characterization of Nanocomposite Hydroxy-Sodalite/Ceramic Membrane via Pore-Plugging Hydrothermal Synthesis Technique," *Journal of Membrane and Separation Technology,* vol. 4, pp. 1-7, 2015.

[15] T. Moteki, W. Chaikitisilp, A. Shimojima and T. Okuba, "Silica sodalite without occluded organic maatter by topotactic conversion of lamellar precursor," *American Chemical Society,* vol. 130, pp. 15780-15781, 2008.

[16] K. Momma and F. Izumi, "VESTA 3 for three-dimensional visualization of crystal, volumetric and morphology data," *Journal of applied crystallography,* vol. 44, pp. 1272-1276, 2011.

[17] S. Khajavi, J. Jansen and F. Kapteijn, "Production of ultra pure water by desalination of seawater using a hydroxy sodalite membranes," *Journal of membrane science,* vol. 356, pp. 52-57, 2010.

[18] M. Daramola, B. Silinda, S. Masondo and O. Oluwasina, "Polyethersulphone-sodalite (PES-SOD)Polyethersulphone-sodalite (PES-SOD) mixed-matrix membranes: prospects for acid mine drainage (AMD) treatment," *The South African Institute of Minning and Metallurgy,* vol. 115, pp. 1221-1228, 2015.

[19] T. Moteki, W. Chaikitisilp, Y. Sakamoto, A. Shimojima and T. Okuba, "Role of Acidic Pretreatment of Layered Silicate RUB-15 in its Topotactic Conversion into Pure Silica Sodalite," *Chemistry of materials,* vol. 23, pp. 3564-3570, 2011.

[20] M. Koike, Y. Asakura, M. Sugihara, Y. Kuroda, H. Tsuzura, H. Wada, A. Shimojima and K. Kuroda, "Topotactic conversion of layered silicate RUB-15 to silica sodalite through interlayer condensation in N-methylformamide," *Dalton Transactions,* vol. 46, pp. 10232-10239, 2017.

[21] B. Marler, N. Stroter and H. Gies, "The structure of the new pure silica zeolite RUB-24, Si32O64, obtained by topotactic condensation of the intercalated layer silicate RUB-18," *Microporous and Mesoporous Materials,* vol. 83, pp. 201-211, 2005.

[22] Y. X. Wang, H. Gies and B. Marler, "Synthesis and Crystal Structure of Zeolite RUB-41 Obtained as Calcination Product of a Layered Precursor: a Systematic Approach to a New Synthesis Route," *Chemistry of materials,* vol. 17, no. 1, pp. 43-49, 2005.

[23] R. A. Fischer, The design of experiments, 1st ed., New York: Hafner publishing company, 1935.

[24] D. C. Montgomery, Design and analysis of experiments, 8th ed., Arizona: Wiley and Sons, Inc., 2013.

[25] U. Oberhagemann, P. Bayat, B. Marler, H. Gies and J. Rius, "A Layer Silicate: Synthesis and Structure of the Zeolite Precursor RUB-15 [N(CH3)4]8[Si24O52(OH)4).20H2O," *Angewandte Chemie International Edition in English ,* vol. 35, no. 23, pp. 2869-2872, 1996.

[26] F. Kooli, Y. Liu, K. Hbaieb and R. Al-Faze, "A novel synthetic route to obtain RUB-15 phase by pseudo solid-state conversion," *Microporous and Mesoporous Materials,* vol. 228, pp. 116-122, 2016.

[27] International Zeolite Association, "Database of Zeolite Structures," 2007. [Online]. Available: http://europe.iza-structure.org/IZA-SC/framework.php?STC=SOD.

[28] B. Marler and H. Gies, "Hydrous layer silicates as precursors for zeolites obtained through topotactic condensation: a review," *European Journal of Mineralogy,* vol. 24, pp. 405-428, 2012.

[29] D. D. Reible and F. H. Shair, "A technique for the measurement of gaseous diffusion in porous media," *Journal of soil science,* vol. 33, pp. 165-174, 1982.

[30] T. L. Chitsiga, M. O. Daramola, N. Wagner and J. M. Ngoy, "Parametric effect of adsorption variables on CO2 adsorption of amine-grafted polyaspartamide composite adsorbent during post-combustion CO2 capture: a response surface methodology approach," *International Journal of Oil, Gas and Coal technology,* vol. 17, no. 3, pp. 321-336, 2018.

[31] S. Münzer, J. Caro and P. Behrens, "Preparation and characterization of sodium-free nanocrystalline sodalite," *Microporous and Mesoporous Materials,* vol. 110, pp. 3-10, 2008.

[32] S. Chen, R. Liou, Y. Lin, C. Lai and J. Lai, "Preparation and characterizations of asymmetric sulfonated polysulfone membranes by wet phase inversion method," *European Polymer Journal,* vol. 45, pp. 1293-1301, 2009.

[33] Z. Huang, Y. Li, R. Wen, M. M. Teoh and S. Kulprathipanja, "Enhanced Gas Separation Properties by Using Nanostructured PES-Zeolite 4A Mixed Matrix Membranes," *Journal of applied polymer science,* vol. 101, pp. 3800-3805, 2006.

[34] Y. Li, F. Liang, H. Bux, W. Yang and J. Caro, "Zelitic imidazolate framework ZIF-7 based molecular sieve membrane for hydrogen separation.," *Journal of membrane science,* vol. 354, pp. 48-54, 2010.

[35] P. Jha and J. D. Way, "Carbon dioxide selective mixed-matrix membranes formulation and characterization using rubbery substituted polyphosphazene," *Journal of Membrane Science,* vol. 324, no. 1-2, pp. 151-161, 2008.

[36] E. Karatay, H. Kalıpçılar and L. Yılmaz, "Preparation and performance assessment of binary and ternary PES-SAPO 34-HMA based gas separation membranes," *Journal of membrane science,* vol. 364, no. 1-2, pp. 75-81, 2010.

CARBON CAPTURE WITH METAL OXIDES IN MOLTEN SALTS: MgO, SrO AND CaO AS SORBENTS

Å. Grøtan*, E. Olsen, H.S. Nygård

Faculty of Science and Technology, Norwegian University of Life Sciences, Ås, Norway

* Corresponding author e-mail: ashild.grotan@gmail.com

Abstract

Carbon Capture in Molten Salts (CCMS) is an absorption-based method of separating CO_2 from a flue gas or industrial gas through a thermal swing technique, where the sorbent is dissolved or partially dissolved in molten salts. The method takes advantage of the reversible carbonation reaction of alkaline earth metal oxides and has previously been studied with CaO as sorbent, showing excellent absorption capacity, regeneration and cyclability compared to similar methods. If the molten salt contains certain alkaline metal halides, these may react with the formed metal carbonates in an exchange reaction, shifting the equilibrium towards further carbonation. The CCMS process is however energy intensive and the regeneration of the sorbent has been identified as a main cost driver due to high operating temperatures and high reaction enthalpy. In this study, a screening of alternative chemical systems with MgO, SrO and CaO as sorbents has been performed. The aim is to find chemical systems with lower operating temperatures and reaction enthalpies that work as efficiently as in previous studies, as this could reduce energy demand and thus operational costs. Promisingly high reaction stability and conversion ratio was found with MgO-FLiNaK, but more experiments are needed to see if the absorption efficiency may be sufficiently improved. SrO-NaCl-$CaCl_2$ showed an even higher conversion ratio, but lower reaction stability which may be improved in a different salt mixture. Furthermore, it was found that the chemical system CaO-LiF-CaF_2, which has been very efficient in previous studies, seemed to have no active exchange reaction when the CaF_2 was replaced by $CaCl_2$. Another new finding is that even though studies have shown that CCMS may operate well above the solubility limit of the sorbent, the sorbent does need to have a certain solubility in the melt in order to absorb any CO_2.

Keywords: *Carbon Capture in Molten Salts (CCMS), Carbonate Looping, Metal Oxides as CO_2 sorbents*

1. Introduction

In the 2018 special report on the 1.5DS from IPCC, all four pathways involve net negative CO_2 emissions after year 2050 [1]. It is highly unlikely that the required rate of emission reductions can be covered by a transition to renewable energies alone, which means that carbon capture and storage (CCS) will have to play an important role in reaching the climate goals.

Carbon Capture in Molten Salts (CCMS) is a high-temperature carbon capture technology which could be especially interesting for industrial processes with residual heat at high temperatures, such as ferro-silicon or cement production. The method builds upon the same chemical principle as Calcium Looping (CaL), where CaO reacts reversibly with CO_2, as described in eq. (1).

$$CaO(s) + CO_2 \leftrightarrow \mathrm{CaCO_3}(s) \quad (1)$$

Through a thermal swing technique, the CO_2 may be alternately absorbed and desorbed around an equilibrium temperature $T_{\Delta G=0}$, around 885°C in the case of eq. (1). Alternatively, a pressure swing technique may also be used.

CCMS differs from CaL in that the sorbent is dissolved or partially dissolved in molten salts. The sorbent may also be other alkaline earth metal oxides (MO), as described on its general form in eq. (2).

$$MO(s, diss) + CO_2 \leftrightarrow MCO_3(s, diss) \quad (2)$$

M: Ca, Mg, Sr, Ba, Be.

Most salts that are used in the melt are inert to the sorbent, but certain alkaline metal halides (AH) lead to an exchange reaction, as in eq. (3).

$$MCO_3(s, diss) + 2AH(l) \leftrightarrow MH_2(l) + A_2CO_3(s, diss) \quad (3)$$

A: Li, Na, K, Rb, Cs

H: F, Cl.

This keeps the activity of the MCO_3 low, shifting the equilibrium in eq. (2) towards further carbonation [2, 3], and thus enabling an even higher absorption efficiency and conversion ratio than in a melt with no alkaline metal halide.

This leads to the total reaction in eq. (4).

$$CO_2 + MO(s, diss) + 2AH(l) \leftrightarrow MH_2(l) + A_2CO_3(s, diss) \quad (4)$$

Generally, the melt also needs to contain some inert salts in addition to the chemically active AH. The role of the inert salt is mainly to reduce the melting point of the melt, as salt mixtures generally have lower melting points than pure salts, and in this application a melting point well below the equilibrium temperature of eq. (4) is needed. Other important properties of the salt mixtures are explained later in this section.

A simplified flowchart of the CCMS system is illustrated in figure 1. The equilibrium temperature $T_{\Delta G=0}$ and reaction enthalpy ΔH will vary depending on the chosen

MO and AH. One hypothesis from earlier studies is that even though the thermochemical properties of the total reaction in eq. (4) is governing in the system, the properties of the main reaction in eq. (2) and the exchange reaction in eq. (3) also could affect the reaction equilibrium.

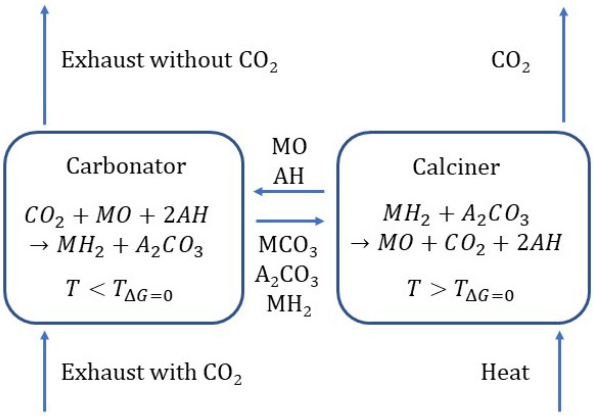

Figure 1: Simplified flowchart of the CCMS process.

CCMS has previously been studied with CaO as sorbent and has shown very promising results with respect to absorption capacity, regeneration and cyclability [2, 4-6]. The hypothesis is that the continuous dissolving of the sorbent and the carbonates in the molten salts liberates sorbent surface area for the CO_2 to react with, leading to faster reaction kinetics than in the solid state. The method also shows excellent cyclability: while similar methods operating in the solid state, such as CaL, experience great challenges with degradation of the sorbent after a few cycles [7, 8], experiments with CCMS have been done with up to 12 cycles without any detectable degradation of the sorbent [9]. Furthermore, chemical systems with exchange reaction have shown close to total absorption of CO_2 from synthetic flue gas with 14vol% CO_2, until saturation of the sorbent. On the other hand, regeneration tends to be less efficient in such chemical systems, as the alkaline carbonates are more stable [2].

The process is energy intensive and the regeneration of the sorbent has been identified as a main cost driver, as this in an endothermal reaction operating at high temperature. Consequently, the reaction enthalpy ΔH is an important parameter for operational costs, as well as the equilibrium temperature $T_{\Delta G=0}$.

The aim of this study is to investigate alternative chemical systems for CCMS, preferably with low ΔH and $T_{\Delta G=0}$ in order to reduce energy demand and thereby operational costs, as well as generally exploring the properties of alternative chemical systems.

This is first done through a theoretical modelling of thermochemical properties of eq. (2)-(4), with all combinations of alkaline earth metal oxides (MO) as sorbent and alkaline metal halides (AH) as active salt, as listed in eq. (2) and (3). The data is found in the database HSC Chemistry 6.12 [10]. Based on the modelling, some promising chemical systems are then chosen for an experimental screening. The systems are chosen based mainly on the properties of the total reaction in eq. (4), but knowledge to suitable salt mixtures is also a limiting factor. These need to have properties such as melting point at least 100°C below the equilibrium temperature, low vapor pressure, low viscosity, and they must not hydrolyse in contact with water or form stable carbonates. Melting points of potential salt mixtures are found in the database ACerS-NIST 3.1 [11], and further properties are found through literature search.

2. Modelling

An excerpt of the modelling is given in table 2, below the reference list. The table displays the equilibrium temperature $T_{\Delta G=0}$ and the reaction enthalpy ΔH at this temperature for the main reaction in eq. (2), the exchange reaction in eq. (3) and the total reaction in eq. (4). This is done for each relevant alkaline earth metal oxide (MO) combined with the different alkaline metal halides (AH). Promising combinations should have a low equilibrium temperature, but higher than 400°C (with respect to the possibility of using residual heat for power production), and a reaction enthalpy as low as possible. For reference, the most absorption- and desorption efficient chemical system in previous studies has been CaO-LiF, with $T_{\Delta G=0}$ = 950°C and ΔH = -161 kJ/mol. Alternative chemical systems should have lower values than this.

Systems with BeO and BaO are left out of table 2, as these do not have an equilibrium temperature within the desired range and are therefore not suitable for carbonate looping.

The systems that stand out as interesting in this modelling, are mainly MgO along with fluorides, with equilibrium temperatures from 410°C to 675°C and reaction enthalpies below (absolute value) 136 kJ/mol, as well as SrO along with certain chlorides, with equilibrium temperatures from 396°C to 785°C and reaction enthalpies below (absolute value) 127 kJ/mol.

3. Experimental

3.1 Equipment and preparations

The experimental setup, as shown in figure 2, consists of a tubular electric furnace and a reactor in stainless steel. A ceramic tube separates the reactor and the furnace, for protection of the heating elements in the furnace. The reactor contains a nickel crucible (5.2cm x 16cm inner diameter and height) which in turn contains the molten salt and the sorbent. All equipment which is in contact with the salt during experiments is made from nickel, due to the very corrosive conditions around molten salts. The inlet gas, a synthetic flue gas with 14vol% CO_2 (99.995%) in N_2 (99.999%), controlled by mass flow controllers (Mass-stream, M+W Instruments GmbH) and logged in LabView 8.2, is led through a nickel pipe (7mm inner diameter) to the bottom of the melt. The gas bubbles through the molten salt, where the CO_2 reacts with the sorbent. The outlet gas is led through tubes (PTFE, 4x6mm) to an electrostatic filter where traces of salt are removed, and further to an FTIR (Thermo Scientific, Nicolet 6700 model) for gas analysis. The FTIR interferometer is held at 120°C for at least 24h before experiments. A thermocouple of type S (Pt10%Rh-Pt) or type K (NiCr-NiAl) measures the temperature in the melt. A small, continuous flow of Ar (99.99%) through the furnace ensures inert atmosphere around the reactor to reduce corrosion.

In all experiments, 10wt% sorbent and eutectic salt mixtures are used, as long as the eutectic concentration is known. The sorbents CaO (Sigma-Aldrich reagent, 96-100.5%), MgO (VWR, 99.3%) and $SrCO_3$ (Sigma-Aldrich, >98%) were calcined before experiments. The calcination was done at 1000°C for 3h and 10h for CaO and MgO respectively, and $SrCO_3$ was calcined to SrO at 1200°C for 10h. $CaCl_2$•$2H_2O$ (VWR, 100.3%) was dried under Ar atmosphere through the procedure described by Freidina and Frey (2000) [12] to remove all the crystalline water, due to its hygroscopic nature. The $CaCl_2$•$2H_2O$ is heated to 300°C at 0.5°C/min, then to 800°C at 2.78°C/min and held at 800°C for 10h. Other salts that are used are CaF_2 (Sigma-Aldrich, 99.9%), LiF (Sigma-Aldrich, 98.5%), NaF (VWR, 100%), KF (VWR, 99%), $ZnCl_2$ (Sigma-Aldrich, 98-100.5%), KCl (Sigma-Aldrich, 99.5-100.5%) and NaCl (Sigma-Aldrich, >99.8%). These are dried in a heating cabinet at 200°C for at least 24h.

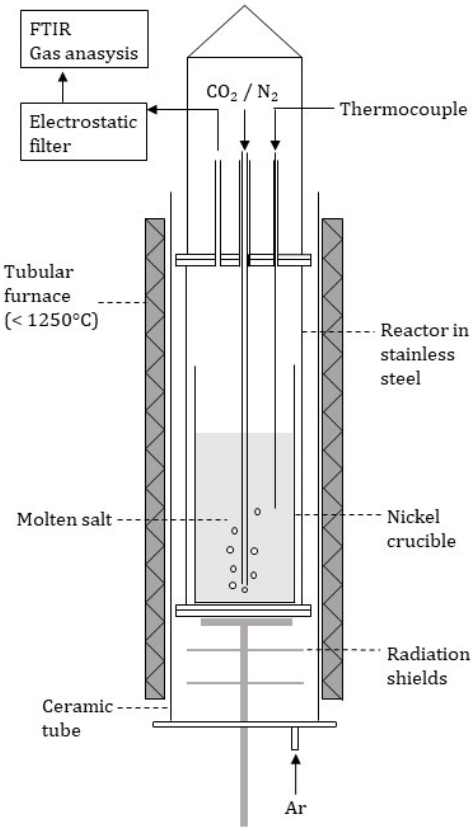

Figure 2**:** Schematic representation of the experimental setup.

3.2 Experimental procedure

Before experiments, the nickel crucible is filled with as much powder salts and sorbent as there is room for. When melted, the volume of the salt is strongly reduced and the final melt height under the experiments varies from 2-7 cm, depending on the densities of the salts. The crucible is placed in the reactor and in the furnace, and the nickel pipe and the thermocouple are put in place as illustrated in figure 2, but above the powder salt. 0.2 L/min N_2 flows through the nickel pipe for inert atmosphere while the furnace heats up. Once the salt is melted, the nickel pipe and thermocouple are lowered to around 1 cm above the bottom of the crucible. The flow of N_2 through the melt ensures mixing of the salts and sorbent for at least 30 minutes while the temperature stabilizes. Also, the FTIR is purged with 0.6 L/min of N_2 for at least 30 minutes before every experiment.

When the temperature is stable at the chosen absorption temperature, the experiment is started by turning on 14vol% CO_2 in the inlet gas. The CO_2 concentration in the outlet gas is then measured until it is close to the same as in the inlet gas. Absorption calculations are based on these concentration measurements, where the conversion ratio is defined as the amount of absorbed CO_2 as a fraction of the theoretical maximum, given that one mole of sorbent can react with one mole of CO_2. The carrying capacity is defined as the mass of absorbed CO_2 as a fraction of the mass of sorbent in the melt.

Melt heights are found after the experiment by measuring the height from the top of the crucible to the crust of the cooled salt. In some cases, this was not possible due to a very uneven crust, and these are marked with a parenthesis in table 1.

4. Results and discussion

The experiments are summarized in table 1 and discussed in the following, and more experimental details are given in table 3 below the reference list.

Table 1: Overview of the experiments. All salt mixtures are eutectic, except LiF-$CaCl_2$ for which no phase diagram was found. The exact concentration for this system is also uncertain due to drifting off and corrosion on the crucible during drying of $CaCl_2$. Melt heights in parenthesis were not possible to measure properly, as they had an especially uneven crust when cooled. A more detailed table (table 3) is given below the reference list.

#	Sorbent	Salt	Melt height (cm)	Conv. Ratio (%)	Carrying capacity (%)
1	MgO	LiF-NaF-KF	2-3	73	80
2	SrO	NaCl-$CaCl_2$	6-7	90	38
3	CaO	LiF-$CaCl_2$	(4-5)	53	41
4	CaO	LiF-CaF_2	2-3	98	77
5	MgO	$ZnCl_2$-NaCl-KCl	(2-3)	2	2
6	CaO	LiF-KCl	(2-3)	7	5

4.1 MgO-FLiNaK

One experiment (#1 in table 1) was done with MgO as sorbent, dissolved in the salt mixture FLiNaK, a eutectic mixture of LiF, NaF and KF (46.5-11.5-42 mol%) (figure 3). FLiNaK is being studied for applications in concentrated solar power [13, 14], so its properties are well-known, and it will be suitable to an up-scaling.

In this system, the total reaction with MgO-KF has the highest equilibrium temperature (table 2), and KF will thus be the active component in the salt.

The result is given in figure 3, where it is evident that a great part of the CO_2 is going through the melt already from the first minute, and only around 20% of the CO_2 is absorbed. The absorption is stable at this level for the first 200 minutes, where about 50% conversion ratio is

reached, and after this point the absorption gradually becomes less efficient.

The low absorption efficiency in this experiment is likely due to the low melt height, which was 2-3 cm. A low melt height leads to short residence time in the melt and thus little time for the gas to react with the sorbent. It is likely that the plateau region of the absorption curve would be shifted to more efficient absorption with a higher melt. Also, the plateau shape of the absorption curve indicates stable reaction kinetics for the first 200 minutes (until around 50% saturation of the sorbent). This flat curve shape is typical for systems with an active exchange reaction, so if the plateau region can be shifted toward more efficient absorption by increasing the melt height, this can be a promising result for this chemical system.

Furthermore, the total conversion ratio of the sorbent was high: 73%. This is high compared to what has been reported in recent literature on MgO as sorbent for CO_2, which is typically less than 10% with pure MgO in the solid phase. Yang et al. have summarized the absorption capacities of MgO based absorbents promoted with nitrates and carbonates and found that MgO with an optimal combination of carbonates and nitrates had a stable conversion ratio at 30% [15]. Hwang et al. achieved up to 77% conversion in the first cycle with MgO promoted with alkali nitrates and carbonates, but this capacity was strongly reduced in the second cycle [16]. It could be interesting to see in further work whether the experience with high cyclability of CaO in CCMS compared to similar methods, is transferable to MgO. Hwang et al. also conclude that K_2CO_3 and alkali metal nitrates play an important role for the CO_2 capture capacity of MgO [16]. As the melt in this experiment contains KF which gets carbonated to K_2CO_3, the same effect may be present here.

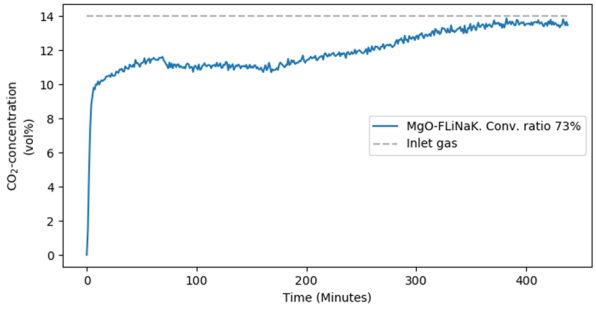

Figure 3**:** Absorption experiment with 10 wt% MgO as sorbent in the salt mixture FLiNaK (eutectic LiF-NaF-KF). The figure shows CO_2 concentration in the outlet gas (blue) after absorption, and the concentration in the inlet gas (grey). $T_{(abs)} = 600°C$. Melt height: 2-3 cm.

4.2 SrO-NaCl-CaCl₂

Figure 4 shows an experiment (#2) with 10 wt% SrO in eutectic NaCl-$CaCl_2$ (52-48 mol%). Due to the pre-melting of $CaCl_2$, the total melt in this experiment was relatively high, around 7 cm.

Roughly 60% of the CO_2 is absorbed for the first hour, but the absorption curve has an increasing slope throughout the experiment as the absorption efficiency gradually decreases. This absorption profile is similar to those from chemical systems without exchange reaction, which could indicate that the NaCl does not react in this melt. On the other hand, the total conversion ratio of 90% is very high, and typical for a system with an active exchange reaction. A possible explanation for these mixed signals could be that the NaCl is reacting, but that the reaction kinetic is slow and decreasing over time. This is further discussed under section 4.4.

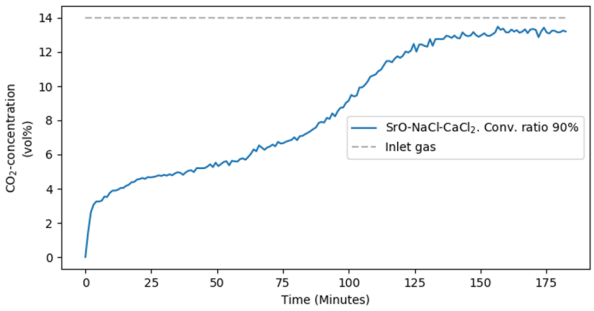

Figure 4: Absorption experiment with 10 wt% SrO as sorbent in eutectic NaCl-$CaCl_2$. The figure shows CO_2 concentration in the outlet gas (blue) after absorption, and the concentration in the inlet gas (grey). $T_{(abs)} = 663°C$. Melt height: 6-7 cm.

4.3 CaO-LiF

Three experiments were conducted with CaO as sorbent and LiF as the active alkaline metal halide in the melt: one of the experiments was with $CaCl_2$ (#3 in table 1, LiF-$CaCl_2$ 25-75 mol%. Eutectic concentration is unknown) and one with CaF_2 (#4, LiF-CaF_2 80.5-19.5 mol%) as inert salt. These two are discussed in the following, and the third (#6, LiF-KCl) in section 4.5.

Unfortunately, a phase diagram for LiF-$CaCl_2$ has not been found in literature. The molar fraction of LiF was set to 25% to be above the stochiometric limit for the total reaction. The exact concentration is uncertain due to salt drifting off and strong corrosion on the crucible during the drying of $CaCl_2$. The system CaO-LiF-CaF_2 has been investigated in previous studies with very efficient absorption and high capacity, probably due to a very active exchange reaction with LiF [2]. The objective of the experiment with $CaCl_2$ was to see if the CO_2 absorption abilities of CaO-LiF could also be achieved in $CaCl_2$, which has some practical benefits compared to CaF_2. For example, water solubility greatly simplifies cleaning out the crucible between experiments. However, for commercial applications, this is of less importance.

The result with $CaCl_2$ shows a steep absorption profile with gradually decreasing absorption efficiency, and a total conversion ratio of 53%. This was surprising, as it is almost identical, both in absorption profile and conversion ratio, to previous experiments with CaO-$CaCl_2$, i.e. without any alkaline metal halide for exchange reaction. This strongly indicates that the LiF does not react in the melt with $CaCl_2$, even though it reacts very actively in the melt with CaF_2. The high efficiency and stable reaction kinetics of the system CaO-LiF-CaF_2, which was known from previous work, was again confirmed in this experiment. Considering that the melt height was very low in the experiment with CaO-LiF-CaF_2, only 2-3 cm, this strongly demonstrates the high efficiency of this chemical system even with a very short residence time. The two experiments are compared in figure 5.

One possible explanation to this surprising difference could be the solubility of Li_2CO_3 in $CaCl_2$. The hypothesis from earlier studies, as mentioned in the introduction, is that the dissolving of the sorbent and the carbonates enables continuous contact between the sorbent and the CO_2, and thereby contributes to fast reaction kinetics. However, if the Li_2CO_3 has low solubility on $CaCl_2$, it does not dissolve in the melt and LiF will be unavailable to the $CaCO_3$, quickly halting the exchange reaction. Information on the solubility of Li_2CO_3 in $CaCl_2$ has unfortunately not been found in literature.

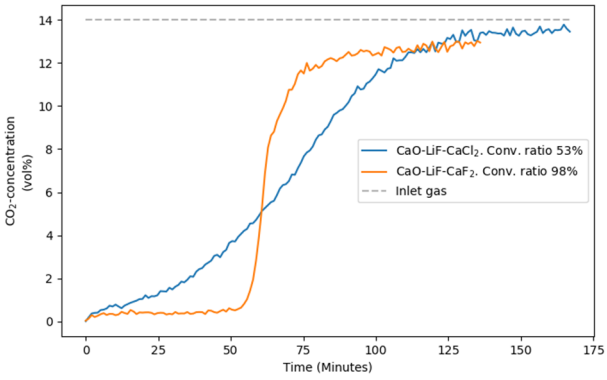

Figure 5: Comparison of two absorption experiments with 10 wt% CaO as sorbent in LiF-$CaCl_2$ (25 mol% LiF. Eutectic concentration is unknown. Melt height: 4-5 cm) (blue) and in eutectic LiF-CaF_2 (80.5 mol% LiF. Melt height: 2-3 cm) (yellow). The figure shows CO_2 concentration in the outlet gas from the two experiments, and the concentration in the inlet gas (grey). $T_{(abs)} = 787°C$. The experiments show that the exchange reaction with $CaCO_3$ and LiF is strongly dependent on which inert salt is present in the melt.

4.4 Comparing the results

If the above-mentioned hypothesis about the solubility of Li_2CO_3 is correct, it could be transferrable to the experiment with SrO-NaCl-$CaCl_2$. If the initially formed Na_2CO_3 does not dissolve, or very slowly dissolves, in $CaCl_2$, it could in the same way prevent NaCl from further carbonation as the $SrCO_3$ would have to diffuse through a layer of Na_2CO_3 to react with the NaCl. This could be a fitting explanation to the slow reaction kinetics and high final conversion ratio. Information on the solubility of Na_2CO_3 in $CaCl_2$ has unfortunately not been found in literature.

One hypothesis from earlier studies is that the Gibbs free energy ΔG of the exchange reaction alone could affect the equilibrium of the total reaction. In the system SrO-NaCl, ΔG>0 at all temperatures for the exchange reaction (eq. (3)), meaning that the reaction equilibrium always goes towards decarbonation. This, along with the slow reaction kinetics in figure 4, could support the hypothesis mentioned above. For comparison, eq. (3) for the systems MgO-KF and CaO-LiF both have ΔG<0 for all temperatures and have shown a plateau shaped absorption profile in experiments, also supporting the hypothesis.

4.5 MgO-$ZnCl_2$-NaCl-KCl and CaO-LiF-KCl

In addition to the already mentioned experiments, two chemical systems were also tested but resulted in close to no absorption. 10 wt% MgO in eutectic $ZnCl_2$-NaCl-KCl (#5 in table 1, 60-20-20 mol%, figure 6) and 10 wt% CaO in eutectic LiF-KCl (#6, 19-81 mol%, figure 7) had almost identical results with close to no absorption of CO_2. Also, in both these experiments, lumps were observed in the molten salt after the experiments, which was probably the sorbent which had not dissolved in the melt and likely the reason why no absorption was observed. In the case of MgO, this explanation is supported by the findings of Cherginets (1997) [17], where a low solubility of MgO in NaCl-KCl was shown.

This is also an interesting result, as while earlier studies have shown that CCMS can operate above the solubility limit of the sorbent [2], this result shows that the sorbent must have a certain solubility in the melt.

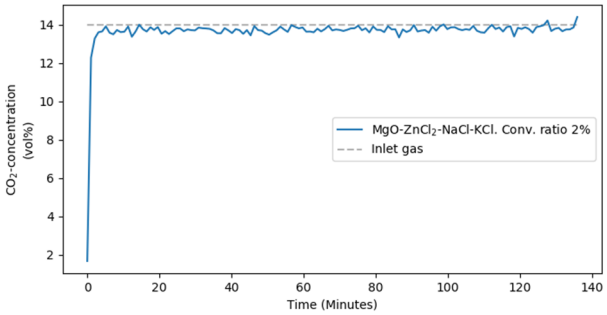

Figure 6: Absorption experiment with 10 wt% MgO as sorbent in eutectic $ZnCl_2$-NaCl-KCl. The figure shows CO_2 concentration in the outlet gas (blue) after absorption, and the concentration in the inlet gas (grey). $T_{(abs)} = 260°C$. Melt height: 2-3 cm.

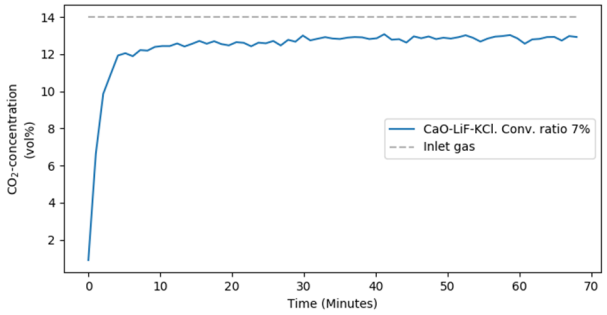

Figure 7: Absorption experiment with 10 wt% CaO as sorbent in eutectic LiF-KCl. The figure shows CO_2 concentration in the outlet gas (blue) after absorption, and the concentration in the inlet gas (grey). $T_{(abs)} = 780°C$. Melt height: 2-3 cm.

5. Conclusions

An experimental screening of alternative chemical systems with MgO, SrO and CaO as sorbents for CCMS has been conducted. Chemical systems in the screening are chosen based on a broad, theoretical modelling of alternative chemical systems with alkaline earth metal oxides as sorbents and alkaline metal halides as active salts. It was found that MgO, dissolved in the salt FLiNaK, absorbed stably until around 50% saturation, and reached a total conversion ratio of 73%. This is high compared to other studies and shows a potential for MgO as a sorbent for CO_2. Further research is however needed, especially with regards to the absorption efficiency, which was low in this experiment.

The experiment with SrO-NaCl-$CaCl_2$ also shows some promising results, particularly with a very high

conversion ratio of 90%, but the reaction efficiency was decreasing. Further research with SrO in different salts could be interesting in the future.

It was also shown that a chemical system with CaO-LiF, which has been very efficient with CaF_2 as inert salt in earlier studies, performed very similarly to a system without LiF when the CaF_2 was replaced by $CaCl_2$. A suggested explanation to this is the possibility of low solubility of Li_2CO_3 in $CaCl_2$ compared to in CaF_2, which would limit the exchange reaction. The same explanation could be transferrable to the system with SrO-NaCl-$CaCl_2$, if Na_2CO_3 dissolved slowly in $CaCl_2$.

Furthermore, experiments were performed where close to no CO_2 was absorbed, probably due to the low solubility of the sorbent in the salt. These systems were MgO-$ZnCl_2$-NaCl-KCl and CaO-LiF-KCl. This shows that the sorbent needs a certain solubility in the melt, even though research has shown that CCMS can operate above the solubility limit of the sorbent. A comparison of the experiment with SrO with the systems MgO-FLiNaK and CaO-LiF-CaF_2 support the hypothesis that the Gibbs free energy of the exchange reaction alone may affect the reaction equilibrium of the total reaction.

References

[1] Masson-Delmotte, V., et al., *Global warming of 1.5C. An IPCC Special Report on the impacts of global warming of 1.5C above pre-industrial levels and related global greenhouse gas emission pathways, in the context of strengthening the global response to the threat of climate change, sustainable development, and efforts to eradicate poverty*. 2018, IPCC.

[2] Olsen, E. and V. Tomkute, *Carbon capture in molten salts.* Energy Science & Engineering, 2013. **1**(3): p. 144-150.

[3] Tomkute, V., et al., *Reactivity of CaO with CO2 in molten CaF2-NaF: formation and decomposition of carbonates.* Energy Science & Engineering, 2016. **4**(3): p. 205-216.

[4] Tomkute, V., A. Solheim, and E. Olsen, *CO2 Capture by CaO in Molten CaF2-CaCl2: Optimization of the Process and Cyclability of CO2 Capture.* Energy & Fuels, 2014. **28**(8): p. 5345-5353.

[5] Tomkute, V., et al., *Reactivity of CaO with CO2 in molten CaF2–NaF: formation and decomposition of carbonates.* Energy Science & Engineering, 2016. **4**(3): p. 205-216.

[6] Tomkute, V., A. Solheim, and E. Olsen, *Investigation of High-Temperature CO2 Capture by CaO in CaCl2 Molten Salt.* Energy & Fuels, 2013. **27**(9): p. 5373-5379.

[7] Dean, C.C., et al., *The calcium looping cycle for CO2 capture from power generation, cement manufacture and hydrogen production.* Chemical Engineering Research and Design, 2011. **89**(6): p. 836-855.

[8] Blamey, J., et al., *The calcium looping cycle for large-scale CO2 capture.* Progress in Energy and Combustion Science, 2010. **36**(2): p. 260-279.

[9] Tomkute, V., A. Solheim, and E. Olsen, *CO2 Capture by CaO in Molten CaF2–CaCl2: Optimization of the Process and Cyclability of CO2 Capture.* Energy & Fuels, 2014. **28**(8): p. 5345-5353.

[10] Outotec Research Oy, F., *HSC Chemistry v. 6.12*.

[11] ACerS-NIST, *Phase equilibria diagrams database, v. 3.1*. 2005.

[12] Freidina, E.B. and D.J. Fray, *Phase diagram of the system CaCl2–CaCO3.* Thermochimica Acta, 2000. **351**(1): p. 107-108.

13. Olsin , L.C.e.a., *Materials corrosion in molten LiF-NaF-KF salt.* J. Fluorine Chem Soc Rev, 2009. **130**: p. 67–73.

[14] Williams, D.F., *Assessment of Candidate Molten Salt Coolants for the NGNP/NHI Heat-Transfer Loop.* Oak Ridge National Laboratory: Oak Ridge, TN, 2006.

[15] Yang, X.F., et al., *Magnesium Oxide-Based Absorbents for CO2 Capture at Medium Temperature.* Current Pollution Reports, 2018. **4**(1): p. 13-22.

[16] Hwang, B.W., et al., *CO2 capture and regeneration properties of MgO-based sorbents promoted with alkali metal nitrates at high pressure for the sorption enhanced water gas shift process.* Process Safety and Environmental Protection, 2018. **116**: p. 219-227.

[17] Cherginets, V.L., *On studies of oxide solubilities in melts based on alkaline halides.* Electrochimica Acta, 1997. **42**(23): p. 3619-3627.

Table 2: Excerpt from modelling of thermochemical properties of alternative chemical systems for CCMS. The table contains equilibrium temperature $T_{\Delta G=0}$ and the reaction enthalpy ΔH at this temperature for carbonation reactions with combinations of alkaline earth metal oxides (MO) as sorbents and alkaline metal halides (AH) as active salts. ΔG<0 below the given temperature and ΔG>0 above the given temperature, except the temperatures marked with *. In cases where ΔG<0 or ΔG >0 for all temperatures in the total reaction, the system does not have a equilibrium temperature and is therefore not an alternative system for CCMS. All data is from the database HSC Chemistry v. 6.12.

Sorbent (MO)	**Salt (AH)**	**Total reaction (eq. (4))**		**Main reaction (eq. (2))**		**Exchange reaction (eq. (3))**	
		$T_{\Delta G=0}$ [°C]	**ΔH [kJ/mol]**	**$T_{\Delta G=0}$ [°C]**	**ΔH [kJ/mol]**	**$T_{\Delta G=0}$ [°C]**	**ΔH [kJ/mol]**
MgO	LiCl	0	-48	305	-99	4160	149
	NaCl	ΔG > 0				ΔG > 0	
	KCl	ΔG > 0				ΔG > 0	
	LiF	410	-103			ΔG < 0	
	NaF	475	-93			ΔG < 0	
	KF	675	-125			ΔG < 0	
	RbCl	ΔG > 0					
	RbF	675	-130			ΔG < 0	
	CsCl	ΔG > 0					
	CsF	685	-136			ΔG < 0	
CaO	LiCl	690	-194	885	-166	2300	52
	NaCl	235	-73			ΔG > 0	
	KCl	25	-45			ΔG > 0	
	LiF	950	-161			ΔG < 0	
	NaF	1115	-171			ΔG < 0	
	KF	1190	-182			ΔG < 0	
	RbCl	ΔG > 0					
	RbF	ΔG < 0					
	CsCl	ΔG > 0					
	CsF	1155	-185			ΔG < 0	
SrO	LiCl	1230	-171	1215	-202	335	-8
	NaCl	785	-127			ΔG > 0	
	KCl	530	-111			ΔG > 0	
	RbCl	425	-100			ΔG > 0	
	CsCl	395	-89			ΔG > 0	
	LiF	1155	-180			1640 *	26
	NaF	1325	-188			800 *	46
	KF	1390	-202			ΔG < 0	
	RbF	1345	-210			ΔG < 0	
	CsF	1340	-207			ΔG < 0	

Table 3: Experimental data. All salt mixtures are eutectic, except LiF-$CaCl_2$ for which no phase diagram was found. The exact concentration of this system is also uncertain due to drifting off and corrosion on the crucible during drying of $CaCl_2$. Melt heights in parenthesis were not possible to measure properly, as they had an especially uneven crust when cooled.

#	**Sorbent**	**Salt**	**Salt concentration (mol%)**	**T_{melt} (°C)**	**$T_{\Delta G=0}$ (°C)**	**T_{abs} (°C)**	**Total mass (g)**	**Melt height (cm)**	**Conv. Ratio (%)**	**Carrying capacity (%)**
1	MgO	LiF-NaF-KF	46.5-11.5-42	454	675	600	150	2-3	73	80
2	SrO	NaCl-$CaCl_2$	48-52	507	785	663	326	6-7	90	38
3	CaO	LiF-$CaCl_2$	25-75 (ca)	-	950	783	228	(4-5)	53	41
4	CaO	LiF-CaF_2	80.5-19.5	769	950	787	161	2-3	98	77
5	MgO	$ZnCl_2$-NaCl-KCl	60-20-20	203	305	260	150	(2-3)	2	2
6	CaO	LiF-KCl	19-81	710	950	780	250	(2-3)	7	5

HIGH CONCENTRATED MEA SOLVENT SYSTEMS FOR CO_2 ABSORPTION – AN FT-NIR AND RAMAN SPECTROSCOPIC INVESTIGATION

M.H.W.N. Jinadasa*, J.L. Badalge, M. Halstensen, D. Eimer, K.-J. Jens

Faculty of Natural Sciences and Maritime Sciences – University of South-Eastern Norway, Campus Porsgrunn, Norway

* Corresponding author e-mail: wathsala.jinadasa@usn.no

Abstract

This study investigates the use of Fourier Transform Near-Infrared (FT-NIR) spectroscopy and Raman spectroscopy to monitor the CO_2 absorption process when over 65 wt % concentrated monoethanolamine (MEA) solutions are used. Using high concentrated amines instead of the conventional 30 wt %, is a strategy to decrease the cost of CO_2 capture plants by minimizing the energy consumption spent for amine regeneration and reducing the size of the process equipment. In addition, higher solvent concentration has a positive impact on mass transfer. CO_2 loading and solvent strength are two main parameters that are used to characterize the well-known CO_2 capture process by MEA. Several analytical methods are in practice to determine these two parameters but most of them are time-consuming and not favourable when quick results are demanded. Process analyzers such as Raman spectroscopy or NIR (Near Infrared) spectroscopy can be used for real-time monitoring of chemical or physical attributes in a system and have advantages over traditional analytical methods. Authors have previously published spectroscopic methods combined with chemometrics to determine CO_2 loading in 30 wt % MEA solutions by Raman spectroscopy in laboratory scale and pilot plant experiments. The aim of this paper is to extend these spectroscopic investigations when both the amine concentration and loading are spanned in a range. CO_2 loading range was selected between 0-0.6 mol CO_2 / mol MEA and solvent concentration was varied between 66-99.5 wt %. Two analyzers were selected; Raman and Fourier transform near infrared (FT-NIR) spectrometers. It is relatively easy to generate data in a short time by these instruments, however identification of components of a chemical mixture and calibration methods become challenging as the FT-NIR and Raman spectral data are not straightforward. Many spectral responses appear similarly and therefore the choice of chemometrics methods is more reliable than the traditional univariate methods. In this study, chemometrics has been applied for data preprocessing, data exploration and finally for multivariate calibration of four models to predict CO_2 loading and MEA concentration from FT-NIR and Raman spectroscopy.

Keywords: *high concentrated MEA, CO2 loading, MEA weight percentage, spectroscopy, chemometrics*

1. Introduction

Body Carbon capture, utilization and storage (CCUS) is an obligatory action in the global climate change mitigation plans. Electricity/thermal power generation and transport account for two thirds of total CO_2 emissions and 32.8 billion tons of global CO_2 emissions in the atmosphere are the results of fuel combustion [1]. Post-combustion CO_2 capture using amines is the most widespread method in CCUS. Monoethanolamine (MEA) has prioritized the other amines to remove CO_2 from flue gas at atmospheric pressure and is considered to be a "first generation solvent".

30 wt% MEA has been the benchmark for most of the experimental, theoretical and modelling work. 15-20 wt% was the recommended amine concentration and since 1960s 30 wt % has been the standard [2, 3]. The limitations to avoid using higher amine concentration are the thermal degradation, corrosion and fouling problems [4, 5]. Raksajati, Ho [6] show that the development of aqueous chemical absorption technology for CO_2 capture should also focus on new solvents with high solvent concentration to make a significant impact on the capture cost. They claim if the solvent concentration increases from 30 to 50 wt %, the capture cost decreases by about 16% from US$88 to US$72 per metric ton of CO_2 avoided. When the solvent concentration is increased, the solvent flow rate decreases and the mass transfer increases which makes to have a reduced absorption unit size [6]. In this aspect, moving from the traditional '30 wt % MEA based capture process' to 'high concentrated MEA process' has a significant interest. However, the corrosion, degradation and fouling effects which are more in high concentrated MEA process should also be carefully addressed [7, 8]. EFG plants by Fluor Inc. and CO_2 capture plants by Union Engineering in Denmark have upgraded amine technology for commercial applications using over 30 wt % MEA.

Process information described by CO_2 loading (mol CO_2/mol amine) and the amine concentration (wt%) are used in R&D experiments and capture plant operations to characterize absorption and regeneration. Loading is defined as the ratio between number of moles of CO_2 and the number of moles of the solvent and the solvent concentration, is expressed as the solvent mass fraction. Samples extracted from rich stream, lean stream and water wash in amine based CO_2 capture plants, are continuously analyzed offline for CO_2 loading and amine

concentration. The frequency of sample extraction is limited by several factors such as the time spent for lab analysis, sample preservation facilities during lab-to-plant transport, risk factors during sample extraction and availability of laboratory resources such as chemical and skilled manpower. In addition, operational delays are unavoidable when decisions are dependent on laboratory results. In this aspect, process analytical technology (PAT) plays a vital role which speeds up the analysis time and opens the opportunity to give live feedback while minimizing sampling errors, risk and health issues [9].

1.1 PAT tools

PAT tools in industrial applications has more than 70 years history, and today many sophisticated analyzers are across chemical and petrochemical industries [9]. Some types of spectroscopic methods have been tested for liquid and gas analysis in CO_2 capture plants particularly during last 10 years and have shown a positive impression. A list of published work where spectroscopic methods were used for liquid analysis in amine based CO_2 capture process is given by Jinadasa [10]. IR (Infrared), UV/Vis (Ultra-Violet Visible) and NIR (Near Infrared) and Raman spectrometers have been used for qualitative and quantitative analysis of chemical components. NIR spectral data was combined with other measurement data to determine MEA wt% and CO_2 % [11, 12]. CO_2 absorption by an amine mixture at high pressure was monitored by a predictive statistical model where NIR data was one of measurements [13]. Raman spectroscopy has also become a popular method in liquid phase analysis in laboratory experiments and pilot plant trials as reported in several literature [14-19]. These authors have used the high spectral features of Raman data to determine species concentration.

Spectroscopy reveal in-depth chemical information of a system because molecular vibrations produce unique spectra. Weak Raman scattering for water, compact chemical information in fingerprint area for organic solvents and non-invasive remote monitoring facility are some of the features which have made Raman spectroscopy appropriate to analyse MEA-CO_2-H_2O system. Various organic compounds exhibit selective absorption for infrared radiation. Water molecules provide a very strong signal on the NIR spectra as they are highly polarized and used as an indication on water content in a sample. FT-NIR spectroscopy is considered as the best performing among other NIR analysers based on speed of analysis, higher signal (S/N) to noise ratio and precision and accuracy of wavelength. It uses the Fourier transform algorithm on the interferogram to convert a spectrum and provides easy transfer of calibration models between instruments [20].

Figure 1 shows a schematics representation of using an immersion probe for in-situ analysis of gas loading and solvent concentration. The immersion probe is connected to a process analyzer such as Raman spectrometer where it acquires data from a process stream. The spectral data is converted into chemical data using a calibration model. This model can be prepared using a univariate analysis or a multivariate analysis (Næs & Martens, 1984), and the figure mentions a PLS model which is one type of a multivariate analysis method (described in section 2.4.3).

For highly correlated data, multivariate analysis become the preferred choice over univariate. Our previous studies demonstrated the use of Raman spectroscopy for a complete in-situ speciation of CO_2 capture by 30 % MEA [19, 21]. In this study, a similar approach was used for developing multivariate regression models for CO_2 absorption by higher concentrated MEA.

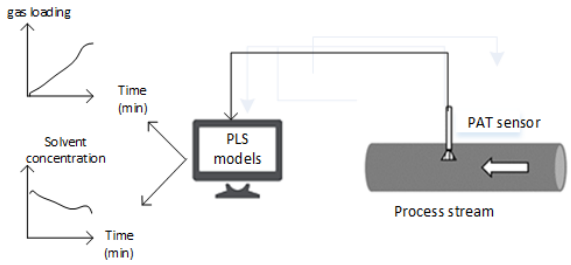

Figure 1: An immersion probe used as a process monitoring tool in gas absorption process; (PLS = partial least squares regression)

2. Experimental section

2.1 Chemicals and samples

MEA purchased from Merck (>99%) and CO_2 from AGA were used as received without further purification. Degassed milli-Q water (18.2 MΩ.cm) was used for all the sample preparation. 105 samples were prepared for both calibration and validation at room temperature (25 °C) and pressure maintaining the same experimental conditions.

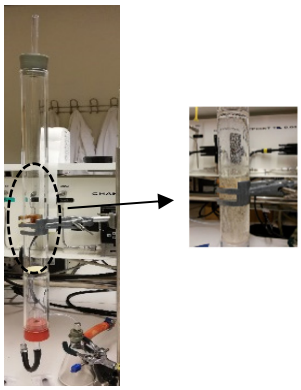

Figure 2: CO_2 loading apparatus

Amine stock solutions were prepared by mixing (>99%) MEA and degassed Milli-Q water in different ratios. To ensure the homogeneity of the mixture, these stock solutions were stirred for 20 minutes at 300 rpm after mixing. The prepared stock solutions were then loaded with CO_2 by bubbling a CO_2 gas stream (0,15 l/min) using a fritted glass column (Figure 2). CO_2 feeding was carried out for a sufficient period of time, to ensure saturation of stock solutions with gaseous CO_2 at experimental conditions. After that, the CO_2 loaded solutions were stirred for 20 minutes at 300 rpm in a closed vessel and kept for 24 hours to give adequate time for equilibrium. To obtain a sample set having variation in both amine and CO_2 concentration, each sample was prepared by mixing a liquid portion from CO_2 unloaded MEA stock solution with a portion from CO_2 loaded MEA stock solution. Analytical balance Mettler Toledo

(±0.0001 g) was used to prepare samples gravimetrically. Figure 3 and Figure 4 show the actual MEA strength and CO_2 loading values of 105 samples as obtained from titration measurements for each sample.

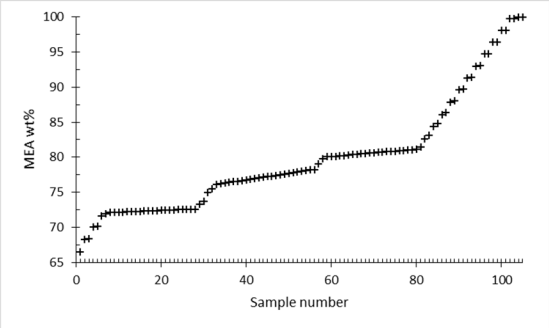

Figure 3. MEA concentration of calibration and validation samples

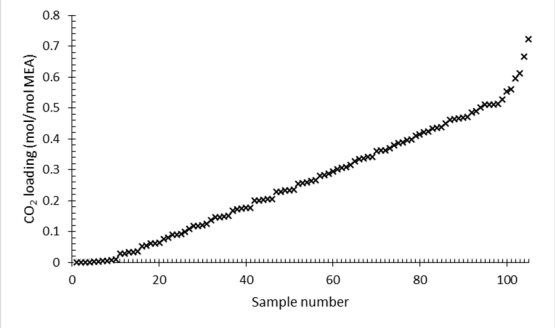

Figure 4. CO_2 loading of calibration and validation samples

2.2 Raman spectroscopy

The Raman measurements were taken with a 785 nm RXN2 Kaiser Raman System (Figure 5). Since the Raman measurements are light sensitive, the sample to be measured was placed inside a black plastic sample holder to avoid fluorescent disturbances and was covered with an aluminium foil to further get rid of any disturbances from the background light. The immersion probe was washed with deionized water followed by acetone before each measurement to remove impurities on the probe tip and avoid contamination of measurements by each other. Presence of air bubbles on the probe tip gives incorrect spectra. Therefore, the Raman probe tip was examined for any air bubbles after immersing in the liquid. S/N ratio was optimized by varying the acquisition time and the number of scans. 4 scans having 30 second exposure time per scan was selected as the optimum S/N ratio. Raman measurements were taken from several spatial locations inside the each sample bottle and compared to ensure that the solutions were chemically and physically homogeneous throughout the sample.

2.3 FT-NIR spectroscopy

Figure 6 shows the FT-NIR instrument (Q-Interline; MB 3000, 760nm laser wavelength) used for this study. The optimized instrument setting used per each measurement was 128 scans and a resolution of 16. Wavelength between 0–15000 cm^{-1} was considered for all the measurements. It was not possible to maintain stable

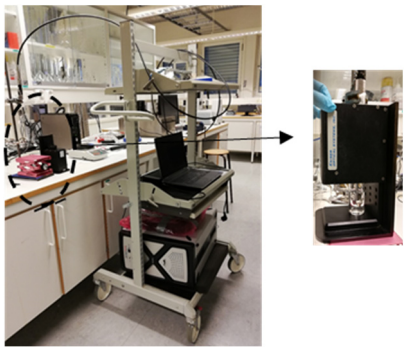

Figure 5: Raman instrument and sample compartment

temperatures below 40°C inside the FT-NIR sample holder accessory due to instrument configuration. Therefore, all the measurements were taken at 40°C in 5mm diameter sample vials. Since the solutions were highly viscous it was difficult to fill the solution into the small diameter vials without forming air bubbles. By tapping few times and holding upwards the sample vials, most of the trapped air bubbles could be released.

2.4 Spectral data

2.4.1. Data pretreatment

A process analyzer such as Raman or NIR spectroscopy generate several responses, but very often the irrelevant response to solve the analytical problem is larger. These responses hinder the relevant information and usually dominate the entire spectra such as by giving baseline offsets and multiplicative effects. The environmental light, stray light, fluctuation of laser intensity, fluorescence from the sample and instrument inherited noise are some of components that come with the raw spectroscopic data. These data ("*noise part"*) should be stripped from raw data to keep the most relevant chemical responses ("*structure part*"). In chemometrics, data pretreatment (preprocessing) algorithms are applied on raw data prior to the detailed data analysis for this purpose. The selection of the type of pretreatment methods is dependent on several parameters such as the type of chemical/physical system that we analyze and the instrument. In addition, the selected pretreatment methods highly affect the subsequent data analysis. The preprocessing methods can be classified into five categories such as offsetting, variable-wise scaling, sample-wise scaling, filtering and compression [22].

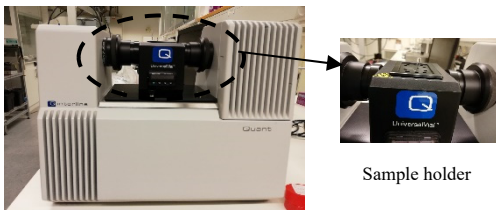

Figure 6: FT-NIR instrument and the sample compartment

There are some common pretreatment algorithms which fits well with many NIR data such as scatter correction

methods and spectral derivatives [23]. The impact of preprocessing methods of Raman data for chemometric modelling has been reviewed by [24, 25].

2.4.2. Exploratory analysis – PCA

Principal component analysis (PCA) is a popular data compression method in chemometrics where a several number of original measured variables are compressed into fewer number of uncorrelated variables called principal components (PCs). The PC1 which includes the highest variance describes the maximum variation of the data set. PCA decomposes data into scores (which describe the relationship between observations) and loadings (which show the relationship of the variables) using a mathematical algorithm [26].

2.4.3. Developing calibration models - PLS

Partial least squares regression (PLS) is a multivariate calibration method which can be used to directly correlate a chemical or physical property of a sample with a spectra collected [27]. In this method, the co-variance existing between the observation data (*x* data) and the reference values (*y* data) is explored. Then a linear regression model is built by estimating the regression coefficients ***b*** in such a way as to maximize the covariance between ***y*** and $\boldsymbol{x}_{\mathbf{preprocessed}}$, as shown in equation (1).

$$\mathbf{y} = \mathbf{x}_{\mathbf{preprocessed}}\,\mathbf{b} + \mathbf{f} \qquad \text{Equation 1}$$

f is the vector of residuals [27]. Instead of using raw ***x*** data, preprocessed ***x*** data are used in equation 1 to get rid of noisy data. In our case, *x* data is the spectroscopic measurements (FT-NIR or Raman spectra). ***y*** is a vector of CO_2 loading or MEA concentration of calibration samples. ***x*** variables represent values in *x* data matrix which are Raman shifts for Raman data and wavenumbers for FT-NIR data.

The chemical information distributed inside large number of ***x*** variables are compressed into a small number of variables called latent variables or PLS components when the covariance between x and y data are maximized. These fewer number of latent variables can interpret the entire chemical system which would otherwise become impractical with thousands of variables. The most common performance indicators of PLS models are root mean square error of cross validation (RMSECV), root mean square error of prediction (RMSEP), coefficient of determination (r^2) and *bias*.

$$RMSE = \sqrt{\frac{\sum_{i=1}^{n}(y_i - \hat{y}_i)^2}{n}} \qquad \text{Equation 2}$$

The root mean square error (RMSE) is defined as in equation 2 (when all samples are included in the model), where n is the number of samples (observations), $\hat{y}_i$ is the values of the predicted property value (CO_2 loading or MEA wt in our case)and y_i is the measured property value. RMSECV is defined similar to the equation 2 where y_i are samples not included in the model formulation. RMSEP is also calculated similar to equation 2 where all y are new data. y_i and $\hat{y}_i$ are measured property values and predicted property values respectively from previously calibrated model (using calibration data). RMSEP is an indicator how well the model predicts for future samples and therefore all the models in this study were validated with a validation data set to obtain RMSEPs for each model. r^2 gives the measure of how well the regression predictions approximate the real data points. *Bias* shows the tendency of overestimate or underestimate of parameter.

Figure 7 shows, four PLS calibration models in this study where two models were developed from each spectrometer for each chemical property. Preprocessing of x and y data and PLS regression were carried out in PLS toolbox 8.6 in Matlab 2017.

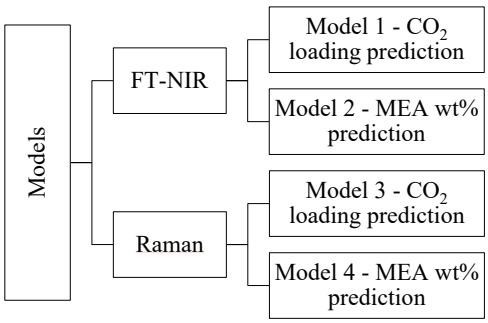

Figure 7: Description of four calibration models

3. Results and Discussion

3.1 Data exploration

3.1.1. FT-NIR data

Identifying the "*structure part*" and "*noise part*" becomes primarily important to extract the useful chemical information from spectral data. The *structure part* from a signal acquired by Raman spectroscopy or FT-NIR for this study represents correlation with CO_2 loading and amine concentration. Knowledge on NIR overtones and Raman vibrational modes related to the MEA-CO_2-H_2O chemical system is helpful to identify this *structure part*.

The raw FT-NIR data in this study are 105 multivariate signals of different CO_2 loaded amine samples in the range of 5500 – 10000 cm^{-1}. They are shown in Figure 8 which are also grouped according to their CO_2 loading value. It is possible to see variations between each sample with naked eye through this figure but they are not systematic sufficiently to correlate with CO_2 loading values due to overlap of overtones. The MEA-CO_2-H_2O system has bonds between C, H, N and O atoms which generate different vibrations when excited by laser power. The C-H stretching vibration makes first and second overtone in the NIR region 5500-6250 cm^{-1} [28]. Deformation vibration of the O-H group occurs at 7140 cm^{-1} and primary amines have two bands for N-H first overtone region in 6500-7000 cm^{-1} [28]. These vibrational modes are not clearly visible in Figure 8 however, they are apparent in the baseline corrected FT-NIR data as shown in Figure 10 (a) and (b).

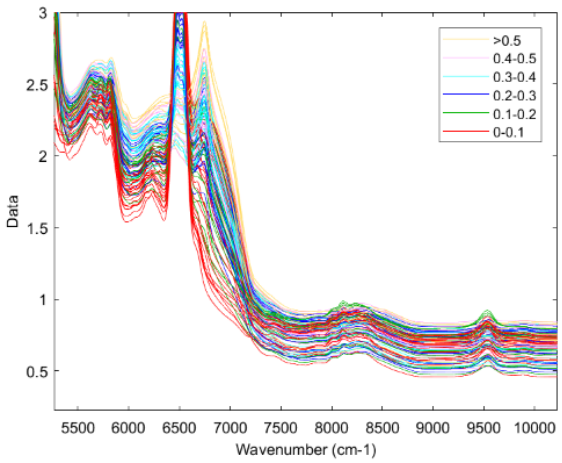

Figure 8: FT-NIR wavenumber vs absorbance data for different CO_2 loaded amine samples

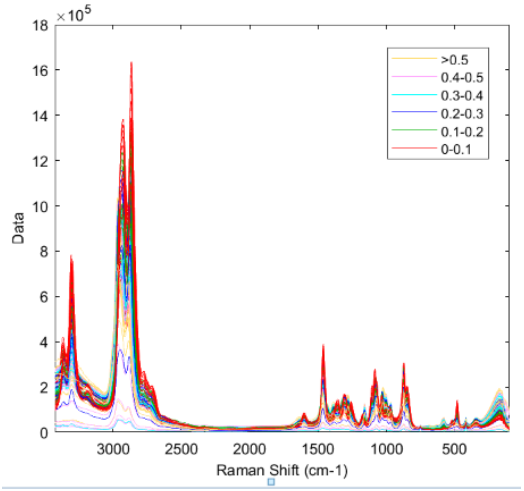

Figure 9: Raman shift vs Raman intensity (a.u.) for different CO_2 loaded amine samples

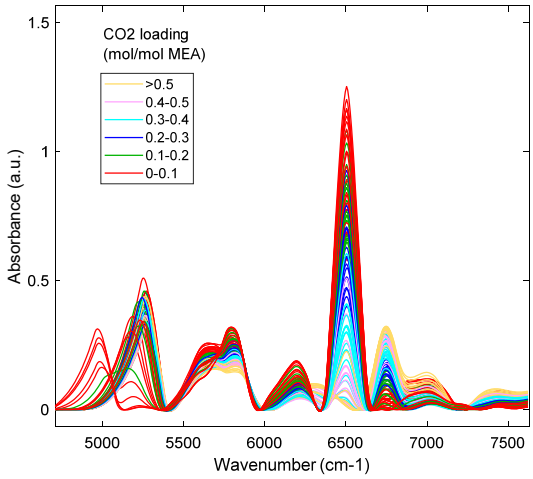

(a) Variation according to CO_2 loading

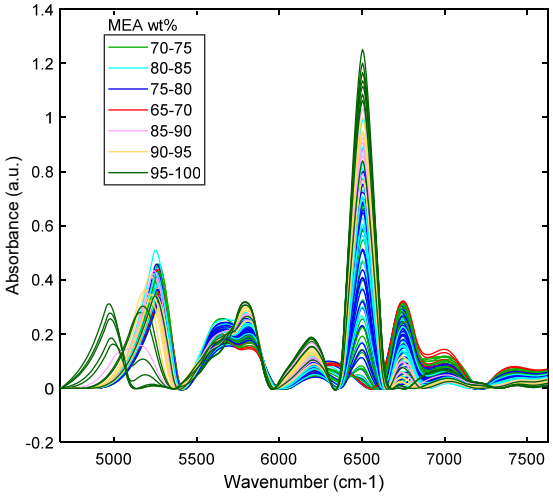

(b) Variation according to MEA wt%

Figure 10: FT-NIR data in the wavenumber range 4500-7500 cm^{-1} after baseline correction

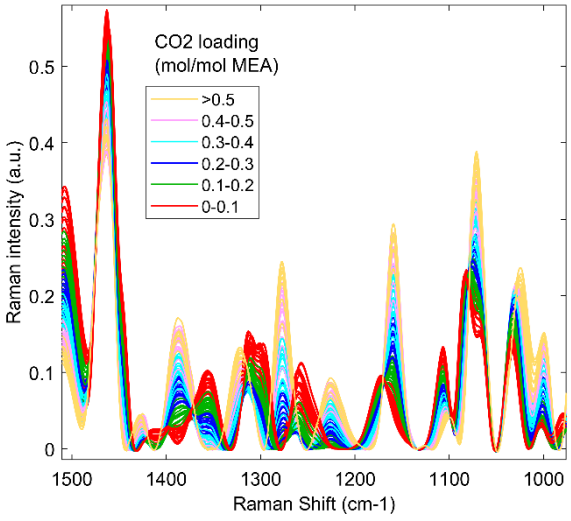

(a) Variation according to CO_2 loading

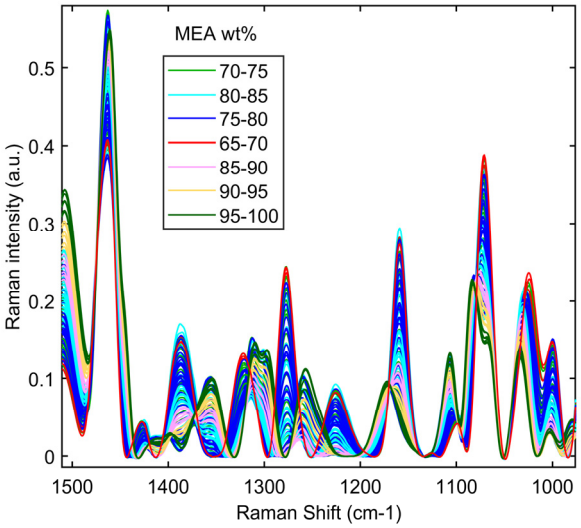

(b) Variation according to MEA wt%

Figure 11: Raman data in the fingerprint region after baseline correction

3.1.2. Raman data

The raw data obtained from Raman spectrometer between wavenumber 100-3426 cm^{-1} for different CO_2 loaded amine samples are shown in Figure 9. Spectral variations can be hardly correlated to distinguish between chemical compositions of samples. After removing the baseline variations of Raman data, the spectra become more informative as shown in Figure 11. Raman active vibrational modes for CO_2 loaded amine data are densed in the fingerprint region from 1000 -1500 cm^{-1} Raman wavenumbers. They belong to bands rising due to carbon species in the system which are carbonate, bicarbonate and carbamate as well as protonated amines and free amines. The bands observed in this study are comparable with our previous studies [19, 21].

3.2 Qualitative data analysis – PCA

The *structure parts* of FT-NIR and Raman data which have correlations with CO_2 loading and MEA concentration identified in section 3.1, were used for the PCA.

3.2.1. PCA for FT-NIR

Figure 12 shows the results of the PCA, which shows the score plot for PC1 vs PC2 for FT-NIR data. The preprocessing methods applied for input data were, Savitzky-Golay method, detrend, standard normal variate, and mean centering [23]. The best PCA results were achieved for 6000-7190 cm^{-1} wavenumbers. PCA analysis proves high correlation of spectroscopic data when both solvent strength and gas loading vary. According to Figure 12, PC1 describes 73% and PC2 describes 24% of the data variation for FT-NIR. The number of samples which belong to the amine concentration 70-75 wt%, 75-80 wt% and 80-85 wt% are considerably higher in the data set (refer Figure 3). Samples which belong to these categories are aligned tangentially in the score plot. Arrow A in Figure 12 (a) marks the direction of increasing CO2 loading of the samples while Arrow B marks the increasing MEA concentration in Figure 12 (b).

3.2.2. PCA for Raman

Score plot of PC1 vs PC2 for Raman data is shown in Figure 13. The input data was preprocessed using standard normal variate, Whittaker filter [29] and mean centered. The wavenumbers in the range 790-1525 cm^{-1} and 2734-3077 cm^{-1} resulted more meaningful overview for PCA. Among these two Raman shifts regions, the first one includes most of the vibrational modes related to carbon species and the second region include mainly the vibrational modes related to protonated amines and free amines. PC1 describes 85% and PC2 describes 11% of the data variation. On the other hand, as the CO_2 loading is expressed as mole CO_2 absorbed per mole MEA, even when there are different amounts of CO_2 moles absorbed, different MEA concentration can yield same CO_2 loading. PC1 vs PC2 plot in Figure 13 (a) shows sample distribution according to the CO2 loading. Line 1, Line 2 and Line 3 represent CO_2 loaded samples for 70-75 MEA wt %, 75-80 MEA wt % and 80-85 MEA wt % in these figures. These lines are distinct at lower CO_2 loading concentrations, but overlap at higher CO_2 loading concentrations. This is due to the complex correlation of spectroscopic data when both solvent and gas concentration vary.

3.3 PLS for FT-NIR and Raman

Quantitative determination of CO_2 loading and MEA concentration are shown in this section. Derivatives of raw data were used to preprocess FT-NIR data because they have the capability to remove both additive and multiplicative effects in NIR data [23]. Similarly, Whittaker filter was used to correct baseline in Raman data [29]. The overview of the four calibration models is shown in Table **1**. Model 1 and 2 correspond to FT-NIR spectroscopy to determine CO_2 loading and MEA concentration respectively. The NIR region from 5570-7291 cm^{-1} were included for the PLS model and this region includes the first overtones of C-H, O-H and N-H [28]. Some samples were removed as outliers from the data set and the reasons were abnormal spectra due to instrument noise, unstable temperature in the sample holder compartment and human errors during the reference analysis.

Model 3 and 4 correspond to Raman spectroscopy to determine CO_2 loading and MEA concentration respectively. The Raman wavenumber region from 940-1490 cm^{-1} was included as it represented chemical characteristics for all the carbon and amine species in the system [16, 19, 30, 31]. This wavenumber region also gave the minimum RMSEP value for each model. Few samples were removed as outliers which negatively affected to the stability of the model. The reasons for removing them were mainly the instrument related noise.

Table 1:Summary of the model results

Model no:	Model name (instrument_ measured property)	No.of cal*	No of val*	Wavenumber range (cm^{-1})	RMSEP
1	FT-NIR_CO_2	43	33	5570 -7291	0.01695 mol/mol MEA
2	FT-NIR_MEA	43	31	5570 -7291	0.72893 wt%
3	Raman_CO_2	44	43	940 - 1490	0.01338 mol/mol MEA
4	Raman_MEA	44	49	940 - 1490	0.90178 wt%

*(after removing outliers); cal = calibration samples; val = validation samples

The results of PLS calibration models which are significant for quantitative determination are shown from Figure 14 to Figure 17.

Each figure shows the measured property (i.e. CO_2 loading and MEA wt% from titration which were considered as actual property of the sample) and the predicted property (based on the developed PLS model in this study) for calibration and validation set. The number of calibration and validation samples after removing outliers are also shown in Table **1**. Presence of outliers makes the model unstable (poor predictability) and therefore such samples were removed after a careful investigation. The RMSEP value, r^2 and bias values can be used to understand the fit of correlation between an actual property and modelled property.

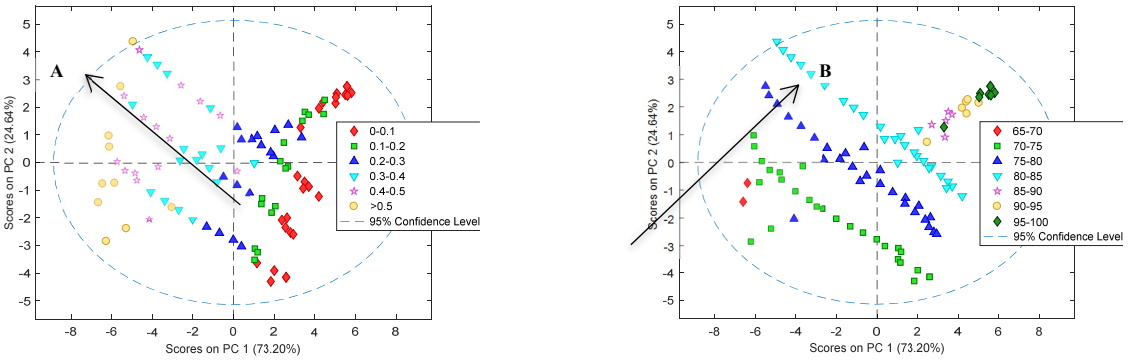

(a) Grouped according to CO_2 loading values (b) Grouped according to MEA wt %

Figure 12: PCA analysis for preprocessed FT-NIR data - sample distribution in PC1/PC2 space

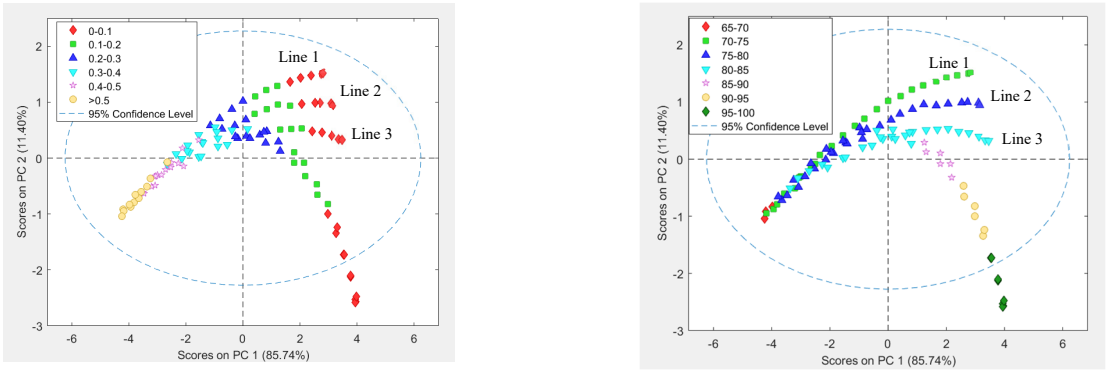

(a) Grouped according to CO_2 loading values (b) Grouped according to MEA wt %

Figure 13: PCA analysis for preprocessed Raman data - sample distribution in PC1/PC2 space

Estimated uncertainty of the model predictions have been shown as error bars. The line "fit" corresponds to the regression line and 1:1 is the target line when measured and predicted values overlap. For all the models, *fit* and 1:1 lines were almost same and r^2 value was more than 0.98. The red points mark the validation samples which are a completely new data set (data not used for model calibration) and therefore they represent future data. The good agreement of these validation samples with the 1:1 line is an indicator of the model predictability with future samples.

The wavelength of the spectrometer included in the calibration model and the RMSEP value are shown in Table **1**. For model 1 the RMSEP is 0.0169 mol/mol MEA which implies for a future sample tested by the FT-NIR spectrometer, the CO_2 loading will be the actual value ± 2*0.01695. When the same sample is measured by Raman spectrometer this value will be predicted by Model 3 as actual value ± 2*0.01338. The MEA wt% of a future sample will be predicted with an RMSEP of 0.7 and 0.9 by FT-NIR and Raman instruments respectively. The wavenumber region for FT-NIR PLS models were 5570 -7291 cm^{-1} where the first overtone of N-H, C-H and O-H absorption bands occur. The Raman wavenumber region for model 3 and 4 was selected from 940-1490 cm^{-1} because it contains most of the vibrational modes related to characterize amine and absorbed CO_2 concentration.

4. Conclusion

This study aimed for developing a quick and reliable analysis method to determine two most important chemical properties frequently measured in an amine based CO_2 capture process which are the gas loading and solvent strength. The standard procedure of analysis these parameters are offline laboratory methods such as titration. Raman spectroscopy and FT-NIR spectroscopy were used for this study to investigate their feasibility to report quantitative determination of CO_2 loading (mol/mol) and MEA wt%.

Both spectroscopic methods show similar competencies for these analyses in the CO_2 loading range from 0 – 0.6 mol CO_2/mol MEA and MEA strength from 66-99.5 wt %. The paper shows the methodology of transforming a difficult-to-explain spectra into meaningful chemical information by a chemometric approach. Qualitative analysis of data was performed by PCA for the pretreated spectral data. Results show that there is possibility to distinguish samples in different CO_2 loading and MEA concentration using score plots. Eventhough PCA did not provide a perfect discretization of the data it proved having opportunity to explore data. PLS algorithm was used to develop prediction models for CO_2 loading and solvent strength. There was a reasonable fit between calibration and validation data in the PLS regression. RMSEP values for 4 PLS models were in an acceptable

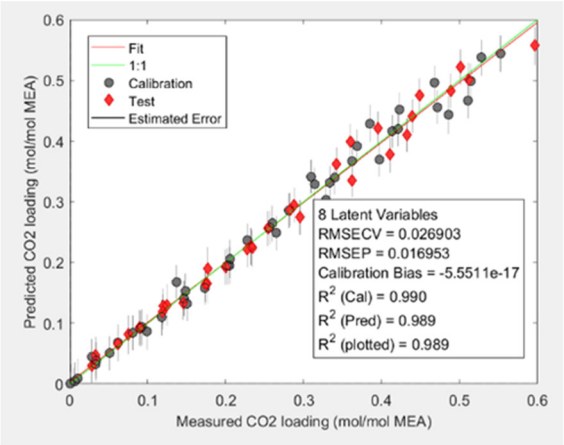

Figure 14: CO_2 loading prediction by FT-NIR (Model 1)

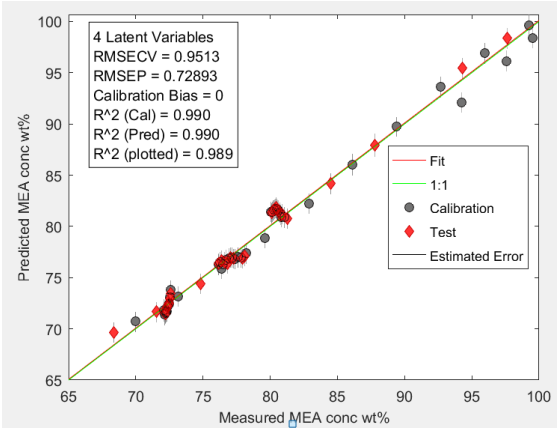

Figure 15: MEA wt prediction by FT-NIR (Model 2)

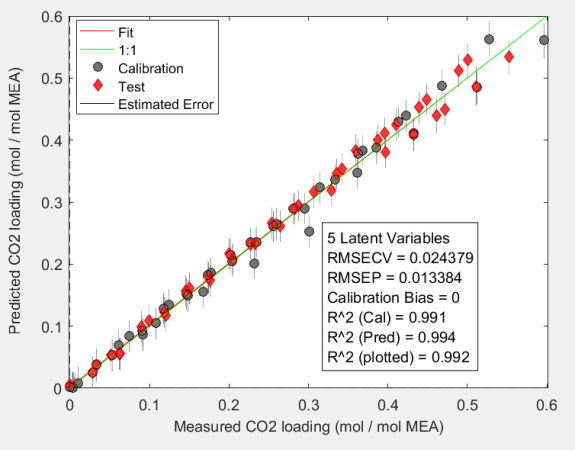

Figure 16:CO_2 loading prediction by Raman (Model 3)

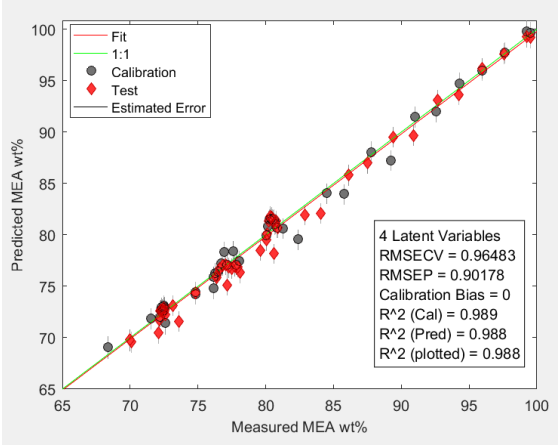

Figure 17. MEA wt prediction by Raman (Model 4)

region. The models are competent enough to be used as real-time monitoring tools when high concentrated amine is used. In addition, these models are also useful in optimization of CO_2 capture process such as to find the absorption capacity with time, optimum lean and rich loadings, minimum liquid & steam flow rates and optimum CO_2 feed gas flow rate.

References

[1] IEA, CO_2 Emissions from Fuel Combustion 2019: Overview. 2019.

[2] Kohl, A.L. & Nielsen R., Gas Purification. 5 ed. 1997, Texas: Gulf Professional Publishing.

[3] Eimer, D., Gas Treating: Absorption Theory and Practice. 2014, United Kingdom: John Wiley & Sons, Ltd.

[4] Davis, J., Thermal Degradation of Aqueous Amines Used for Carbon Dioxide Capture. 2009, University of Texa Austin, USA.

[5] Strazisar, B.R., Anderson, R.R. & White, C.M., Degradation Pathways for Monoethanolamine in a CO2 Capture Facility. Energy & Fuels, 2003. 17(4): p. 1034-1039.

[6] Raksajati, A., Ho, M., & Wiley, D., Reducing the Cost of CO_2 Capture from Flue Gases Using Aqueous Chemical Absorption. Industrial & Engineering Chemistry Research, 2013. 52: p. 16887-16901.

[7] Flø, N.E., et al., Results from MEA Degradation and Reclaiming Processes at the CO_2 Technology Centre Mongstad. Energy Procedia, 2017. 114: p. 1307-1324.

[8] Dumée, L., et al., Purification of aqueous amine solvents used in post combustion CO_2 capture: A review. International Journal of Greenhouse Gas Control, 2012. 10: p. 443-455.

[9] Overview of Process Analysis and PAT, in Process Analytical Technology. p. 1-15.

[10] Jinadasa, M.H.W.N., Process analytical technology for real-time quantitative speciation of aqueous phase CO_2 capture solvents. 2019, University of South-Eastern Norway: Porsgrunn.

[11] van der Ham, L.V., et al., Inline Monitoring of CO_2 Absorption Processes Using Simple Analytical Techniques and Multivariate Modeling. Chemical Engineering and Technology, 2014. 37(2): p. 221-228.

[12] Kachko, A., et al., Comparison of Raman, NIR, and ATR FTIR spectroscopy as analytical tools for in-line monitoring of CO_2 concentration in an amine gas treating process. International Journal of Greenhouse Gas Control, 2016. 47: p. 17-24.

[13] Kachko, A., et al., In-Line Monitoring of the CO_2, MDEA, and PZ Concentrations in the Liquid Phase during High Pressure CO_2 Absorption. Industrial &

Engineering Chemistry Research, 2016. 55(13): p. 3804-3812.

[14] Puxty, G., et al., A comparison of Raman and IR spectroscopies for the monitoring and evaluation of absorbent composition during CO_2 absorption processes. International Journal of Greenhouse Gas Control, 2016. 49: p. 281-289.

[15] Beumers, P., et al., Model-free calibration of Raman measurements of reactive systems: Application to monoethanolamine/water/CO_2. Fluid Phase Equilibria, 2016. 424: p. 52-57.

[16] Kachko, A., et al., Speciation of MEA-H_2O-CO_2 by Raman spectroscopy :The impact of spectral analysis. in 7th Trondheim CCS Conference. 2013. Trondheim.

[17] Idris, Z., Jens, K.J., and Eimer, D.A., Speciation of MEA-CO_2 Adducts at Equilibrium Using Raman Spectroscopy. Energy Procedia, 2014. 63: p. 1424-1431.

[18] Samarakoon, P.A.G.L., et al., Equilibria of MEA, DEA and AMP with Bicarbonate and Carbamate: A Raman Study. Energy Procedia, 2013. 37: p. 2002-2010.

[19] Jinadasa, M.H.W.N., et al., Raman Spectroscopy as an Online Monitoring Tool for CO_2 Capture Process: Demonstration Using a Laboratory Rig. Energy Procedia, 2017. 114: p. 1179-1194.

[20] Hans Villemoes Andersen, H. V., Wedelsbäck, A. H., & Hansen, P. W. NIR Spectrometer Technology Comparison. 2013. P/N 1026672.

[21] Jinadasa, M.H.W.N., Jens, K.-J., & Halstensen, M., Process Analytical Technology for CO_2 Capture, in Carbon Dioxide Chemistry, Capture and Oil Recovery, J.S. Iyad Karamé, Hassan Srour, Editor. 2018, IntechOpen.

[22] Chemometrics in Process Analytical Technology (PAT), in Process Analytical Technology. p. 353-438.

[23] Rinnan, Å., Berg F.v.d., & Engelsen, S.B., Review of the most common pre-processing techniques for near-infrared spectra. TrAC Trends in Analytical Chemistry, 2009. 28(10): p. 1201-1222.

[24] Afseth, N.K., Segtnan, V.H., & Wold, J.P., Raman Spectra of Biological Samples: A Study of Preprocessing Methods. Applied Spectroscopy, 2006. 60(12): p. 1358-1367.

[25] Liland, K.H., Kohler, A., & Afseth, N.K., Model-based pre-processing in Raman spectroscopy of biological samples. 2016. 47(6): p. 643-650.

[26] Wold, S., Esbensen, K.H., & Geladi, P., Principal component analysis. Chemometrics and Intelligent Laboratory Systems 1987. 2(1): p. 37-52.

[27] Wold, S., Sjöström, M., & Eriksson, L., PLS-regression: a basic tool of chemometrics. Chemometrics and Intelligent Laboratory Systems, 2001. 58(2): p. 109-130.

[28] Socrates, G., Alkane Group Residuals: C–H Group Infrared and RamanCharacteristic Group Frequencies: Tables and Charts. 3 ed. 2000: John Wiley & Sons Ltd.

[29] Whittaker, E.T. On a new method of graduation. in Proceedings of the Edinburgh Mathematical Society. 1922.

[30] Wong, M.K., Bustam M.A., & Shariff A.M., Chemical speciation of CO_2 absorption in aqueous monoethanolamine investigated by in situ Raman spectroscopy. International Journal of Greenhouse Gas Control 2015. 39: p. 139–147.

[31] Vogt, M., Pasel, C., & Bathen, D., Characterisation of CO_2 absorption in various solvents for PCC applications by Raman spectroscopy. Energy Procedia, 2011. 4: p. 1520-1525.

STORAGE RESOURCES FOR FUTURE EUROPEAN CCS DEPLOYMENT; A ROADMAP FOR A HORDA CO_2 STORAGE HUB, OFFSHORE NORWAY

A.E. Lothe*, P.E.S. Bergmo, A.-A.Grimstad
SINTEF Industry, Trondheim, Norway
* Corresponding author e-mail: ane.lothe@sintef.no

Abstract

Deployment of Carbon Capture and Storage (CCS) at large scale will be necessary to be able to fulfil the goal from the Paris Agreement to keep the global mean temperature in year 2100 well below two degrees Celsius above pre-industrial levels. Consequently, it is anticipated that there will be a significant increase in demand for CO_2 storage capacity. Offshore areas, such as the North Sea part of the Norwegian Continental Shelf, are prime candidates to provide this storage capacity. Given that the development of a storage site can take five years or more, it is of major importance to start the planning of expandable storage hubs. Anticipating and planning of additional stores will give industry clusters and power producers confidence that there will be sufficient operative storage capacity available for the expected increasing supply of captured CO_2. In this study, which is part of the ALIGN-CCUS project, we outline how an expansion in annual storage capacity of a CO_2 storage hub offshore the west coast of Norway can be achieved. Simulation of CO_2 storage and capacity estimates show that the Horda Platform study area has at least four potential storage sites with capacities in million tonnes (Mt) or thousand million tonnes (Gt) CO_2 as follows: 1) Aurora structure, in the Johansen Formation, south-east of the Troll Gas Field (120–293 Mt); 2) Alpha structure, in the Sognefjord Formation, northern Smeaheia area (40–50 Mt); 3) Gamma structure, in the Sognefjord Formation, southern Smeaheia area (0.15–3 Gt) and 4) Troll Field, Sognefjord Formation, after cessation of gas production (3–5 Gt). We sketch a timeline for which possible sites could be used for the development of the industrial-scale Horda CO_2 Storage Hub over the next thirty years. The annual storage capacity is matched to the estimated CO_2 supply rates (million tonnes per year) from sources in Norway, Sweden and Northern Europe. These estimates indicate cumulative totals of CO_2 stored in range of 810 Mt by 2050, and 1.85 Gt by 2065.

Keywords: *Horda CO_2 Storage Hub, road map, deployment*

1. Introduction

In the ERA-ACT ALIGN-CCUS project several European industrial Carbon Capture and Storage (CCS) clusters are described, with sources, transport solutions and linked geological storage. The development of such clusters will facilitate a rapid deployment of CCS and thereby contribute to the urgently needed reduction in emissions of CO_2 to the atmosphere.

The present paper discusses possible storage options on the Norwegian Continental Shelf (NCS), expanding from the storage solution for the Norwegian full-scale CCS demonstration project [1] [2]. This demonstration project plan to capture CO_2 at industrial sources in Oslo and Brevik, transport the CO_2 by ship to Øygarden west of Bergen, and from there transport the CO_2 via a pipeline to a permanent geological storage site south-west of the Troll Gas Field. The joint venture project 'Northern Lights', with partners Equinor, Total and Shell, is at present developing the storage solution for the demonstration project [3][4].

In the pre-feasibility study for the demonstration project [2] the outlined project would at most inject 1.25 million tonnes of CO_2 per year for 25 years. The required storage capacity of maximum 31 million tonnes would be met by the eastern part of the late Jurassic Sognefjord Formation which had at the time been subject to several modelling and simulation studies. A storage site prospect named 'Smeaheia Alpha' was believed to have a storage capacity of 100 million tonnes within a structural trap. The wider Smeaheia area, consisting of the Sognefjord Formation east of the Vette Fault, was believed to have a storage capacity of at least 500 million tonnes, based on earlier studies.

The giant Troll Field has its reservoir in the Sognefjord Formation in several fault blocks west of the Vette Fault. Production of gas from the field is believed to be influencing the pore pressure in the Sognefjord Formation in the whole region. The effect east of the Vette Fault at present is uncertain, but on the long term the pressure depletion effect is believed to be significant also in the Smeaheia Alpha prospect [5][6][7][9][10]. The resulting uncertainty in the density of the CO_2 and the risk of spill-over of expanding CO_2 into the Øygarden Fault complex has led the Northern Lights project to shift the focus for developing a CO_2 storage site to the south-western part of the early Jurassic Johansen Formation. A storage site prospect called 'Aurora' has been identified in the Johansen Formation, based on earlier studies [11][12]. These studies and others [13][14] have indicated a storage capacity in the Johansen Formation of at least 160 million tonnes.

The Smeaheia area, the Johansen Formation and the Troll Field all lie in the wider Horda Platform. Fig. 1 shows the location of the Horda Platform in relation to the west coast of Norway. Earlier simulation studies have investigated several possible injection locations for CO_2 in this area. Eigestad et al. [13] simulated injection of 3.5 million tonnes per year for 110 years in the southern part of the Johansen Formation. Bergmo et al. [14] simulated injection of 3 million tonnes per year for 110 years in the western part of the Johansen Formation. Bergmo et al. [15] also investigated the effect of extracting formation brine for pressure control in simulations of up to 540 million tonnes CO_2 injected into the western part of the Johansen Formation over a 50-year period.

Lauritsen et al. [10] simulated injection into the Smeaheia Alpha structure during depletion from the Troll Field gas production and found that the maximum injected amount should be kept below 40 million tonnes to avoid spill-over into the Øygarden Fault complex. Nazarian et al. [9] investigated, in addition to studies of the long-term expansion of the CO_2 plume at Smeaheia Alpha, a larger scenario with injection of massive amounts of CO_2 into the 'Smeaheia Gamma' structure further south in the Sognefjord Formation. Scenarios with as much as 100 million tonnes CO_2 injection per year over a period of 30 years was tested. Results show that if the injection rate is increased significantly this can counteract the pressure depletion caused by the gas production at the Troll Field, and the injected CO_2 will remain in a dense state and have a smaller final footprint.

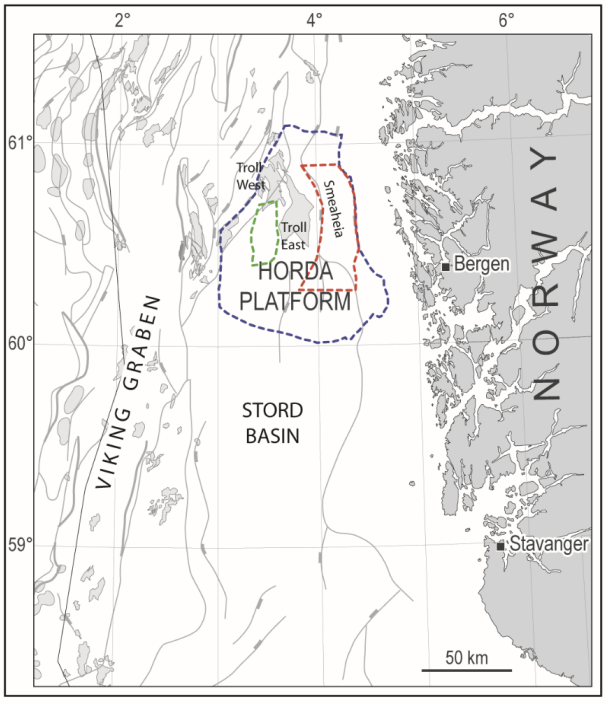

Fig. 1. The location of the Horda Platform area, offshore Norway. Blue outline show area for pressure simulations in [7], green online show outline of Aurora simulation model, and red Smeaheia reservoir model. Modified from [8].

Lothe et al. [7] investigated the effect of various assumptions for the transmissibility of the faults in the region (see Fig. 1, blue outline) and particularly Vette Fault with two fault ramps near the Smeaheia area (Fig. 2). Simulation results show that the final extent of the CO_2 plume at Smeaheia Alpha is much smaller if low transmissibility of the fault is assumed, since the higher local pressure will give a smaller occupied pore volume.

The prospective storage sites in the Smeaheia area and the Johansen Formation represents a potential storage capacity much larger than what is needed for the Norwegian full-scale demonstration project. The sites are located within an area of about 50 x 50 km. It is therefore interesting to consider development of a CO_2 storage hub in the area, combining the individual storage sites into a larger infrastructure that can receive and store an increasing annual amount of CO_2 from sources in Norway and other parts of Northern Europe.

The practical CO_2 storage capacity of a storage site is dependent on several factors like connected pore volume, permeability, depth, structural trapping and the boundary conditions (open/semi-open/closed). In this paper we investigate in more detail how the storage prospects will respond to CO_2 injection at increasing annual rates, and how the capacity can be matched to the requirement for storage from various CO_2 sources.

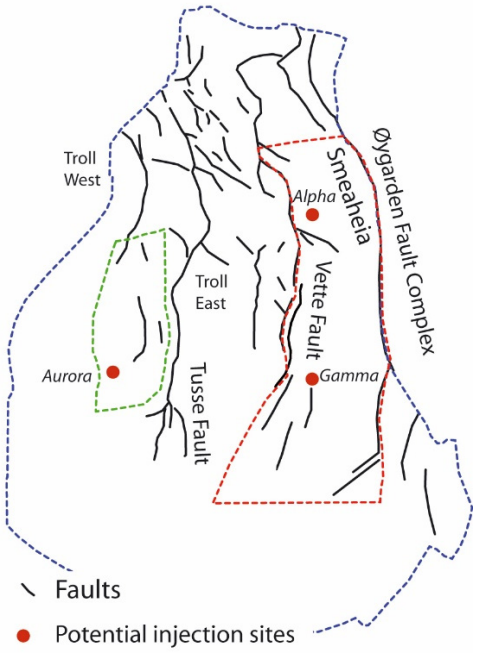

Fig. 2. Major fault systems and storage prospects in the Horda Platform area. The red and green outlined areas show, respectively, the outline of the Smeaheia reservoir simulation model and the Aurora simulation model. Modified from [8].

2. Geological setting

The study area covers the Horda Platform and the northern part of the Stord Basin in the northern North Sea (Fig. 1). The Smeaheia prospect is located on the eastern margin of the Horda Platform, approximately 20 to 35 km offshore Western Norway. The giant Troll Field (1310 x 10^9 Sm^3 recoverable gas) within a thick sandstone reservoir, is located west of Smeaheia. The Aurora prospect is located in the western part of the Horda Platform, south-west of the Troll Field (Fig. 2).

The northern North Sea has experienced three main extensional rift episodes in the Devonian, Permian-to-Early Triassic, and Middle Jurassic to Early Cretaceous (e.g. [16]). The present-day rift structure being

predominantly a result of reactivation of the Permian structures during Middle Jurassic to Early Cretaceous (see e.g. [17]). During these rift episodes the structural inventory of the area was developed. The fault pattern of the Horda Platform is dominated by three North-South striking basement-involved faults, named from east to west the Øygarden, Vette and Tusse Fault Complex (Fig. 2). The Tusse Fault Complex divides the Troll Field into the Troll West and Troll East. These three main faults dip toward the west, bounding major half-graben basins, with the basement displaced across these faults by a maximum of around 4 kilometres. Depth conversion of seismic lines indicates the faults have dip values of approximately 40° where they separate Permian-Triassic sediments from crystalline basement and steepen upward to roughly 55° where they offset Jurassic and Cretaceous stratigraphy [18]. In addition to the northerly trending large faults, there are smaller structures observed in the area. Duffy et al. [19] mapped smaller North-West trending faults 2 to 10 kilometres in length with displacements of less than 100 metres.

2.1 Major storage options

The main possible CO_2 storage reservoir units in the Horda Platform area are the Middle to Upper Jurassic Sognefjord, Fensfjord and Krossfjord formations and the deeper Lower Jurassic Johansen Formation.

The Sognefjord Formation (Upper Jurassic, Oxfordian to Kimmeridge), the Fensfjord Formation (Upper Middle Jurassic, Callovian) and Krossfjord Formation (Upper Middle Jurassic, Bathonian) represents three coastal shallow-marine sandstones in the Viking Group that interfinger with the shaly Heather Formation on the Horda Platform (Fig. 3). The total thickness of the three formations is around 400 to 500 metres [20].

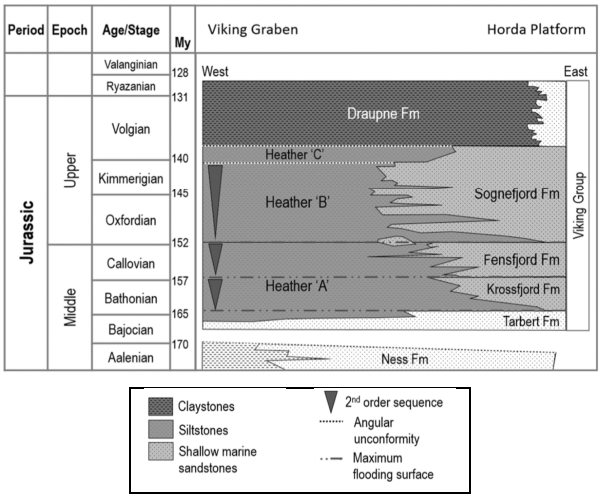

Fig. 3. Middle to Upper Jurassic chronostratigraphic framework for the Viking Graben and Horda Platform. The shallow marine Sognefjord, Fensfjord and Krossfjord formations build out from the east. From [21].

The Early Jurassic Johansen Formation and Cook Formation sandstones of the Dunlin Group (Fig. 4) are deposited on the Horda Platform area, with the Amundsen Formation mudstones separating the formations, in part of the study area (northern part of the Horda Platform). The whole of the parent Dunlin Group has a thickness in order of 320 metres, with Johansen Formation approximately 120 metres thick. The top-Johansen surface is buried between 2- and 3-kilometres depth, with gentle tilting towards north (approximately 0.6°).

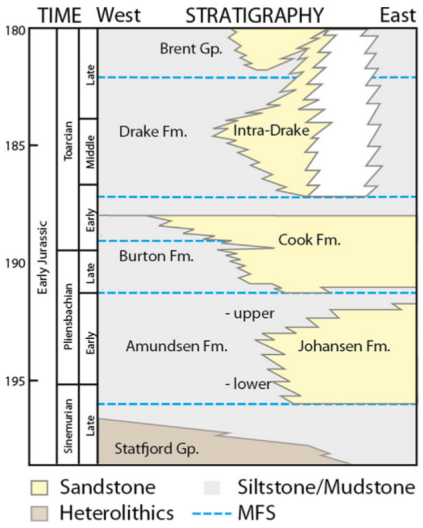

Fig. 4 Stratigraphy for the Early Jurassic Dunlin Group, with Johansen and Cook formations marked. Slightly modified from [11] with references therein.

2.1 Sognefjord, Fensfjord and Krossfjord Formations

The Oxfordian to Kimmeridgian Sognefjord Formation consists of sands and sandstones, grey-brown in colour, medium to coarse-grained, well sorted and friable to unconsolidated. It is the main reservoir in the Troll Field with a thickness of 100–170 m and individual target sands are in the order 3 to 45 metres thick with permeability values ranging from 1 to 20 Darcy. Porosities at the Troll Field range between 19 % and 34 %. These sands alternate with more fine-grained micaceous units. In addition, calcite cemented zones can be found in both Sognefjord and Fensfjord formations typically being in the order of a couple of metres thick and with a lateral extent between tens of meters to a few kilometres [22]. Gibbson et al. [22] using petrographical analysis, showed that early diagenetic, near-surface cementation has occurred in connection with maximum flooding surfaces and sequence boundaries at the Troll Field. These cemented horizons have a large impact on the oil production strategy in the field [23]. Patruno et al [24] show in detail, how the shallow-marine clinoform sets to the Sognefjord Formation has prograded in the Troll field area. Internally, in the Sognefjord Formation, there are four stratigraphic series mapped, bounded by regional maximum flooding surfaces, each corresponding to a westward dipping clinoforms.

The Fensfjord and Krossfjord formations compromise sandstone, around 195 m thick in the Troll Field area, that is sourced from the Norwegian mainland to the east. Six facies have been mapped, representing wave- and tide-dominated deltaic, shoreline and shelf deposits. Coastal plain facies are absent, indicating that the strata of the Troll Field were deposited in a fully subaqueous environment [21]. Four bio-stratigraphically distinctive, regional maximum flooding surfaces are recognized in cored wells. The series, bounded by maximum flooding

surfaces have relatively uniform thickness, that indicates little tectonic influence [21].

2.2 Johansen and Cook formations

The Lower Jurassic Johansen Formation sandstones (Dunlin Group) represents shallow-marine deposits at the Horda Platform [25]. The sandstone consists of E-W prograding delta front deposits, with clinoforms building out into deep waters, associated with delta front and pro-delta turbidites. During an aggradation stage, thick NNW-SSE oriented spit bar facies were deposited down-current. The sandstones, deposited in the proximal delta top and shallow shore-face environments of the delta front have high porosity and permeability [11][12].

Several interlayers of mudstone and siltstone with low porosities are observed within the Johansen Formation [12] that are associated with flooding events. They are rather thin (a few metres) but are observed laterally over a kilometre scale. Carbonate layers i.e. calcite cemented sandstone, usually <1 m thick, are frequent in the Johansen Formation [11].

The sandy Early Jurassic Cook Formation lies stratigraphically above the Johansen Formation. In part of the study area, it directly overlay the Johansen Formation. In other areas, they are separated by the shaly Amundsen Formation. The Cook Formation is commonly erosionally based [26]. In the Horda Platform area, the Cook Formation is described as progradation shoreface sand deposits, locally influenced by tidal processes (Sundal et al. [11] and references therein).

3. Methodology and model set up

For storage sites in the Sognefjord Formation the pressure depletion caused by gas production at the Troll Field has been an important part of the boundary conditions of the simulations. The site-specific modelling issues are discussed in the following subsections.

3.1 Sognefjord and Fensfjord Formation reservoir model

For the model setup, seismic horizons and faults interpreted on high quality 3D seismic data by the Norwegian Petroleum Directorate (NPD) is used [5][6]. The reservoir model built by NPD, consists of data from Sognefjord Formation and Fensfjord Formation. The model is set up for a large area, and effect of pressure depletion were simulated for the whole region (Lothe et al. [7]). However, to be able to simulate capacity of CO_2 injection in the Smeaheia area, a detailed model has been set up east of the Vette Fault (see the red model outline in Fig. 2). The heterogeneous flow properties in the model is guided by a reservoir model released by Equinor for use in the Pre-ACT and ALIGN projects.

3.1.1 Boundary condition with pressure depletion from the Troll Field

The boundary conditions, and effect of pressure depletion from Troll area are taken from Lothe et al. [7]. In that study pressure depletion from Troll Field were simulated varying the influence of faults (effect of fault transmissibilites), and the effect of open and closed relay zones along the Vette Fault (Fig. 5).

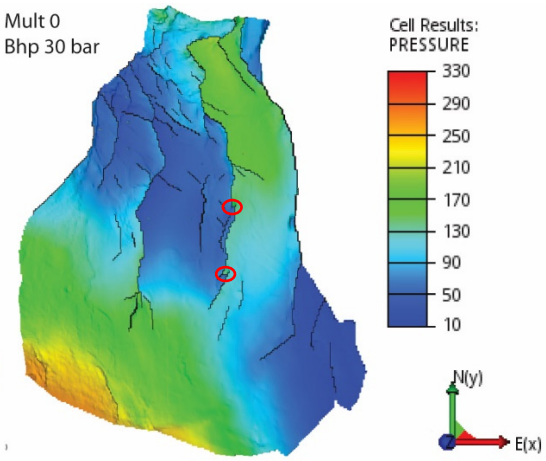

Fig. 5. Map with modelled pressure in year 2072 with two extended faults in the relay zones along the Vette Fault (marked with red), using sealing (mult 0.0) faults. Pressures in bar Modified from [7].

In that study it was assumed to be no-flow boundary conditions in all directions and the model is initialised with only water at hydrostatic conditions. To represent the production and future pressure depletion in the Troll Field, 10 water production wells are evenly distributed between the Troll West and Troll East. The water production wells are set to produce at a desired bottom-hole pressure (BHP). The base case was set up assuming a constant pressure depletion rate in the Troll Field from 1995 till 2022, with 2.66 bar depletion every year (see also Eiken et al. [27]). This is done by reducing the controlling BHP in the production wells by 8 bar every third year. From year 2022 until 2072 we assume a constant pressure depletion rate down to a final controlling BHP in the production wells equal to 30 bar in 2072.

3.1.2 Upscaling of sedimentary heterogeneities

In the original NPD model for the Sognefjord and Fensfjord formations, four layers (three in Sognefjord and one from Fensfjord to top Brent) were modelled. In the southern part of the study area, a deltaic lobe and associated channel structures were defined for the Fensfjord Formation The channels were correlated with ancient valley systems routed from the Norwegian mainland [5]. The porosity values in the model were varied between 15 and 35 %. The vertical permeability varies between 0–1760 mD, with a mean permeability of 31 mD. The horizontal permeability varies between 0.25–22 000 mD, with a mean permeability of 456 mD.

To model the dynamic behaviour of injected CO_2 a new refined simulation model is required. A smaller more refined model (400 m by 400 m grid) east of the Vette Fault has been constructed with the objective to refine the model in the vertical direction. The resulting model has 27 layers (Fig. 6). In the new model three intra sand shale layers have been constructed in the Sognefjord formation in addition to the shale layers (maximum flooding surfaces) between Sognefjord and Fensfjord and between Fensfjord and Krossfjord formations. For the base case a stochastic distribution of properties is assumed where the shale layers are not continuous but have localized zones of high permeabilities (green patches in Fig. 6a). The

shale layers within and between the Sognefjord and Fensfjord formations have an average permeability of 1 mD, while the sand "holes" are in range of 1 Darcy (Fig. 6b).

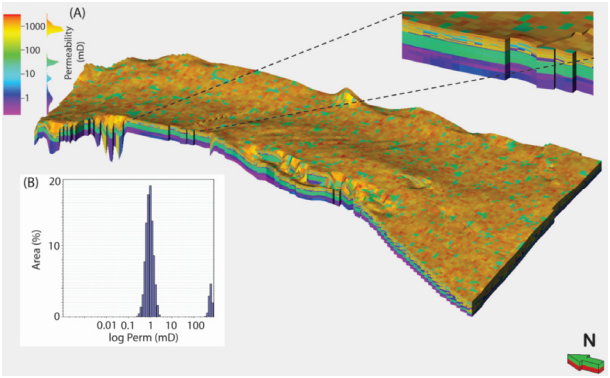

Fig. 6 a) Smeaheia Reservoir model set up with permeability distribution for Sognefjord, Fensfjord and Krossfjord formations east of Vette Fault, b) Logarithmic base case permeability (mD) versus area (%) distribution for the clay-rich layers, with sand patches. Modified from [8].

3.1.3 Simulation set-up

For the simulations, it is assumed that constant depletion from the Troll Field will affect the CO_2 injection in the Smeaheia area. We use the simulated pressure history from Lothe et al. [7], with extended faults in the two relay zones along the Vette Fault, and fault transmissibility set to 0, as boundary conditions for the model. The dynamic boundary conditions are imposed on the model by use of five water production wells along the boundary. The CO_2 is injected at a constant injection rate of 3 million tonnes per year over 50 years (total 150 Mt). The injection well is located close to the Alpha structure (Fig. 1) and the simulations are run for a total period of 1000 years.

3.2 Johansen and Cook Formation reservoir model

The reservoir model used for the simulations was defined by Gassnova [28] and Sundal et al.[11], covering an area of 475 km^2 south of the Troll Field (green model outline in Fig. 2). The model resolution is 250 by 250 metres laterally, with 120 layers vertically, incorporating the Johansen and Cook Formations. The porosity is calculated from interpreted acoustic impedance in the GN10M1 3D seismic volume [28]. The horizontal permeability is calculated form porosity based on core measurements [11]. The vertical to horizontal permeability anisotropy is set to 0.1, which is a common assumption for low-energy clastic deposits (see e.g. [29],[11]). Sundal et al. [11] assume ordinary transmissibility calculation of non-neighbour connections across the faults, i.e., no transmissibility modifier for faults. Large faults to west and east, Tusse and Vette faults, are assumed to be sealing. The full connected volume of the Johansen and Cook formations is modelled through the use of pore volume multiplicators on the northern boundary of the model. The southern boundary, as well as the boundaries to the east and west are closed.

4. Results from reservoir simulations

4.1 Smeaheia Alpha structure

For the Smeaheia Alpha simulation studies the effect of various assumptions for the reservoir heterogeneity is tested. This serves to further illuminate the potential storage capacity of the structure, which in previous work has varied from 40 Mt to several hundred Mt. The pressure depletion effect from the Troll Gas Field is modelled using "pseudo-wells" in the southern boundary of the model. The drawdown schedule in these wells is determined from simulations of the regional pressure development in the Sognefjord Formation during production from the Troll Field. See Lothe et al. [7] for details. Long-term simulations are run for a period of 1000 years.

4.1.1 Effect of pressure depletion

The effect of pressure depletion from the Troll Field was studied by Lothe et al. [8] for several assumptions on the sealing properties of the faults in the larger study area. Using boundary conditions based on the pressure modelling from Lothe et al. [7], the effect on injected CO_2 in the Smeaheia was modelled. The CO_2 injection rate used was 3 million tonnes per year over a period of 50 years from 2022 to 2072. Rapid migration into the eastern Øygarden Fault Zone was observed in all three scenarios. This behaviour is mainly controlled by the topography of the top layer and shows that this injected amount (150 Mt) is probably larger than the storage capacity of the Smeaheia Alpha structure. With this CO_2 injection rates the effect of Troll gas production on the pressure depletion in the area is temporarily counteracted, in particular for the cases with low fault transmissibility. Still, the CO_2 density decreases rapidly after the injection period, and the largest reduction is seen using the open fault assumption, that gives a large depletion from Troll Field. Pressure depletion on the long term is significant even with closed faults, due to pressure communication in the southern part of the Sognefjord Formation, where the faults die out.

4.1.2 Effect of facies heterogeneities

It is known from other studies that heterogeneities like calcite layers or clay layers may have a major impact on the storage capacity. Lothe et al. [8] also studied the effect of different sealing properties of the shale layers in three simulation scenarios. The base case (a) is as described in the geology section above. In a low-permeability case (b) the permeability in the shales layers is multiplied by 0.001. In a third case (c) a constant permeability of 0.1 mD is assigned to the shale layers, with no holes or weak zones. The CO_2 injection rate also in these simulations was 3 Mt/year over 50 years. The injection well is, however, a horizontal well placed somewhat deeper in the model. The simulation results showed that the shales layers have a large impact on the saturation distribution during and directly after the injection, with a larger CO_2 footprint in the deeper layers when shale layers have lower permeability. All simulations show some migration of CO_2 into the Øygarden Fault Zone and the main difference is the amount of residually trapped CO_2 close to the injection

well. The larger footprint of CO_2 around the injection well will also result in more CO_2 dissolving into the water phase.

4.1.3 Lower injection rate – 1 million tonnes per year

To give an estimate of the practical storage capacity of the Alpha structure new simulations are performed for this paper, with the injection rate reduced to 1 million tonnes per year for the same injection period of 50 years. This gives a total injection of 50 Mt CO_2. The injection site is also moved 800 metres westward compared to the simulations in Lothe et al. [8], to increase the distance to the spill point of the Alpha structure. The other parameters of the model are kept constant. The simulation is run for 1000 years from the start of the simulation. In this simulation the main amount of the injected CO_2 migrates westwards and to the north, while only a small volume migrates east to the Øygarden Fault Zone (Fig. 7). From these simulations, we estimate that a total of 50 Mt CO_2 can be stored in the Alpha structure, with minor migration into the Øygarden Fault Zone.

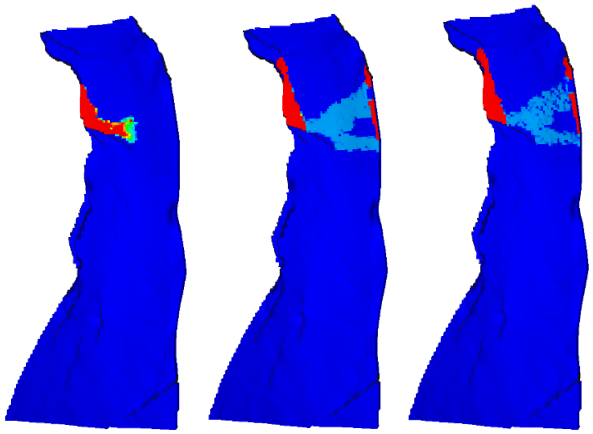

End of injection 500 years 1000 years

Fig. 7. Maps of simulated CO_2 injection at a rate of 1 Mtpa for 50 years in a vertical well in the Smeaheia Alpha structure. Red colours indicate high gas saturations, while blue indicate low gas saturation at left; end of injection, middle figure 500 years and right 1000 years.

4.2 Smeaheia Gamma Structure

Simulations have been carried out injecting CO_2 into the Gamma structure in the southern part of the Smeaheia area. We assume injection in one vertical well (located down-flank of the structure) with injection rate of 3 million tonnes per year over 50 years, and otherwise the same model setup as earlier described in Section 3.1.1. Pressure depletion from the Troll Field is incorporated into the model assuming sealing faults. The simulation has been run for 1000 years. The shale layers are assumed to have "holes" as described in the base case, Section 3.1.2.

Fig. 8 show the CO_2 saturation at the end of injection (50 years), where the gas fills the Gamma structure. After 500 years, some of the CO_2 have migrated into the Øygarden Fault Zone, and finally after 1000 years, more of the gas have migrated northwards along the Øygarden Fault Zone.

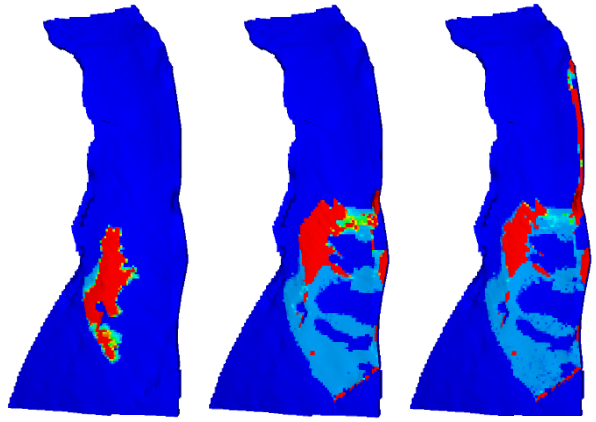

End of injection 500 years 1000 years

Fig. 8. Map view of CO_2 gas saturation from injection into one vertical well situated in the Smeaheia Gamma Structure. Colours as in Fig. 7.

4.3 Aurora Structure

For the Johansen Formation the goal was to simulate CO_2 injection with gradually increasing rate, matching a CO_2 supply scenario where new sources are added to the full-scale demonstration project after an initial period with only the sources defined in the full-scale project. When the total annual rate exceeds the capacity of a single well (assumed to be 3 million tonnes per year) a new well is drilled and added to the set of injection wells. The number of injection wells is increased further for each 3 million tonne rate increase, up to a maximum of 6 injection wells (with a total rate of 18 million tonnes per year). After a slower increase in annual rates in the first five years the annual rate is increased by 1.5 million tonnes per year. This means that a new injection well is drilled every second year. The locations of the wells in the simulation model are shown in Fig. 9.

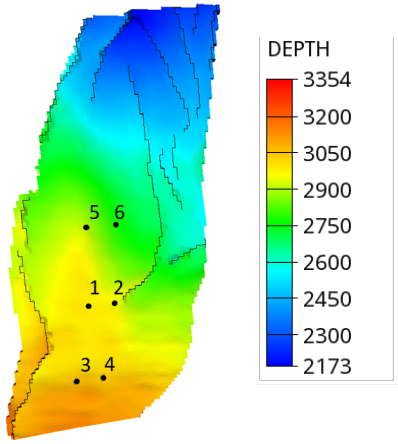

Fig. 9. Depth map in metres of the top Johansen Formation used for the detailed reservoir model of the Aurora site. Injection well locations (1 to 6) used in this work is shown. The distance between the wells in each pair is 2 km.

The injection schedule is shown in Fig. 10. Sensitivity cases are simulated with one and two injection wells. Fig. 11 shows the CO_2 footprint injecting CO_2 from the years 2023 to 2050 (27 years) using a) one well, b) two wells and c) six wells. For the two and six well cases, a ramp-up of the injection rate shown in Fig. 10 is used. The one well case injects 3 Mtpa from the start. Total injected amount of CO_2 in the shown cases are a) 81 Mt, b) 136

Mt and c) 322 Mt. The wells in the model are vertical wells and penetrate the top of the model at depths between 2700 and 3000 m below sea level. The minimum distance between wells is 2 km, with the reasoning that two slightly deviated wells can be drilled from the same template with distance of 2 km between the wells at reservoir depth.

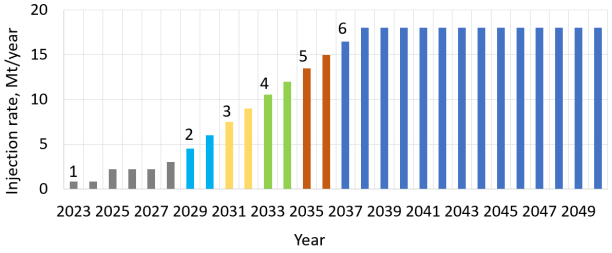

Fig. 10. Annual CO_2 injection rate schedule 2023 to 2050 in the simulations for the Aurora case with 6 injection wells. The numbers above the bars, and the colours indicate when a new well is added to the pool of active wells.

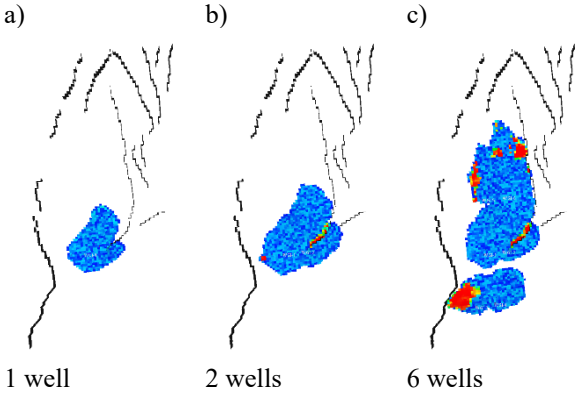

Fig. 11. Maps showing grid cells with CO_2 gas saturations and the major faults in the model area for the Aurora storage prospect. For well placement, see Fig. 9, for colour scale see Fig. 13.

4.3.1 Total pore volume

Sensitivities have been run on the assumed total pore volume in pressure communication with the Aurora storage site. In the Norwegian CO_2 Storage Atlas [20] the pore volume of the combined Johansen and Cook Formations is given at 90 Gm^3. This includes the part of the Johansen Formation east of the Tusse Fault. The simulations in Fig. 11 have been run with pore volume multipliers along the northern model edge that give the model a total pore volume of 280 Gm^3. This case assumes that a larger pore volume is in connection with the Johansen and Cook formations. A sensitivity case has also been run with a smaller multiplier giving a total model pore volume of 50 Gm^3 representing only the Johansen and Cook formations west of the Tusse Fault. The individual injection rates for the different wells are kept constant for the first 20 years, thereafter, reduced for the low case, see Fig. 12a) and b) for comparison. The size of the connected pore volume for the Aurora structure is uncertain and a more precise estimate of pore volume can only be assessed after several years of injection, by monitoring and modelling the injection pressure. The simulated cases should be considered upper and lower estimates for pore volume.

Simulation results show that the smaller model volume impacts the injection rate of the wells, which are all bottom-hole pressure restricted at 1.5 times the initial hydrostatic pressure at the top of the model at the position of each well. Fig. 13 shows in map view, that smaller pore volume, reduces the distribution on the CO_2 slightly. The reduction in injection rate at the end of the injection period leads to injection of a total of 293 Mt CO_2, compared to 322 Mt for the base case with larger pore volume.

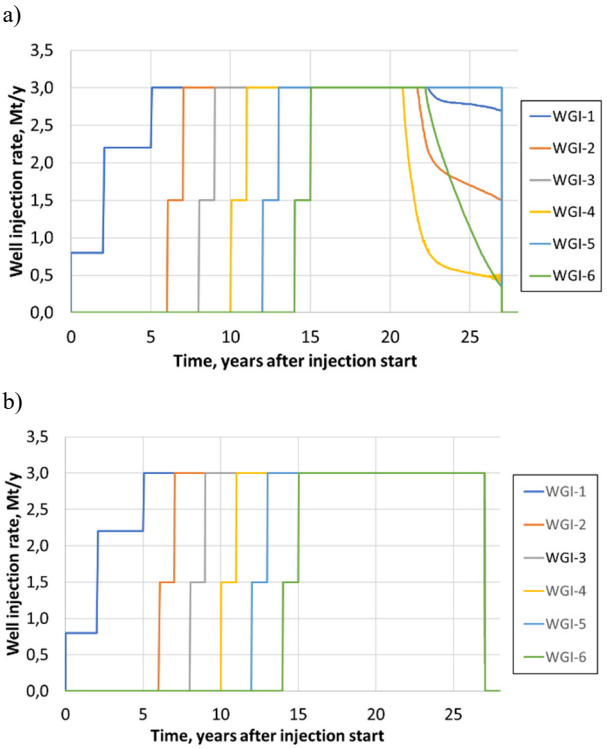

Fig. 12. Individual injection rates per well in the a) 50 Gm^3 and b) 280 Gm^3 pore volume cases.

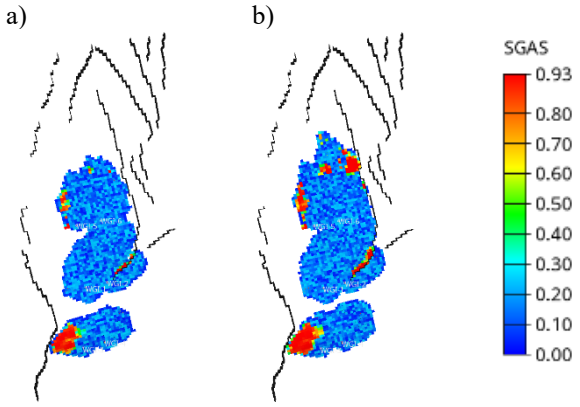

Fig. 13. CO_2 footprint at the end of the injection period for two cases with different total pore volume of a) 50 Gm^3 and b) 280 Gm^3. The case with pore volume 50 Gm^3 has slightly smaller total injected CO_2 amount due to pressure constraints in the injection wells towards the end of the simulation period.

5. Discussion

From earlier studies and from ongoing research, four potential storage sites at the Horda Platform have been identified (Fig. 14):

(1) Aurora structure: For the deeper Johansen Formation, several studies have been carried out over the

last years at different locations. Eigestad et al. [13] simulated CO_2 storage of 3.5 Mt per year over 110 years at the southern end of the Tusse Fault. Bergmo et al. [14] simulated CO_2-storage with injection of 3 Mt per year over 110 years in one well further north in the formation, west of the Tusse Fault. They showed a promising storage site, with permanent storage, although in a worst-case scenario, the injected CO_2 would migrate to the Troll Field after 150 years of injection. Sundal et al. [11] simulated injection in the western part of the formation, about half-way between the injection site of [13] and [14]. Sundal et al. [11] targeted a section of the formation where seismic attribute analysis indicated high porosity. They used a single vertical well perforated in the lower half of the Johansen Formation (location as in the present study), with injection of 3.2 Mt per year over 50 years (160 Mt). Their study also tested the impact of geological heterogeneities and its effect on residual trapping and up-dip migration of CO_2.

In the present work we have modelled the full pore volume for the Johansen Formation. Several injection wells have been progressively introduced, with increasing rate of CO_2 supply. Assuming an injection rate of 3 Mt per year for each well, up to six wells were introduced. The total injected volumes of CO_2 simulated for a period of 27 years, from 2023 to 2050, by number of injection wells are: injecting in only one well stores 81 Mt; ramping up to two wells stores 136 Mt; injecting at six well sites store 322 Mt. These simulation results indicate that Johansen Formation seem very promising for CO_2 storage.

(2) Alpha structure: For the Alpha structure at Smeaheia, Lauritsen et al. [10] simulated injection in one well, with an injection point deep in the Viking Group, assuming strong pressure influence from nearby fields. The modelled storage capacity was up to 40 Mt CO_2, above which CO_2 would spill from Alpha to the more uncertain Beta structure and to the Øygarden Fault Complex. Lothe et al. [7] on the other hand simulated storage of 3 million tonnes per year over 50 years with no spill to Beta. However, in this work a coarse gridding of the Sognefjord Formation was used, with low resolution at the top of the structure, which is well suited for single-phase pressure modelling, but less valid for CO_2-injection modelling.

Whether the Øygarden Fault Zone is sealing or not for CO_2 storage, is not clear with the present knowledge of the area, but recent literature indicate that caution is required. Ksienzyk et al. [30] documents several episodes of deformation in the Bergen area, just onshore the Øygarden Fault Zone. The Øygarden Fault Complex represents the eastern boundary of the Mesozoic rift, and thereby control the reactivation of this major structure. As shown in the modelling, the storage capacity for the Alpha structure is in the range of 50 Mt CO_2, using an injection rate of 1 Mt per year for 50 years. This indicates that a storage potential in the range 40–50 Mt, given a conservative approach, without migration eastwards into the Øygarden Fault Zone.

(3) Gamma structure: For the Gamma Structure in the southern part of the Smeaheia area, [9] simulated storage of between 600 Mt and 3 Gt CO_2, even under continuous pressure depletion from the Troll Field. In this work, we simulate storage in range of 150 Mt, using injection in one well with 3 Mt per year for 50 years, which is on a smaller scale than in Nazarian et al. [9] simulation results. However, [9] have simulated three injection sites and, most importantly, we anticipate that Equinor have access to newer data. New interpretation of the top Sognefjord Formation surface would provide better representation of the structural traps in the area than those available for the present work.

(4) Troll Field: The fourth potential site for large-scale CO_2 storage is the giant Troll Gas Field itself. The field will stay in production for several decades, perhaps until the year 2060. However, it represents a vast potential for CO_2 storage that can be phased in as the other large storage sites comprising a CO_2 storage hub, i.e. Johansen Formation and Smeaheia Formation Gamma structure, become filled. Simple mass-balance calculations based on recoverable gas reserves, the initial formation volume factor for gas and the initial pressure show a CO_2 storage capacity of 5 Gt. Influx of water from the regional Sognefjord Formation will reduce the practical storage capacity, but even at two-thirds of the mass balance estimate the storage capacity will be several thousand million tonnes.

6. CO_2 supply

The Norwegian process industry has issued a roadmap for reduction of CO_2 emissions [31]. Their vision is to reduce CO_2 emissions to zero by 2050 while maintaining value creation, increasing production, and developing new processes and products. CCS is identified as an important tool to fulfil this vision. The roadmap from Norsk Industri gives a possible timeline for implementation of the various CO_2 reduction technologies [31]. In the presented scenario the annual amount of CO_2 captured in 2030 is about 1.8 million tonnes, and in 2050 about 5.5 million tonnes.

CO_2 can also be collected from other Scandinavian sources and from Northern Europe and transported to the onshore CO_2 transport hub near Bergen. The need for emissions reductions is large, and even in Northern Europe the amount that needs to be captured annually by 2030 is much larger than a single storage hub can accommodate. Several demonstration projects with specific sources and sinks are in development, as shown by the other ALIGN cluster studies and also by other ERA-Net ACT projects. These other clusters represent a joint effort to demonstrate that CO_2 storage can be managed in a safe and cost-efficient manner.

The effort of the Northern Lights project to secure additional CO_2 sources to fill the first pipeline to capacity could be met by first movers in the European industry and energy production sectors. Individual possible sources have not been identified in this work, except for the refinery at Lysekil. Cross-border transport is still a big unknown factor, which could delay implementation of CO_2 transport form Sweden or any of the other European countries with large point sources of CO_2.

7. Roadmap for a Horda CO_2 Storage Hub

Published studies, in addition to simulations of CO_2 storage in the Sognefjord and Johansen formations in this work, show the large potential for rapid increase in the annual storage capacity in the Horda Platform area to match an expected increasing storage demand from CO_2 sources in Norway and in Northern Europe. Fig. 15 shows a scenario for tie-in time and amount for storage sites in a Horda Storage Hub. The figure shows a sketch of how the potential storage units in the Horda Platform area can match CO_2 supply rate from sources in Norway, Sweden and northern Europe. In the roadmap we suggest to commence injection in the Johansen Formation Aurora site in 2023 with continuous injection till 2050, assuming injection in up to six injection wells. We estimate the total capacity of Aurora to be 293 Mt CO_2, using the lower limit pore volume (e.g. 50 Gm^3). Thereafter, injection into the Sognefjord Fm. Alpha structure could be started in 2032, and the possible commencement of CO_2 storage operations in the Gamma structure in the south of the Horda Platform in 2034 (Fig. 15).

However, the timing of the different CO_2 storage sites is tentative. For instance, the availability of (3) Smeaheia Gamma structure is dependent on the outcome of future oil and gas exploration in the area and may be either postponed or never be carried out. Equinor will drill a hydrocarbon exploration well (Gladsheim in the Gamma structure) in near future, and the outcome of that well will most likely influence the interest to use this structure for CO_2 storage. Also, the order of (1) and (2), is still very open, and will be decided by the Northern Lights project and Gassnova in the coming years.

In long-term context it is also interesting to consider including the Troll Gas Field into the development plans for the storage hub. The field will be in production for several decades, possibly until year 2060. However, it represents a large potential for CO_2 storage that can be phased in as the other large storage sites in the hub are getting filled. In Fig. 15, we have anticipated that CO_2 injection can start in 2055.

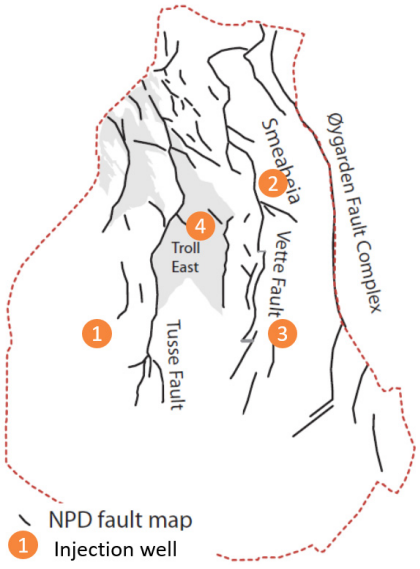

Fig. 14 Location of potential storage sites in the Horda CO_2 Storage Hub. (1) Aurora structure, (2) Alpha structure, (3) Gamma structure and (4) Troll Field. See Fig. 15 for timing for the storage sites.

All sites have been mapped with seismic surveys and have been subjected to several desktop studies, including the simulations in this work. However, the geological horizons and fault descriptions used have not been consistent from one study to the next. Likewise, the representation of petrophysical heterogeneities varies considerably. There are, therefore, still large uncertainties in the simulated storage capacities. The situation can be expected to improve when additional data have been obtained and interpreted. The results from two new exploration wells, in the Smeaheia Formation Gamma structure and Johansen Formation Aurora structure, are anticipated towards the end of year 2019-early 2020.

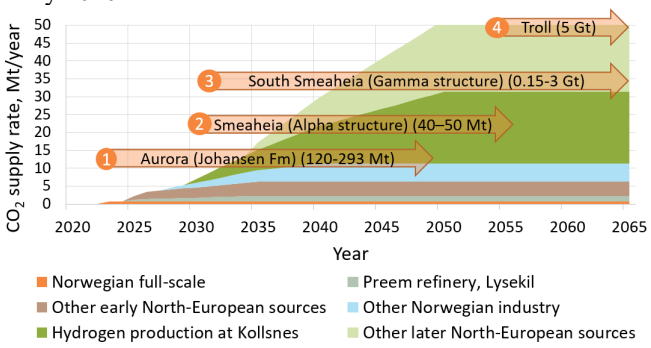

Fig. 15. Horda CO_2 Storage Hub deployment for CO_2 supply (million tonnes per year) from sources in Norway, Sweden and Northern Europe. A possible schedule for tie-in of the prospective storage sites linked to a Horda CO_2 Storage Hub, as discussed in this paper, is marked with arrows. The arrows show possible starting dates and estimated potential storage capacity. For location see Fig. 14.

8. Conclusions

In this work, which is part of the ALIGN-CCUS project we have evaluated the potential of using the Horda Platform, offshore western Norway as a European industrial CCS Cluster, with the focus and investigation of the storage potential and options. The effect of large-scale depletion due to the gas production at the Troll Field, has been considered in the simulation approaches.

The simulation and resulting range of CO_2 capacity estimates show that the study area has at least four potential storage sites: the

1) The Aurora structure, southeast of Troll in the Johansen Formation (120- 293 Mt),

2) The Smeaheia Alpha structure, in the northern part of the Sognefjord Formation (40-50 Mt),

3) The Smeaheia Gamma structure (Sognefjord Formation) (0.15-3 Gt) and

4) Troll Field, after cessation of gas production in the Sognefjord Formation (3-5 Gt).

We sketch an annually rate and timeline for which possible sites could be used for the development of the industrial-scale Horda CO_2 Storage Hub over the next thirty years. Possible CO_2 supply rates (million tonnes per year) from sources in Norway, Sweden and Northern Europe is used as input. These estimates show potentially totally CO_2 stored by 2050 in range of 810 Mt, and 1.85 Gt in 2065.

Acknowledgements

ACT ALIGN CCUS Project No 271501, funded by RVO (NL, FZJ (PtJ (DE), Gassnova (NO), UEFISCDI (RO), BEIS (UK) and the European Commission under the Horizon 2020 programme ACT, Grant Agreement No. 691712. We will also acknowledge NPD for kindly providing the large-scale reservoir model, Gassnova and Sundal (UiO) for the Johansen reservoir model and Equinor for the Smeaheia model.

References

[1] Gassnova, 2019. Full-scale CCS project web-page. https://ccsnorway.com/

[2] Gassnova, 2016. Feasibility study for full-scale CCS in Norway.

[3] Bakke, K. (2019). Northern Lights – "open source" access to transport and storage service. Presentation at the 10th Trondheim CCS Conference (TCCS-10), 17-19 June 2019, Book of Abstract, 59-60.

[4] Equinor, 2019. Northern Lights web site. https://www.equinor.com/en/magazine/carbon-capture-and-storage.html

[5] Riis. F, Pedersen N, Birkeland MA et al. (2017). Troll Area, Norwegian North Sea: Case Study of CO2 Storage Sites in an Aquifer Under Depletion. Presentation at AAPG/SEG International Conference and Exhibition, London, England, October 15-18, 2017.

[6] Riis, F. (2018). Norway CCS Demonstration project: Evaluation of Jurassic reservoirs for safe CO2 injection and storage. Fifth CO2 Geological Storage Workshop, 21-23 Nov. 2018, Utrecht, The Netherlands, We CO2 06.

[7] Lothe, A., Bergmo, P., Emmel, B.U., Eliasson, P., (2018). "Effects of uncertainties in fault interpretations on pressure depletion and CO_2 storage injection at Horda Platform, offshore Norway." Poster presented at GHGT-14, Melbourne, Australia, Oct. 2018.

[8] Lothe, A.E., Emmel, B.U., Bergmo, P., 2019. Heterogeneities in the reservoir models; effect on CO_2 storage capacity and plume modelling in areas with pressure depletion. 10th Trondheim CCS Conference, TCCS-10, 17-19 June 2019. Book of Abstracts, 311-312.

[9] Nazarian, B., Thorsen, R. and Ringrose, P. (2018). Storing CO_2 in reservoir under continuous pressure depletion: A simulation study. GHGT-14, Melbourne, Australia, October 2018.

[10] Lauritsen, H., Kassold, S., Menuguolo, R., Furre, A., (2018). Assessing potential influence of nearby hydrocarbon production on CO_2 storage at Smeaheia. Talk at the Fifth CO_2 Geological Storage workshop, 21-23 Nov. 2018, Utrecht, the Netherlands.

[11] Sundal, A., Miri, R., Ravn, T. and Aagaard, P. (2015). Modelling CO_2 migration in aquifers; considering 3D seismic property data and the effect of site-typical depositional heterogeneities. International Journal of Greenhouse Gas Control, 39, pp. 349–365.

[12] Sundal, A., Nystuen, J.P., Rørvik, K.-L., Dypvik, H. and Aagaard, P. (2016). The Lower Jurassic Johansen Formation, northern North Sea – Depositional model and reservoir characterization for CO_2 storage. Marine and Petroleum Geology, 77, pp. 1376–1401.

[13] Eigestad, G.T., Dahle, H.K., Hellevang, B., Riis, F., Johansen, W.T., Øian, E., 2009: Geological modelling and simulation of CO_2 injection in the Johansen formation. Computational Geosciences, vol. 13, p. 435.

[14] Bergmo, P.E.S., Lindeberg, E., Riis, F., Johansen, W.T., 2009: Exploring geological storage sites for CO_2 from Norwegian gas power plants: Johansen formation. Energy Procedia, vol. 1, pp. 2945-2952.

[15] Bergmo, P.E.S., Grimstad, A.-A., Lindeberg, E. 2011: Simultaneous CO_2 injection and water production to optimise aquifer storage capacity. International Journal of Greenhouse Gas Control, vol. 5, pp. 555-564.

[16] Færseth, R., 1996. Interaction of Permo-Triassic and Jurassic extensional fault-blocks during the development of the northern North Sea. J. Geol. Soc., vol. 153, pp. 931-944.

[17] Badley, M., Price, J.D., Rambech Dahl, C, et al., 1988: The structural evolution of the northern Viking Graben and its bearing upon extensional modes of basin formation. J. Geol. Soc., vol. 145, pp. 455–472.

[18] Bell, R.E., Jackson, C.A.L., Whipp, P.S. et al. 2014: Strain migration during multiphase extension: observations from the northern North Sea. Tectonics, 33, 1936–1963.

[19] Duffy, O.B., Bell, R.E., Jackson, C. et al., 2015. Fault growth and interactions in a multiphase rift fault network: Horda Platform, Norwegian North Sea. Jour. of Structural Geology, 80, 99–119.

[20] Halland, E.K., Mujezinovic, J. and Riis, F., 2014. "CO_2 Storage Atlas Norwegian Continental Shelf." Norwegian Petroleum Directorate. 163 p.

[21] Holgate, N.E, Jackson, A.-L., Hampson, G.J. and Dreyer, T. 2013: Sedimentology and sequence stratigraphy of the Krossfjord and Fensfjord formations, Troll Field, northern North Sea. Petroleum Geoscience, 19, 237-258.

[22] Dreyer, T., Whitaker, M., Dexter, J., et al. 2005: From spit system to tide-dominated delta: integrated reservoir model of the Upper Jurassic Sognefjord formation on the Troll West Field. In: Petroleum Geology Conference Series. Geological Society, London, pp. 423–448.

[23] Gibbson, K., Hellem, T., Kjemperud, A. et al. 1993: Sequence architecture, facies development and carbonate-cemented horizons in the Troll Field reservoir, offshore Norway. In: Advances in Reservoir Geology, Ashton, M (ed.), Geological Society Special Publication, 69, 1–31.

[24] Patruno, S., Hampson G.J., Jackson, A.-L.C. et al. 2015: Clinoform geometry, geomorphology, facies character and stratigraphic architecture of a sand-rich subaqueous delta: Jurassic Sognefjord Formation, offshore Norway. Sedimentology, 62, pp. 350–388.

[25] Vollset, J. & Dore, A.G. 1984: A revised Triassic and Jurassic lithostratigaphic nomenclature for the Norwegian North Sea. Norwegian Petroleum Dir. Bull. 3, 1-33.

[26] Marjanac, T. & Steel, R.J. 1987: Dunlin group sequence stratigraphy in the northern North Sea: a model for Cook sandstone deposition, AAPG Bull., 81 (2), 276-292.

[27] Eiken, O., Stenvold, T., Zumberge, M. et al. 2008: Gravimetric monitoring of gas production from the Troll field. Geophysics, 73, 6, WA149-WA154.

[28] Gassnova, 2012: Geological storage of CO_2 from Mongstad. Interim report Johansen Formation. Report TL02-GTL-Z-RA-000, available from Gassnova on request.

[29] Ringrose, P., Sorbie, K., Corbett, P., Jensen, J., 1993. Immiscible flow behaviour in laminated and cross-bedded sandstones. Journal of Petrol. Engineers, 9 (2), 103-124.

[30] Ksienzyk, A.K., Wemmer, K., Jacobs, J. et al. 2016: Post-Caledonian brittle deformation in the Bergen area, West Norway: results from K-Ar illite fault gouge dating. Norwegian Journal of Geology, 275-299.

[31] Norsk Industri 2016: The Norwegian process industries' roadmap. Combining growth and zero emissions by 2050. Summary in English. https://www.norskindustri.no/.

CO_2 CAPTURE OPPORTUNITIES IN THE NORWEGIAN SILICON INDUSTRY

A. Mathisen[1*], F. Normann[2] , M. Biermann [2], R. Skagestad[1], A.T. Haug[3]

[1] SINTEF Industry, Porsgrunn, Norway

[2]Chalmers University of Technology, Division of Energy Technology, Gothenburg, Sweden

[3] Elkem, Oslo, Norway

* Corresponding author e-mail: anette.mathisen@sintef.no

Abstract

CO_2 capture opportunities for the Norwegian silicon industry have been assessed through a techno-economic investigation. Two silicon plants have been studied for integration with a split-flow MEA-based CO_2 capture plant. The two plants considered produce different silicon products, and while the base production process is similar, there are differences that affect implementation of CO_2 capture. Initially, the purpose of the investigation was to identify partial capture scenarios that could reduce the cost of capture and thereby the threshold for implementing CO_2 capture. The investigation showed that there was sufficient excess heat to achieve a capture rate of 90% for both plants. However, as there are silicon plants that do recover the energy today for power and heat production, a seasonal partial capture scenario was developed. Here, the energy is converted to district heating and sold during the winter months and assumed available for CO_2 capture during the summer months. Due to there being sufficient heat, a major part of the investigation was still centered around exploring 90% capture rate scenarios. The first plant is a small plant (~55 kt CO_2 annually) with a low CO_2 concertation in the furnace off-gas (1 vol%), which resulted in a high capture cost, ~ 120 €/t CO_2. The second plant is a larger plant (~250 kt CO_2 annually) with a higher CO_2 concentration in the furnace off-gas, but still quite low from a CO_2 capture perspective at ~4 vol%. For this plant, the effect of off-gas recycling to increase the CO_2 concertation was assessed. Three scenarios were studied, and the result gave a capture cost between 45 – 55 €/t CO_2 captured. Even though the plants both produce silicon products, they have a very different starting point and economic potential when it comes to implementation of carbon capture and storage (CCS). The investigation into seasonal partial capture gave some interesting results and warrants further investigation.

Keywords: *CO_2 capture, process industry, excess heat recovery*

1. Introduction

The most abundant element in the Earth's crust after oxygen is silicon (Si), more than 25%, in the form of silicates [1]. The Norwegian silicon industry is the 4th largest in the world with a reported annual production of 380 000 metric tons in Year 2018 [1]. The silicon industry is an energy-intensive industry, which consumes both electricity and carbon-based raw materials. Silicon produced in Norway has one of the lowest overall CO_2 emissions in the world, mainly because of high energy efficiency and the majority of Norway's electricity stemming from hydro power [2]. Still, the industry is a significant contributor to the industrial CO_2 emissions in Norway due to the carbon consumed in the process. The industry is pursuing several pathways to reduce emissions in addition to carbon capture and storage (CCS), such as development of the production process, excess heat recovery, and increased share of carbon from biomass.

The work presented is part of the CO_2stCap project [3]. CO_2stCap is a Norwegian-Swedish research initiative aiming to reduce the cost of carbon dioxide (CO_2) capture in the process industry by developing concepts for partial capture. The project started in 2015 and ends in June 2019. Four different industries were investigated; iron & steel, cement, pulp & paper, and silicon.

The aim of this paper is to assess the potential for CO_2 capture at two different silicon production plants located in Norway. The developed scenarios are investigated using techno-economic assessment.

1.1 The silicon production plants

Two different silicon production plants form the basis of the investigation. They consist of one or more electric arc furnaces, in which quartz (SiO_2) is reduced by carbon;

$SiO_2 + 2C = Si + 2CO$

With the present production process, all CO from the process is oxidized above the charge level. The off-gas leaves the furnace at temperatures in the range of 400 - 700°C, it is then cooled before entering a filter (typically baghouse) where the valuable byproduct microsilica is recovered. The two plants considered produce different silicon products, and while the base production process is similar, there are differences that affect the implementation of CO_2 capture. A scheme of the production process is presented in Figure 1.

Plant one is a real plant, REC Solar, located in Kristiansand. It has one furnace with an annual production of ~10 kt silicon metals. The product is mainly used in solar panels. The corresponding CO_2 emissions are ~55 kt, of which ~20% are of biogenic origin. The main challenge for CO_2 capture for this plant is the rather small amount of CO_2 emitted in combination

with a low concentration of CO_2 in the furnace off-gas of ~1 vol%.

The second, larger plant has two furnaces, and produces ferrosilicon (FeSi) primarily for use in the iron and steel industry. Here, the expected CO_2 concentration in the furnace off-gas is ~4 vol%, and the annual CO_2 emissions are ~250 kt. This is a generic plant, still it is representative of FeSi plants operating in Norway today. The industry is working on increasing the CO_2 concentration, and one of the focus areas is off-gas recycling. For a plant with multiple furnaces, this might entail off-gas recycling on one or several furnaces.

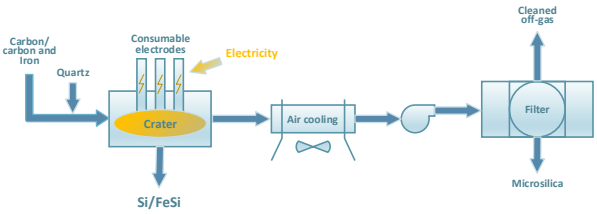

Figure 1: Scheme of the silicon production process.

2. Methodology

Figure 2 gives a schematic overview of the methodology applied in both the CO_2stCap project and the present study. The design of cost-efficient capture processes is determined in a techno-economic analysis in form of an iterative procedure between costing and process modelling. The technical investigation is based on detailed process simulations in Aspen Plus to design and dimension the MEA capture unit. In the work presented, the silicon production plants are coupled with a rich-solvent split-flow MEA-based CO_2 capture plant followed by compression of the CO_2 to 110 bar, see Figure 3. The process models used have been presented in, amongst others [4] and [5].

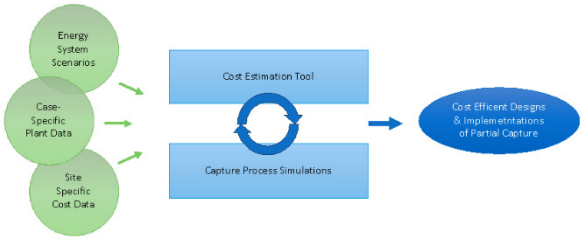

Figure 2: Methodology adopted in the project.

The cost estimation is performed with the Aspen In-plant Cost Estimator combined with a well- proven, in-house developed installation factor model, [6] - [8].

The investment cost (CAPEX) is estimated from equipment lists containing dimensions that are derived from the process simulations. The operational cost (OPEX) is based on mass and energy flows across the battery limits of the plant per hour and is obtained from these simulations. The annual OPEX are calculated based on a utility and personnel price list, and maintenance cost, see Table 1 for details.

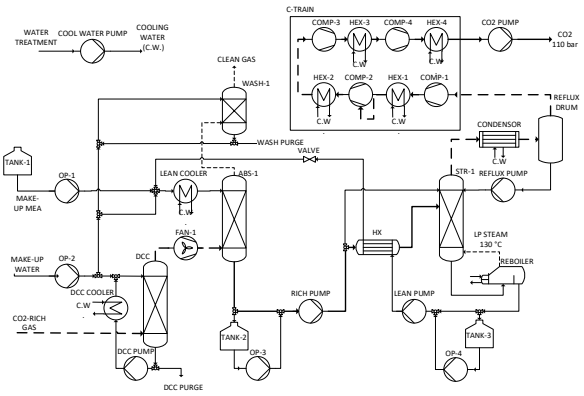

Figure 3: Illustration of the MEA capture process with rich-solvent split-flow configuration.

Table 1: Parameters used for OPEX calculation.

Parameter	Unit	Value
Electricity price	EUR/kWh	0.055
Cooling water	EUR/m^3	0.02
MEA make-up*	EUR/m^3	1 867
Personnel – operators (1 person per shift)	kEUR/an	663
Personnel – engineers (1 person)	kEUR/an	158
Maintenance (% of installed cost)	%	4
Uptime	H	8 760
Rate of return	%	7.5
Number of years		25

* MEA make-up is based on IEAGHG [9] assumed 1 wt% of lean MEA stream to continuous reclaimer and 5% MEA loss during thermal reclaiming.

2.1 Assumptions

The main assumptions are;

- 30 wt% MEA, split flow configuration
- Steam to reboiler, 2.7 bara and 133ºC
- CO_2 compression to 110 bar
- Onsite steam generation for the stripper reboiler is included, electric boiler (EB) and excess heat steam generation (WHSG)
- Brownfield site
- Only direct plant emissions considered
- CAPEX
- Project contingency (20%) is included
- The detailed factor estimation method normally has an uncertainty of ± 40% (80% confidence interval)
- Cost year 2015
- nth of a kind (NOAK)
- Start-up cost is not included

2.2 Partial capture

A rule of thumb in carbon capture and storage (CCS) from power plants has been to achieve a capture rate of

90% or higher. From a technical perspective, it is relatively straight forward in many cases to achieve such high rates, for instance when applied to power generation. However, in many process industries such high capture rates could imply excessive cost and a different CO_2 capture strategy, i.e. partial capture should be adopted. The partial capture concept is defined as capture of only a fraction of the available CO_2 emissions on site. The following examples illustrates plants where partial capture could be favorable to full capture, i.e. yields lower absolute and specific cost (€/t CO_2) – further aspects are discussed in;

- Plants that have excess energy or an energy system that constantly or depending on market conditions may produce a part of the heat needed for carbon capture at low-cost.
- For plants with multiple stacks, targeting the most suitable stack(s) instead of total site emission.
- Plants where carbon capture is cost-efficient in combination with other mitigation measures, such as biomass, electrification, energy efficiency measures, etc.

This work assesses also, whether applying partial capture is a relevant strategy for the Si/FeSi plants investigated here.

3. CO_2 capture scenarios

The scenarios investigated for the two silicon production plants are presented in the sections below. Because of the difference in the plants, different scenarios have been developed.

One of the most important aspects in CO_2 capture is energy supply to the stripper reboiler. In the scenarios studied, the steam is either supplied from an electric boiler or from excess energy from the furnace off-gas recovered in a WHSG.

A general observation from both plants is that there is sufficient heat available from the furnace off-gas (~ 600°C) to cover the energy (steam) needed in the stripper reboiler. This excess energy is to varying degree utilised today in Norwegian Si/FeSi plants. The most likely CO_2 capture scenario for both plants is that excess heat is utilised in the capture plant to reduce the capture cost. However, to increase the flexibility of the results (adaption to other plants where excess heat is not available) and to provide a reference, a scenario with an electric boiler is included.

Developing partial capture scenarios within this premise is limited as scenarios that are governed by how much CO_2 can be captured utilsing the excess heat is not applicable. However, if the alternatives for utilising the excess heat is either for CO_2 capture or for sale of district heating, one could consider seasonal capture, i.e. CO_2 capture during the seasons of the year where the district heating demand is low. Seasonal (partial) capture was only explored for plant 1.

3.1 Plant 1 – Si production

An overview of the scenarios studied for plant 1 is provided in Table 2. The CO_2 concentration after the filter is ~1 vol%, however it was calculated to be 3.7 vol% before the filter, see Figure 1. Therefore, scenarios with both CO_2 concentration were included. However, the pre-filter capture scenario will entail changes in the existing Si production process as CO_2 capture from an off-gas containing particles is not recommended. In addition, the particles in this case is a valuable bi-product (microsilica) and must be recovered. The most obvious change would be a different filter design with less air dilution. The technical feasibility of such changes and associated costs has not been considered. Further, a study into increased plant size was also performed to investigate the effect of size. The sizes chosen, in addition to 1x55 kt CO_2 plant (original plant), were, 3x55 kt CO_2 and 5x55 kt CO_2.

Table 2**:** Scenario overview, plant 1.

Scenario	CO_2 capture details
1a	1 vol% CO_2 in off-gas, 90% capture rate, energy supplied thorough an electric boiler
1b	1 vol% CO_2 in off-gas, 90% capture rate, energy supplied thorough a WHSG
1c	3.7 vol% CO_2 in off-gas, 90% capture rate, energy supplied thorough a WHSG

3.2 Plant 1 – seasonal (partial) capture

Commonly for Si and FeSi plants in Norway is that they seek to recover the excess heat when there is a market for it. For plants with a favorable location, e.g. if there is a market for the heat as district heating in the surrounding area. However, if the heat recovered is sold, it could limit its availability for use in the CO_2 capture plant (steam to the stripper reboiler). To assess the consequences of such a scenario, the investigation into plant 1 was extended to assess seasonal capture. The main assumptions adopted for seasonal capture are;

- Excess heat for district heating is only sold during the winter months (six months of the year)
- Excess heat can be used "free of charge" for CO_2 capture during the summer months. CAPEX for WHSG is included.
- A full-sized capture plant is built (capacity to capture 90% of the CO_2 produced at the given time)
- The value of the steam as district heating was set equal to the value of 16.67 €/t
- All year capture includes a loss of revenue from sales of district heating during winter

The scenarios included in the investigation into seasonal capture are presented in Table 3.

Table 3: Scenario overview of seasonal capture for plant 1.

Scenario	CO_2 capture details
2a	1 vol% CO_2 in off-gas, 90% capture rate all year, steam from WHSG
2b	1 vol% CO_2 in off-gas, summer only capture, steam from WHSG
2c	3.7 vol% CO_2 in off-gas, 90% capture rate all year, steam from WHSG
2d	3.7 vol% CO_2 in off-gas, summer only capture, steam from WHSG

3.2 Plant 2 – FeSi production

In Table 4, the scenarios studied for the second plant are presented. The focus of this investigation was the effect of applying off-gas recycling for increased CO_2 concentration. The scenarios are, one where both furnaces were operated as normal (3a), one where both furnaces have off-gas recycling (3b), and one where the one furnace operates as normal and one has off-gas recycling (3c). The furnace off-gases in these scenarios enter the same CO_2 capture plant. A modified version of Figure 1 is presented in Figure 4 that illustrate the off-gas recycling. The energy needed in the stripper reboiler is supplied through a WHSG.

Table 4: Scenario overview, plant 2.

Scenario	CO_2 capture details
3a	Two furnaces, no recycling, 4.4 vol% CO_2 in off-gas, 90% capture rate
3b	Two furnaces, recycle in both, 15.1 vol% CO_2 in off-gas, 90% capture rate
3c	Two furnaces, recycle in one, off-gases combined, 6.8 vol% CO_2 in off-gas, 90% capture rate

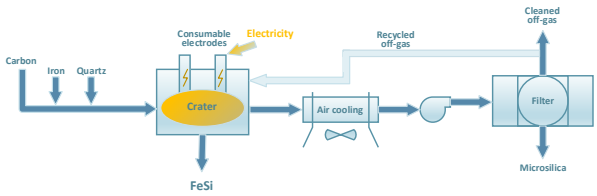

Figure 4: Plant 2 with off-gas recycling.

4. Results and discussion

The scenarios presented in the previous section were simulated and cost estimated. In this section the results are presented and discussed.

4.1 Plant 1 – Si production

The results from the tecno-economic investigation of plant 1 is presented in Table 5 and Figure 5. For plant 1, two CO_2 concentrations are considered, in addition the effect of plant size is also studied. The results of the process evaluation showed that there is sufficient excess heat available from the furnace off-gas to fully cover the need of the stripper reboiler duty at 90% capture rate.

Table 5: The main technical results for plant 1.

Scenario	Specific reboiler duty, SRD	Steam supply
1a	3.53 MJ/kg CO_2 captured	All steam from electric boiler
1b	3.53 MJ/kg CO_2 captured	All steam from WHSG boiler
1c	3.34 MJ/kg CO_2 captured	All steam from WHSG

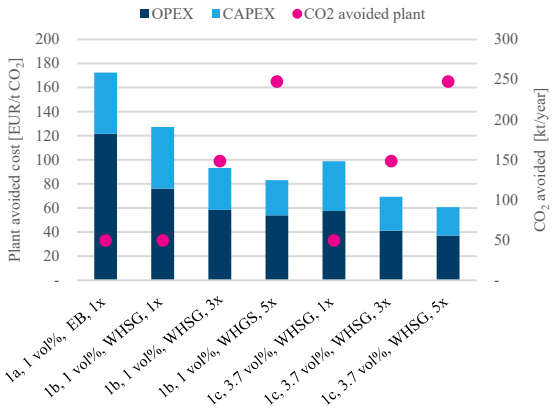

Figure 5: Results of the investigation into plant 1.

The results in Figure 5 show that the combination of low CO_2 concentration and small CO_2 amounts makes CO_2 capture costly with prices in the range of 125 – 175 €/t CO_2 for the current plant size (1x), depending on whether excess heat is utilised or not. A relatively small increase in CO_2 concentration, ~ 4 vol%, reduces cost significantly by ~30 €/t CO_2. The feasibility of increasing the concentration has not been assessed, the current process configuration needs to be reassessed, primarily the type of filter used, as CO_2 capture needs to take place after the filter to avoid operational issues in the capture plant and to ensure recovery of microsilica. Increasing the plant size is also beneficial in regard to capture cost. The specific CAPEX decreases due to economy of size. The breakdown of the OPEX is given in Figure 6.

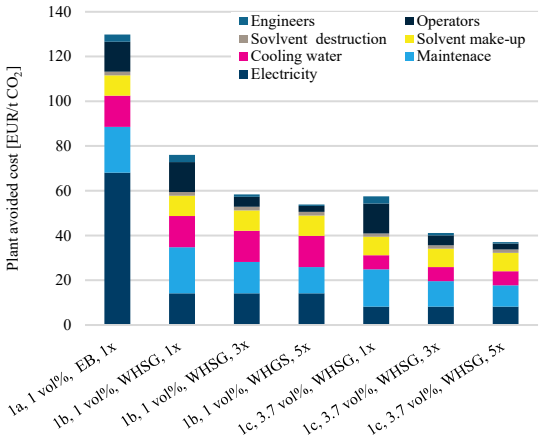

Figure 6: Breakdown of OPEX for plant 1.

The figure shows that the maintenance and personnel cost contribute disproportionally for the small plants (1x55 kt CO_2 annually). Finally, the utilisation of excess heat is highly beneficial as expected, clearly observed when comparing steam from an electric boiler (EB) versus a

WHSG. Note that for the EB case, the energy supply to the stripper reboiler (steam) is in the form of electricity as the boiler is electrically driven.

4.2 Plant 1 – seasonal (partial) capture

The results form the seasonal capture investigation are presented in Figure 7. The results show that for the summer-only capture, the CAPEX contribution to the cost increases and becomes the dominant one, compared to OPEX being the dominating element for all year capture.

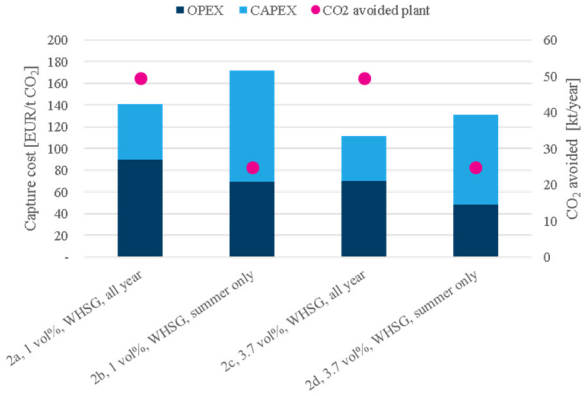

Figure 7**:** Results of the investigation into seasonal (partial) capture for plant 1.

4.3 Plant 2 – FeSi production

The focus of this investigation into plant 2, was the effect of applying off-gas recycling for increased CO_2 concentration, which yields a lower specific reboiler duty (SRD) for off-gas recycling, as illustrated in Table 6.

Table 6**:** The specific stripper reboiler duty for plant 2.

Scenario	Specific reboiler duty, SRD	Steam supply
3a	3.34 MJ/kg CO_2 captured	All steam from WHSG, 23.6 MW
3b	3.15 MJ/kg CO_2 captured	All steam from WHSG, 22.3 MW
3c	3.26 MJ/kg CO_2 captured	All steam from WHSG, 23.0 MW

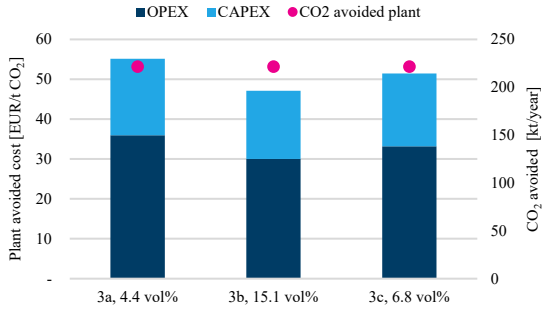

Figure 8**:** Results of the investigation into plant 2.

A comparison between the estimated cost for scenario 1a (50 kt CO_2 captured) and 3a (220 kt CO_2 captured), which represents todays situation for plant 1 and plant 2, illustrates again the benefit of size on the cost of capture.

Figure 8 shows that the increase to ~7 vol% and further to 15 vol%, reduces the specific capture cost as expected, with 4 and 8 €/t CO_2, respectively. The CAPEX is reduced as the flue gas volume is reduced, while the reduction in OPEX is due to the reduced SRD with increased concentration. In addition. It should be pointed out that higher concentrations (> 10 vol%) make other post-combustion capture technologies more attractive, e.g. pressure swing adsorption (PSA), membrane, and low temperature/ cryogenic.

5. Concluding remarks

For plant 1, the capture cost was estimated to between 125 – 175 €/t CO_2, where the lowest cost represents the scenario for which the excess heat is utilized for capture. The combination of a low CO_2 concentration and small amounts of CO_2 makes CO_2 capture costly. A relatively small increase in CO_2 concentration, to ~4 vol%, is beneficial regarding cost. If such a scenario is possible the cost of capture is reduced with ~30 €/t CO_2. Increasing the plant size, and taking advantage of economy of size, gave further reduction in capture cost.

Seasonal capture could under the right circumstances be considered, still utilising the excess heat for CO_2 capture seems to be preferable. The results are highly dependent on the value of district heating A further investigation into the possibility of combining steam to stripper reboiler and district heating is recommended.

For plant 2 the current CO_2 concentration is ~4 vol% CO_2 with an associated cost of 55 €/t CO_2. With flue gas recycling there is a potential of reaching 6.8 vol% CO_2 with partial recycling and 15 vol% CO_2 with full recycling, resulting in a cost reduction of 4 and 8 €/t CO_2, respectively. In addition, higher concentrations may make other capture technologies attractive.

Acknowledgements

The authors wish to thank the research partners, RISE Bioeconomy, Swerim AB, and the University of South-Eastern Norway, as well as the industry partners SSAB, GCCSI, IEAGHG, Elkem AS, Norcem Brevik AS and AGA Gas AB. The project is funded by the Norwegian CLIMIT–Demo programme via Gassnova, The Swedish Energy Agency and, participating industry and research partners.

References

[1] USGS, National Minerals Information Center, *Silicon Statistics and Information*, https://www.usgs.gov/centers/nmic/silicon-statistics-and-information

[2] Statistics Norway – Statistisk sentralbyrå SSB, The share of hydro power in electricity production in 2017, accessed 2019-06-16, https://www.ssb.no/en/energi-og-industri/statistikker/elektrisitet/aar

[3] CO2stCap, https://www.sintef.no/en/projects/co2stcap-cutting-cost-of-co2-capture-in-process-industry/

[4] Garðarsdóttir S.Ó., Normann F., Andersson K., Johnsson F., *Post combustion CO_2 Capture Using Monoethanolamine and Ammonia Solvents: The Influence*

of CO_2 Concentration on Technical Performance, Ind. Eng. Chem. Res. , 2015. **54**(2): p. 681-690.

[5] Biermann, M.N., F.; Johnsson, F.; Skagestad, R., *Partial Carbon Capture by Absorption Cycle for Reduced Specific Capture Cost.* Ind. Eng. Chem. Res., 2018. **57**(45).

[6] Eldrup, N.H., Mathisen, A., Skagestad, R. Haugen, H.A., 2018, *A Cost Estimation Tool for CO_2 Capture Technologies*, GHGT 14 conference paper, Melbourne Australia

[7] van der Spek M., Sanchez Fernandez E., Eldrup, N. H.; Skagestad, R.; Ramirez A., Faaij A., *Unravelling Uncertainty and Variability in Early Stage Techno-Economic Assessments of Carbon Capture Technologies*, Int. J. Greenh. Gas Control 2017. **56**: p. 221–236.

[8] Ali H., Eldrup N.H., Normann F., Skagestad R., Øi L.E., *Cost Estimation of CO_2 Absorption Plants for CO_2 Mitigation – Method and Assumptions*. *Int. J. Greenh. Gas Control* **2019**, *88*, 10–23

[9] IEAGHG, *Evaluation of reclaimer sludge disposal from post-combustion CO_2 capture*, 2014/2, March 2014

MODELLING BIO-ELECTROCHEMICAL CO_2 REDUCTION TO METHANE

G. Samarakoon[1*], C. Dinamarca[1], A.B.T. Nelabhotla[1], D. Winkler[2], R. Bakke[1]

[1] Department of Process, Energy and Environment

[2] Department of Electrical Engineering, Information Technology and Cybernetics, University of South-Eastern Norway, Kjølnes ring 56, 3918, Porsgrunn, Norway

* Corresponding author e-mail: gamunu.arachchige@usn.no

Abstract

The most common platform for biogas process modelling, ADM-1, was extended adding the bio-electrochemical active CO_2 reduction to CH_4 reaction. The Nernst expression was incorporated as Monod-type kinetic expression to formulate the reaction rate, which is controlled by the electrical potential. The proposed model is applied to a complete mixed separate cathode compartment running in a continuous flow mode of operation. The model modification is relatively simple, mainly as a learning tool focused on the differences between an AD process with and without a Bio-electrochemical system (BES). The simulations demonstrate the basic concepts of BES for biogas upgrade and its limitations. The simulations show that biogas methane content can be increased up to 85 % under the reactor settings selected for the simulations. The rate of the reduction reaction can be constrained by the local potential of the cathode and the substrate concentration. The necessity of maintaining some buffering from CO_2 partial pressure to prevent the inhibition due to rise in pH is also pointed out. The simulations suggest that simultaneous bio methanation of CO_2 from endogenous and external sources can be achieved using an AD with BES.

Keywords: *CO_2 negative solutions, CCUS, CO_2 utilisation, BES, bio-methane*

1. Introduction

Anaerobic digestion (AD) process is a highly economical and efficient method to produce methane (CH_4). It consists of a series of biochemical conversions that uses a variety of organic wastes in a controlled environment. AD produces biogas containing 50 -70 % CH_4 and 50-30 % CO_2, meaning that the typical biogas has low calorific value, which limits its use [1]. Therefore, biogas is upgraded by removing CO_2 before selling as a transport fuel. Water scrubbing, physical absorption using organic solvents, chemical absorption using amine solutions are some of the technique commonly used for CO_2 separation from biogas. This study is focused on the alternative to convert CO_2 to CH_4. The conversion can be done with anaerobic digestion integrated with bio-electrochemical systems (BES) and can also be extended to utilise CO_2 captured from other sources [2].

The bio-electrochemical system (BES) refers to processes that involve electrode reactions catalysed by microorganisms. CO_2 reduction to CH_4 (reaction 1) directly at the cathode using electricity as energy source and microorganisms as the catalyst has been demonstrated [3]. Electricity for BES should be from renewable sources, as a way of storing renewable surplus electricity as methane [4].

$$CO_2 + 8H^+ + 8e^- \rightarrow CH_4 + 2H_2O \quad (1)$$

Conversion of CO_2 to CH_4 with intermediate production of hydrogen (H_2) is also possible. It follows two steps. The first step is protons reduction to H_2 (reaction 2) and then the produced H_2 reacts with CO_2 (reaction 3). The later step is completely biological conversion.

$$8H^+ + 8e^- \rightarrow 4H_2 \quad (2)$$

$$CO_2 + 4H_2 \rightarrow CH_4 + 2H_2O \quad (3)$$

The protons (H^+) and electrons (e) needed for the reduction reaction at the cathode are produced by oxidizing water or acetate (or easily degradable organics) at the anode. However, oxidation of acetate (or easily degradable organics) results in the production of CO_2.

The thermodynamic potential of CO_2 reduction to CH_4 and potential of water oxidation are reported to be -0.24 V vs NHE (Normal Hydrogen Electrode) [5] and 0.81 V vs NHE [6] respectively. All reported potentials are standard potentials under biologically relevant conditions at pH 7 and 25 ^{0}C. Additional cathode potential over the thermodynamic potential should be always applied to overcome other potential losses (energy losses) and derive the intended reaction. The other potential losses are mainly a result of activation energy required to drive the electrochemical reactions, ohmic losses as a result of resistance to the flow of charges, concentration losses as a result of mass transfer limitation and bacterial metabolic losses[7].

Electrode "respiring" bacteria involve this bio electroactive process via extra-cellular electron transfer (EET), the process by which microorganisms can transport electrons into and out of the cell from or towards an insoluble electron donor or acceptor (in this case, solid cathode). The current understanding on interactions of the microorganism with solid electron donors and their importance in nature and for bio-sustainable technologies has been explored by Tremblay et al. [8]. Conductive based and diffusion-based are the main two routes that the electrons are transferred. The conduction-based EET relies on the transmission of electrons through a conductive biofilm matrix composed of extracellular polymeric substances, acquiring electrons directly from a solid donor at a given redox

potential (In the biofilm matrix, the microorganisms are known to produce conductive pili to electronically connect the solid electrode.). The diffusion-based EET relies on the migration, diffusion, and/or advection of soluble electrochemically active molecules (mediators) to carry electrons from cells to the electron-accepting surface [8].

Although several studies have verified the applicability of this technology in lab-scale, many limitations still need to be addressed to optimize the technology and make it economically feasible. Constraints regarding side reactions, mass transfer, inoculum type, electrode material, anode-cathode separation, operation parameters, system design or scaling-up are some of the bottlenecks [2]. In this scenario, process modelling is instrumental to understand the extensive experimental work to eventually commercialize the technology.

Recio-Garrido et al. [9] have reviewed several BES modelling approaches. The models reviewed were classified based on their complexity of the mass balances, transport phenomena and microbial populations. However, the complexity or the level of details of a model depends on the specified modelling objectives. Simple models are more accommodating to understand basics in this process which is demanding multidisciplinary knowledge (from microbiology, electrochemistry, material science, electrical engineering, etc.).

In this work, the generally accepted anaerobic digestion model no.1 (ADM1) [10] as a common platform was modified by taking into account the bio-electrochemical reaction (1): This integration of BES-AD to study CO_2 capture and utilization as methane is a first-of-kind (to the best of our knowledge) and the main objective is "model for learning". The level of the details of the model can be expanded later, based on the initial model simulations and as more experimental results are generated. The simulations will also give essential directions in planning experiments.

The extended model was used to evaluate the change in the biogas composition and other operation parameters when the electrochemical reaction was employed and controlled by the electrical potential, and to identify the process limitations. The focus was given to observe the differences between AD process with and without BES. The possibility of using externally-produced CO_2 to produce methane biologically (biomethanation) was also used as a simulation case.

2. Method of model development approach

The ADM-1 was extended adding an electrochemical active biological reaction (1) controlled by the electrical potential. The ADM-1 model is the common platform of modelling and simulations AD process developed by IWA (International Water Association, 2002). The model was implemented in the simulation tool AQUASIM 2.1.

The following assumption were made:

1. CO_2 reduction to CH_4 (reaction 1) is catalysed by the microbial group, hydrogenotrophic methanogens. It is assumed that this microbial group can acquire electrons directly from the solid cathode).
2. Only hydrogenotrophic methanogens are active on the cathode surface (any other parallel biochemical and bio-electrochemical reactions on the cathode surface are neglected.)
3. The reactor compartment is a continuous flow and complete mixed separate cathode compartment.
4. A separate anode compartment (which is not included in the model modification) supplies an unrestricted proton flow (to the liquid phase of the cathode compartment) and electron current (to the cathode).
5. The biochemical reduction reaction (reaction 1) is the rate-limiting step within the reactor compartment, while the transport of CO_2 and H^+ to the solid cathode is comparatively fast and the electroactive microorganism are abundant on the cathode.

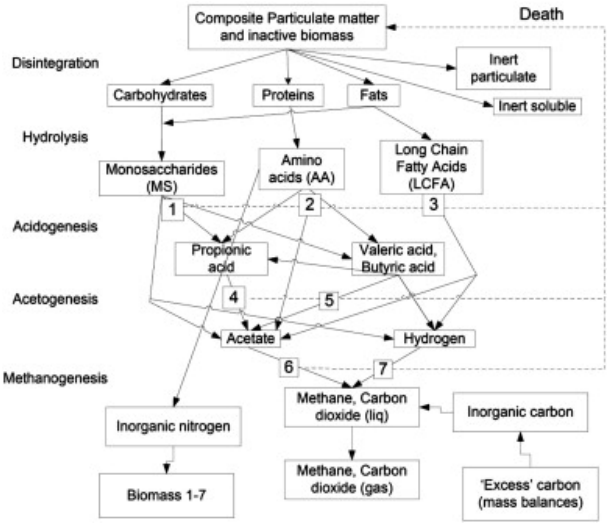

Figure 1: The reaction paths described in ADM-1 [10], with the following microbial groups: (1) sugar degraders, (2) amino acid degraders, (3) LCFA degraders, (4) propionic acid degraders, (5) butyric and valeric acid (VFA) degraders, (6) acetoclastic methanogens, and (7) hydrogenotrophic methanogens, taken from [11].

2.1 ADM-1 model

The ADM-1 is structured on anaerobic biochemical reactions catalysed by intra or extracellular enzymes and act on the pool of biologically available organic material (Figure 1). The complex organic materials are decomposed to the final product, biogas (mainly CH_4 and CO_2) through a number of decomposition steps. The first step is the disintegration complex organic material (sludge or organic waste) into particulate constituents (carbohydrates, proteins, and lipids). The next step is hydrolysis of those particulate constituents into sugars, amino acids and long-chain fatty acids (LCFAs). The hydrolysis products are then fermented into volatile fatty acids (Acidogenesis). These acids are broken down to acetate and hydrogen (Acetogenesis). The final step is Methanogenesis in which the Acetoclastic methanogenesis converts acetate to methane, and hydrogenotrophic methanogenesis converts carbon dioxide and hydrogen to methane.

The rate expressions and stoichiometric coefficients of these steps as biological processes are given in a Peterson matrix [12]. The matrix incorporates the biological processes as rate equations, the components and the stoichiometric coefficients of the processes. The substrate uptake rates are described using Monod saturation type [13] kinetic equations. The stoichiometric coefficients for inorganic carbon and nitrogen are determined by balance equations. There are two types of physico-chemical reactions are also included: 1. Acid-base reactions implemented as equilibrium processes in an implicit algebraic equation set and 2. Liquid-gas transfer, implemented as non-equilibrium diffusive processes [10].

2.2. Kinetic equation for bio-electrochemical reaction

To account for the BES effect, the bio-electro active reactions associated with extracellular electron transfer (EET) are incorporated into ADM-1. Hydrogenotrophic methane production may occur either directly (reaction 1) or indirectly via H_2 (reactions 2 and 3). H_2 gas produced at the cathode will be rapidly utilized by hydrogenotrophic methanogens. Therefore, to simplify the model, only the reaction 1 (the electrons are directly taken up from the electrode and used to reduce the CO_2 to methane) was considered.

The Monod equation is used to describe the microbial growth kinetic on all substrates in ADM-1. In this case, the specific bacterial group is hydrogenotrophic methanogens assumed to grow at the cathode surface. The bacteria receive electrons from the cathode and deliver them to CO_2 as the final acceptor and use CO_2 as the carbon source to produce biomass. Thus, the rate of the reaction can be restricted by the availability of both the electron donor and the electron acceptor. When both substrates (the donor and the acceptor) are soluble, the rate can be defined as rate equation (r1) [14]:

$$\rho = k_m^0 X \frac{S_a}{K_a+S_a}\frac{S_d}{K_d+S_d} \qquad \text{(r1)}$$

Where: ρ- kinetic rate, k_m^0 - maximum uptake rate, X – microorganisms' concentration, S_a and S_d – two "limiting-substrate'' concentrations, K_a and K_d – half-maximum rate concentrations for substrates S_a and S_d.

The acceptor part (S_a / (K_a+S_a)) of the Monod expression account the CO_2 which is soluble. However, the donor part (S_d / (K_d + S_d)) has no concentration and is solid cathode which allows electrons to pass in response to the electrical-potential gradient. The soluble concertation of donor part (S_d) is instead related to the cathodic potential using the Nernst equation [15]. Based on this, the overall rate equation can be defined as rate equation (r2):

$$\rho_{c1} = k_{m\_eet}^0 X_{eet}\left(\frac{S_{co2}}{K_{s\_co2}+S_{co2}}\right)\left(\frac{1}{1+exp\left[-\frac{F}{RT}\eta\right]}\right) \qquad \text{(r2)}$$

The last term in the parenthesis (r2) which is derived from the Monod equation is referred as the Nernst-Monod term. The main assumption for its use is that microbial kinetics control the electron consumption. The Nernst-Monod term shows that the rate of substrate uptake increases as the local potential increases until a plateau is reached (Figure 2). X_{eet} is the concentration of electrically active microorganisms, R: ideal gas constant, T: absolute temperature, F: Faraday constant. η: local potential in reference to E_{KA}. E_{KA} is the potential in which the substrate consumption rate will reach half of the maximum substrate consumption (analogous to K_d) and can be determined experimentally. η is defined as $\eta = E_{KA} - E_{cathode}$. Since E_{KA} is used as reference potential ($E \equiv 0$), η becomes $-E_{cathode}$.

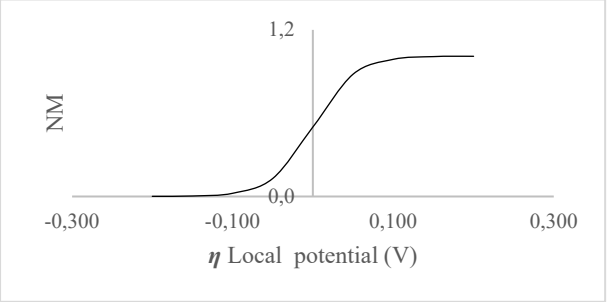

Figure 2**:** Plot of the Nernst-Monod (NM) term for E_{KA} = 0 V and T = 308 K and the local potential (η) from -0.2 to 0.2 V.

Further, two inhibitions effects are incorporated to the substrate utilization rate as given in the rate equation (r3); for describing microbial growth inhibition due to 1. Extreme pH conditions (I_{ph}) and 2. Limitation of soluble inorganic nitrogen (I_NH_limit).

$$\rho_{c1} = k_{m\_eet}^0 X_{eet}\left(\frac{S_{co2}}{K_{s\_co2}+S_{co2}}\right)\left(\frac{1}{1+exp\left[-\frac{F}{RT}\eta\right]}\right) I_{ph} I\_NH\_limit \qquad \text{(r3)}$$

Table 1**:** Parameters used for the bio electrochemical process

Parameters	Description	Unit	value
$k_{m\_eet}^0$	Maximum electrons uptake rate	Kmol-e kg COD X d^{-1}	4.5
X_eet	Concentration Of electron up taking organism	kg COD m^{-3}	
S_{co2}	Con. of CO_2 in bulk liquid	M	
Ks_co2	Half saturation constant for CO_2 reduction	M	0.06
F	Faraday's constant	C mol-e^{-1}	96485
R	Ideal gas constant	J mol^{-1} K^{-1}	8.3145
η	Local potential	V	
T	Temperature	K	308
I_{ph}	Microbial growth inhibition due to pH	-	
I_NH_limit	Microbial growth inhibition due to limitation of soluble inorganic nitrogen	-	
Y_eet	Yield of bio-electro active biomass uptake of electron	kg COD-X/ kmol -e	0.48

2.2.1 Kinetic and stoichiometric parameters

The developed ADM-1 modification is relatively simple, and the main objective is to use it as a learning tool and study the BES effects qualitatively. Therefore, attempts were not taken to precisely estimate the values for the kinetic and stoichiometric parameters. The values were either taken based on the parameter used in original ADM-1 or assumed roughly.

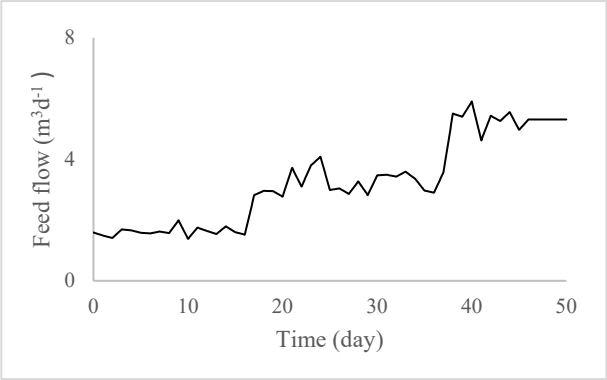

Figure 3**:** The sludge feed flow to the AD reactor [16].

2.3 Simulation outline

Below is outlined how the simulation process was carried out to study BES effects on AD, and AD-BES for using CO_2 (Externally-produced) for biomethanation.

1. First, a simulation was run for a conventional AD reactor for baseline data (The reactor settings were those used for ADM -1[10].). A reactor of V = 28 m^3, continuous flow and completely mixed (CSTR) is fed sludge from a wastewater treatment plant for 50 days (Figure 3). The feed step increases at day 16 and 37 [16] and the composition of the feed is given in Table 2. AD reactors are in general started with low organic loading and then gradually increased so that stable reactor operation is achieved.
2. The bio-electrochemical process was activated at day 50 (end of the published experiment [10]) while maintaining a constant feed rate (5.31 m^3/d). The local cathode potential (η) was increased from -0.200 to +0.200 V stepwise every 50 days, to evaluate how the rate of the bio-electrochemical reaction varied and to identify its constraints.
3. The soluble CO_2 in the reactor compartment as an input from an "external CO_2 source" was altered to find out the possibility of using additional CO_2 for bio methanation. The total volumetric biogas production rate is always limited to the rate in which organic matter is converted to biogas. The volume of CO_2 produced that can be converted to methane by BES thus constrained by the applied carbon source (organic load) and the rate of its conversion to biogas. It could be hypothesized that the overall methane production capacity might be increased by increasing the input of gaseous carbon from external sources. Thereby, a source of soluble CO_2 was added to the digester with BES activated when running at the highest local potential simulated (η = 0.200 V). The CO_2 loading rate simulated were 0.01, 0.015 and 0.02 M d^{-1}. However, the gas-liquid mass transfer (which was not accounted in detail in this simulation) may limit CO_2 gas solubility in the liquid phase.

Table 2**:** Input feed composition to the reactor.

Components in the reactor feed	Concentrations kg COD/m^3
Amino acids	4.2
Fatty acids	6.3
Monosaccharides	2.8
Complex particulates	10.0
Total	23.3

3. Simulation results and discussion

Figure 4 shows the biogas production rate and the composition of the biogas from the reactor (which is chosen for this study) running under conventional condition. As the feed rate is increased, the biogas production rate increases. The reactor produces biogas with ~ 65 % methane (CH_4) content.

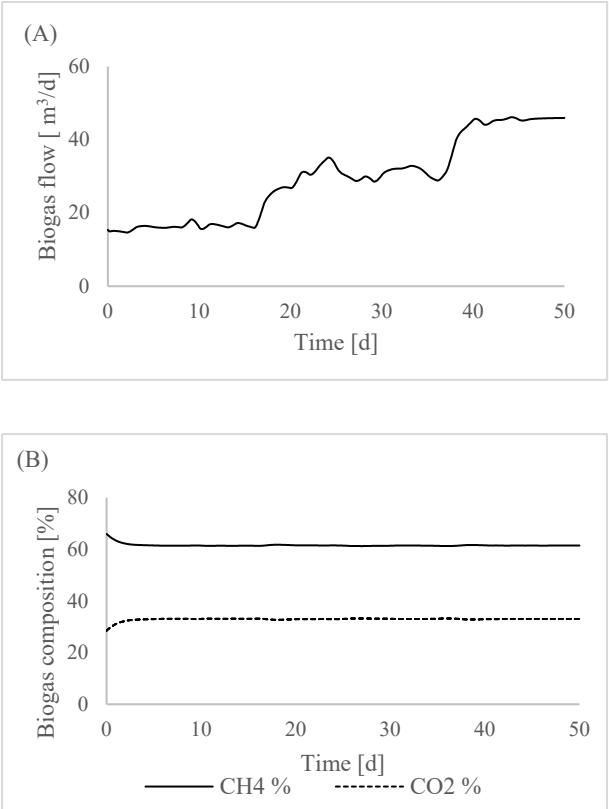

Figure 4**:** Biogas production rate (A) and composition (B) for the conventional biogas reactor (selected to simulate for the baseline data). The feed rate changes at day 16 and 37.

The bio-electrochemical process was activated at day 50 and the local potential (η) was increased from -0.2 to + 0.2 V (with the step size = 0.05 V). The simulation was run for 50 days for each step.

As the local potential increases, the methane content of the biogas increases up to 85 % as shown in Figure 5. Increasing η further does not rise the biogas methane

content. The simulation demonstrates that 30 % methane increase could be expected by employing BES in this reactor settings chosen for the study.

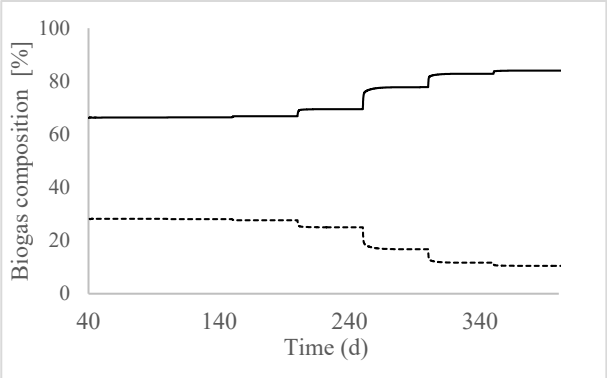

Figure 5: Response of biogas composition (— CH_4 %, ··· CO_2 %) to step increases of the local potential (η) from -0.2 to 0.2 V (step size =0,05). The bio-electrochemical process is activated at day 50.

When the local potential is sufficiently high, the cathodic donor saturates, and it is acceptor, in this case, dissolved CO_2 that limits the rate. Figure 6 shows how the value which accounts for the electron acceptor part of the rate expression decreases as the local potential increases. However, it should be noted that the effect shown here is qualitative and the exact values depend on the values assumed for the constant parameters (e.g. Ks_co2). Since the concentration of CO_2 decreases, the overall reaction rate decreases, thus it could result in the reaction (1) to cease completely. Applying this finding to a practical setting; the cathodic compartment would be biofilm (not a completely mixed reactor as assumed here), thus the mass transfer in the biofilm can limit the reaction rate.

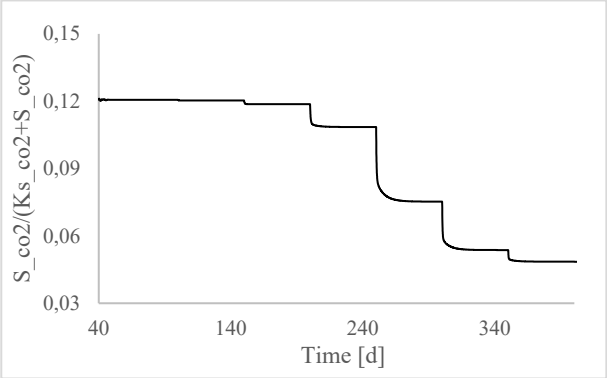

Figure 6: The Monod-type kinetic expressions (r3) due to available electron acceptor (soluble substrate, CO_2) after the bio-electrochemical process is activated at day 50, and the local potential (η) from -0.2 to 0.2 is increased stepwise (step size =0.05).

pH is one of the main parameters that can affect the performance of AD. Figure 7 shows the variation of pH in the digester. The digester with the conventional settings (selected to simulate for the baseline data) has pH at 7.2. The pH of the digester with BES increases as the local potential increases. The pH rises because of a fall in the bicarbonate strength due to depletion of headspace CO_2 as it is converted to methane. The elevated pH inhibits AD. The elevated pH can lead to deprotonation of ammonium ion, releasing free ammonia. Free ammonia is strictly inhibition for acetoclastic methanogens, the bacterial group which is responsible for decomposition of acetate into methane (Figure 1). In the conventional AD, a major portion of the methane is produced via this acetate pathway. The simulation result showed an increased acetate concentration and slight reduction in total biogas production (The results are not presented). Here, the pH elevation is not so significant to inhibit the process. The upper limit of pH at which anaerobic digestion is not inhibited is reported to be around pH 8.5[17].

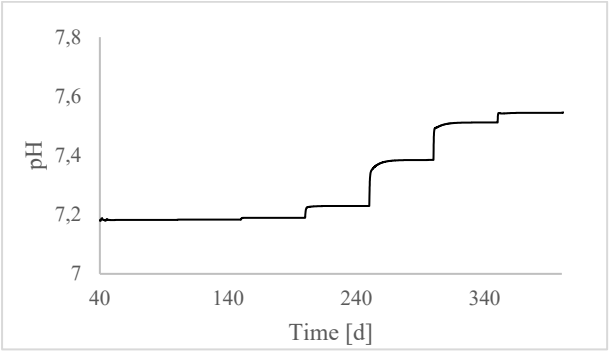

Figure 7: Response of pH in the digester to stepwise increases of the local potential (η) from -0.2 to 0.2 (step size =0.05). The bio-electrochemical process is activated at day 50.

This finding suggests that importance of controlling pH increase, when employing BES in AD.

3.1 Biomethanation of CO_2 from external source

The simulation result shows that CO_2 addition from external sources increases the overall biogas production (Figure 8, A). However, it reduces the biogas methane content, compared to the methane production without external CO_2 (Figure 8, B). Yet, the methane content is higher than that from the conventional AD (i.e. without BES). Therefore, the methane yield (m^3 CH_4 / kg COD organic loading to the digester) also increases (Figure 8, C). In order to keep the methane content at the desired level (e.g. 85%), the rate of CO_2 input to the digester, should thus be controlled according to the rate of the reduction reaction (r3). The carbon element balance showed that around 80 % of CO_2 moles added from the external source have been converted to CH_4, in the all three cases.

It can be anticipated that the reduction of CO_2 from an external source could be possible because the AD with BES was adapted gradually, by increasing EET hydrogenotrophic methanogens population by increasing local potential (η), before the CO_2 addition. In general, every AD has a maximum level of handling organic loading beyond which complete reactor failure may occur. Simultaneous biomethanation from the reduction of CO_2 from both endogenous and external sources demonstrates that the biogas production can be increased beyond the organic loading limitation and it does not interfere with substrate degradation.

Further, pH inhibition effect can be avoided when CO_2 is added from external sources to AD with BES (Figure 9). With increased CO_2 concentration in the liquid phase the substrate limitation, which affects the kinetics of the bio-electrochemical reaction (r3), is also overcome.

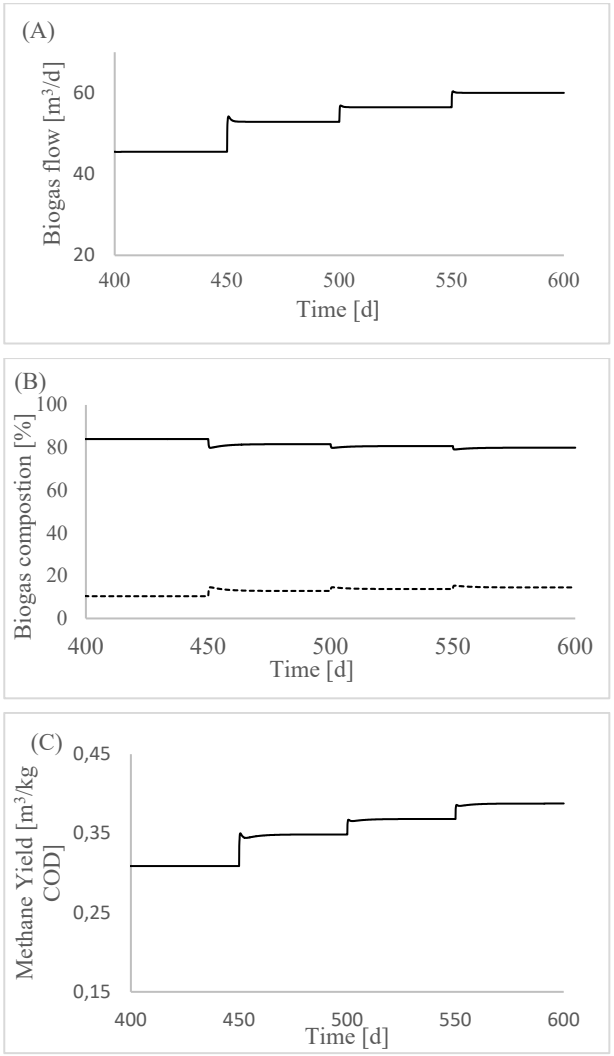

Figure 8: Biogas production rate (A), biogas composition (B) ─ CH_4 %, ··· CO_2 %, methane yield (C); after CO_2 addition form external source to the digester (AD with BES) at day 450. (η=0.200 V). The CO_2 loading rate simulated were 0.01, 0.015; and 0.02 M d^{-1}.

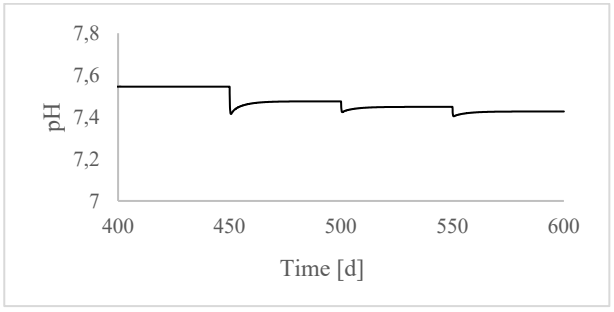

Figure 9**:** pH variation in the digester (AD with BES) after CO_2 addition form external source to the digester at day 450. (η=0.200 V). The CO_2 loading rate simulated were 0.01, 0.015, and 0.02 M·d^{-1}.

4. Conclusion

- The proposed model modification shows the basic concept of BES integrated with AD for biogas upgrade by converting CO_2 to CH_4 bio-electrochemically and limitations of such.
- The simulations show that by employing BES in AD, the methane content in biogas can be increased (up to 85 % under the reactor conditions simulated and further if substrate limitations are avoided).
- The rate of the reduction reaction can be constrained by the local potential of the cathode and the substrate concentration.
- The rise in pH (because of decreasing CO_2 that is being converted to CH_4) inhibits the digestion process. Therefore, it is essential to maintain a minimum CO_2 partial pressure to prevent the inhibition.
- Simultaneous biomethanation of CO_2 from endogenous and external sources can be achieved.
- The study also shows the capacity of an AD with BES for CO_2 reduction to CH_4, beyond the constraints of the applied organic load.

References

[1] Angelidaki, I., L. Treu, P. Tsapekos, G. Luo, S. Campanaro, H. Wenzel, and P.G. Kougias, *Biogas upgrading and utilization: Current status and perspectives.* Biotechnology Advances, 2018. **36**(2): p. 452-466.

[2] Blasco-Gómez, R., P. Batlle-Vilanova, M. Villano, M.D. Balaguer, J. Colprim, and S. Puig, *On the Edge of Research and Technological Application: A Critical Review of Electromethanogenesis.* International Journal of Molecular Sciences, 2017. **18**(4): p. 874.

[3] Nelabhotla, A.B.T. and C. Dinamarca, *Electrochemically mediated CO2 reduction for bio-methane production: a review.* Reviews in Environmental Science and Bio/Technology, 2018. **17**(3): p. 531-551.

[4] Geppert, F., D. Liu, M. van Eerten-Jansen, E. Weidner, C. Buisman, and A. ter Heijne, *Bioelectrochemical Power-to-Gas: State of the Art and Future Perspectives.* Trends in Biotechnology, 2016. **34**(11): p. 879-894.

[5] Cheng, S., D. Xing, D.F. Call, and B.E. Logan, *Direct Biological Conversion of Electrical Current into Methane by Electromethanogenesis.* Environmental Science & Technology, 2009. **43**(10): p. 3953-3958.

[6] Logan, B.E., B. Hamelers, R. Rozendal, U. Schröder, J. Keller, S. Freguia, P. Aelterman, W. Verstraete, and K. Rabaey, *Microbial Fuel Cells: Methodology and Technology.* Environmental Science & Technology, 2006. **40**(17): p. 5181-5192.

[7] Kadier, A., M.S. Kalil, P. Abdeshahian, K. Chandrasekhar, A. Mohamed, N.F. Azman, W. Logroño, Y. Simayi, and A.A. Hamid, *Recent advances and emerging challenges in microbial electrolysis cells (MECs) for microbial production of hydrogen and value-added chemicals.* Renewable and Sustainable Energy Reviews, 2016. **61**: p. 501-525.

[8] Tremblay, P.-L., L.T. Angenent, and T. Zhang, *Extracellular Electron Uptake: Among Autotrophs and Mediated by Surfaces.* Trends in Biotechnology, 2017. **35**(4): p. 360-371.

[9] Recio-Garrido, D., M. Perrier, and B. Tartakovsky, *Modeling, optimization and control of bioelectrochemical systems.* Chemical Engineering Journal, 2016. **289**: p. 180-190.

[10] Batstone, D.J., J. Keller, I. Angelidaki, S.V. Kalyuzhnyi, S.G. Pavlostathis, A. Rozzi, W.T.M. Sanders, H. Siegrist, and V.A. Vavilin, *The IWA Anaerobic Digestion Model No 1 (ADM1).* Water Science and Technology, 2002. **45**(10): p. 65-73.

[11 Lauwers, J., L. Appels, I.P. Thompson, J. Degrève, J.F. Van Impe, and R. Dewil, *Mathematical modelling of anaerobic digestion of biomass and waste: Power and limitations.* Progress in Energy and Combustion Science, 2013. **39**(4): p. 383-402.

[12] Henze, M., W. Gujer, T. Mino, and M.C. van Loosdrecht, *Activated sludge models ASM1, ASM2, ASM2d and ASM3*. 2000: IWA publishing.

[13] Monod, J., *The Growth Of Bacterial Cultures.* Annual Review of Microbiology, 1949. **3**(1): p. 371-394.

[14] Bae, W. and B.E. Rittmann, *A structured model of dual-limitation kinetics.* Biotechnology and Bioengineering, 1996. **49**(6): p. 683-689.

[15] Marcus, A.K., C.I. Torres, and B.E. Rittmann, *Conduction-based modeling of the biofilm anode of a microbial fuel cell.* Biotechnology and Bioengineering, 2007. **98**(6): p. 1171-1182.

[16] Siegrist, H., D. Vogt, J.L. Garcia-Heras, and W. Gujer, *Mathematical Model for Meso- and Thermophilic Anaerobic Sewage Sludge Digestion.* Environmental Science & Technology, 2002. **36**(5): p. 1113-1123.

[17] van Leerdam, R.C., F.A.M. de Bok, M. Bonilla-Salinas, W. van Doesburg, B.P. Lomans, P.N.L. Lens, A.J.M. Stams, and A.J.H. Janssen, *Methanethiol degradation in anaerobic bioreactors at elevated pH (⩾8): Reactor performance and microbial community analysis.* Bioresource Technology, 2008. **99**(18): p. 8967-8973.

TECHNO-ECONOMIC STUDY OF THE CCMS TECHNOLOGY FOR CO_2 CAPTURE FROM FERRO-SILICON PRODUCTION

H. S. Nygård[1*], J. Meyer[2], L. di Felice[2], N.H. Eldrup[3], A.T. Haug[4], E. Olsen[1]

[1]Faculty of Science and Technology, Norwegian University of Life Sciences, Ås, Norway

[2]Institute for Energy Technology (IFE), Department of Environmental Technology, Kjeller, Norway

[3]SINTEF Tel-Tek, Porsgrunn, Norway

[4]Elkem, Oslo, Norway

* Corresponding author e-mail: heidi.nygard@nmbu.no

Abstract

Carbon Capture in Molten Salts (CCMS) is a method for capturing CO_2 from a variety of flue gases related to power generation and energy intensive industry processes. The chemical principles are similar to those of the calcium looping process in solid state (using CaO-based solid sorbents), where CO_2 is captured in a carbonation reaction to form $CaCO_3$, and then released through the reverse calcination reaction in a second step. In the CCMS concept, the novelty is to operate the process in the liquid state in CaO-rich molten salts. The formed $CaCO_3$ dissolves continuously in the melt, thus leaving highly reactive CaO readily available for the incoming CO_2. In the present study, the technical and economic feasibility of the CCMS process has been investigated for capturing CO_2 from metallurgical ferro-silicon (FeSi) production using relevant industrial parameters. We have evaluated a generic plant based on one of the existing 40 MW FeSi furnaces the company Elkem owns and operates, but with theoretical considerations regarding recycling of the flue gas with the purpose of recovering energy. The input parameters for the capture process are based on experimental data. With the assumption of 85 % CO_2 capture and CO_2 compression to 70 bar (at 20 °C), the capture cost is estimated to be 60 EUR/ton, indicating that CCMS is a promising competitive alternative technology for full-scale CO_2 capture for FeSi production. The main cost driver for the process has been identified as the cost of desorption. The desorber has a high investment cost, and also requires high temperature heat transfer for operation. However, the evaluations show that the introduction of an integrated system with combustion and heat pipes is a viable technical option.

Keywords: *CCMS, Techno-economic study, FeSi production*

1. Introduction

Fossil fuels and carbon-intensive industries play dominant roles in the world's economy owing to their established infrastructure for exploitation and distribution. It is likely that carbon capture and storage (CCS) has to be an important part of the necessary reduction of CO_2 emissions on short to medium term. According to analyses performed by the International Energy Agency (IEA), CCS has to contribute to one-sixth of the total CO_2 emission reductions required by 2050 in order to reach the 2 degree increase scenario [1]. There are various capture options that are being pursued, with CO_2 capture using solvents, membranes, oxy-fuel combustion and emerging technologies like chemical looping combustion or calcium looping CO_2 capture showing most potential for commercial deployment in the near to medium term [2].

In the Calcium Looping process (CaL), CO_2 reacts with CaO to form $CaCO_3$ at temperatures around 650 °C. The CO_2 is subsequently regenerated through the reverse calcination reaction by raising the temperature above 900 °C. This cycle is described by Eq. 1 [3]:

$$CaO\ (s)\ +\ CO_2\ (g)\ \leftrightarrow\ CaCO_3\ (s) \qquad (1)$$

In general, any oxide of an alkaline earth metal element (e.g. Mg, Ca, Sr, Ba) can be used, with a higher turning point temperature for heavier cations. Limestone ($CaCO_3$) is often chosen as the raw sorbent material due to its low cost and large abundance compared to the other natural carbonates [4].

CaL offers the advantages of using an abundant, cheap and environmentally friendly sorbent, relatively low efficiency penalty on the power / industrial process and possible synergy with cement manufacture, as the sorbent is also used as raw material in this process [4]. Since CO_2 is captured at high temperature, the process also produces high quality heat that can be used to produce additional power. The main challenge with CaL in the *solid state* is the chemical and physical stability of the sorbent. After several absorption-desorption cycles, the sorbent particles lose sorption capacity due to sintering and pore closure. To cope with the large flue gas volumes, the *solid state calcium looping* process is operated in a double circulating fluidized bed configuration (fast fluidization) where solids attrition and loss play an important role on the operation costs of the process [4, 5].

A novel approach to CaL is Carbon Capture in *Molten Salts* (CCMS). In CCMS, the idea is to avoid the problems with chemical and physical stability and degradation of the sorbent by using molten salts as chemical solvents of CaO and $CaCO_3$. A flue gas containing CO_2 enters an absorption chamber (absorber) where CaO is present in a molten salt matrix. $CaCO_3$ is formed through Eq. 1 and dissolves continuously in the melt, leaving highly reactive CaO readily available. The CO_2-loaded molten salt containing $CaCO_3$ is transferred to a desorption chamber (desorber) operated at higher temperature than the absorber. The reverse reaction takes place (calcination), and the CO_2 is removed from the desorber. The cycle is completed by transferring the regenerated CaO-rich molten salt back to the absorber. All the active substances are dissolved or in a

supersaturated suspension in the molten salt medium which then acts as a solvent as well as a carrier.

The characteristics of absorption and desorption of CO_2 by CaO in molten salts have been investigated experimentally in a one-chamber reactor by bubbling simulated flue gases (0.76 – 15 vol % CO_2 in N_2) through various chloride and fluoride based melts [6-10], with eutectic CaF_2-$CaCl_2$ showing most promising results [8]. In this system, CO_2 capture has been successfully demonstrated in a melt containing up to 40 wt % CaO, showing that CaO can be present substantially above its solubility limit in the molten salts [10]. However, supersaturation of CaO leads to increased viscosities of the formed slurry, and the practical limit of the CaO content is 30 wt%. It has been shown that 70 – 85 % of the initial CaO reacted during absorption, and ~100 % of the $CaCO_3$ was decomposed during desorption. A series of 12 cycles has been performed, and the results show an increase in capacity in the first few cycles. This was followed by stable sorption capacities throughout the remaining cycles, without any deterioration of the reaction kinetics [8, 11].

Recent experimental work has focused on more realistic flue gases by investigating the effect of H_2O [12] and SO_2 / O_2 [13]. It has been shown that hydrolysis does occur at elevated temperatures, and that HCl forms to a larger extent than HF. Addition of CaO has a marked, limiting effect on the hydrolysis. For this reason, the temperature in the absorption reactor should be kept below 850 °C while maintaining a high CaO content when molten $CaCl_2$ is employed [12]. For flue gases containing SO_2 and O_2, it has been shown that all the SO_2 is converted into $CaSO_4$ through indirect and direct sulfation (reactions with CaO and $CaCO_3$, respectively). This means that it would be possible to clean the exhaust gas for both SO_2 and CO_2 in the same process. However, the formed $CaSO_4$ from the sulfation would then need to be handled, for instance by a purge stream of fresh molten salt [13].

In the present techno-economic study, we turn our attention to industrial applications where residual heat is available and not utilized today. This is the case in for instance the cement and metal industry. Preliminary basic design has been evaluated with special focus on heat transfer methods and reactor concepts. The main aim of the study is to verify the previously assumed advantages of the CCMS technology, as well as to identify uncertainties and weaknesses that should be improved to promote CCMS as a realistic alternative for full-scale industrial CO_2 capture.

2. Technical evaluation

Laboratory scale experiments have shown that CCMS is applicable for capturing CO_2 from a variety of flue gases related to both energy intensive industry and power generation [6-8]. In the present techno-economic evaluation, the focus is on industrial processes, and we evaluate the use of CCMS for capturing CO_2 from a theoretical 40MW FeSi furnace with energy recovery. The base design proposed by Elkem for generic plant with energy recovery and flue gas recycling, but without CO_2 capture, is shown in Figure 1. The chosen process parameters regarding recirculation of the flue gas are given in Table 1. The main objective for recycling is to recover the energy in the flue gas. As a consequence, the CO_2 concentration is increased. This is of particular interest for the CCMS process, because higher CO_2 concentrations favor efficient CO_2 capture.

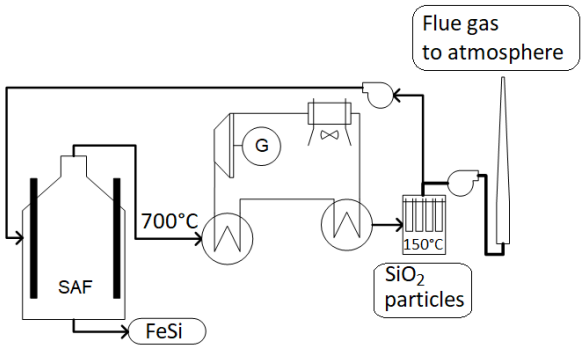

Figure 1: Base design for a theoretical 40MW FeSi furnace with energy recovery and flue gas recycling.

Table 1: Flue gas composition and properties for a generic 40 MW FeSi plant with no flue gas recycle and 73 % flue gas recycle.

Characteristic	Value		
	No recycle	73 % recycle	
	After filter	Before filter	After filter
Flow rate (Nm^3/h)	173 833	188 459	188 459
Pressure (mbarg)	-75	-45	-75
Temperature (°C)	130	150	130
O_2 content (vol %)	16.4	6.00	6.00
CO_2 content (vol %)	4.43	15.1	15.1
Water content (vol %)	4.28	11.8	11.8
N_2 content (vol %)	74.9	67.1	67.1

For the theoretical considerations regarding flue gas recycling, the oxygen content in the flue gas and the amount of gas recycling have been used to reach 700 °C out of the furnace. This is achieved with 73 % recycling, and raises the CO_2 concentration in the flue gas from 4.43 to 15.1 vo l%. Recycling also lowers the oxygen content from 16.4 to 6 vol %, and raises the water content from 4.28 to 11.8 vol %. Hydrolysis of the water that is present in the flue gas is not an issue for the CCMS process as long as CaO is present in abundance or T < 850 °C [12].

Besides the gas components listed in Table 1, the flue gas contains trace components such as SO_2, NO_x and heavy metals. As mentioned in the introduction, it has been shown that SO_2 will be absorbed by CaO / $CaCO_3$ in the CCMS process [13]. With significant amounts of SO_2, a purge stream of fresh sorbent may be required to account for the formed $CaSO_4$. Another viable option would be to install SO_2 scrubbers before the absorber. The content of NO_x is expected to be much lower with the recirculation system, and NOx are not expected to react in the CCMS process. Any presence of heavy metals could accumulate in the melt through the formation of stable substances, and would also require a purge stream. The above-mentioned trace components have not been taken into account in the current evaluation, but should be considered in more detailed studies in the future.

A retrofitting design for the CCMS process was selected for the present case study, leaving the FeSi production process untouched. Figure 2 shows a simplified sketch of the selected absorber – desorber system. The main elements are an absorber, a desorber, storage tanks for absorber and desorber raw materials (CaO, $CaCl_2$ and CaF_2), a bubbling fluidized bed combustor including cyclones, and high temperature heat pipes for transferring heat from the combustor to the desorber.

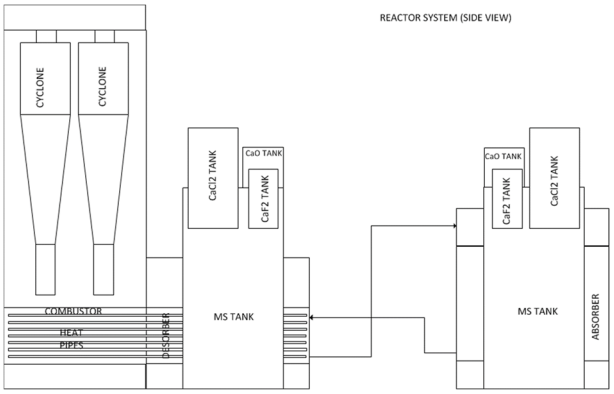

Figure 2: Simplified sketch of the absorber – desorber system for CCMS.

The desorber requires heat supply in order to regenerate the molten salt mixture. In conventional CaL, heat is supplied by oxy-fuel combustion (usually with coal as fuel). Direct heat transfer using an oxy-fuel configuration is difficult to achieve in the case of the CCMS process, meaning that an indirect heat transfer has to be used. In the present study, we have introduced fuel combustion similar to the conventional CaL process to deliver heat in the regeneration step. Combustion of cheap fuels such as coal was considered because this combustion process is well known and the properties of the combustion gases were compatible with existing models. The CO_2 from this combustion would be captured together with the CO_2 from the FeSi-furnace, so the fuel itself does not have to be CO_2 neutral. However, for more detailed and realistic studies in the future, more environmentally friendly fuels such as biomass will be considered.

To minimize the investment and operation costs, the use of an air separation unit for oxy-combustion is avoided, and a solid fuel is combusted directly in air in the fluidized bed combustor, using typically sand as bed material. The indirect heat exchange is carried out with high temperature heat pipes using sodium as working medium to transfer efficiently the required heat from the combustor to the desorber. The heat pipes are submerged in both the combustor's bed and in the desorber.

Heat pipes are sealed cavities filled with small amounts of heat transfer liquids in the case of high temperature applications above 650 °C. They provide largest heat transfer rates due to evaporation–transport–condensation cycles of the heat carrier within the heat pipe. They are passive devices that are driven by external heat sources or sinks, even without or against gravity as a result of capillary forces created in the internal wick structure. In spite of the high heat transfer rates, only small temperature differences between evaporation and condensation zones are formed due to heat conduction through the casing (equivalent thermal conductivities of over 15 kW m^{-1} K^{-1} [14]). Thus, the heat pipe can be assumed as an almost isothermal heat transport device within its working limits. Liquid metal heat pipes have proven their functionality in a large variety of technical high temperature applications, such as in gasification reactors [15], solid oxide fuel cells [16, 17] or calciners in carbon capture technologies [18, 19]. The coupling of a bubbling fluidized bed combustor with heat pipes is sought to provide an efficient heat transfer required by the CCMS process.

A process flow diagram of the base design for the SAF furnace combined with the selected retrofitting design for the CCMS process is shown in Figure 3. The grey area represents the components belonging to the CCMS process, and the SAF process remains untouched. A more detailed process flow diagram of the proposed system is shown in Figure 4, and this defines the scope of the present techno-economic evaluation. Larger versions of both figures may be found in the Appendix.

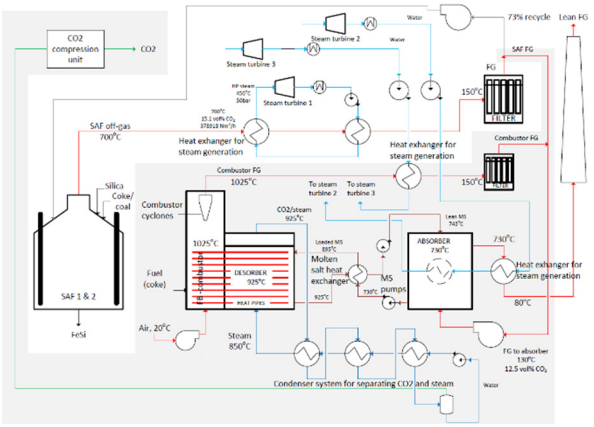

Figure 3: Process flow diagram of CO_2 capture based on the CCMS process for a theoretical 40 MW FeSi furnace with 73 % recycling. A larger version of the figure may be found in Appendix A (Figure A.1).

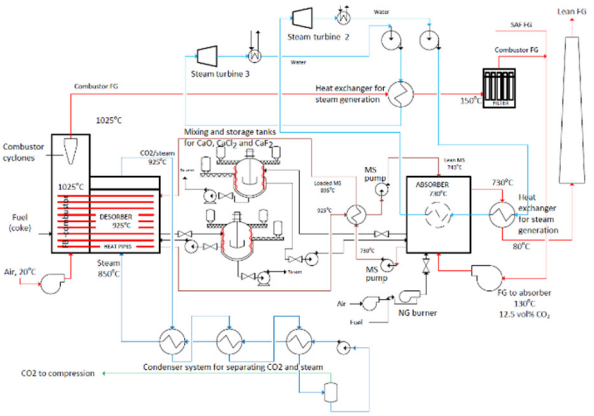

Figure 4: Detailed process flow diagram of CO_2 capture based on the CCMS process for a theoretical 40 MW FeSi furnace with 73 % recycling. This defines the scope of the present techno-economic study. A larger version of the figure may be found in Appendix A (Figure A.2).

The flue gas from the FeSi furnace (SAF FG) is merged with the flue gas from the desorber combustor FG to a combined stream and sent to the absorber through a gas blower. The CO_2 content into the absorber is 12.5 vol %, which is somewhat lower than the 15.1 vol % in the SAF FG due to mixing of two FG streams. The total FG volumetric flow into the absorber is 215 631 Nm^3/h, which corresponds to a CO_2 mass flow of about 53 t/h. The CO_2 capture rate is assumed to be 85 %, meaning that around 45 t/h CO_2 is captured. The inlet flue gas temperature is 130 °C, while the absorption temperature in the absorber is set to be 730 °C. The absorption process is designed to be auto-thermal, i.e. no external heat supply to the absorber is required. However, a natural gas (NG) burner is included in the flow diagram for start-up purposes, to heat up the absorber and the molten salt mixture.

In the absorber, the molten salt (MS) is assumed to contain 9.7 wt % CaF_2, 60.3 wt % $CaCl_2$, and 30 w t% CaO. This has been found to be the upper practical limit for the CaO content after conclusions from experimental viscosity studies [20]. The CaO

conversion to $CaCO_3$ in the molten salt is assumed to be 52.5 %, and the specific sorption capacity rate is 0.024 kg CO_2 captured / h / kg MS. These numbers are based on linear sorption rates obtained from recent kinetic studies of the CCMS process [11]. Based on the above mentioned assumptions, the absorber dimensions have been calculated. The absorber width and length are found to be 12.1 m (inner dimensions, square area), while the total reactor height is 14.4 m, including a reaction zone height of 9.1 m. The gas velocity in the absorber has been set to maximum 1.5 m/s, resulting in a gas contact time of about 6 seconds.

The loaded and lean molten salts are transferred by pumps between the reactors. The loaded and lean mass flows are 131.7 and 119.2 kg/s, respectively. A molten salt heat exchanger is included to pre-heat the loaded molten salt before it enters the desorber and to cool the lean molten salt before the absorber.

In order to supply the required heat of 51.8 MW to the desorber, a fluidized bed combustor and heat transfer system is introduced. The desorber width and length are calculated to be 13.1 m and 14.5 m, respectively, and the total desorber height is 10.5 m. The dimensions for the combustor are width and length of 11.3 m and 14.5 m, respectively. The resulting total ground area for the combustor and desorber system is 353 m^2. The temperature in the combustor has been set to 1025 °C, while it is set to be 925 °C in the desorber for best desorption performance. Four combustor cyclones in parallel, each with a total length of 20.0 m, are part of the combustor system to return entrained bed material.

The heat is transferred from the combustor to the desorber through heat pipes (red lines in Figure 4 / Figure A.2), which are submerged both in the combustor bed and in the desorber. A total of 154 tubes are needed, each with an outer diameter of 0.168 m and a length of 23.8 m. These are organized in 7 rows with 22 horizontal tubes per row. The required liquid sodium mass flow for the heat transfer is found to be 12.2 kg/s.

The CO_2 is swept from the desorber with superheated steam, with a steam / CO_2 weight ratio of 0.55. The CO_2 and steam from the desorber are separated by condensation through a system consisting of a superheater, evaporator / condenser and a cooler. The released CO_2 is further dried and compressed to standard conditions (20 °C and 70 bar).

A solution with desorption in pure CO_2 was considered, as this would eliminate the subsequent condensation system, as well as to reduce the streams and hence equipment size. This option is feasible, however, experiments show that it would require a desorption temperature of 1070 °C [6], and such high temperatures will be a challenge with regards to reactor materials.

Systems for storing and filling MS to the absorber and desorber (circulation system) are proposed as shown between the desorber and the absorber in Figure 4 / Figure A.2. Each raw material (CaO, $CaCl_2$, CaF_2) has its own storage tank, and the components are filled into a MS mixing tank by screw conveyors. The mixing tanks are electrically heated, and once the molten salt mixtures are completely melted, they can be transferred to the absorber and desorber. The feeding takes place in several batches. The same tanks can be used for emptying the reactors when needed, for instance during planned (or unplanned) stops in the FeSi furnace or maintenance of the reactors. Vacuum pumps have been included in order to create under-pressures in the tanks before emptying MS from the reactors. A typical FeSi plant has planned maintenance stops for a few weeks every 5-7 years, in addition to 4-5 hours stops every 14 days.

To benefit from the high temperatures involved in the capture process, high quality steam is produced and additional electricity is generated in two steam turbines. By assuming that steam enters the turbines at 450 °C and 50 bar, and that the turbines operate with 35 % efficiencies, the additional electricity generated in total will be 32.5 MW. The CO_2-lean absorber exhaust gas enters a steam generator, in which steam is produced for generation of electricity in steam turbine 2. The steam is further condensed in a condenser that consists of several heat exchangers in series, before it is pumped back into the steam generator. A similar system is proposed for recovering heat from the combustor FG through a steam generator and steam turbine 3.

After the heat exchanging process, the flue gas from the combustor is filtered and combined with the SAF flue gas. This completes the cycle.

3. Cost estimation

The cost estimation is based on the components defined in the detailed process flow diagram (Figure 4 / Figure A.2). The main assumptions for the calculations of CAPEX (capital expenditure), OPEX (operating expenses) and economic profitability are listed in Table 2. CAPEX includes commissioning but not start up. It is assumed a construction time of 3 years, followed by 22 years operation. OPEX includes sale of electricity produced by the additional steam turbines that recover energy from the CO_2-lean absorber exhaust gas (steam turbine 2) and from the combustor flue gas (steam turbine 3).

Table 2: Main assumptions for the cost estimation of the CCMS process as a CO_2 capture retrofitting option for ferro-silicon production.

CAPEX	**Value / comment**
Cost date	2018
Location	Generic, North-West Europe
Plant type	N^{th} of a Kind (NOAK), retrofitting
Plant site	Existing plant area (brown site)
Utilities	All utilities available (unit cost)
Access	Access to existing offices, control room, etc.
Materials	Stainless steel and high temperature materials
OPEX	**Value / comment**
Absorption medium	30 wt % CaO in molten $CaCl_2$-CaF_2
Organization	Operator (2 extra shifts + 3 day time, total 15 persons extra)
Coal price	80 EUR/ton
Cost of electricity	40 EUR/MWh
Maintenance cost	4 % of investment per year
Cost of cooling water	0.03 EUR/m^3
Economic	**Value / comment**
Rate of return	7.5 %
Number of years	25 years
Number of operating hours	8760 h/year

The cost estimation has been carried out using a detail factor cost estimate method. The equipment cost for the standard equipment has been estimated using the commercial "Aspen In-plant" cost estimator. The not standard equipment has been designed and the cost estimated by unit cost. For each equipment, an installation factor has been calculated. Details about the installation costs for all the components defined in

Figure 4 / Figure A.2 can be found in the Appendix, sorted by the main systems given in Table 4.

The estimated CAPEX, OPEX and capture cost are summarized in Table 3. The accuracy of the estimations are ± 35%, corresponding to AACE International Estimate Class 5. This is regarded as a standard accuracy for a process with low TLR-level.

Table 3: Summary of CAPEX, OPEX and capture cost.

	CCMS
CAPEX [MEUR]	192.4
OPEX [MEUR / year]	4.5
Capture cost [EUR / tonne CO_2]	60

The capture cost was estimated to be EUR 60 per tonne CO_2 captured. This number lies in the same range as other existing and emerging technologies for post combustion / end of pipe CO_2 capture. The cost estimates show that, with the chosen parameters, CCMS is a promising competitive alternative technology for full-scale CO_2 capture for FeSi production.

The costs divided per system/large component are summarized in Table 4 and Figure 5, while details about installation costs within each subsystem are given in the Appendix. The number for electricity generation is subtracted from the rest, since the OPEX is reduced by selling the electricity. The capture cost for the absorber and desorber are further detailed in Figure 6 and 7, respectively.

Table 4: CAPEX and OPEX divided per system / large component. Detailed installation costs for the equipment within each system / large component are found in the Appendix.

	CAPEX [MEUR]	OPEX [MEUR/ year]	Detailed installation cost
Desorber/ combustion system	77	8.5	Table A.1
Absorber	31.5	2.1	Table A.2
Circulation system	14.6	0.77	Table A.3 and A.4
Electricity generation (sold)	32.8	- 10.2	Table A.5 and A.6
CO_2/steam separation	2	0.09	Table A.7
CO_2 compression	23.9	2.7	Table A.8
Bag filters	10.6	0.5	Table A.9
Total MEUR	192.4	4.46	

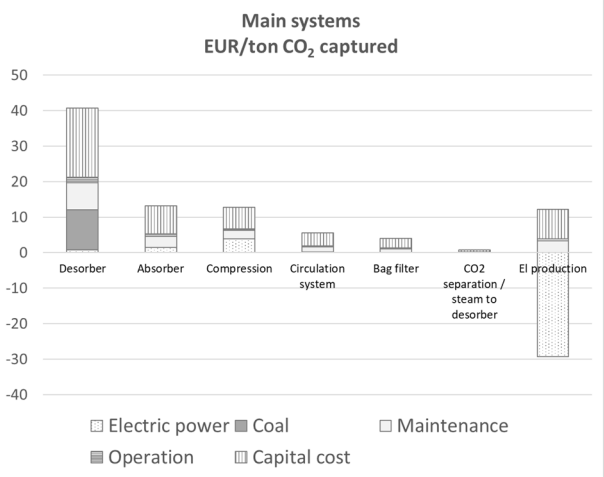

Figure 5: Capture cost divided by main system / large component.

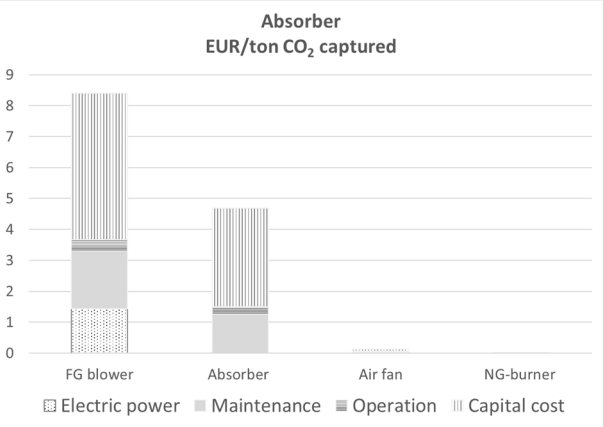

Figure 6: Capture cost for absorber.

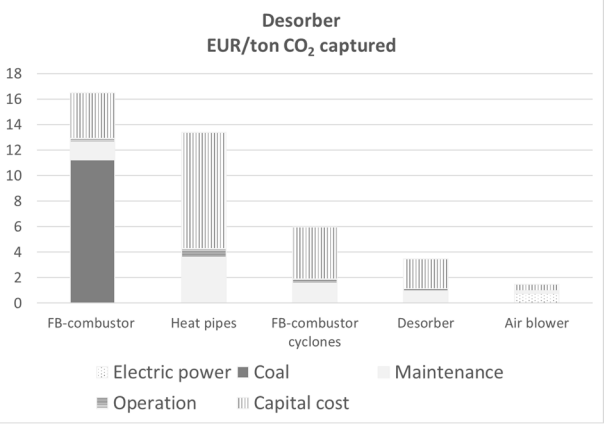

Figure 7: Capture cost for desorber.

The main cost driver has been identified as the cost of desorption, both for CAPEX and OPEX. This is due to the heat management system to transfer the required heat to the desorber. The excess high temperature heat from the CCMS is recovered in the form of high-quality steam and converted to electricity in two additional steam turbines, reducing the OPEX to an acceptable level.

A sensitivity analysis was performed, showing how a 50 % reduction and 50 % increase of several factors will affect the capture cost. The results are depicted in Figure 8.

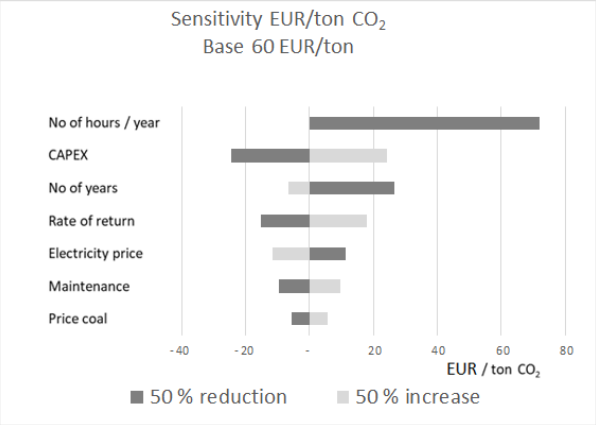

Figure 8: Sensitivity analysis.

The factor affecting the capture cost the most is the number of operating hours per year. As already mentioned, the stops for a typical FeSi plant are rare, and this is not a large risk for the proposed concept. CAPEX is also an important factor. This is an uncertainty when it comes to material choices for the equipment. In this study, the material has been defined as "exotic", giving good margins for the cost, but the choice of materials needs to be investigated in more detail. Higher electricity prices are definitely beneficial for the concept.

4. Conclusion and recommendation

Technical and economical evaluations have been performed for a CCMS capture plant retrofitted to a generic 40 MW ferro-silicon (FeSi) furnace with heat recovery, using realistic parameters provided by Elkem. The main objective was to verify the previously claimed advantages of the CCMS technology, and to apply it to metallurgical industry using relevant industrial parameters. Preliminary designs with special focus on technical solutions to transfer high temperature heat to the desorption process were investigated in detail. A solution with a fuel combustor based on coke (or coal) and indirect heat transfer with high temperature heat pipes using sodium as working medium was chosen. Heat pipes technology has been known for 30-40 years, and has become significantly more attractive in the last decade. There is evidence from several R&D works that this technical solution should be suited to the CCMS process, however, there are uncertainties related to up-scaling and potential safety risks related to the use of liquid sodium.

The capture cost was estimated based on the above-mentioned design, and includes compression of the captured CO_2 to 70 bar (20 ^oC). The investment cost was found to be around 192.4 MEUR, and the operating cost was calculated to be around 4.5 MEUR/year. This includes the sale of electricity that is produced by recovering the excess heat from the CCMS process. The capture cost was found to be 60 EUR/tonne CO_2. Assuming that the capture system performs as anticipated, the results show interesting promise for using the CCMS technology for capturing CO_2 from metallurgical industry.

It was considered to use available heat from the FeSi furnace, but preliminary evaluation indicated that there was little to gain on operational costs because the temperature available was not high enough and the oxygen content of the furnace flue gas was too low. This option could become more attractive in the future, if higher temperature could be made available by for example closing the furnace. If no or less additional heat is required in the desorber, the operating costs would be significantly lower, and the CCMS solution even more attractive.

The main issue with the chosen combustor system is potential erosion due to the vigorous fluidization of the bed material (typically sand). Erosion could lead to potential leaks from the heat pipes allowing sodium to get in contact with steam and air, and this is a safety risk of the proposed system. High quality materials are therefore strictly required for the construction of the heat pipes.

Another challenge is related to the pumping of high temperature molten salts between the reactors. To cope with this, the costs of the pumps have been given good enough margins in this study, assuming that it should be possible to manufacture pumps that can handle molten salts at the required temperatures.

Finally, the technical issues related to high temperature heat transfer, and the cost associated, could be significantly reduced if the CCMS process could be operated with molten salts requiring lower temperature for desorption of CO_2. Magnesium oxide based molten salts have been identified as a promising option and should be investigated in future R&D projects.

Acknowledgements

The work was carried out in the framework of the CLIMIT-Demo program (Project 617270). We greatly appreciate the involvement of Henrik Lid Scharff during the work.

References

[1] IEA, Technology Roadmap: Carbon Capture and Storage. 2013, OECD/IEA: Paris, France.

[2] MacDowell, N., et al., An overview of CO_2 capture technologies. Energy & Environmental Science, 2010. 3(11): p. 1645-1669.

[3] Abanades, J.C., et al., Capture of CO_2 from combustion gases in a fluidized bed of CaO. AIChE Journal, 2004. 50(7): p. 1614-1622.

[4] Dean, C.C., et al., The calcium looping cycle for CO_2 capture from power generation, cement manufacture and hydrogen production. Chemical Engineering Research and Design, 2011. 89(6): p. 836-855.

[5] Blamey, J., et al., The calcium looping cycle for large-scale CO_2 capture. Progress in Energy and Combustion Science, 2010. 36(2): p. 260-279.

[6] Olsen, E. and V. Tomkute, Carbon capture in molten salts. Energy Science & Engineering, 2013. 1(3): p. 144-150.

[7] Tomkute, V., A. Solheim, and E. Olsen, Investigation of high-temperature CO_2 capture by CaO in $CaCl_2$ molten salt. Energy & Fuels, 2013. 27(9): p. 5373-5379.

[8] Tomkute, V., A. Solheim, and E. Olsen, CO2 Capture by CaO in Molten CaF_2–$CaCl_2$: Optimization of the Process and Cyclability of CO2 Capture. Energy & Fuels, 2014. 28(8): p. 5345-5353.

[9] Tomkute, V., et al., Reactivity of CaO with CO_2 in molten CaF_2–NaF: formation and decomposition of carbonates. Energy Science & Engineering, 2016. 4(3): p. 205-216.

[10] Alhaj-Saleh, Y., Carbon Capture in Molten Salts: Absorption and Desorption of CO_2 by CaO-sorbent in Eutectic CaF_2/$CaCl_2$-Melt. Master thesis, 2014, Norwegian University of Life Sciences.

[11] Nygård, H.S., V. Tomkute, and E. Olsen, Kinetics of CO_2 Absorption by Calcium Looping in Molten Halide Salts. Energy Procedia, 2017. 114: p. 250-258.

[12] Olsen, E., M. Hansen, and H.S. Nygård, Hydrolysis of molten $CaCl_2$-CaF_2 with additions of CaO. AIMS Energy, 2017. **5 (6)**: p. 873-886

[13] Ruud, N.A.R., Carbon Capture in Molten Salts: The Effect of Sulfation. Master thesis, 2018, Norwegian University of Life Sciences.

[14] Dillig, M., J. Leimert, and J. Karl, Planar high temperature heat pipes for SOFC/SOEC stack applications. Fuel Cells, 2014. 14(3): p. 479-488.

[15] Karl, J., Biomass heat pipe reformer—design and performance of an indirectly heated steam gasifier. Biomass Conversion and Biorefinery, 2014. 4(1): p. 1-14.

[16] Leimert, J.M., M. Dillig, and J. Karl, Hydrogen inactivation of liquid metal heat pipes. International Journal of Heat and Mass Transfer, 2016. 92: p. 920-928.

[17] Dillig, M., T. Meyer, and J. Karl, Integration of planar heat pipes to solid oxide cell short stacks. Fuel Cells, 2015. 15(5): p. 742-748.

[18] Hoeftberger, D. and J. Karl, Self-Fluidization in an Indirectly Heated Calciner. Chemical Engineering & Technology, 2013. 36(9): p. 1533-1538.

[19] Hoeftberger, D. and J. Karl, The Indirectly Heated Carbonate Looping Process for CO_2 Capture—A Concept With Heat Pipe Heat Exchanger. Journal of Energy Resources Technology, 2016. 138(4): p. 042211.

[20] Nygård, H.S., et al., Experimental evaluation of chemical systems for CO_2 capture by CaO in eutectic CaF_2-$CaCl_2$. AIMS Energy, 2019. **7**(5): p. 619-633.

Appendix A

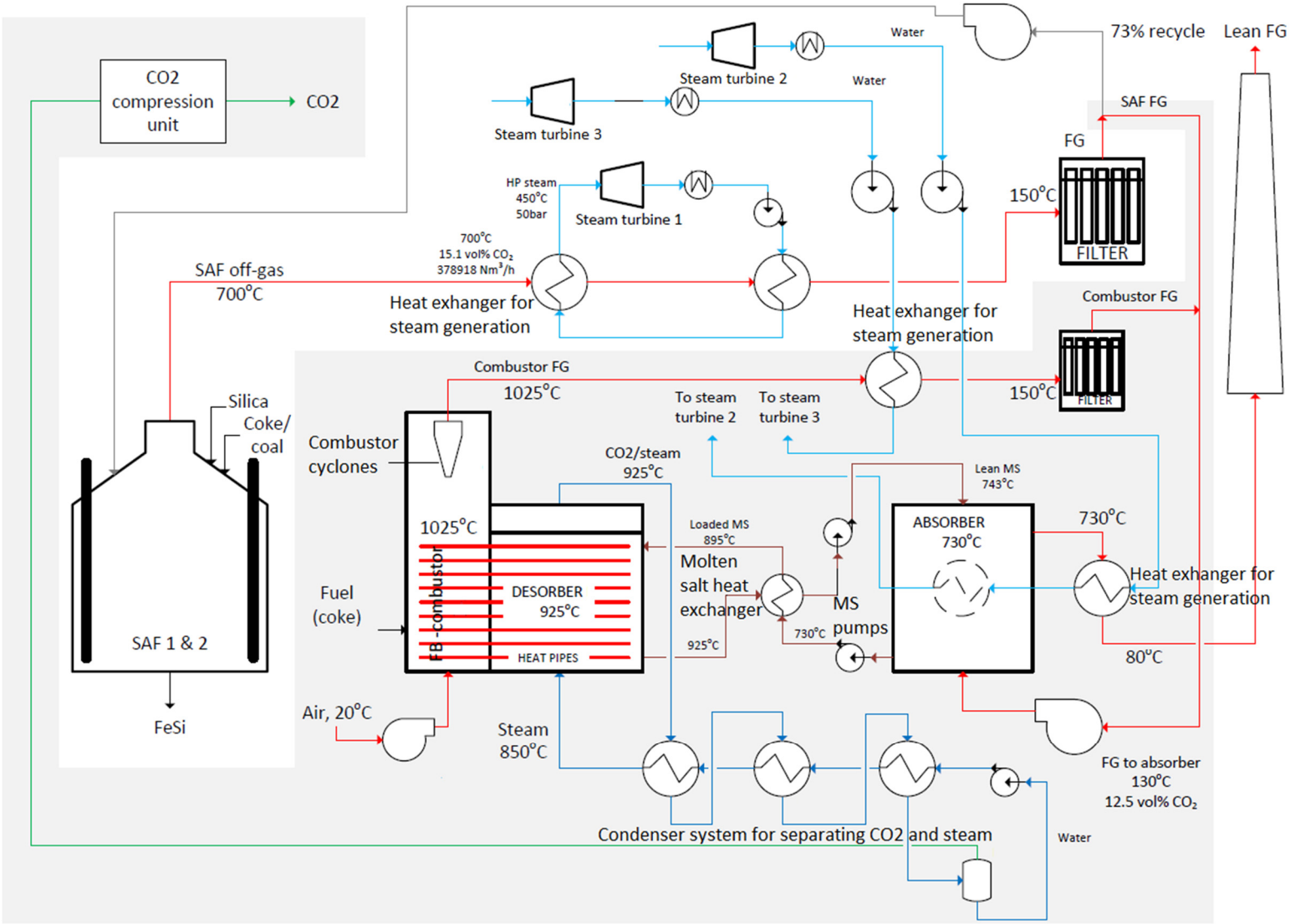

Figure A. 1. Process flow diagram of CO_2 capture based on the CCMS process for a theoretical 40 MW FeSi furnace with 73 % recycling.

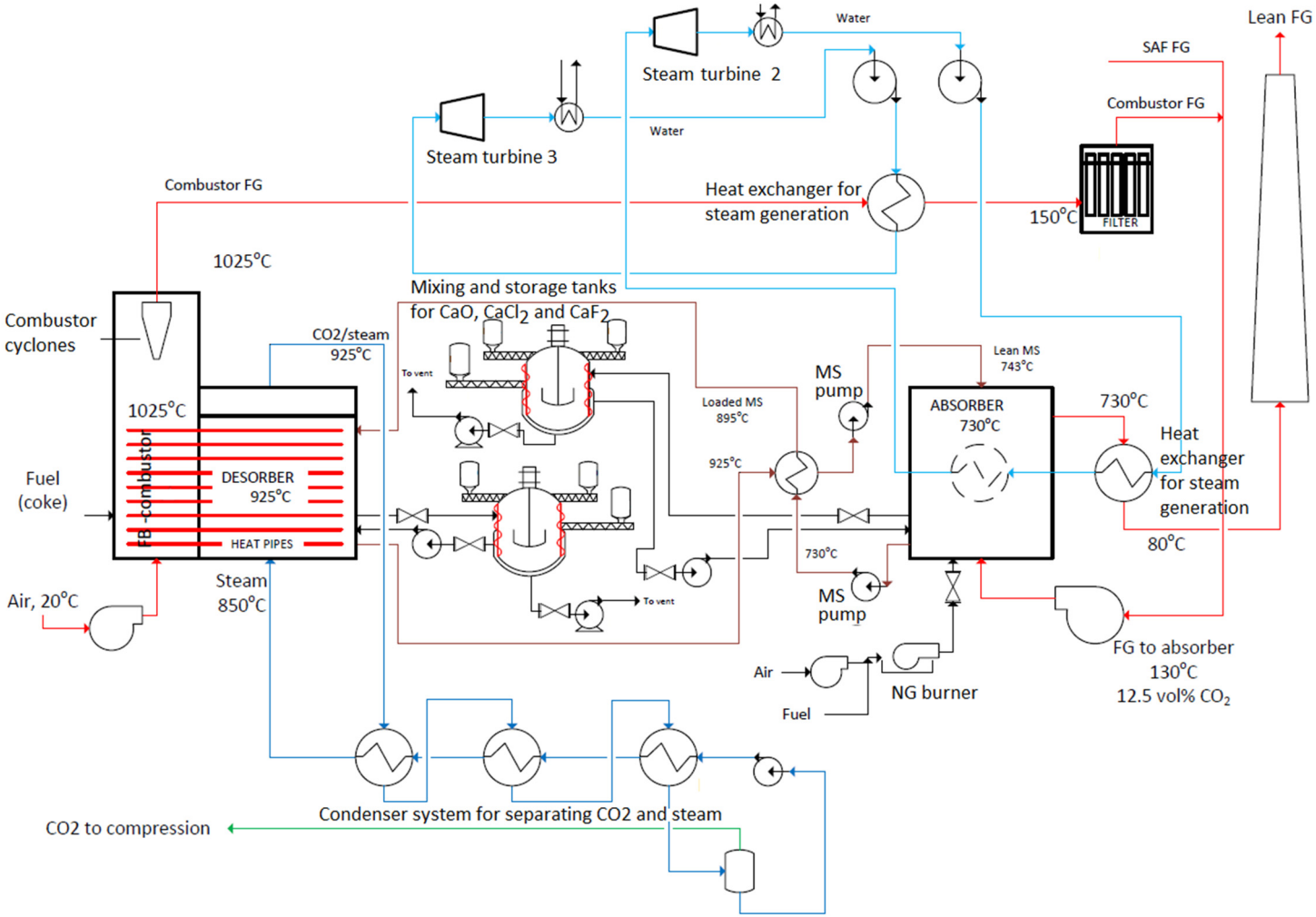

Figure A. 2. Detailed process flow diagram of CO_2 capture based on the CCMS process for a theoretical 40 MW FeSi furnace with 73 % recycling. This defines the scope of the present techno-economic study.

Table A. 1. Characteristic parameters and costs of the components in the desorber / combustion system.

Component	**Power / duty (MW)**	**Area (m^2)**	**Volume (m^3)**	**Material**	**No of**	**Equipment cost kEUR (2018)**	**Installation factor**	**Installed cost kEUR (2018)**
Desorber			1 985	CS steel/ inner refractory	1	2 837	3.29	9 333
Heat pipes		1931	81	HT steel	154	35	6.60	35 836
Air blower	0.84			Stainless steel	4	119	4.06	1 930
FB-combustor		164		CS steel/ inner refractory	1	4 667	3.02	14 094
FB-combustor cyclones				CS steel/ inner refractory	4	1 381	2.89	15 967
Sum								**77 160**

Table A. 2. Characteristic parameters and costs of the components in the absorber system.

Component	**Power / duty (MW)**	**Area (m^2)**	**Volume (m^3)**	**Material**	**No of**	**Equipment cost kEUR (2018)**	**Installation factor**	**Installed cost kEUR (2018)**
FG blower	1.59			Stainless steel	8	506	4.62	18 690
Absorber			1 992	CS steel/ inner refractory/ ceramic packing	1	4 066	3.09	12 563
Air fan	0.03				1	26	11.00	284
NG burner	10				1	2	12.00	30
Sum								**31 566**

Table A. 3. Characteristic parameters and costs of the components in the molten salt circulation system part I (between the absorber and desorber).

Component	**Power / duty (MW)**	**Area (m^2)**	**Volume (m^3)**	**Material**	**No of**	**Equipment cost kEUR (2018)**	**Installation factor**	**Installed cost kEUR (2018)**
Loaded MS pump	0.029			HT steel	2	33	7.38	487
MS heat exchanger	26	1296		HT steel	1	441	3.61	1 592
Lean MS pump	0.025			HT steel	2	33	7.38	487
Sum								**2 566**

Table A. 4. Characteristic parameters and costs of the components in the molten salt circulation system part II (mixing and storage tanks).

Component	**Power / duty (MW)**	**Area (m^2)**	**Volume (m^3)**	**Material**	**No of**	**Equipment cost kEUR (2018)**	**Installation factor**	**Installed cost kEUR (2018)**
MS tank 1			800	CS steel/ inner refractory	1	823	3.47	2 857
CaF_2 tank 1			20	CS steel/ plastic lining	1	61	6.33	387
$CaCl_2$ tank 1			100	CS steel/ plastic lining	1	195	6.33	1 235
CaO tank 1			50	CS steel/ plastic lining	1	127	4.76	603
Screw conveyor CaF_2 tank1	0.005			CS steel	1	19	10.55	203
Screw conveyor $CaCl_2$ tank1	0.005			CS steel	1	19	10.55	203
Screw conveyor CaO tank1	0.005			CS steel	1	19	10.55	203
MS filling pump desorber	0.025			HT-steel	1	17	9.89	169
MS tank 1 vacuum pump	0.025			CS steel	1	25	8.81	222
MS tank 2			800	CS steel/ inner refractory	1	1176	2.97	3 493
CaF_2 tank 2			20	CS steel/ plastic lining	1	35	9.04	316
$CaCl_2$ tank 2			100	CS steel/ plastic lining	1	112	6.66	743
CaO tank 2			50	CS steel/ plastic lining	1	72	6.33	458
Screw conveyor $CaCl_2$ tank2	0.005			CS steel	1	19	10.55	203
Screw conveyor CaF_2 tank2	0.005			CS steel	1	19	10.55	203
Screw conveyor CaO tank2	0.005			CS steel	1	19	10.55	203
MS filling pump absorber	0.025			HT-steel	1	17	9.54	163
MS tank 2 vacuum pump	0.025			CS steel	1	25	8.81	222
Sum								**12 088**

Table A. 5. Characteristic parameters and costs of the components in the system for additional electricity part I (turbine 2).

Component	**Power / duty (MW)**	**Area (m^2)**	**Volume (m^3)**	**Material**	**No of**	**Equipment cost kEUR (2018)**	**Installation factor**	**Installed cost kEUR (2018)**
Water pump	0.005			Stainless steel	1	12	10.93	136
Steam generator – economizer	50	1964		Stainless steel/ HT steel	1	304	4.37	1 328
Steam generator – evaporator				Stainless steel	1	78	6.08	471
Steam generator – superheater				Stainless steel	1	136	5.32	726
Steam turbine 2	17.50			Stainless steel	1	3323	3.20	10 634
Condenser	35	4033		Stainless steel	4	253	4.37	4 417
Sum								**17 712**

Table A. 6. Characteristic parameters and costs of the components in the system for additional electricity part II (turbine 3).

Component	Power / duty (MW)	Area (m^2)	Volume (m^3)	Material	No of	Equipment cost kEUR (2018)	Installation factor	Installed cost kEUR (2018)
Water pump	0.005			Stainless steel	1	102	6.18	629
Steam generator – economizer	43	519		Stainless steel/HT steel	1	109	5.55	606
Steam generator – evaporator				Stainless steel	1	34	7.31	252
Steam generator – superheater				Stainless steel	1	71	6.10	432
Steam turbine 3	15			Stainless steel	1	2869	3.28	9 411
Condenser	29	3362		Stainless steel	4	216	4.37	3 779
Sum								**15 109**

Table A. 7. Characteristic parameters and costs of the components in the CO_2/steam separation system.

Component	Power / duty (MW)	Area (m^2)	Volume (m^3)	Material	No of	Equipment cost kEUR (2018)	Installation factor	Installed cost kEUR (2018)
Water pump	N.A.			Stainless steel	1	10	11.92	114
Cooler	2.16	460		Stainless steel	1	150	5.08	760
Evaporator/condenser	16	159		Stainless steel	1	67	6.17	413
Superheater	14	393		Stainless steel	1	134	5.23	698
Sum								**1 985**

Table A. 8. Characteristic parameters and costs of the components in the CO_2 compression system.

Component	Power / duty (MW)	Area (m^2)	Volume (m^3)	Material	No of	Equipment cost kEUR (2018)	Installation factor	Installed cost kEUR (2018)
1st stg CO_2 comp. S drum			14.97	CS steel	1	35	9.21	325
2nd stg comp. S drum			4.61	CS steel	1	22	10.36	231
3rd stg comp. dis drum			1.15	CS steel	1	15	11.70	174
1st stg CO_2 comp. cooler		98.68		Stainless steel	1	210	9.98	2 099
2nd stg CO_2 comp cooler		75.19		Stainless steel	1	196	10.15	1 990
3rd stg CO_2 comp cooler		53.57		Stainless steel	1	210	9.98	2 096
CO_2 product pump	0.27			CS steel	1	473	4.77	2 258
CO_2 compressor 1st stage	4.02			CS steel	1	3 071	3.29	10 104
CO_2 water removal adsorber				CS steel	1	1 174	3.94	4 624
Sum								**23 900**

Table A. 9. Characteristic parameters and costs of the bag filter.

Component	**Power / duty (MW)**	**Area (m^2)**	**Volume (m^3)**	**Material**	**No of**	**Equipment cost kEUR (2018)**	**Installation factor**	**Installed cost kEUR (2018)**
Bag filter				CS steel/ textile fabric	1	3 308	3.20	10 585

FREE ENERGIES OF ACTIVATION FOR VISCOUS FLOW OF DIFFERENT AMINE MIXTURES IN POST COMBUSTION CO_2 CAPTURE

S.S. Karunarathne, D.A. Eimer, L.E. Øi*
Faculty of Natural Sciences and Maritime Sciences - University of South-Eastern Norway, Norway

* Corresponding author e-mail: lars.oi@usn.no

Abstract

The viscosity of ternary mixtures of N-methyldiethanol amine (MDEA) + monoethanol amine (MEA) + H_2O, N-methyldiethanol amine (MDEA) + diethanol amine (DEA) + H_2O and 2-amino-2-methyl-1-propanol (AMP) + diethanol amine (DEA) + H_2O were correlated using Eyring's viscosity model based on absolute rate theory. The correlations were capable of representing viscosity data within AARD 1.9%, 1.4% and 2.1% for the mixtures MDEA + MEA + H_2O, MDEA + DEA + H_2O and AMP + DEA + H_2O respectively. These accuracies are acceptable in engineering calculations. The excess properties of volume V^E, viscosity η^E and free energy of activation for viscous flow ΔG^{E*} were studied to understand the intermolecular interactions in the mixtures. The study shows that all mixtures have a negative sign for V^E, η^E and a positive sign for ΔG^{E*}. This indicates weak intermolecular interactions in mixtures compared to the pure liquids and strong molecular attractions like H-bonds in the mixtures.

Keywords: *Viscosity, Excess free activation energy, Eyring's viscosity model, Amines*

1. Introduction

The applicability of different amine mixtures to capture CO_2 in a post-combustion absorption and desorption process has gained interest during past years. The combined effect of higher equilibrium capacities of tertiary and sterically hindered amines with the fast reaction rates of primary and secondary amines make this technology more feasible for large scale implementations. MEA (monoethanol amine) is regarded as the benchmark solvent in Post Combustion Capture (PCC) as it shows high CO_2 absorption rate, is relatively cheap and is less harmful to the environment compared to other commercial amines in PCC [1]. The main disadvantage of MEA is the high energy demand for regeneration and that limits the use of MEA + H_2O mixture as a solvent. DEA (diethanol amine) is a secondary amine that exhibits high absorption rate [2]. The irreversible side reactions and the formation of corrosive products are the disadvantages of using DEA. A tertiary amine like MDEA (N-methyldiethanol amine) has a relatively low absorption rate and high absorption capacity compared to MEA. The reaction between MDEA and CO_2 has a low heat of reaction and reduces the energy penalty of the amine regeneration. AMP (2-amino-2-methyl-1-propanol) is a sterically hindered primary amine that has both acceptable absorption capacity, absorption rate and regeneration energy demand, which is suitable for PCC.

Some studies of blends of aqueous alkanolamines as solvents in acid gas treating have been reported in the literature. As the studies reveal, those blends can enhance the physicochemical properties compared to amine and water mixtures with one amine [3,4]. There, the primary or secondary amine is mixed with a tertiary amine and water. Primary and secondary amines enhance the absorption rate while tertiary amines increase the absorption capacity and reduce the regeneration energy.

Densities and viscosities are important for the design of process equipment due to the influence on flow behavior, typically in pumps and pipes. Densities and viscosities are also influencing the heat and mass transfer performance in heat exchangers, absorbers and stripper units. Especially the density and viscosity appear in correlations for estimating heat and mass transfer coefficients and interfacial areas in random and structured packings. Reduction of the uncertainty in estimation methods for the density and viscosity in mixtures will improve design methods considerably. Several studies have been reported in the literature regarding density and viscosity measurements for the mixtures of (MEA + MDEA + H_2O), (DEA + MDEA + H_2O) and (DEA + AMP + H_2O) under different amine concentrations and temperatures [5].

In this study, the Eyring's [6] absolute rate theory approach on dynamic viscosity of Newtonian fluids was considered to evaluate the free energy of activation for viscous flow of different amine solutions based on available density and viscosity data that have been published by Mandal *et al.* [5]. The excess volume and the excess viscosity were determined to analyze the intermolecular attractions of the mixtures.

2. Methodology

The excess free energies of activation were calculated and correlated according to a Redlich-Kister [7] type polynomial. Eyring's viscosity model for Newtonian fluids is given in Eq (1).

$$\eta = \frac{hN}{V} exp\left(\frac{\Delta G^*}{RT}\right) \quad (1)$$

Where, $\eta, V, \Delta G^*$, h, N, R and T are dynamic viscosity, molar volume, free energy of activation for viscous flow, Planck's constant, Avogadro's number, gas constant and temperature respectively. In order to compare with ideal solutions and calculate the excess activation energy properties following Eq (2) and (3) are obtained by using Eq (1).

$$ln(\eta V) = ln(\eta V)_{ideal} + \frac{\Delta G^{E*}}{RT} \quad (2)$$

$$ln(\eta V) = \sum_i x_i ln(\eta_i V_i^o) + \frac{\Delta G^{E*}}{RT} \quad (3)$$

The excess free energy of activation for viscous flow ΔG^{E*} was determined from the density and viscosity data reported by Mandal *et al*. [5] as shown in Eq (3). A Redlich-Kister type polynomial with temperature dependency as given in Eq (5) and Eq (6) is proposed to correlate ΔG^{E*} of the amine mixtures according to the Eq (4). Here η_i and V_i^o are viscosity and molar volume of the pure liquids.

$$\frac{\Delta G^{E*}}{RT} = \Delta G_{12}^{E*} + \Delta G_{13}^{E*} + \Delta G_{23}^{E*} \quad (4)$$

$$\Delta G_{jk}^{E*} = x_j x_k \sum_{i=0}^{n} A_i (x_j - x_k)^i \quad (5)$$

$$A_i = a + b(T) + c(T)^2 \quad (6)$$

There are several ways to determine ideal viscosity contribution in a mixture [8-10]. The excess viscosity η^E as given in Eq (7) provides a quantitative approach to determine the deviation of the viscosity of a real mixture from its ideal conditions. The sign of η^E signifies the molecular interactions between unlike molecules in the mixture [11]. The molecular interaction between molecules in the mixture has a significant effect on viscosity. Heric and Brewer [12] explained, $\Delta G^{E*} > 0$ for a mixture that exhibits higher viscosities in the real mixtures than that of the ideal mixture.

$$\eta^E = \eta - \sum_{i=1}^{n} x_i \eta_i \quad (7)$$

A positive sign of η^E indicates that the mixture exhibits strong intermolecular interaction and negative sign specify weak interaction among the unlike molecules [13]. Intermolecular interaction is not the only aspect that influences the viscosity deviation of liquid mixtures [14, 15]. The excess molar volume of mixtures also can reveal intermolecular attractions in a liquid mixture [16]. The excess molar volume V^E represent the molar volume variation of a real mixture compared to its ideal condition. Three characteristics have been discussed in the literature that contribute to determining the sign of V^E. The mixtures having specific or chemical interactions including charge transfer, forming of H-bonds and other complex forming interactions provide a negative contribution for V^E. The molecules with different shape and size can rearrange within vacant spaces by giving a negative contribution to V^E [17].

$$V^E = V - \sum_{i=1}^{n} x_i V_i \quad (8)$$

The V^E gets a positive contribution where the mixtures have interactions owing to the dispersion forces or weak dipole-dipole interaction.

The Eyring's viscosity model enables to analyze viscosity data from a thermodynamic point of view to extract further information about liquid mixtures. Meyer *et al.* [18] reported the possibilities of using ΔG^{E*} to examine molecular interactions as the viscosity deviation. A positive deviation ΔG^{E*} signifies strong specific interactions between unlike molecules and classifiable as dispersion forces show negative deviation as suggested by authors in the references [18, 19]. All these parameters of ΔG^{E*}, η^E and V^E help to understand the nature of molecular interactions, size and shape of the molecules. Further, they are useful to correlate measured density and viscosity data of liquid mixtures.

3. Results and Discussion

The proposed correlation able to predict excess free energy of activation for viscous flow of the amine mixture with below 2% average absolute relative deviation (AARD %) for all mixtures. Table 1-3 give the calculated parameters of the correlation given in Eq 4-6 for the mixtures. Viscosity predictions were compared with measured data. Figure 1 shows the comparison between measured and correlated data for MDEA + MEA + H_2O mixtures. The correlation was able to fit the data within AARD 1.9% and maximum deviation (AMD) of 0.1 mPa·s.

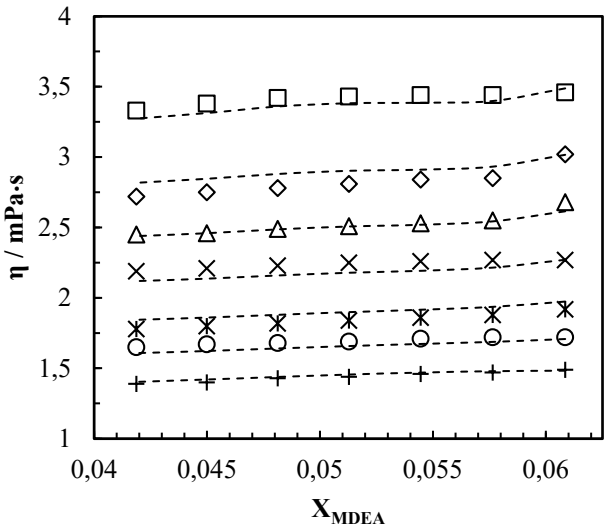

Figure 1: Viscosity variation of MDEA + MEA + H_2O mixtures with MDEA mole fraction and temperature: Experimental data from ref [5]; 293.15 K, '□'; 298.15 K, '◇'; 303.15 K, '△'; 308.15 K, 'x'; 313.15 K, 'ж'; 318.15 K, '○'; 323.15 K, '+'. The dotted lines represent the correlation in this work.

A comparison between measured and correlated viscosities was performed for the MDEA + DEA + H_2O mixtures as shown in Figure 2. It was found that the AARD and AMD for this mixture were 1.4% and 0.14 mPa·s respectively. Figure 3 illustrates the measured data with correlation for AMP + DEA + H_2O mixtures in which AARD and AMD were determined as 2.1% and 0.15 mPa·s respectively. The parameters of the correlation for the mixtures are given in Table 1 and the

accuracies of the data fit are acceptable for engineering calculations.

A qualitative analysis was performed to investigate the intermolecular attractions in the mixtures. The summary of the excess properties of the amine mixtures is given in Table 4. The η^E was calculated as shown in the Eq (7). The calculated η^E is negative for all mixtures at considered concentrations and temperatures. It emphasizes weak intermolecular interactions between the unlike molecules compared to pure liquids. The pure MDEA, DEA and AMP are able to form strong H-bonds due to the presence of O-H in the molecule [20]. MDEA and DEA have two O-H groups while AMP has only one to contribute for H-bonds. During the mixing of amines with water, the breaking of H-bonds may result in a negative sign in η^E. The temperature has an effect of η^E in such a way that η^Ebecomes less negative with the increase of temperature. The strength of molecular interactions may get weaker due to the increase of thermal energy of the molecules.

Table 1: Binary parameters A_o, A_1 and A_2 of the equation $\Delta G_{jk}^{E*} = x_j x_k \sum_{i=0}^{n} A_i (x_j - x_k)^i$ for the excess free energy of activation for viscous flow for MDEA + MEA + H_2O

Parameter		Binary pair		
		MDEA + MEA	MEA + H_2O	MDEA + H_2O
A_0	a	5.3631 x 10^4	1.7589 x 10^4	-7.2961 x 10^3
	b	-1.6978 x 10^2	1.0270 x 10^1	9.8700
	c	2.1304 x10^{-1}	1.5794 x 10^{-1}	3.4820 x10^{-1}
A_1	a	1.1958 x 10^5	2.5656 x 10^4	-3.979 x 10^3
	b	8.4487 x 10^2	-1.4979 x 10^1	1.9979 x 10^1
	c	-4.6806	5.9708 x 10^{-1}	6.3296 x 10^{-1}
A_2	a	1.3708 x 10^6	3.4239 x 10^3	4.6638 x 10^3
	b	-1.8188 x 10^4	-2.0450 x 10^1	1.1958 x 10^1
	c	4.2780 x 10^1	4.6224 x 10^{-1}	2.6581 x 10^{-1}

Table 2: Binary parameters A_o, A_1 and A_2 of the equation $\Delta G_{jk}^{E*} = x_j x_k \sum_{i=0}^{n} A_i (x_j - x_k)^i$ for the excess free energy of activation for viscous flow for MDEA + DEA + H_2O

Parameter		Binary pair		
		MDEA + DEA	DEA + H_2O	MDEA + H_2O
A_0	a	1.0027 x 10^8	4.1277 x 10^7	-5.0908 x 10^6
	b	3.1414 x 10^5	1.1918 x 10^5	-1.7794 x10^4
	c	9.5620 x10^2	3.7002 x 10^2	-6.3678 x 10^1
A_1	a	4.3279 x 10^7	4.5805 x 10^6	-2.5435 x 10^5
	b	1.3742 x 10^5	-1.1254 x 10^4	5.5912 x 10^2
	c	4.7546 x 10^2	-3.3341 x 10^1	-3.5906 x 10^{-3}
A_2	a	1.4787 x 10^7	-5.0089 x 10^7	6.3095 x 10^6
	b	-4.8893 x10^4	-1.7303 x10^5	2.3706 x10^4
	c	4.8911 x 10^1	-5.3515 x 10^2	8.2541 x 10^1

Table 3: Binary parameters A_o, A_1 and A_2 of the equation $\Delta G_{jk}^{E*} = x_j x_k \sum_{i=0}^{n} A_i (x_j - x_k)^i$ for the excess free energy of activation for viscous flow for AMP + DEA + H_2O

Parameter		Binary pair		
		AMP + DEA	DEA + H_2O	AMP + H_2O
A_0	a	1.1157 x 10^4	2.7551 x 10^3	1.5131 x 10^3
	b	8.4643 x 10^1	2.0589 x 10^1	2.3656
	c	-9.8481 x 10^{-1}	5.2882 x 10^{-1}	-1.0803 x 10^{-1}
A_1	a	-3.0081 x 10^5	7.6788 x 10^3	4.2936 x 10^2
	b	1.0653 x 10^3	-1.7424 x 10^1	5.1912
	c	2.0884 x 10^{-1}	1.1355	3.6564 x 10^{-1}
A_2	a	4.4827 x 10^6	4.7115 x 10^3	-1.5476 x 10^3
	b	-2.5146 x 10^4	-4.9228 x 10^1	2.6677
	c	3.3641 x 10^1	6.1636 x 10^{-1}	5.8774 x 10^{-1}

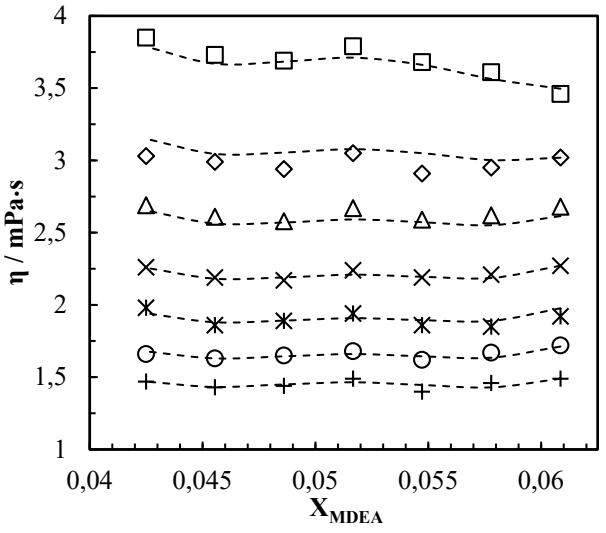

Figure 2. Viscosity variation of MDEA + DEA + H_2O mixtures with MDEA mole fraction and temperature: Experimental data from ref [5]; 293.15 K, '□'; 298.15 K, '◇'; 303.15 K, '△'; 308.15 K, 'x'; 313.15 K, 'ж'; 318.15 K, '○'; 323.15 K, '+'. The dotted lines represent the correlation in this work.

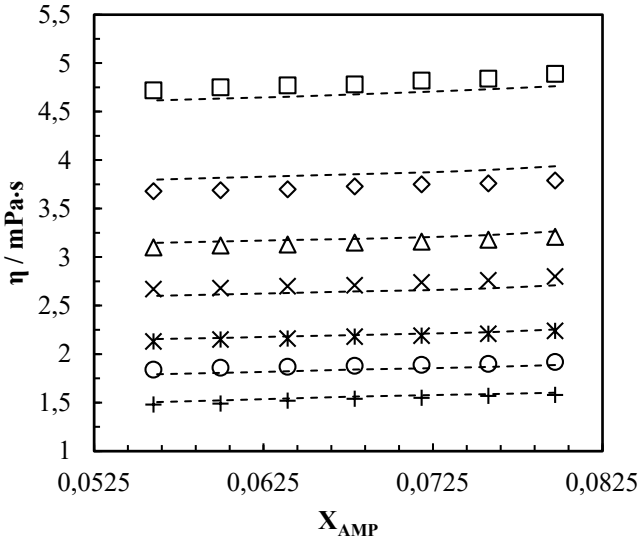

Figure 3. Viscosity variation of AMP + DEA + H_2O mixtures with AMP mole fraction and temperature: Experimental data from ref [5]; 293.15 K, '□'; 298.15 K, '◇'; 303.15 K, '△'; 308.15 K, 'x'; 313.15 K, 'ж'; 318.15 K, '○'; 323.15 K, '+'. The dotted lines represent the correlation in this work.

As shown by Kauzmann and Eyring [21], the viscosity of a mixture highly depends on the entropy of the mixture that is related to the molecular structure, interaction between molecules and enthalpy of the mixture [22, 23]. The negative deviation of V^E for all mixtures in their different compositions and temperatures indicates strong intermolecular interactions among the unlike molecules. Further, V^E gets a negative contribution by arranging molecules within vacant spaces in each other's structure due to the different size and shape of the molecules. This also affects the viscosity of a mixture as intermolecular interactions.

As shown in Figure 4, the calculated ΔG^{E*} from Eyring's viscosity representation is positive for the considered mixture compositions and temperatures indicating that the mixtures have strong intermolecular interactions. This is supported by excess volume property giving a negative sign for V^E. The formation of new H-bond between unlike molecules can result in a positive deviation in ΔG^{E*}. MEA has the potential to form H-bonds with other amines and H_2O due to the presence of hydroxyl and amino functional groups. For (MDEA + MEA + H_2O) mixtures at 293.15 K, highest excess activation energy is shown at the mixture composition of 30 mass% MDEA + 0 mass% MEA + 70 mass% H_2O mixture and it gradually decreased with the decrease of MDEA and increase of MEA concentrations under constant weight percent of H_2O. The decrease of ΔG^{E*} with the increase of MEA mole fraction shows that intermolecular attractions have been weakened by MEA.

Table 4: Excess properties of ΔG^{E*}, η^E and V^E of the amine mixtures.

Mixture	ΔG^{E*}	η^E	V^E
MDEA + MEA + H_2O	> 0	< 0	< 0
MDEA + DEA + H_2O	> 0	< 0	< 0
AMP + DEA + H_2O	> 0	< 0	< 0

For the AMP + DEA + H_2O mixtures at 293.15 K, highest excess free activation energy is observed at the mixture composition of 30 mass% AMP + 0 mass% DEA + 70 mass% H_2O mixture. The increase of DEA mole fraction decreases the ΔG^{E*} indicating weak intermolecular interactions compared to the mixture of 30 mass% AMP + 0 mass% DEA + 70 mass% H_2O.

The excess free energy of activation for viscous flow of MDEA + DEA + H_2O mixtures shows a peak at the mixture composition of 25.5 mass% MDEA + 4.5 mass% DEA + 70 mass% H_2O at 293.15 K. This indicates that the intermolecular interactions are stronger at that particular composition than the other amine composition at 293.15 K.

The free energy of activation for viscous flow was determined by using Eq (1). Figure 5 illustrates the variation of ΔG^* with amine mole fraction of the mixtures at 293.15 K. The AMP + DEA + H_2O mixtures show the highest free energy among the considered mixtures while MDEA + MEA + H_2O has the lowest free energy.

The increase in temperature decreases both ΔG^{E*} and ΔG^*. Figure 6 shows the influence of temperature on ΔG^* for the mixtures with 24 mass% AMINE (1) + 6 mass% AMINE (2) + 70 mass% H_2O. The increase in molecular energy has weakened the strength of H-bonds and has enhanced the movements of the molecules. The decrease in ΔG^{E*} indicates that solution characteristics change toward the ideal conditions with the increase of temperature.

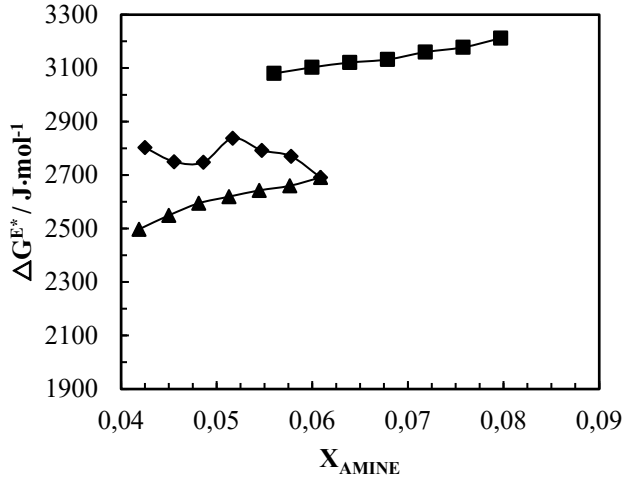

Figure 4. Variation of ΔG^{E*} with amine mole fractions at temperature of 293.15 K. X_{AMP} in AMP + DEA + H_2O '■'; X_{MDEA} in MDEA + DEA + H_2O '◆'; X_{MDEA} in MDEA + MEA + H_2O '▲'.

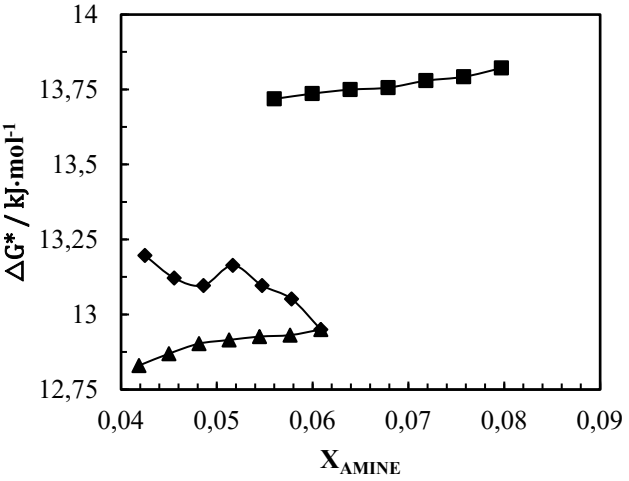

Figure 5. Variation of ΔG^{*} with amine mole fractions at temperature of 293.15 K. X_{AMP} in AMP + DEA + H_2O '■'; X_{MDEA} in MDEA + DEA + H_2O '◆'; X_{MDEA} in MDEA + MEA + H_2O '▲'.

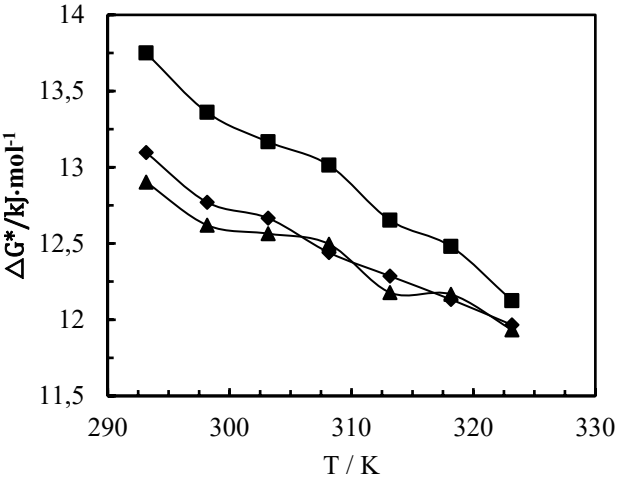

Figure 6. Variation of ΔG^{*} with temperature. AMP + DEA + H_2O '■'; MDEA + DEA + H_2O '◆'; MDEA + MEA + H_2O '▲'.

This study analyzed the density and viscosity of amine and water ternary mixtures to understand the molecular interactions. The correlation represents the viscosity data of ternary amines and water mixtures with acceptable accuracy to use them in engineering calculations. Further, the correlations can be improved to fit viscosities of CO_2 loaded amine and water mixtures as they are important in post-combustion amine based CO_2 capture.

4. Conclusions

Three aqueous amine mixtures of MDEA + MEA + H_2O, MDEA + DEA + H_2O and AMP + DEA + H_2O were analyzed based on viscosity and density data in the literature for their free energy of activation for viscous flow. The excess free energy was evaluated and correlated by a Redlich-Kister polynomial to fit the viscosity data. The proposed correlations were able to correlate the ΔG^{E*} within 2% AARD.

The same correlation was able to represent viscosities of MDEA + MEA + H_2O mixtures within AARD 1.9% and AMD of 0.1 mPa·s. For the MDEA + DEA + H_2O mixtures the viscosity data were fitted within AARD 1.4% and AMD 0.14 mPa·s. And for the AMP + DEA + H_2O mixtures that are of AARD 2.1% and 0.15 mPa·s. These accuracies are acceptable in engineering calculations.

The excess properties of molar volume, viscosity and free energy of activation for viscous flow show the presence of strong intermolecular interactions in all mixtures. The negative and positive signs for excess volume and excess free energy of activation for viscous flow indicate the presence of H-bonds between unlike molecules while negative signs of excess viscosity predict weak intermolecular interactions compared to the ideal mixture condition. This may occur due to the breaking of H-bond during the mixing. The mixtures exhibit $\Delta G^{E*}_{AMP+DEA+H_2O} > \Delta G^{E*}_{MDEA+DEA+H_2O} > \Delta G^{E*}_{MDEA+MEA+H_2O}$ for the considered amine concentrations. Accordingly, AMP + DEA + H_2O mixtures possess the highest intermolecular interactions among the unlike molecules and MDEA + MEA + H_2O mixtures indicate the lowest.

References

[1] Øi, L.E. Removal of CO_2 from exhaust gas, in Faculty of Technology. 2012, Telemark University College: Porsgrunn, Norway.

[2] Dawodu, O.F., & Meisen, A. Solubility of carbon dioxide in aqueous mixtures of alkanolamines. J. Chem. Eng. Data, 1994. 39: p. 548-552.

[3] Li, M. H., & Lai, M. D. Solubility and Diffusivity of N_2O and CO_2 in (Monoethanolamine + N-Methyldiethanolamine + water) and in (Monoethanolamine + 2-Amino-2-methyl-1-propanol+water), J. Chem. Eng. Data, 1995. 40: pp. 486-492.

[4] Glasscock, D. A., Critchfield, J.E., & Rochelle, G. T. CO_2 absorption/desorption in mixtures of methyldiethanolamine with monoethanolamine or diethanolamine. Chemical Engineering Science, 1991. 56: pp. 2829-2845.

[5] Mandal, B.P., Kundu, M., & Bandyopadhyay, S.S. Density and viscosity of aqueous solution of (N-Methyldiethanolamine + Monoethanolamine), (N-Methyldiethanolamine + Diethanolamine), (2-Amino-2-methyl-1-propanol + Monoethanolamine), and (2-Amino-

2-methyl-1-propanol + Diethanolamine). J. Chem. Eng. Data, 2003. 48: p. 703-707.

[6] Eyring, H. Viscosity, Plasticity, and Diffusion as example of absolute reaction rates. Journal of chemical physics, 1936. 4: p. 283-291.

[7] Redlich, O., & Kister, A.T. Algebraic representation of thermodynamic properties and the classification of solutions. Ind. Eng. Chem., 1948. 40(2): p. 345-348.

[8] Kendall, J., & Monroe, P. The viscosity of liquids. II. The viscosity-composition curve for ideal liquid mixtures. J. Am. Chem. Soc, 1917. 39: p. 1787-1802.

[9] Bingham, E.C. Fluidity and plasticity 1922, New York: McGraw-Hill.

[10] Cronauer, D.C., Rothfus, R.R., & Kernmore, R.I. Viscosity and density of the ternary liquid system acetone-benzene-ethylene dichloride J. Chem. Eng. Data, 1965. 10: p. 131-133.

[11] Fort, R.J., & Moore, W.R. Viscosities of binary liquid mixtures. Transactions of the faraday society, 1966. 62: p. 1112-1119.

[12] Heric, E.L., & Brewer, J.G. Viscosity of some binary liquid nonelectrolyte mixtures. J. Chem. Eng. Data, 1967. 12(04): p. 574-583.

[13] Bhatia, S.C., Bhatia, R., & Dubey, G.P. Studies on transport and thermodynamic properties of binary mixtures of octan-1-ol with chloroform, 1,2-dichloroethane and 1,1,2,2-tetrachloroethane at 298.15 and 308.15 K. Journal of Molecular Liquids, 2009. 144(3): p. 163-171.

[14] Ćwiklińska, A., & Kinart, C.M. Thermodynamic and physicochemical properties of binary mixtures of nitromethane with {2-methoxyethanol+2-butoxyethanol} systems at T=(293.15, 298.15, 303.15, 308.15, and 313.15)K. The Journal of Chemical Thermodynamics, 2011. 43(3): p. 420-429.

[15] Iloukhani, H., & Mohammadlou, Z.B. Densities, viscosities, and refractive indices for binary and ternary mixtures of formamide (1)+N,N-dimethylacetamide (2)+2-methyl-1-butanol (3) at 298.15K for the liquid region and at ambient pressure. Arabian Journal of Chemistry, 2016.

[16] Aminabhavi, T.M., Aralaguppi, M.I., Gopalakrishna, B., & Khinnavar, R.S. Densities, Shear Viscosities, Refractive Indices, and Speeds of Sound of Bis(2-methoxyethyl) Ether with Hexane, Heptane, Octane, and 2,2,4-Trimethylpentane in the Temperature Interval 298.15-318.15 K. Journal of Chemical & Engineering Data, 1994. 39(3): p. 522-528.

[17] Mahajan, A.R., & Mirgane, S.R. Excess molar volumes and viscosities for the binary mixtures of n-Octane, n-Decane, n-Dodecane, and n-Tetradecane with Octan-2-ol at 298.15 K. Journal of Thermodynamics, 2013: p. 1-11.

[18] Meyer, R., Meyer, M., Metzger, J., & Peneloux, A. Thermodynamic and physicochemical properties of binary solvent Journal de Chimie Physique et de Physico-Chimie Biologique, 1971. 68: p. 406-412.

[19] Oswal, S. & Rathnam, M.V. Viscosity data of binary mixtures: ethyl acetate + cyclohexane, + benzene, + toluene, + ethylbenzene + carbon tetrachloride, and + chloroform at 303.15 K. Canadian Journal of Chemistry, 1984. 62(12): p. 2851-2853.

[20] Abdollahi, F., Razmkhah, M., & Moosavi, F. The role of hydrogen bond interaction on molecular orientation of alkanolamines through temperature and pressure variation: A mixed molecular dynamics and quantum mechanics study. Computational Materials Science, 2017. 131: p. 239-249.

[21] Kauzmann, W., & Eyring, H. The Viscous Flow of Large Molecules. Journal of the American Chemical Society, 1940. 62(11): p. 3113-3125.

[22] Rafiee, H.R., Ranjbar, S., & Poursalman, F. Densities and viscosities of binary and ternary mixtures of cyclohexanone, 1,4-dioxane and isooctane from T=(288.15 to 313.15)K. The Journal of Chemical Thermodynamics, 2012. 54: p. 266-271.

[23] Ma, D., Liu, Q., Zhu, C., Feng, H., & Ma, Y. Volumetric and viscometric properties of ternary solution of (N-methyldiethanolamine + monoethanolamine + ethanol). The Journal of Chemical Thermodynamics, 2019. 134: p. 5-19.

ASPEN HYSYS AND ASPEN PLUS SIMULATIONS FOR AMINE BASED ABSORPTION PROCESS COMPARED TO RESULTS FROM EXPERIMENTS IN CO_2-RIG

S.S. Karunarathne, L.E. Øi*
Faculty of Natural Sciences and Maritime Sciences - University of South-Eastern Norway, Norway

* Corresponding author e-mail: lars.oi@usn.no

Abstract

In this study, equilibrium-based and rate-based simulations in Aspen HYSYS and Aspen Plus were performed to compare the removal efficiency and physical properties of density and viscosity in a CO_2 absorption column. The experimental results from our previous study were used for comparison. In the equilibrium-based simulations, removal efficiency at 40 kg/hr of solvent flow rate was fitted with simulation by adjusting the Murphree efficiency of 12% in all stages. Accordingly, the equilibrium-based performed for other considered flow rates by keeping adjusted constant Murphree efficiency for all the stages in the absorber column. The variations of physical properties like density and viscosity were simulated and compared with measured properties under three different liquid to gas (L/G) ratios. Performed rate-based simulations with default molar volume/density and viscosity models of Clarke model and Jones-Dole model respectively were able to predict the properties with acceptable accuracy, but a deviation of 25% between measured and simulated viscosities for the lean MEA mixture was observed.

Keywords: *Equilibrium-based, Rate-based, CO_2 capture, MEA*

1. Introduction

Process simulation provides the ability to understand the process behavior under various process conditions and help to identify optimum conditions. The process of post-combustion carbon dioxide (CO_2) capture through amine based absorption process has been evaluated in various ways through mathematical modelling and simulations to identify the key factors in order to optimize the configuration and efficiency of the process [1-4].

Aspen HYSYS and Aspen Plus are two process simulation packages that are widely used in the industry for steady state process simulations and calculations of equilibrium data for various gas liquid mixtures. Two approaches of equilibrium-based and rate-based modelling are facilitated for simulation of the amine-based post-combustion CO_2 capture process. For equilibrium-based modelling, an amine package with Kent-Eisenberg [5] and Li-Mather [6] equilibrium models is available in Aspen HYSYS. The equilibrium-based column model can be refined using a Murphree efficiency on each stage. For rate-based modelling, the Electrolyte-NRTL equilibrium that is based on Austgen *et al.* [7] model is adopted to model the vapour-liquid equilibrium of the reacting system in Aspen Plus. The column can be modelled based on both equilibrium stages with Murphree efficiencies and rate-based approaches.

In literature, studies related to process simulations using Aspen HYSYS and Aspen Plus are widely available for amine based post-combustion CO_2 capture. An Aspen Plus model was developed by Lim et al. [8] and performed a validation against a pilot plant operated at Boryeong, South Korea. There was a good agreement for the estimation of CO_2 loading, heat duty and temperature in the stripper between developed model and pilot plant results. Plaza et al. [9] worked with absorber and stripper models in Aspen Plus in which a thermodynamic model proposed by Hilliard [10] was used for modeling CO_2 removal from aqueous MEA (monoethanol amine). Zhang and Chen [11] also performed validation of a rate-based MEA model in Aspen Plus with a pilot plant. The study extended from simulation model for CO_2 absorption with MEA to both absorption and desorption process and was validated against recently published pilot plant data. For Aspen HYSYS simulation, different absorption and desorption configurations were investigated using an equilibrium-stage model in Aspen HYSYS for natural gas based pilot plants [12]. A comparison between equilibrium-based model in Aspen HYSYS and rate-based model in Aspen Plus was performed by Øi [1] for the CO_2 absorption into MEA from atmospheric gas. Results show that it is difficult to conclude which model gives more accurate predictions. According to Zhang and Chen [11], a rate-based model is capable of predicting the overall performance of the CO_2 capture system excellently.

In this work, CO_2 absorption into MEA was studied using the two simulation packages Aspen HYSYS (equilibrium-based model) and Aspen Plus (equilibrium and rate- based models). Series of laboratory experiments have been performed in an experimental CO_2-rig located at the University of South-Eastern Norway [13]. The experiments were done to investigate the CO_2 removal efficiency under different inlet CO_2 concentrations and solvent flow rates. The measured physical properties of density and viscosity at the absorber top for lean MEA and the bottom for rich MEA were compared with rate-based simulations from Aspen Plus.

2. Murphree efficiency based and rate – based simulation

2.1 Murphree efficiency

In distillation and absorption, the tray efficiency is described in several ways [14]. The point efficiency is defined as the ratio of change of composition at a point to the change of composition that would occur on a theoretical stage. Instead of a single point, Murphree efficiency is defined for the entire tray as given in Eq (1).

$$E_M = \frac{(y_n - y_{n-1})}{(y_n^* - y_{n-1})} \quad (1)$$

Where, y_n^* is the composition of vapour in equilibrium with the liquid leaving the tray, y_n is the actual composition of vapour leaving the tray.

The overall column efficiency E_o is given as

$$E_o = \frac{number\ of\ ideal\ stages}{number\ of\ real\ stages} \quad (2)$$

And these two efficiencies can be related as

$$E_o = \frac{ln\left[1+E_M\left(\frac{mV}{L}-1\right)\right]}{ln\left(\frac{mV}{L}\right)} \quad (3)$$

Where, m is the slope of the equilibrium line, V and L are molar flow rates of the vapour and liquid respectively.

For a packed column, Murphree efficiency of a tray is applicable for a packing section with a certain height.

2.2 Rate-based model

The rate-based approach considers the mass and heat transfer and chemical kinetics as the governing phenomena in the separation process. The driving force for the mass transfer is directly proportional to the deviation from the equilibrium between gas and liquid and is proportional to the contact area between the two phases [15]. The reaction model for MEA + CO_2 + H_2O is given in reactions R1 to R5 as described by the Austgen *et al.* [7] for primary and secondary amines.

Ionization of water

$$2H_2O \leftrightarrow H_3O^+ + OH^- \quad (R1)$$

Dissociation of carbon dioxide

$$2H_2O + CO_2 \leftrightarrow H_3O^+ + HCO_3^- \quad (R2)$$

Dissociation of bicarbonate

$$H_2O + HCO_3^- \leftrightarrow H_3O^+ + CO_3^{2-} \quad (R3)$$

Dissociation of protonated MEA

$$H_2O + MEAH^+ \leftrightarrow H_3O^+ + MEA \quad (R4)$$

Carbamate reversion to bicarbonate

$$MEACOO^- + H_2O \leftrightarrow MEA + HCO_3^- \quad (R5)$$

3. Methodology

3.1 Pilot plant and process description

An amine-based laboratory CO_2-rig located at the University of South-Eastern Norway is shown in Figure 1. The process is consisting of absorption and desorption columns for chemical absorption and stripping of CO_2. Feed with air and CO_2 pass through the absorber countercurrently with aqueous MEA and the structured packing enhances the mass transfer between CO_2 and absorbent. The absorber column is filled with Sulzer 250Y packing to build a packing section with 1500 mm height. Detailed information about the laboratory CO_2-rig can be found in a previous publication with a piping and instrumentation diagram (P&ID) [13].

Figure 1: Amine based CO_2 capture pilot plant at USN

3.2 Experiments

3.2.1 CO_2 rig experiments

A controlled flow of CO_2 with purity 99.5% from AGA Norge AS was mixed with constant air supply to achieve 5% and 10% CO_2 concentration (mol%) in the gas feed. The solvent flow rate was adjusted from 10 kg/hr to 100 kg/hr with 10 kg/hr increments. Finally, the CO_2 concentration of the treated gas was measured to determine the CO_2 removal efficiency. All the gas analysis were performed by an NDIR (Non-Dispersive InfraRed) instrument from ADC.

For the study of physical property variations of the absorber column, experiments that were performed in our previous work [16] were used for the simulations. There, three different liquid flows were considered. Samples were taken from liquid streams at the top and the bottom of the absorber and the temperatures were recorded in each case. Density and viscosity of collected samples were measured in the laboratory.

3.2.2 Density measurements

Density measurements of the liquid MEA + H_2O + CO_2 mixtures were performed using a DMA 4500 density meter from Anton Paar. A liquid volume of 5 ml approximately was injected into the U-tube of the density meter using a syringe. The temperature was set as it was recorded at the sampling point. The measurements were

repeated three times to verify the repeatability of the measurements and the average was taken as the final reading. A density check was performed with degassed water frequently to verify the validity of the previous calibration at 293.15 K.

3.2.3 Viscosity measurements

Viscosity measurements of the MEA + H_2O + CO_2 mixtures were carried out using a Physica MCR 101 rheometer from Anton Paar. A double-gap measuring system was adopted, as it was suitable for low viscous fluids. The calibration of the rheometer was performed using a standard calibration fluid S3S from Paragon Scientific Ltd. The viscosities of the calibration fluid measured were compared with the standard given by the supplier. The deviations of the measurements were noted at different temperatures and viscosities of the MEA + H_2O + CO_2 mixtures and corrected accordingly.

3.3 Simulations

The equilibrium-based simulations were carried out in Aspen HYSYS V10 environment. The amine package with Kent-Eisenberg [5] model was used to perform relevant calculations in the vapour and liquid phases. An absorber with four stages with defined Murphree efficiencies in each stage simulated the CO_2 removal efficiencies under different flow conditions.

In Aspen Plus rate-based simulations, an absorber column developed from RadFrac absorber model was used for the simulations. The property method of Electrolyte-non-random two-liquid (ELECNRTL) was selected as the mixture behaves as an electrolyte. All the simulations were performed under open-loop conditions.

For the physical properties, it is possible to regress experimental density and viscosity results of MEA + H_2O + CO_2 from Weiland *et al.* [17] or Hartono *et al.* [18] to estimate relevant model parameters in Aspen Plus. The Clarke model, called VAQCLK in Aspen Plus for liquid molar volume is available with regressed model parameters. The model calculates liquid molar volume of aqueous electrolytes solutions using Amagat's law as given in Eq (4) and the relationship between partial molar volume of an electrolyte and its mole fraction in the solvent as given in Eq (5) [19].

$$V_m^l = \sum_i x_i V_i \tag{4}$$

Where, V_m^l, x_i and V_i are molar volume of the mixture, mole fraction and the molar volume of component respectively.

$$V_{ca} = V_{ca}^{\infty} + A_{ca}\frac{\sqrt{x_{ca}}}{1+\sqrt{x_{ca}}} \tag{5}$$

Where, $V_{ca}$is the partial molar volume of electrolytes, $x_{ca}$is the apparent electrolyte mole fraction and V_{ca}^{∞}, A_{ca} are regression parameters.

The option code 1 represents the quadratic mixing rule for solvent in which the interaction parameter VLQKIJ for MEA and H_2O can be regressed against MEA + H_2O density data from Kapadi *et al.* [20] and Han *et al.* [21]. The Clarke model parameters V_{ca}^{∞} named as VLCLK/1 can also be regressed for the main electrolyte ($MEAH^+$, HCO_3^-), ($MEAH^+$, $MEACOO^-$) and ($MEAH^+$, CO_3^{2-}) against experimental MEA + H_2O + CO_2 density data. The Jones-Dole electrolyte correction model, referred as MUL2JONS in Aspen Plus can be adopted to model the liquid viscosities in a MEA + H_2O + CO_2 mixture. Due to the presence electrolytes, model calculates the correction to the liquid mixture viscosity of a solvent mixture. The Jones-Dole electrolyte correction model is given as follows [19],

$$\eta = \eta_{solv}(1 + \sum_{ca} \Delta\eta_{ca}) \tag{6}$$

Where, η, η_{solv} and $\Delta\eta_{ca}$ are viscosity of the liquid mixture, viscosity of the liquid mixture calculated by the Andrade/DIPPR model and contribution to the viscosity correction due to apparent electrolyte *ca* from cation *c* and anion *a* respectively.

The interaction parameters between MEA and H_2O in the Aspen liquid mixture model, MUKIJ and MULIJ, can be regressed against experimental MEA + H_2O viscosity data. Further, the Jones-Dole model parameters in $\Delta\eta_{ca}$, IONMUB, for $MEAH^+$ and $MEACOO^-$ are possible to regress against MEA + H_2O + CO_2 viscosity data [22]. The data regression to estimate parameters is beyond the scope of this study, and density and viscosity predictions were obtained using default parameter values in Aspen Plus.

The experimental input data for the physical property simulations are given in Table 1 and Table 2. The Aspen Plus simulations were performed in the Aspen Plus V10 environment.

Table 1: Scenarios considered in CO_2-rig experiments

Case no	Air flow rate (Nm^3/hr)	Liquid flow rate (kg/hr)	CO_2 in feed (%)	$T_{Absorber,in}$ (°C)
Case 1	15	47.92	10.2	19.5
Case 2	15	106.56	9.9	25.7
Case 3	15	151.17	9.9	30.1

Table 2: Lean amine loading with corresponding (L/G) in mass basis

Case no	Liquid flow rate (kg/hr)	(L/G)	Lean MEA loading (mol CO_2 / mol MEA)
Case 1	47.92	2.3	0.213
Case 2	106.56	5.4	0.280
Case 3	151.17	7.8	0.279

4 Results

4.1 CO_2 removal efficiency

For the investigation of CO_2 removal efficiency, two case studies were performed by keeping inlet gas CO_2 concentration at 5% and 10% (mole basis) of total gas flow. Figure 2 illustrates the variation of CO_2 removal efficiency under different liquid flow rates from 10 kg/hr to 100 kg/hr, which is equivalent to a range of liquid to gas (L/G) ratio from 0.3 to 3 on a mass basis approximately.

As shown in Figure 2 the CO_2 removal efficiency increases with the increase of liquid flow rate. Under low flow rates, the driving force for the mass transfer is reduced as the aqueous amine solution reaches high CO_2 loadings rapidly. This is reversed under high flow rates as more liquid with high driving force increase the CO_2 removal efficiency. Further, the increase of amine flow enhances the gas/liquid interfacial area while passing through the structured packing. This effect also increases the mass transfer through the gas/liquid interface.

In the equilibrium-based model, the Murphree efficiency on each of four plates were fitted to 12% for 40 kg/hr to get equal CO_2 removal efficiency in simulation and experiment. At other liquid flows the Murphree efficiency were kept constant at 12%. The rate-based simulations in Aspen Plus were performed by adjusting the interfacial area factor (IAF) to 1.98 to achieve a similar removal efficiency at 40 kg/hr compared to experiment. The results for other flow rates were taken at the adjusted IAF of 1.98.

This high interface area factor indicates that the rate-based model does not describe the absorption mechanisms accurately. Because the IAF is expected to increase with increasing liquid flow, the liquid flow influence on removal efficiency with a constant IAF in Figure 2 is opposite of what was expected. In Table 3 the IAF shows a more reasonable dependence of increasing liquid flow. A possible factor that may also influence on the CO_2 removal efficiency is the temperature, which may vary in the measured data in Figure 2.

Table 3. IAF and CO_2 out (%) in treated gas

Case no	IAF	CO_2 out (%) in treated gas
Case 1	1.04	5.8
Case 2	1.37	4.8
Case 3	1.43	4.1

As shown in Figure 2, the equilibrium-based model with constant Murphree efficiency predicted removal efficiency closer to the experiments at low flow rates below 50 kg/hr. The deviation between measured and simulation increases at higher flow rates. For the rate-based model, predictions are closer to the experiment at higher flow rates and the deviations are greater at low flow rates.

Neither the equilibrium based nor the rate-based model give a good qualitative description of the CO_2 removal as a function of liquid flow. This was also the conclusion in comparisons of equilibrium-based and rate-based models with performance data at TCM Mongstad [4]. The accuracy in simulated CO_2 removal efficiencies shown in Figure 2 are however reasonable for both models.

In Aspen HYSYS simulations, the removal efficiency increased with liquid flow rate, until it reached 30 kg/hr. Subsequently, the removal efficiency became a steady value after 30 kg/hr of liquid flow rate. Similar behavior was observed for 10% inlet CO_2 concentration in which a steady removal efficiency of 33% after 60 kg/hr of liquid flow in the HYSYS simulation.

In case of using a rate-based model in Aspen Plus, the absorption efficiency will vary slightly with the liquid flow and the removal efficiency as a function of liquid flow will be expected to be simulated more accurately.

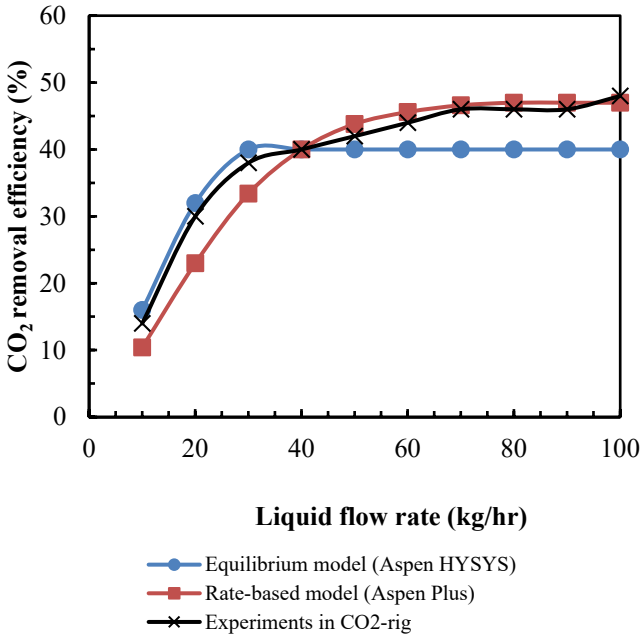

Figure 2: Comparison of CO_2 removal efficiency from experiments, equilibrium-based model and rate-based model

4.2 Physical property analysis

Density and viscosity of the lean and rich MEA solvent have been measured at three different liquid flow rates as shown in Table 1 [16] were used for the rate-based simulations in Aspen Plus. For each case, the interfacial area factor was adjusted to achieve the removal efficiency observed during the experiments. IAF was adjusted by trial and error until the relative deviation between measured and simulated CO_2 concentrations at the treated gas becomes < 1%. The simulated CO_2 concentration of the treated gas at absorber out and corresponding IAFs are given in Table 3.

Accordingly, the corresponding density and viscosity of the lean and rich amine stream were evaluated. Figure 3 compares the experimental results with the simulation of the density variations in the liquid stream at the top and bottom of the absorber. Absorption of CO_2 increases the CO_2 loading in the solvent. The experiments revealed that the density of the MEA + H_2O + CO_2 increased at the absorber bottom compared to the absorber top even though the temperature increases due to the exothermal reaction between MEA and CO_2. The simulations were able to predict this trend as shown in Figure 3. The maximum relative deviation of measured density from the simulation is 6%. The model called VAQCLK with option code 1 in the property set was adopted to simulate the measured densities.

Rate-based simulations for the density of liquid streams were able to predict the trend of density variation with the increase of liquid flow in the absorber. Further simulations follow the trend of increase of density in the rich amine solution compared to that of lean amine. The temperature obtained through the simulations for rich amine mixture deviates around 5% from the measured.

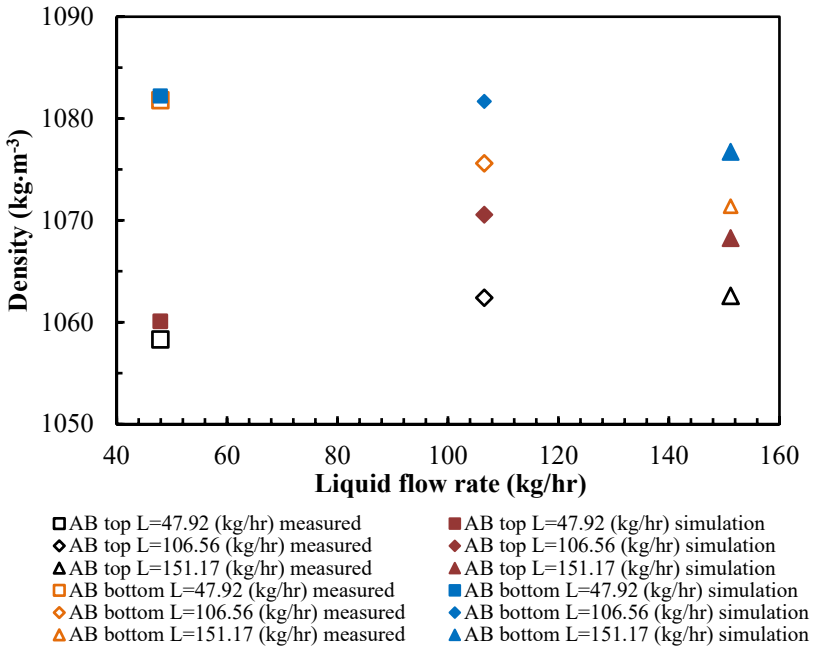

Figure 3: Comparison of the measured densities with the simulation

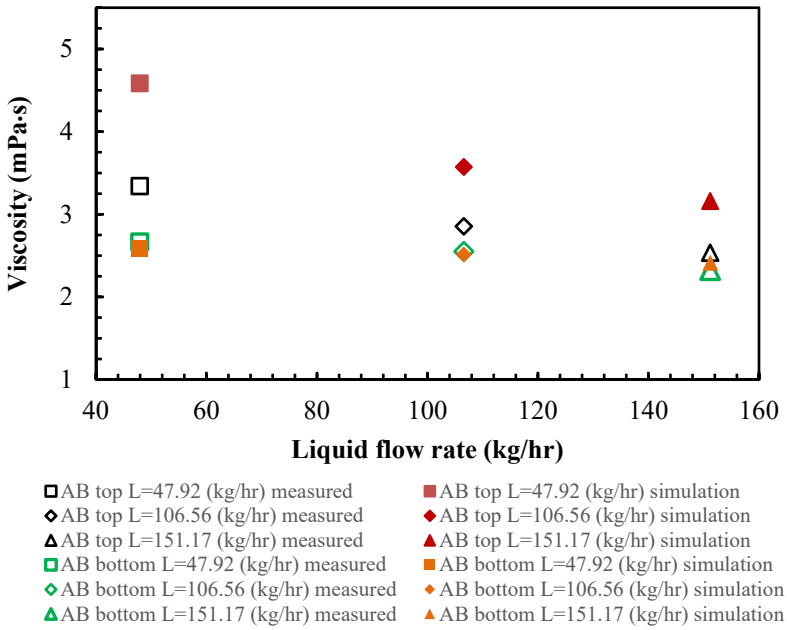

Figure 4: Comparison of the measured viscosities with the simulation

For the viscosity predictions based on rate-based simulations in Aspen Plus, Figure 4 illustrate the comparison between simulated viscosities and measured data at both lean and rich amine solutions. As shown by the experiments, viscosity at the lean MEA solution is higher than that of rich MEA. Generally, the increase of CO_2 in MEA + H_2O + CO_2 mixture increase the viscosity [17, 23], but the increase of temperature dominate to reduce the viscosity at rich MEA mixture.

Rate-based simulations were able to predict the trend of viscosity variation in the absorber column under different liquid flow rates. As described in Figure 4, simulated viscosities showed large deviations around 25% compared to that of measured at the lean MEA mixture. Lower deviations were reported for the viscosity of rich MEA mixture and it was around 4%. The measured viscosities agree with the viscosity data published for MEA + CO_2 + H_2O mixtures under different CO_2 loadings and temperatures [18]. A possible cause for such deviations can be that the property model parameters were not regressed against the actual measured data. The causes can be found by performing simulations after estimating the required parameters through a regression.

Several other viscosity models such as Andrade model (MUL2ANDR), TRAPP model (MUL2TRAP) and Eyring-NRTL model (EYRING) for liquid mixture viscosity were also examined and compared with measured viscosities. The predictions deviate highly compared to the Jones-Dole electrolyte viscosity model with a factor around 2. This indicates that the selection of property models needs to be selected carefully to acquire the best results.

4.3 Uncertainty of experiments and simulations

The experiments in the CO_2-rig involve different types of uncertainties. These uncertainties are related to inaccuracies of the measuring instruments and the process samplings. The extracted samples for the density and viscosity measurements should be representative of the system. The CO_2-rig in USN has performed several modifications in order to achieve theories of process sampling to improve the accuracy of the measurements. In earlier work [13], uncertainties have been evaluated. It has been problems with the consistency in the amount of absorbed CO_2 calculated from the gas and liquid side. The absorbed CO_2 amount calculated from the liquid side has been assumed to have the highest uncertainty due to the uncertainty in measured difference of CO_2 concentration between lean and rich amine. In this work, the CO_2 removal efficiency is calculated based on CO_2 concentrations in the gas in and out which are assumed to have reasonable accuracy.

In the simulations, equilibrium and physical property models have uncertainties due to the assumptions considered during the model developments. Our recent publication on uncertainty analysis of interfacial area and mass transfer coefficient models [24] revealed the propagation of uncertainty of physical properties through such models. Those uncertainties in physical properties can appear from the sampling to measuring device. Uncertainties in viscosity are expected to give more impact on design than uncertainties in density.

5 Conclusion

Simulations based on an equilibrium-based model in Aspen HYSYS and a rate-based model in Aspen Plus were performed and compared with CO_2 removal efficiencies obtained via experimental study performed with the CO_2-rig located at USN, Norway.

In the equilibrium-based model, for the study of 5% CO_2 feed gas concentration, the Murphree efficiency was adjusted to 12% to fit the removal efficiency at 40 kg/hr of liquid flow rate. The assumption of a constant Murphree efficiency is doubtful when variables like gas or liquid flow are varied. But performance data can be fitted by adjusting the Murphree efficiency as a function of gas- or liquid flow.

In case of using a rate-based model, the IAF can be adjusted. So far, neither fitting the Murphree efficiency in an equilibrium model or fitting the IAF in a rate-based model give qualitatively reasonable results. The calculated CO_2 removal as a function of liquid flow are however reasonably accurate for both models.

For the physical properties based on rate-based simulations, the default Jones-Dole model (MUL2JONS) was able to predict the measured viscosities with measurable deviation and may be improved by estimating model parameters through a regression using available measured viscosity data in the literature. Other considered models the Andrade model (MUL2ANDR), TRAPP model (MUL2TRAP) and Eyring-NRTL model (EYRING) for liquid mixture viscosity deviated largely from measured data. Accordingly, they are not adopted in this application. The default molar volume and density model VAQCLK was able to predict densities in the MEA + H_2O + CO_2 with acceptable accuracy.

Acknowledgements

The authors would like to thank Chameera Jayarathna for the support given in this study.

References

[1] Øi, L.E. Comparison of Aspen HYSYS and Aspen Plus simulation of CO_2 absorption into MEA from atmospheric gas. Energy Procedia, 2012. 23: p. 360-369.

[2] Kvamsdal, H.M., Chikukwa, A., Hillestad, M., Zakeri, A., & Einbu, A. A comparison of different parameter correlation models and the validation of an MEA-based absorber model. Energy Procedia, 2011. 4: p. 1526-1533.

[3] Kvamsdal, H.M., & Hillestad, M. Selection of model parameter correlations in a rate-based CO_2 absorber model aimed for process simulation. International Journal of Greenhouse Gas Control, 2012. 11: p. 11-20.

[4] Øi, L.E., Sætre, K.A., and Hamborg, E.S. Comparison of simulation tools to fit and predict performance data of CO_2 absorption into monoethanol amine at CO_2 technology centre mongstad (TCM), in Proceedings of the 59th conference on simulation and modelling (SIMS 59), 26-28 September 2018. 2018: Oslo Metropolitan University Norway. p. 230-235.

[5] Kent, R.L., & Eisenberg, B. Better data for amine treating Hydrocarbon Processing, 1976. 55(2): p. 87-90.

[6] Li, Y., & Mather, A.E. Correlation and prediction of the solubility of carbon dioxide in a mixed alkanol solution Ind. Eng. Chem. Res, 1994. 33: p. 2006-2015.

[7] Austgen, D.M., Rochelle, G.T., Peng, X., & Chen, C.C. Model of vapor-liquid equilibria for aqueous acid gas-alkanolamine systems using the electrolyte-NRTL equation. Industrial & Engineering Chemistry Research, 1989. 28(7): p. 1060-1073.

[8] Lim, Y., Kim, J., Jung, J., Lee, C.S., & Han, C. Modeling and Simulation of CO_2 Capture Process for Coal- based Power Plant Using Amine Solvent in South Korea. Energy Procedia, 2013. 37: p. 1855-1862.

[9] Plaza, J.M., Van Wagener, D., & Rochelle, G.T. Modeling CO_2 capture with aqueous monoethanolamine. International Journal of Greenhouse Gas Control, 2010. 4(2): p. 161-166.

[10] Hilliard, M.D. A predictive thermodynamic model for an aqueous blend of potassium carbonate, piperazine, and monoethanolamine for carbon dioxide capture from flue gas, in Chemical Engineering. 2008, The University of Texas at Austin.

[11] Zhang, Y., & Chen, C.C. Modeling CO_2 absorption and desorption by aqueous monoethanolamine solution with Aspen rate-based model. Energy Procedia, 2013. 37: p. 1584-1596.

[12] Øi, L.E., Bråthen, T., Berg, C., Brekne, S.K., Flatin, M., Johnsen, R., Moen, I.G., & Thomassen, E. Optimization of Configurations for Amine based CO_2 Absorption Using Aspen HYSYS. Energy Procedia, 2014. 51: p. 224-233.

[13] Øi, L.E., Hansen, P.M., & Henriksen, M. CO_2 absorption efficiency and heat consumption measured at high gas to liquid ratios in laboratory rig Energy Procedia, 2017. 114: p. 1273-1281.

[14] Kister, H.Z. Distillation Design 1992, USA: McGraw-Hill, Inc.

[15] Eimer, D.A. Gas Treating: Absorption Theory and Practice. 2014: John Wiley & Sons. Ltd

[16] Karunarathne, S.S., Eimer, D.A., & Øi, L.E. Density and viscosity variations in an amine based absorption column,

in 14th Greenhouse Gas Control Technologies Conference (GHGT-14). 2018: Melbourne

[17] Weiland, R.H., Dingman, J.C., Cronin, D.B., Browning, G.J. Density and viscosity of some partially carbonated aqueous alkanolamine solutions and their blends. J. Chem. Eng. Data, 1998. 43: p. 378-382.

[18] Hartono, A., Mba, E.O., & Svendsen, H.F. Physical properties of partially CO_2 loaded aqueous monoethanolamine (MEA). J. Chem. Eng. Data 2014. 59: p. 1808-1816.

[19] Aspen physical property system: Physical property methods and models 11.1, USA: Aspen Technology, Inc., 2001.

[20] Kapadi, U.R., Hundiwale, D.G., Patil, N.B., & Lande, M.K. Viscosity, excess molar volume of binary mixtures of ethanolamine with water at 303.15, 303.15, 313.15 and 318.15K. Fluid Phase Equilibria, 2002. 201: p. 335-341.

[21] Han, J., Jin, J., Eimer, D.A., & Melaaen, M.C. Density of water (1) + Monoethanolamine (2) + CO_2 (3) from (298.15 to 413.15) K and surface tension of water (1) + Monoethanolamine (2) from (303.15 to 333.15) K. J. Chem. Eng. Data, 2012. 57: p. 1095-1103.

[22] Rate-Based model of the CO_2 capture process by MEA using Aspen Plus. Aspen Technology, Inc, 2008.

[23] Amundsen, T.G., Øi, L.E., & Eimer, D.A. Density and viscosity of monoethanolamine+water+carbon dioxide from (25 to 80) ºC. J. Chem. Eng. Data, 2009. 54: p. 3096-3100.

[24] Karunarathne, S.S., Eimer, D.A., & Øi, L.E. Model uncertainty of interfacial area and mass transfer coefficients in absorption column packings. in Proceedings of the 58th SIMS. 2017. Reykjavik, Iceland.

EXPERIMENTAL STUDY OF THE USE OF PARTICLES FOR TRACKING THE INTERFACES IN PRIMARY CEMENTING OF CONCENTRIC AND ECCENTRIC WELLS

A. Taheri[1*], J.D. Ytrehus[2], A. Taghipour[2], B. Lund[2], A. Lavrov[2], M. Torsæter[2]

[1] NTNU, Trondheim, Norway

[2] SINTEF Industry, Trondheim, Norway

* Corresponding author e-mail: amir.taheri@ntnu.no

Abstract

In this study, our recent and new approach for detailed tracking of the interface between well fluid and cement by using particles is investigated. The particles can enable us to know the precise location of the interface between two fluids and be sure about displacement efficiency in the annulus. This includes the introduction of intermediate buoyant particles that reside at the interfaces between successive fluids in a well (e.g., cement-spacer or spacer-mud). Such particles must overcome strong secondary flows to travel with the interface. For this purpose, the displacement mechanisms of Newtonian and non-Newtonian fluids in the annulus of vertical and inclined wells is investigated by using an experimental set-up with concentric and eccentric annular geometries. For more efficient displacement, the displacing fluid should have a higher density than the displaced fluid, and the intermediate-buoyancy particles that reside at the interface between successive fluids are introduced into the models. Particle motions are investigated in models with different fluid rheology and displacement flow rates. This approach for tracking of the interface can improve the quality of annular cementing of CO_2 wells and thus the storage safety.

Keywords: *annular model, secondary flow, particle tracking*

1. Introduction

CO_2 capture and storage (CCS) is considered as one of the most promising solutions for decreasing the emissions of CO_2 into the atmosphere. Large-scale storage of CO_2 requires understanding the trapping mechanisms of CO_2 into storage sites to prevent and mitigate the leakages of CO_2 to the atmosphere. One part of the stored CO_2 in underground formations is free phase, and hence there is a chance of leakage of CO_2 out to the atmosphere. So the probable leakage points in the storage sites should be recognized. leak-free injection wells (or any other type of wells penetrating a CO_2 storage reservoir) are one of the main concerns in studies related to CO_2 leakage that enhance the demand for high-quality cement along the wellbore, between the casing and the rock formation. The main prerequisite for annular cement sheaths with high integrity and without any leakage paths is high efficiency in the displacement of the drilling fluid and the formation fluids from the annulus by sequential pumping of spacer and cement. For wells penetrating CO_2 storage reservoirs, it is especially important that all the annular cement columns are of high quality. This is because CO_2 is a buoyant fluid, and also such wells are subjected to harsh conditions (e.g., cooling of the well/formation, elevated pressure, and chemical reactions) [1].

One of the most critical operational factors that affect the quality of well cementing is the displacement of the drilling fluid and the formation fluids from the annulus by sequential pumping of spacer and cement. The procedure is such that non-Newtonian yield-stress fluids of progressively higher density and rheology are pumped into the well. Spacer is typically of higher density and rheology than drilling fluid, and cement is ideally of higher density and rheology than the other existing fluids in the annulus. This sequential pumping is done to stabilize the displacement process and the interfaces and to improve the displacement efficiency [2, 3]. Ideally, all the fluids in place are displaced evenly, and the cement takes their place without leaving any mud/spacer pockets or channels along the well. In reality, however, several factors prevent a perfect displacement. These include an uneven borehole due to soft rocks and washouts as well as the eccentric positioning of the casing within the borehole that is still very common, especially in inclined wellbores. Thus, fluid interfaces in the annulus typically do not advance uniformly along the well.

There are numerous computational studies of displacement flow in different geometries; annulus and unwrapped annulus or Hele-Shaw geometry [4, 5, 6 and 7]. There are few experimental studies about displacement flow in eccentric annular geometries. The first detailed study was performed by Tehrani et al. [8]. The experiments were performed in an inclined narrow annulus with an aspect ratio of 0.035 and a length of 3 m. They examined various flow rates and eccentricities, and the results were compared with modeling results in the form of final displacement efficiencies at the end of the experiments. They recorded both visualization data and conductivity changes in the set-up. They used non-Newtonian fluids and found reasonable qualitative agreement between experimental and modeling results. Experimental studies of the laminar flow of both Newtonian and non-Newtonian fluid displacements in vertical narrow eccentric annuli by Mohammadi et al. confirm that small eccentricity, increased viscosity ratio,

increased density ratio, and slower flow rates appear to favor a steady displacement for Newtonian fluids. They believed that qualitatively the same results could be achieved for non-Newtonian fluids, while the role of flow rate is less clear. The secondary flow and dispersion had a dominant effect on the results [9]. In an eccentric annulus where a displacing fluid tends to pass through the wide side, a positive density difference between two fluids produces a hydrostatic pressure imbalance between the wide and narrow sides. This imbalance causes a secondary azimuthal current on the main axial flow whose direction is from the wide side to the narrow side of the annulus in the displacing fluid and from the narrow side to the wide side in the displaced fluid [10].

Since there is no direct access to well annuli, operators have to rely on indirect methods when evaluating the quality of a cementing job. Cement bond log (CBL) is the most popular tool in this case where the degree of zonal isolation is inferred from the degree of acoustic coupling of the cement to the casing and formation. The log can reveal large channels in cement but is not very sensitive to minor channels (de-bonding and micro-annuli). Moreover, the logging is done after finishing the cement job and when the cement has hardened. This means that there is no room left for corrective measures if the cement job went wrong, except performing remedial cementing which requires perforating the casing. Temperature logs, which sense the exothermic cement hardening, can also be performed after placement to detect the top of annular cement. Such logs can, however, not be used to evaluate the quality of the cement column, e.g., the presence of voids or mud pockets. In the past, radioactive tracers were injected together with cement to determine the top of the annular cement column, but this method was abandoned due to HSE issues.

The primary objective of this study is to introduce and check a new approach for more accurate and detailed tracking of the interface between mud and cement by using particles. The particles can enable us to know the precise location of the interface between two fluids and be sure about displacement efficiency in the annulus. This includes the introduction of intermediately buoyant particles that reside at the interfaces between successive fluids in a well (e.g., cement-spacer or spacer-mud). The tracing can happen using radioactive or electromagnetic tracer devices. This use of particles for tracking the interface between fluids in annular displacement flow was studied previously by Frigaard and Maleki by solving the Hele-Shaw model equations and placing the particles in the model. The important active forces in this situation are the drag force and gravity force corrected by the effect of buoyancy. The difference between the wide/narrow side far-field velocity and the mean velocity is a measure of the secondary flow near the interface. Such particles must overcome strong secondary flows in order to travel with the interface. Frigaard and Maleki introduced a dimensionless number by involving fluids and particles properties ($Bu = [(\rho_2 - \rho_1)gd_p^2]/\mu\bar{w}$) and defined a minimum value of 18 for this number for particle selection to be sure that the particles can reach and travel with the interface. In this equation, d_p is the particle diameter, μ is the fluid viscosity, $\bar{w}$ is the mean speed of the interface between two fluids that advance steadily along the annulus, and ρ_1 and ρ_2 are densities of displaced and displacing fluids [11 and 12].

This study consists of two sections. After describing the experimental set-up and the used fluids in the experiments, the results of several flow displacement tests are described. The main purpose of this section is to study the behavior of the interface between two fluids in the flow displacement tests with different pairs of Newtonian/non-Newtonian fluids and different flow rates. In the next section, results of the additional flow displacement tests are reviewed where particles are released at the interface between two fluids, and the goal of this section is to study the behavior and motion of the particles in between of the two fluids during displacement flow with different specified flow rates.

2. Experimental Description

2.1 Experimental Set-up and procedure

A picture of the annular experimental set-up is shown in Figure 1. The experimental tests were performed in a 110 cm long transparent plexiglass tubing with an aluminum tubing (plexiglass tubing in the concentric model) as the inner body. The inner radius of the outer tubing (r_o) and the outer radius of the inner tubing (r_i) are 5.5 and 3.5 cm, respectively. The aspect ratio of circumferential and radial length scales (δ) is defined by $\delta = (r_o - r_i)/\pi(r_o + r_I)$ that is 0.071 in this geometry. The field range for δ is typically in the range of 0.01-0.1 [9]. The scaled length of the model is 7.78 by considering the length scale (L) of 14.14 cm ($L = 0.5\pi(r_o + r_i)$). The distance between the centers of the inner and outer tubings (d) in the eccentric models is 8 mm that corresponds to an eccentricity of 0.4. Our experiments were conducted at two inclinations; $\Theta = 0^o$ (vertical) and $\Theta = 10^o$ (inclined toward the narrow side).

The flow rate during the tests is controlled. Two pumps are required for the flow of displacing and displaced fluids. A centrifugal pump is used for the displacement of the displaced fluid. For the displacing fluid, we use a centrifugal pump as well, and a variable frequency drive controls the flow rate. A Heinriches magnetic flow meter with the output signal of 4-20 mA corresponding to 0-150 l/min is used to measure the flow rate. Moreover, eight conductivity probes have been installed at the two levels of the model for tracking the conductivity of the fluids in contact. Our previous studies show that there is not any consistency between our qualitative visualization in the flow displacement tests and the recorded conductivity changes by the probes and a plausible explanation was that displaced fluids bonds to the probes, and it prevents contact between the probes and the conductive displacing fluid. [13]. So we will not consider the readings by the conductivity probes in this study.

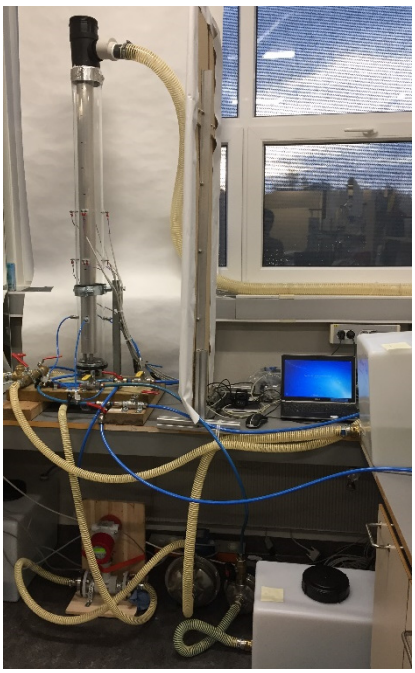

Figure 1: The Experimental Annular Set-Up

For performing the tests and at the beginning, the annulus is filled by a displaced fluid, and this fluid is displaced by a displacing fluid from the bottom and with a specified flow rate. In the cases with particles, the initial displaced fluid is displaced by the displacing fluid with a very small flow rate in order to have a flat interface between the two fluids around 0.2 m above the bottom of the model. Afterward, the particles are released below the interface from four particle ports, and the displacing fluid with the specified flow rate displaces the displaced fluid from the bottom. We used Fluorescent Red Polyethylene Microspheres from Cospheric with diameters of 27-32um and 425-500um and a density of 1.090 g/cc in the tests. Images of the displacement process are recorded using a Canon EOS 5D Mark IV camera at one-second intervals.

2.2 Fluid Preparation and Analysis

In these series of experiments, several pairs of Newtonian and non-Newtonian fluids are prepared and used. Water and sucrose solution are the used Newtonian fluids, and Carbopol-980 solution with different concentrations are the used non-Newtonian fluid with shear thinning and yield stress behavior. Carbopol is widely used as a thickener, stabilizer, and suspending agent. The rheology of Carbopol is significantly influenced by the concentration and pH of the solution, and the yield stress is developed at an intermediate pH on neutralizing with a base agent (in our case NaOH). The neutralized solution is fairly transparent and has the same density as water (for low concentrations). In preparing the Carbopol-980 solution, we gradually add the Carbopol powder (0.1-0.15 wt/wt%) to water in a mixing tank. Mixing proceeds slowly for a few hours. Since the Carbopol concentration in our experiments is not very high, 3-4 hours of mixing is enough. When adding NaOH to the Carbopol–water solution, we have to decrease the mixing rate and be careful not to introduce air bubbles into the gel-like solution. Brilliant Cresyl Blue, a cationic dye that is stable and water-soluble, is added to the displaced fluids for visualization purposes [14]. Rheological measurements showed that this dye does not affect the rheology of the fluids. NaCl is also added to the displacing fluid to be able to measure the fluid conductivities.

Fluid densities and pHs were measured using a DMA-46 densitometer (Anton Paar) and pH meter pH 1000 L (VWR International) respectively. Rheology of fluids was tested before each experiment using Anton Paar MCR 102 rheometer. The temperature was fixed at 21°C. The Carbopol-980 solution rheology data were fitted to a Herschel-Bulkley model $\tau = \tau_y + k\dot{\gamma}^n$ where τ_y is yield stress, κ is consistency index, and n is a power-law index. In order to reset the structure of the polymers between samples, all rheology tests were subjected to a pre-shear of 2 min with a shear rate of 1100 s^{-1} in the rheometer before data acquisition. After pre-shearing, the stress values were recorded by the rheometer for a decreasing and increasing ramp of shear rates (to check for possible hysteresis) in a logarithmic manner.

Table 1 presents an overview of the performed tests, and Table 2 shows the properties of the used fluids in the tests. Subscripts 1 and 2 are representative of displaced and displacing fluids, respectively. Figure 2 compares the rheology behavior of three different non-Newtonian fluids in the tests no. 8 and 11 in a log-log coordinate. From this figure, it can be seen that the yield stress of the displaced fluid in the test no. 8 is higher than the yield stress of the fluids in the test no. 11 and displaced and displacing fluids in the test no. 6 have almost the same rheology. Figure 3 shows the effective viscosities of these fluids and it can be seen that at the range of displacement flow rates (shear rates more than 1 s^{-1}), the viscosity of the displacing fluid in the test no. 11 is more than the viscosity of the displaced fluid in this test, and the viscosity of the displaced fluid in the test no. 8 is less than the other viscosities in this comparison while its yield stress is more than the yield stress of the other ones.

Table 1: The Description of the Performed Tests

Test	Model Type	Displaced Fluid	Displacing Fluid	Model Inclination (degree)	Displacement Flow Rate (L/min)	Particle Size (um)
1	Concentric	Water	Sucrose Solution	0	6.33	500
2	Eccentric	Water	Sucrose Solution	0	10.09	-----
3	Eccentric	Water	Sucrose Solution	0	9.98	425-500
4	Eccentric	Water	Sucrose Solution	0	16.29	425-500
5	Eccentric	Water	Sucrose Solution	10	15.05	425-500
6	Eccentric	Water	Sucrose Solution	0	14.74	27-32
7	Eccentric	Carbopol Solution	Sucrose Solution	0	12.81	425-500
8	Eccentric	Carbopol Solution	Sucrose Solution	10	17.21	425-500
9	Eccentric	Carbopol Solution	Carbopol Solution	0	7.93	-----
10	Eccentric	Carbopol Solution	Carbopol Solution	10	7.47	-----
11	Eccentric	Carbopol Solution	Carbopol Solution	0	4.36	-----
12	Eccentric	Carbopol Solution	Sucrose Solution	10	16.6	-----

Table 2: Properties of the Fluids Used in the Tests at 21° C

Test	ρ_1 (g/cm3)	τ_{y1} (Pa)	κ_1 (Pa s^n)	n_1	ρ_2 (g/cm3)	τ_{y2} (Pa)	κ_2 (Pa s^n)	n_2
1	0.9950	0	0.000956	1	1.1274	0	0.002829	1
2	0.9950	0	0.000956	1	1.1274	0	0.002829	1
3	0.9950	0	0.000956	1	1.1274	0	0.002829	1
4	0.9950	0	0.000956	1	1.1274	0	0.002829	1
5	0.9950	0	0.000956	1	1.1274	0	0.002829	1
6	0.9950	0	0.000956	1	1.1274	0	0.002829	1
7	0.9996	0.92	2.90	0.44	1.1274	0	0.002829	1
8	0.9990	1.77	2.69	0.44	1.1243	0	0.002878	1
9	0.9990	1.13	4.22	0.42	0.9990	0.4	2.66	0.46
10	0.9990	1.13	4.22	0.42	0.9990	0.4	2.66	0.46
11	0.9990	0.45	3.52	0.59	0.9992	0.35	4.37	0.66
12	0.9990	0.92	2.90	0.44	1.1243	0	0.002878	1

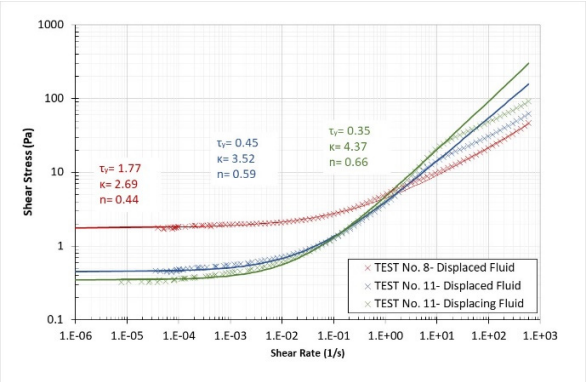

Figure 2: Rheological Behavior of the Carbopol-980 Solutions

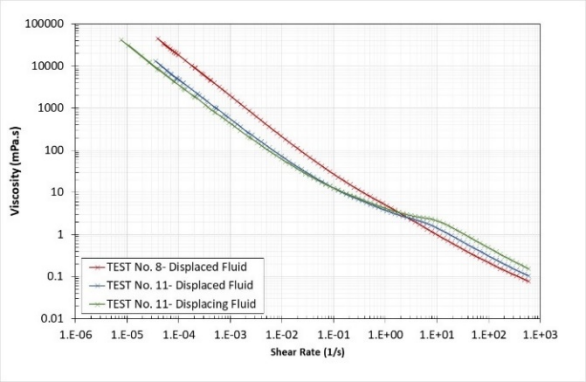

Figure 3: Viscosity of the Carbopol-980 Solutions

3. Experimental Results and Discussion

3.1 Displacement Flow Tests

In this section, the results of several displacement flow tests in the eccentric models are described. The tests were performed using different pairs of Newtonian and non-Newtonian fluids with different displacement flow rates mentioned in Table 1.

Figure 4 shows the snapshots of displacement flow in the test no. 2, where one Newtonian fluid is displaced with another one with higher viscosity and density and with a displacement flow rate of 10.09 L/min. From time 0 s that is the start of the displacement till time 36 s that is the end of displacement, it can be seen that there is a uniform and piston-like displacement in this test. While the displacing fluid tends to pass through the wide side (right-hand side), strong secondary flow from wide side to the narrow side in the displacing fluid causes piston-like displacement and a flat interface between the two fluids. In fact, secondary flow helps for more efficient and piston-like displacement in this case. Figures 5 and 6 represent snapshots of displacement flows in tests no. 9 and 10 where a non-Newtonian fluid with a lower viscosity displaces another non-Newtonian fluid with a higher viscosity and the same density. Model inclinations in the tests no. 9 and 10 are 0 and 10 degrees respectively, and the displacement flow rates in both cases are almost the same (7.93 L/min and 7.47 L/min in test no. 9 and 10 respectively). In both cases, a non-stable displacement is achieved, and the interface between the two fluids is not piston-like. While the displacing fluid advances toward the wide side of the annulus and reaches to the top of the model within 21 s, displaced fluid in the narrow side does not move. This can be due to a weak secondary flow in the model because of the high viscosity of the fluids and also viscous fingering due to the unstable displacement and displacing of a higher viscous fluid with a lower viscous fluid. Figure 7 shows the snapshots of displacement flow in the test no. 11 where both displaced and displacing fluids have almost the same viscosities (refer to Figure 3) and densities. While the yield stress of the displaced fluid (0.45 Pa) is higher than the yield stress of the displacing fluid (0.35 Pa), other rheological parameters cause the viscosity of the displacing fluid to become a bit higher than the viscosity of the displaced fluid in the range of the flow rate in the test. Also, the small flow rate of 4.36 L/min in the test decreases the chance of viscous fingering. Again, we see significant displacement from the wide side and a little movement of displaced fluid from the narrow side. The weak secondary flow in this test is the main reason for the un-stable displacement and the non-flat interface. Figure 8 shows the snapshots of displacement flow in the test no. 12, where a non-Newtonian fluid is displaced with a Newtonian fluid with higher density and lower viscosity. The displacement flow rate is 16.6 L/min and again we can see from the snapshots that due to a weak secondary flow (because of high viscosity in the displaced fluid) and probably viscous fingering (due to high flow rate and displacing of a high viscous fluid with low viscous fluid), the displacement is not stable and the interface between the two fluids is not flat.

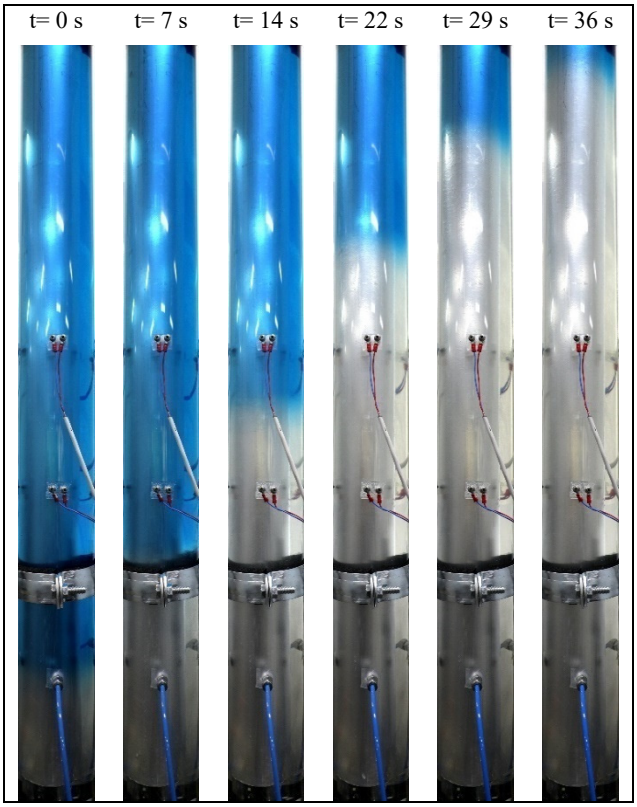

Figure 4: Snapshots of Displacement Flow in Test no. 2

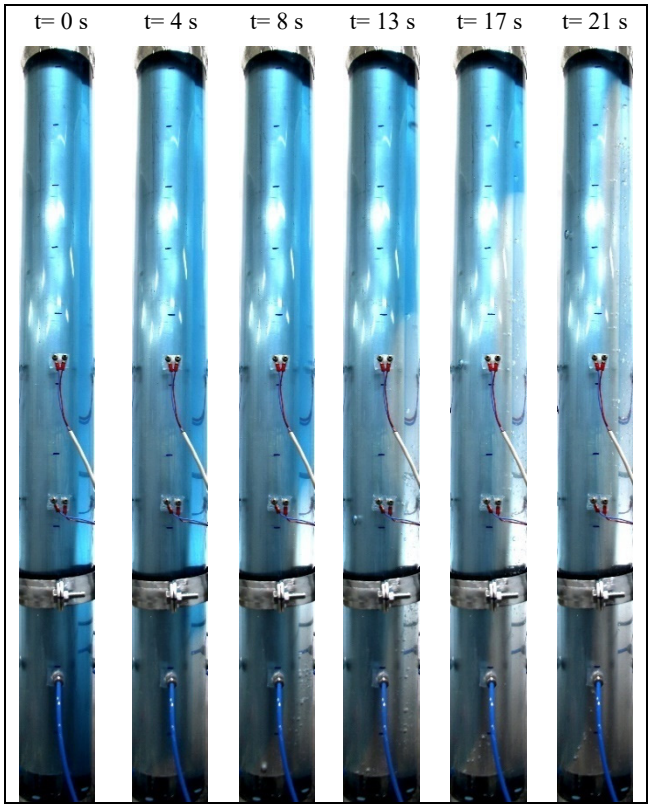

Figure 5: Snapshots of Displacement Flow in Test no. 9

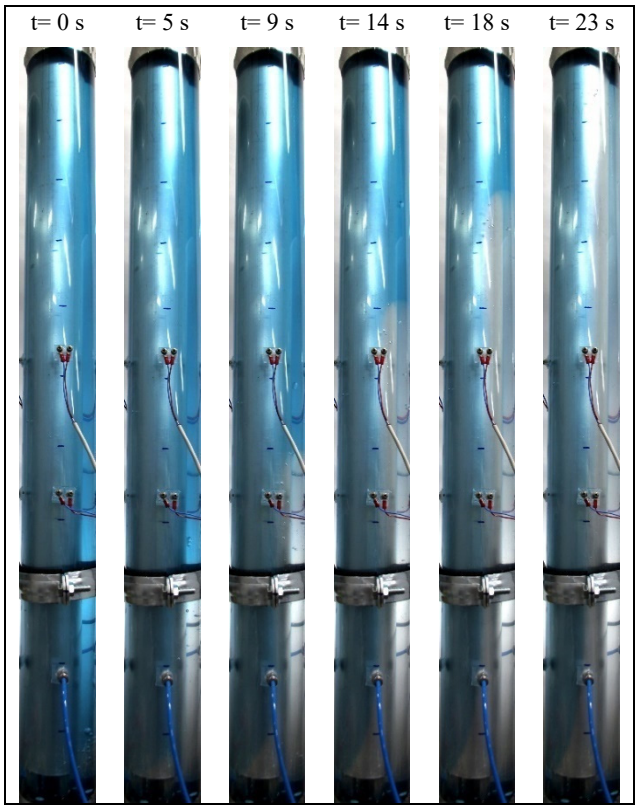

Figure 6: Snapshots of Displacement Flow in Test no. 10

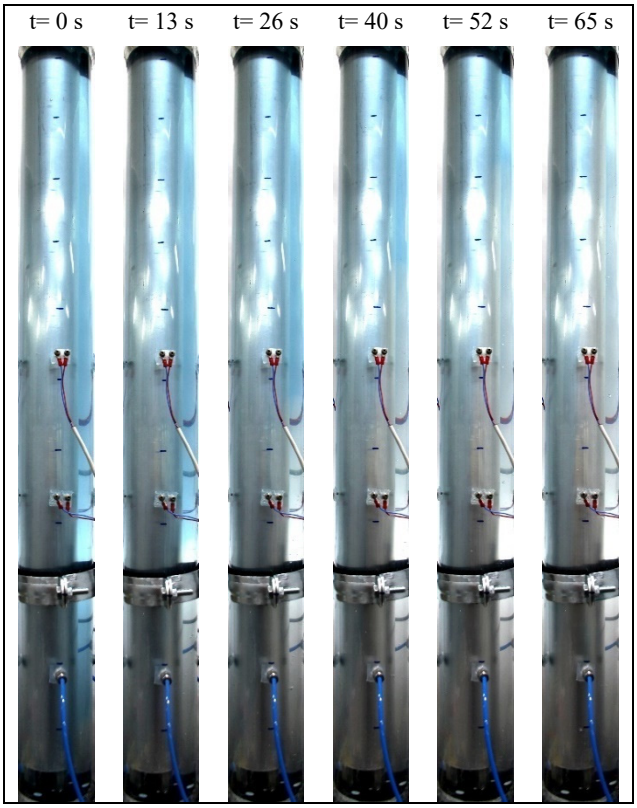

Figure 7: Snapshots of Displacement Flow in Test no. 11

Figure 8: Snapshots of Displacement Flow in Test no. 12

3.2 Particle Behaviors in Displacement Flow Tests

In these sets of the tests, the main objective is the study of the behavior and motions of particles for tracking of the interface in the models with different pairs of fluids. In each test, a fixed amount of particles is released from each four particle ports on the wall of the annulus and below the interface between the displaced and displacing fluids. After a few minutes, the particles distribute uniformly below the surface, and we observe uniform dispersion of the particles from the narrow side to the wide side of the annulus at the time of 0 s. Then the flow starts with a specified value, and the behavior of these particles on the interface of the displaced and displacing fluids is observed.

3.2.1. Concentric Model

Figure 9 shows the snapshots of displacement flow in the vertical concentric model in the test no. 1 where a Newtonian fluid with a higher viscosity and density displaces another Newtonian fluid with lower density and viscosity with a displacement flow rate of 6.33 L/min. This displacement scheme causes no viscous fingering that is obvious in the snapshots also. So due to the lack of eccentricity and viscous fingering we can see piston-like and stable displacement. The released particles with a diameter of 425-500 um also follow the interface and it can be seen that the particles have the capability of tracking the interface in the lack of existence of secondary flow in this concentric model.

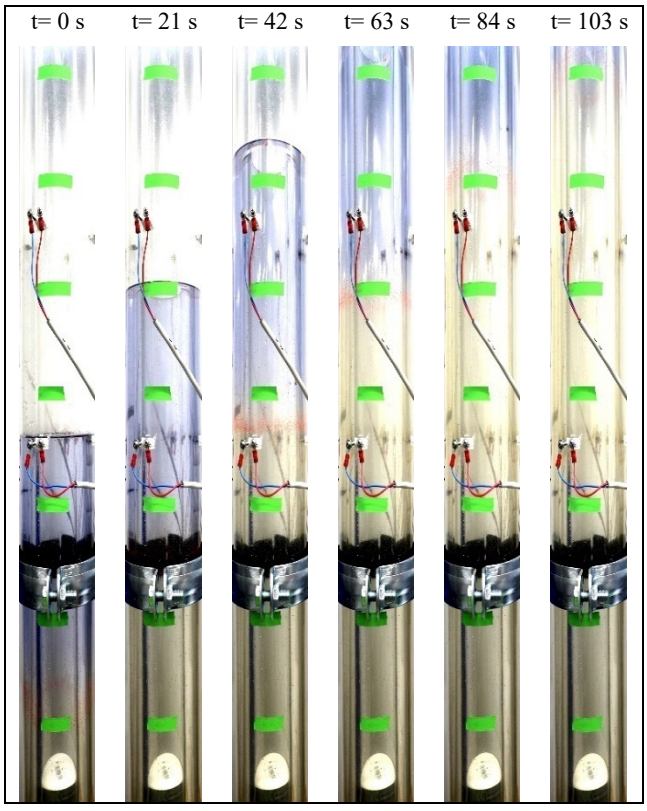

Figure 9: Snapshots of Displacement Flow in Test no. 1

3.2.2. Eccentric Models

Figure 10 shows snapshots of flow displacement by two Newtonian fluids in a vertical model in the test no. 3 from the start till the end of the process at the time of 31 s. It can be seen after the start of the flow with a flow rate of 9.98 L/min, the interface between the two fluids is almost flat, and we can see a piston-like displacement flow. Displacement flow is stable because the displacing fluid has higher density and viscosity than the displaced fluid, and there is no occurrence of viscous fingering. Moreover, the uniform piston-like displacement in this eccentric model confirms the high effect of secondary flow from the wide side to the narrow side in the displacing fluid and from the narrow side to the wide side in the displaced fluid. If we look at the motions of the red particles with a diameter of 425-500 um in the annulus, it is observed that after the start of the flow the particles move from the narrow side to the wide side and accumulate below the interface at the wide side. In fact, the secondary flow affects the particles and causes movement of particles from the narrow side to the wide side. Figure 11 shows the snapshots of flow displacement in the test no. 4 with the same fluids of the test no. 3. The only difference is the displacement flow rate that is higher in the test no. 4 (16.29 L/min) than the test no. 3. The same results are concluded from this test with a higher displacement flow rate. The interface between the two fluids is almost stable, and the piston-like displacement flow confirms the existence and high effect of secondary flow. This secondary flow has an effect on the released red particles in the model, and they move from the narrow side to the wide side and accumulate below the interface at the wide side and move upward by the interface.

Figure 12 shows the snapshots of displacement flow in the test no. 5 in an eccentric model that is inclined 10^{o} to the narrow side. The used displaced and displacing fluids are the same as the previous tests, and the flow rate is 15.05 L/min. In these snapshots, a stable piston-like displacement with a flat interface with a 10^{o} dip is observed. When we look at the motions of the red particles, we can see a difference compared to the first two tests. It can be observed that the uniformly dispersed particles with a diameter of 425-500 um below the interface move by the interface, indicating that they overcome the strong secondary flow. In this test, the particles track the interface accurately.

Figure 13 presents snapshots of the displacement flow in the test no. 6 in a vertical model and with Newtonian fluids like before. Again, we can see stable and piston-like displacement in this test. The released particle in this test have a diameter of 27-32 um, and the particles are not observable in the captured images by eye. However, they affect the blue color of the displaced fluid and change the blue color to purple-blue color. By looking into the snapshots from the start till the end of this test, it can be seen that the fluid color around he interface is purple-blue and it can be stated that these particles are able to track the interface and the strong secondary flow around the interface has no effect on them.

Figure 14 shows the snapshots of displacement flow in the test no. 7 in the same model by using the same

displacing fluid and one non-Newtonian fluid and flow rate of 12.81 L/min. In this case, it is observed that secondary flow has not any significant effect on displacement efficiency due to the higher viscosity of the displaced fluid, and the interface between the two fluids is not piston-like. By looking into these snapshots at different times, it is observed that almost all the red particles with a diameter of 425-500 um move from the narrow side to the wide side and move by the interface toward the top of the model. Figure 15 presents the snapshots of the displacement flow in the test no. 8 using the same Newtonian displacing fluid and a non-Newtonian displaced fluid with higher yield stress than the displaced fluid in the test no. 7. The displacement flow rate is 17.21 L/min that is more than the previous tests. From these snapshots, it can be seen that there is no uniform and stable displacement in this test due to the very weak secondary flow around the interface. Moreover, the displacing fluid had lower viscosity and higher density than the displaced fluid that cannot guarantee a stable displacement. Also, the high flow rate increases the chance of viscous fingering. All of these phenomena cause non-piston like displacement. Also, the high yield stress of the displaced fluid and lower viscosity of the displacing fluid causes bypassing of the displaced fluid by the displacing fluid. The released particles with a diameter of 425-500 um are under different forces, and they do not follow the interface in this test.

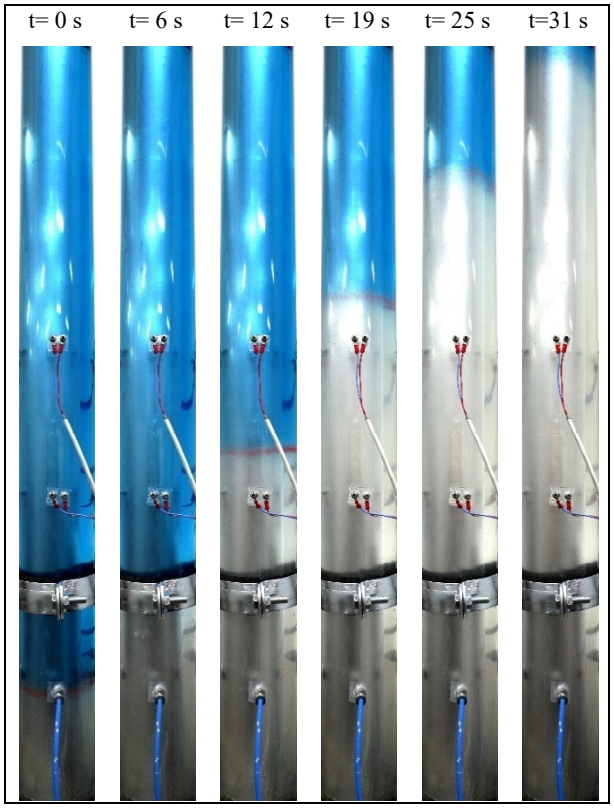

Figure 10: Snapshots of Displacement Flow in Test no. 3

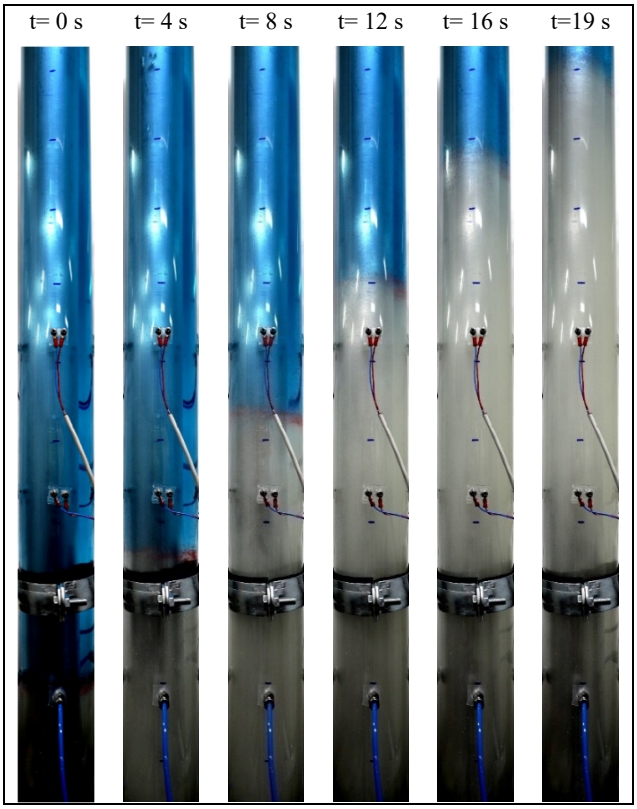

Figure 11: Snapshots of Displacement Flow in Test no. 4

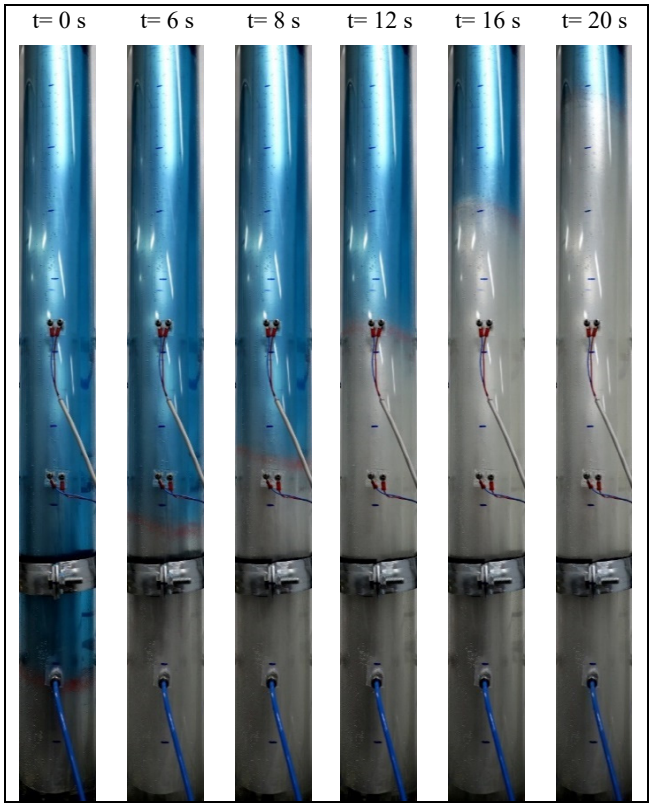

Figure 12: Snapshots of Displacement Flow in Test no. 5

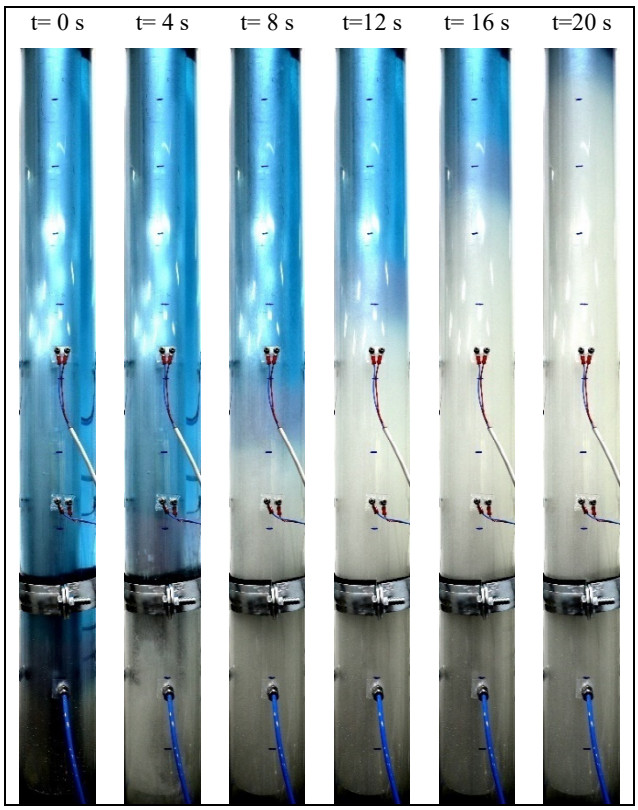

Figure 13: Snapshots of Displacement Flow in the Test no. 6

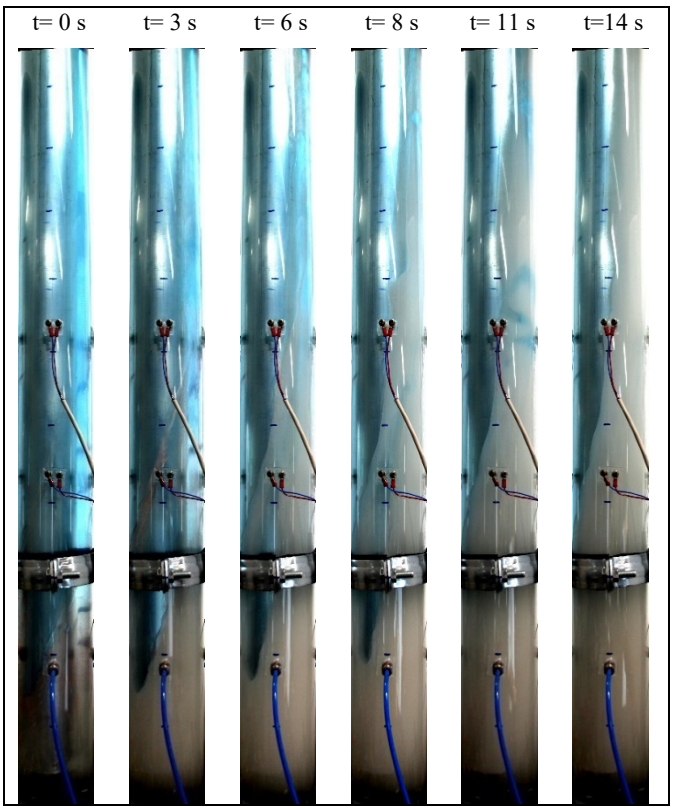

Figure 15: Snapshots of Displacement Flow in Test no. 8

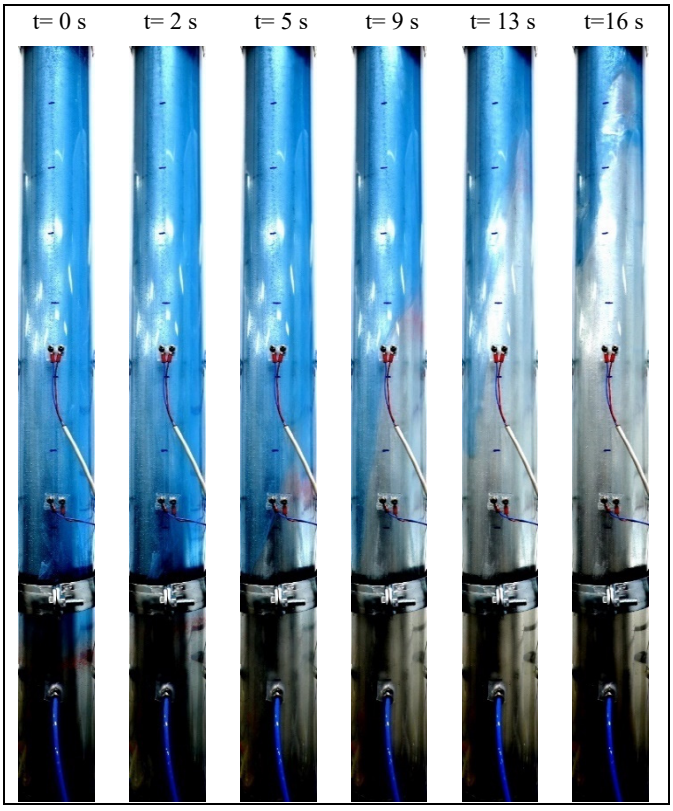

Figure 14: Snapshots of Displacement Flow in Test no. 7

Conclusions

Drag force and gravity force corrected by the effect of buoyancy are the active forces in particle motions in the tracking of the interface between two fluids in displacement flows. The experimentally performed annulus displacement flow in the concentric and eccentric models using Newtonian and non-Newtonian fluids confirm that:

1- Viscous fingering and secondary flow are two crucial displacement mechanisms that affect the efficiency and stability of displacement in annulus models.

2- Particles with a diameter range of 425-500 um are able to track the interface between fluids in the concentric model.

3- Particles with a diameter range of 425-500 um are not able to overcome strong secondary flows in the vertical eccentric models and particles move from the narrow side to the wide side and travel upward by the interface. In the models with a small inclination to the narrow side and when the displacing and displaced fluids have Newtonian behavior, the released particle below the interface resides on the interface, and they can track the interface until the end of the process appropriately.

4- Particle with a diameter range of 27-32 um has enough potential to overcome the secondary flow in a model where both displacing and displaced fluids have Newtonian behavior and the displacement is stable and the interface is flat.

Acknowledgments

This publication has been produced in the project "Studying moving fluid interfaces during cementing of CCS wells" funded by the Research Council of Norway (268510/E20).

References

[1] Lavrov, A., and Torsæter, M., 2016, "Physics and Mechanics of Primary Well Cementing", Springer.

[2] Bishop, M., et al., 2008, "A robust, field friendly, cement spacer system", AADE-08-DF-HO-07 paper presented at the 2008 AADE Fluids Conference and Exhibition held at the Wyndam Greenspoint Hotel, Houston, Texas, April 8-9. 2008.

[3] Nelson, E.B. and D. Guillot, 2006, "Well cementing", Schlumberger.

[4] Bittleston, S., Ferguson, J., and Frigaard, I. A., 2002, "Mud removal and cement placement during primary cementing of an oil well- Laminar non-Newtonian displacements in an eccentric annular Hele-Shaw cell", J. Eng. Math., 43, pp. 229–253.

[5] Pelipenko, S., and Frigaard, I. A., 2004, "On steady state displacements in primary cementing of an oil well", J. Eng. Math., 46, pp. 1–26.

[6] Pelipenko, S., and Frigaard, I. A., 2004, "Two-dimensional computational simulation of eccentric annular cementing displacements", IMA J. Appl. Math. 69, 557–583.

[7] Pelipenko, S., and Frigaard, I. A., 2004, "Visco-plastic fluid displacements in near-vertical narrow eccentric annuli: prediction of travelling-wave solutions and interfacial instability", J. Fluid Mech., 520, pp. 343–377.

[8] Tehrani, A., Ferguson, J., and Bittleston, S., 1992, "Laminar displacement in annuli: A combined experimental and theoretical study", In Society of Petroleum Engineers.

[9] Mohammadi, S. M., Carrasco-Teja, M., Storey, S., Frigaard, I. A., and Martinez, D. M., 2010, "An experimental study of laminar displacement flows in narrow vertical eccentric annuli", J. Fluid Mech. 649, 371.

[10] Tehrani, A., Bittleston, S. H., and Long, P.J.G., "Flow instabilities during annular displacement of one non-Newtonian fluid by another", Experiments in Fluids, 14 (1993), pp. 246-256.

[11] Maleki, A., and Frigaard, I. A. , 2018, "Tracking fluid interfaces in primary cementing of surface casing", Physics of Fluids 30, 093104.

[12] Frigaard, I. A., and Maleki, A., 2018, "Tracking Fluid Interface in Carbon Capture and Storage Cement Placement Application", Paper No. OMAE2018-77630, pp. V008T11A060.

[13] Taheri, A., Ytrehus, J.D., Taghipour, A., Lund, B., Lavrov, A., and Torsæter, M., 2019, "USE of tracer particles for Tracking fluid interfaces in primary cementing", OMAE paper no. 2019-96400, presented at the 38th International Conference on Ocean, Offshore and Arctic Engineering (OMAE2019), June 9-14, 2019, Glasgow, Scotland.

[14] Qwabe, L., Pare, B., and Jonnalagadda, S. B., 2005, "Mechanism of Oxidation of Brilliant Cresyl Blue with Acidic Chlorite and Hypochlorous Acid. A Kinetic Approach", S. Afr. J. Chem., 58, 86–92.

COMBINED CALCINATION AND CO_2 CAPTURE IN CEMENT CLINKER PRODUCTION BY USE OF ELECTRICAL ENERGY

L.-A. Tokheim[1], A. Mathisen[2], L.E. Øi[1], C. Jayarathna[2], N. Eldrup[1,2], T. Gautestad[3]

[1] University of South-Eastern Norway, Porsgrunn, Norway

[2] SINTEF Industry, Porsgrunn, Norway

[3] Norcem AS Brevik, Porsgrunn, Norway

* Corresponding author e-mail: Lars.A.Tokheim@usn.no

Abstract

The technical feasibility of electrifying the calcination process in a precalciner cement kiln system was assessed by studying different electrification concepts. Resistance-based heating was selected as it requires no CO_2 recycling, has a high electricity-to-heat efficiency and has no major safety concerns. Resistance-based heating may be implemented in different types of calcination reactors. In this study, a rotary calciner was selected because the material flow can be readily controlled, it appears to be technically feasible to implement heating elements with a sufficiently high surface temperature to perform calcination, and rotary kilns are already in use in the cement industry, hence can be regarded as well-known technology. It is possible to integrate the electrified calciner with an existing cement kiln system in such a way that minimum disturbance of the production process is obtained. Hence, no negative impacts on the process, product quality or emissions are expected. The required electrical energy input for calcination in a kiln system producing 1 Mt of clinker per year, is about 85 MW. An early-phase cost estimate was conducted resulting in total annualized costs of 67 € per ton of CO_2 avoided. The net avoided CO_2 emission was 72 % (using a CO_2 footprint of 47 g/kWh for electrical energy). The described CO_2 capture concept was technically and economically compared with amine-based absorption of CO_2 from the preheater exhaust gas. Two amine-based cases were calculated, one using electrical energy as the source of solvent regeneration (85 % net CO_2 reduction) and another one using only available waste heat as the energy source (48 % net CO_2 reduction). The annualized costs of these two cases were 75 and 40 € per ton of CO_2 avoided, respectively. Hence, in cement plants where large amounts of waste heat are available, amine-based absorption appears to be the least expensive option for reduction in CO_2 emissions. However, in systems with no such waste heat available, electrified calcination, for example in the form of electrified rotary calciners, may be a competitive alternative to post-combustion capture technology.

Keywords: *CO_2 capture, Calcination, Electrification, Clinker production*

1. INTRODUCTION

Today, cement clinker is produced by combustion of fuels. There are two main sources of CO_2 in the process: Calcination (decarbonation) of the limestone-based raw materials ($CaCO_3 \rightarrow CaO + CO_2$), accounting for about 65 % of the CO_2 emissions, and fuel combustion, accounting for about 35 %. In a modern kiln system, there are two combustion zones; the calciner, where the decarbonation occurs at approximately 900 °C, and the rotary kiln, where clinker minerals are formed at material temperatures around 1400 °C. About 60 % of the fuel energy is fed to the calciner, whereas the remaining 40 % is fed to the rotary kiln.

The thermal energy requirement is relatively high, so a medium size cement plant may typically have CO_2 emissions around 1 Mt per year. And as there are thousands of cement plants in the world, and the production is increasing, the CO_2 emissions from the cement industry (including CO_2 from calcination and fuel combustion) likely constitute around 8 % of the global man-made emissions [1].

In a green future, when renewable energy sources have replaced most of the fossil energy, industrial production processes such as cement clinker production will largely have to be run by electricity instead of fuel combustion. With that in mind, the purpose of the current study was to:

- investigate the technical feasibility of electrifying part of the cement kiln process
- suggest a promising technical solution for combined electrification and CO_2 capture
- determine the impact on the clinker production process
- perform an early-phase estimate of the CO_2-specific costs of implementing the selected concept
- compare the results with those from implementing post-combustion amine absorption technology, which is the most mature method for achieving significant reductions in CO_2 emissions today

2. ELECTRIFICATION OF THE KILN PROCESS

Figure 1 shows different alternatives for combined electrification and CO_2 capture. The length of each area in the figure reflects the approximate CO_2 emission contribution. The reference case (Alt 0) shows the CO_2 emission contributions from a regular kiln system, with

combustion in the precalciner (dark red) and rotary kiln (light red) as well as pre-calcination in the calciner (dark grey) and post-calcination (light grey) in the rotary kiln.

Pure electrification without any CO_2 capture (Alt 1 and 3) will only eliminate the fuel related CO_2 emissions. But if the electrification is combined with capture of the CO_2 (Alt 2, 4, 5 and 6), more significant reduction levels may be achieved.

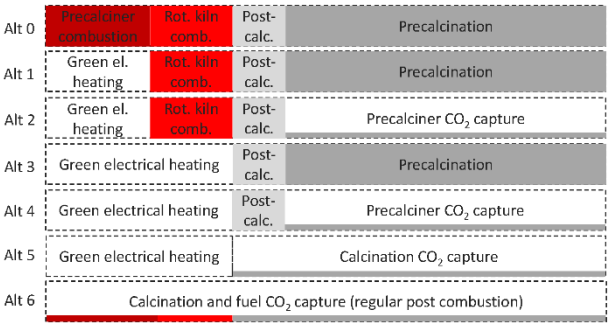

Figure 1: Different ways of reducing CO_2 emissions using CO_2-neutral ("green") electrical heating in combination with CO_2 capture.

By replacing the fuel combustion with electrical energy as the energy source for calcination in the calciner, two simultaneous effects are obtained:

i) The CO_2 formation from the calciner fuel combustion is eliminated, which reduces the total CO_2 formation from the clinker production process.

ii) The exhaust gas from the calciner is (almost) pure CO_2, meaning that this gas can be routed directly to a CO_2 processing unit without the need for a CO_2 separation plant.

Applying electrification and CO_2 capture to the calciner only (i.e. not to the rotary kiln), corresponding to Alt 2 in Figure 1, is attractive because of the following reasons:

- A relatively high reduction rate (in the order of 70 %) may be achieved.
- It is sufficient to supply heat to a zone of ~900 °C; the very high temperature required in the rotary kiln does not have to be considered.
- Only one of the main equipment units in the kiln system (the calciner) needs to be modified.

2.1 Reference kiln system

A regular cement kiln system is illustrated in Figure 2. The raw meal enters at the top of the preheaters, where it is heated to about 700 °C by hot gases coming from the calciner. In the calciner, most of the preheated meal is calcined at ~900 °C by direct contact with hot gases generated by fuel combustion in the calciner. In the rotary kiln the precalcined meal is first completely calcined, then heated further until partial melt phase and clinker minerals are formed at a temperature of 1400-1450 °C. This rotary kiln heating process also requires fuel combustion. Finally, the clinker is cooled by ambient air in the clinker cooler.

A large fraction of the air heated in the cooler is used as combustion air in the rotary kiln ("secondary air") and in the calciner ("tertiary air"), hence recuperating a significant part of the heat. Some low-temperature heat (at about 200 °C) is, however, lost to the surroundings ("cooler vent air"). The hot exhaust gas from the kiln mixes with the calciner gas, hence contributing with some of the energy required for precalcination. Some fuel conveying air and/or cooling air ("primary air") is supplied in both the rotary kiln and the calciner, and there may be some air inleakage ("false air") in the rotary kiln, calciner and preheater tower.

This system, applying pulverized coal as the fuel in both the rotary kiln and the calciner, is used as the reference process in the current study.

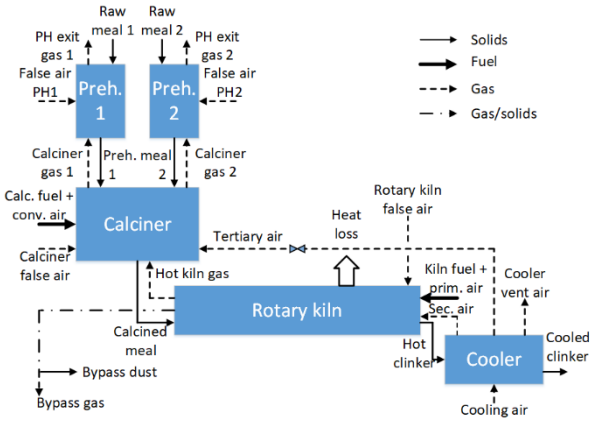

Figure 2: A regular cement kiln system with two preheater strings.

2.2 Kiln system with electrified calciner

A conceptual implementation of calciner electrification combined with CO_2 capture is shown in Figure 3. All calciner fuel is now replaced by heat provided indirectly from electrical energy. The tertiary air is no longer needed in (nor allowed to flow into) the calciner. Instead, its sensible heat is utilized in the preheater. The hot rotary kiln exit gas bypasses the calciner, i.e. it is routed to the preheater, where its sensible heat can be utilized. This means that the only major gas component in the exit gas stream from the calciner is the CO_2 from the decarbonation.

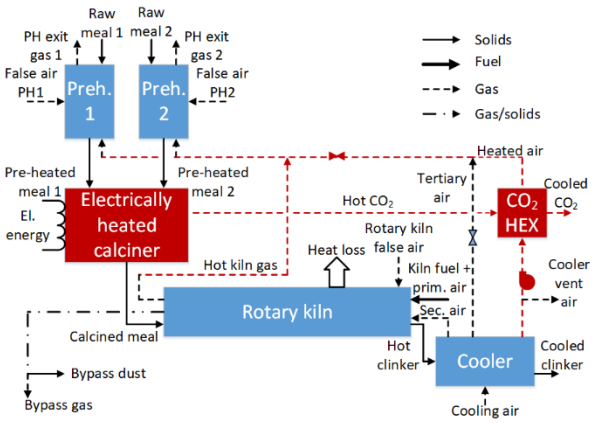

Figure 3: Cement kiln system with two preheater strings equipped with an electrified calciner. (Red-colored units are new/modified, whereas existing units are blue/black.)

A gas-to-gas heat exchanger ("CO_2 HEX") is installed to utilize the heat in the hot CO_2 exiting from the calciner.

A fan (not shown in Figure 3) placed downstream of the CO_2 HEX pulls the CO_2 out of the calciner and through the heat exchanger. A fan is also needed to blow the cooler air from the cooler, via the CO_2 HEX, to the preheater tower.

2.3 Calciner electrification concepts

Different electrical heat transfer concepts were considered in the study. One may distinguish between different electricity-based energy transfer concepts in the way the energy is transferred to the meal, see Table 1. A few concepts may involve direct transfer of electrical energy to the meal in one step ("direct transfer"), but most concepts involve typically two or three transfer steps, i.e. an overall "indirect transfer" process.

Table 1: Potential electricity-based energy transfer concepts.

Energy transfer process	Concept	Number of energy transfer processes	Energy transfer type	Energy medium required?
El → Meal	Microwaves	1	Direct	No
	Induction [b]			
El → Gas → Meal	Plasma	2	Indirect	Yes
	Electrical resistance heating			
	Ultrasound [a]			
El → Solid → Meal	Electrical resistance heating			
	Induction [c]			
El → Solid → Gas → Meal	Electrical resistance heating	3		
	Induction [c]			
El → Liquid → Gas → Meal	Electrolysis of water followed by H_2 combustion in O_2			

[a] Sonification medium needed, [b] Direct induction heating of the raw meal; [c] Induction heating of a solid material used as an intermediate heating medium.

Different types of radiation/waves may be possible to utilize in direct transfer of energy to the meal. In such radiation/wave-based methods, no heat transfer medium is required, which may be a big advantage as only one (direct) energy transfer process is required. If such a scheme is possible, then the calciner exit gas will be only the CO_2 from the decarbonation. As no heat medium is required, there is no need for CO_2 recycling. This category includes microwaves and electromagnetic (direct) induction.

Another possibility is to use a gas, i.e. recycled CO_2, as a heat medium. The gas is heated by electricity and the sensible heat in the hot gas is then transferred to the meal. The heating of the medium may take place by plasma generation or by resistance-based heating. In both cases, recycled CO_2 is heated to a (very) high temperature and will subsequently transfer heat to the meal by radiation and convection.

A gas may also act as a medium for transferring mechanical energy in the form of pressure waves. This is the ultrasound transfer mechanism.

Instead of using a gas as a heat medium, it may be possible to use a solid. In such cases, the solid will be heated by electricity, and then the meal is brought into contact with the hot solid. This may or may not require motion of the solid heat medium, depending on the concept. The solid medium may be heated by induction or by resistance heating. In both cases, the solid must be electrically conducting. The heat transfer will be a combination of direct contact (conduction) and radiation heat transfer.

An even more complex energy transfer concept would be to introduce still one more medium, i.e. a gas (recycled CO_2) which is heated by the hot solid. The heated gas is next used to calcine the meal. The same electrical heating concepts could be applied as in the previous category, i.e. induction heating or resistance-based heating. The solid heat medium could be the walls in a heat exchanger or possibly internals inside a vessel.

Finally, electricity could be used to electrolyse water to form hydrogen and oxygen. Hydrogen is combusted, generating heat required for calcination, which takes place by direct contact between the meal and the hot steam generated in the combustion process. This may require a recycle stream to control the temperature and the combustion properties of the burnable gas. Even though this concept involves combustion, and in that respect is quite similar to the regular calcination process, it is still different in the sense that electricity is the energy source and no CO_2 is generated.

The concepts listed in Table 1 are described in some more detail below.

2.3.1 Microwave heating

It is possible to perform calcination of $CaCO_3$ by radiation from a microwave source [2, 3], usually called a magnetron. General descriptions of different technologies are available for example in a paper from the company Ceralink [4] and in a book from Intech [5]. The company Microwave Research and Applications Inc. can deliver technology and equipment for microwave calcination [6]. Another company involved in development of microwave calcination is C-Tech Inc. [7].

The main advantage of the concept is that it applies direct transfer of energy (in the form of electromagnetic waves) to the meal. Hence, the relatively high heat transfer resistance found in systems with indirect heat transfer may be avoided. Furthermore, due to the nature of the energy form, it is expected that the energy input can be adjusted quickly, giving efficient process temperature control. The paper from Ceralink [4] claims that microwave technology needs less energy consumption than conventional heating. In the documentation from C-Tech Inc. [7] it is claimed that a combination of traditional heating with convection or radiation and microwave heating is advantageous. One paper [8] describes the calcination of mega-crystalline calcite at 950°C and compares a microwave oven with an electric furnace. The authors claim that a microwave oven gives faster calcination.

A review article from Buttress et al. [9] gives a critical review of the potential of microwave processing in the

cement industry. The paper indicates a large energy consumption of the microwave technology, likely related to energy losses. This may in turn be related to $CaCO_3$ not exhibiting good properties for absorption and transformation of microwave energy into heat. Moreover, there may be safety concerns for personnel operating the system. Besides, superheating of materials might be a challenge. The goal is to heat the materials to about 900°C, but it is possible that local hot spots could occur, and that the minerals in the raw meal in such hot spots start to decompose or melt.

2.3.2 Plasma heating

Plasma is considered to be the fourth aggregate state. However, a gas is required for generation of plasma. This gas is commonly referred to as plasma gas. In a plasma, many of the particles are charged, i.e. electrons, protons, and ions. The ratio between electrically charged and neutral particles indicates the degree of ionisation of the plasma. In a plasma, forces will be generated between the electrically charged particles, and this will affect the organisation and movement of the particles. The plasma will be able to conduct electricity, and both influence and be influenced by electromagnetic fields. This allows for manipulation of the plasma externally using electric and magnetic fields [10, 11].

One of the uses for plasma is heat generation for industrial processes. When plasma is formed through interaction between a gas and an electric arc, the gas becomes ionised and consequently both thermally and electrically conductive. This enables the transfer of energy from the arc to the process gas and then to the process or furnace [12]. Such an installation is often called a plasma torch.

According to Westermoen [13], further expansion of plasma technology in industry is dependent on improving the characteristics of plasma torches and electric arc reactors. The main factors to consider are increased operating life of electrodes (currently relatively short due to the high thermal stress) to several hundreds and further to thousands of hours, increased thermal efficiency, working gases of different chemical composition, and increased yield of product.

According to Zhukov and Zasypkin [14], multi-jet plasma chemical reactors with mixing chamber are widely used for waste treatment and production of ultrafine powders. Nyrstar Høyanger operates a high temperature plasma furnace for metal processing [15] and claim that thermal plasma torches could be an alternative to conventional fossil fuel burners in the industry to provide heat in a process.

Advantages include lower operating cost, lower gas volumes, reduced need for flue gas cleaning, and lower greenhouse gas emissions (assuming renewable sources for electricity generation). A relatively high thermal efficiency can be achieved [12, 14]. According to Jensen [16], a 3 MW rotating plasma furnace achieved 90% overall heat efficiency in laboratory testing. Moreover, the response time is short, with good process control and temperature regulation [12, 16]. It has been confirmed experimentally in the CemZero project [17] that CO_2 can be used as a plasma gas.

As mentioned above, a disadvantage of the plasma technology is a relatively short operating life for the electrodes (reportedly 600–1000 hours [12]). Besides, water cooling is required, giving some energy loss, and unwanted reactions may potentially occur in the high temperature arc [13].

2.3.3 Electrical resistance heating

A metal surface can be heated by resistance heating (also called ohmic heating or Joule heating) and in turn transfer heat i) to a gas by convection (and the gas will in turn heat and calcine the meal through convection), ii) directly to the meal by radiation through the gas medium (CO_2) or iii) directly to the meal by conduction, provided that the meal is brought into direct contact with the hot surface.

Calcination via heat transfer from heating elements is well known from lab-scale muffle furnaces used in the cement industry, typically operating up to 1100°C. But in such cases, only a small amount of material is calcined, and the material is not moving.

In an industrial application, the material has to flow through the calciner while being decarbonated. One may implement this in different types of calcination reactors, such as a drop tube [17, 18], a fluidized bed [19] or a rotary kiln [20]. For the concept to work, one has to use heating element materials that are suitable for use at sufficiently high temperature and that can withstand the impacts from the flowing meal.

2.3.4 Ultrasound heating

Ultrasound is a form of vibrational energy (more than 18000 cycles/s) that is propagated as a mechanical wave by the motion of particles within the medium. The wavelengths of ultrasound are in the order of millimetres [21]. Ultrasound does not involve molecular level vibration, such as the heat generation in metals due to induction energy or microwaves. The wave causes compressions and rarefactions of the medium, thus propagating a pressure wave along with the mechanical movement of the particles in the medium.

Apparently, ultrasound has never been used in high-temperature applications or for heating purposes and has not been tested widely. It has mainly been used at small-scale for low-temperature heating, e.g. drying food [22].

A disadvantage of ultrasound is that using a gas as the sonication medium is inefficient as the heat transfer is low [23]. This is a big disadvantage of the method and suggests that the method is not suitable. The method could also create local hot spots. Furthermore, the absorption of ultrasound energy into porous solids is high, and reflection back to the sonication media may lead to high energy losses as it is not absorbed by the solids.

2.3.5 Induction heating

In induction heating, an electrically conducting object is heated through electromagnetic induction. An electronic oscillator passes a high-frequency alternating current through an electromagnet. A rapidly alternating magnetic field will then penetrate the object to be heated and generate eddy currents inside the conductor, and these

currents heat the material by Joule heating [24]. Joule heating is the same as resistance heating, which has already been described above. Hence, the difference between induction heating and electrical resistance heating in this study is mainly the way the electrical energy is transferred.

Induction heating, which is known as an efficient way to reach local high temperatures fast, is applied for example in induction welding [25] and in induction furnaces [26] used for melting different types of metals.

To use induction, the object to be heated must be electrically conducting. And if the object is also made of a magnetic material, such as steel, the induction heating process is more efficient.

As indicated in Table 1, one may envision one of the following energy transfer concepts: i) direct induction heating of the meal, ii) induction heating of a solid, which in turn will heat and calcine the meal through radiation or conduction and iii) induction heating of a solid, which in turn will heat a gas, which in turn will be brought into direct contact with the meal so that it is heated and calcined.

Direct heating of the meal using induction (point i above) appears to be not viable as the meal has a poor electrical conductivity and is also non-magnetic. The next two options (point ii and iii), both involving induction heating of a solid, could be possible if the solid is made of steel, which is electrically conducting and ferromagnetic.

Induction heating of granular media, which are subsequently heating a fluid, is a method described in a technical book published for designers, manufacturers and users of industrial equipment involving induction [27]. One may envision a packed bed of meal containing metallic susceptors disseminated in the meal bed. The susceptors would then be heated by induction and transfer heat to the meal by conduction. Such a process has been tested on preparation of activated carbon. However, it seems to be a challenge obtaining a homogeneous temperature distribution in such a system [27].

A disadvantage of the indirect heating via a hot gas is that a very high gas flow rate is required, contributing to heat losses in the system. Moreover, the induction heating equipment must be cooled, meaning that there may be significant energy losses from an induction system, reducing the efficiency of the calcination process.

2.3.5 Electrolysis of water followed by hydrogen combustion in oxygen

The main idea of this concept is to keep a direct combustion process in the calciner, but avoid CO_2 formation by combusting hydrogen. This has the big advantage that direct heat transfer between the combustion products and the meal is maintained, and no additional heat transfer surfaces are required. Instead, the electrical energy is spent on dissociating liquid water into hydrogen gas and oxygen gas. This mixture is subsequently combusted in the calciner. To control the temperature in the process and to prevent explosions, the mixture of H_2 and O_2 may be mixed with recycled CO_2.

There are several different water electrolysis cell technologies, the three main ones being Alkaline Electrolysis Cells (AEC), Proton Exchange Membrane Electrolysis Cell (PEMEC), and Solid Electrolysis Cells (SOEC). Ogawa et al. [28] and Schmidt et al. [29] provide a review of the current trends and merging technologies, and an expert elicitation study on future cost and performance, respectively. In addition, Schmidt et al. [29] gives an overview of the main characteristics of the three technologies; operational, input and output parameters, lifetime, and investment cost.

2.3.6 Selection of heat transfer concept

The resistance-based heating concept was selected for the following reasons:

- It requires no (or very little) CO_2 recycling, hence losses related to waste heat from a hot CO_2 stream can be minimized.
- It has a high efficiency, i.e. low losses related to conversion of electrical energy into thermal energy.
- It is a relatively simple and well-proven heat transfer technology, hence the costs are likely to be low compared to more sophisticated concepts.
- There are no major safety concerns.

2.4 Rotary calciner with resistance-based heating

As explained above, there are different ways to implement the resistance-based heating concept. In this study, a rotary kiln was selected as the reactor type. There are several reasons for that:

- The meal flow and its residence time in the calciner can be readily controlled in a rotary calciner.
- It appears to be technically feasible to implement heating elements with a sufficiently high surface temperature to perform the heating and calcination of the raw materials.
- Rotary kilns are already in use in the cement industry and can be regarded as well-known technology.

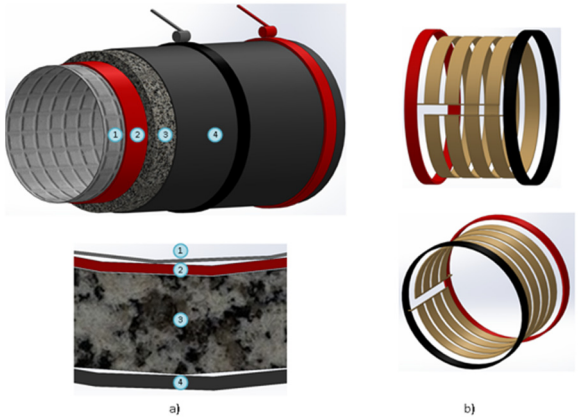

Figure 4**:** Suggested rotary calciner design (a, with 1: protective layer, 2: heating elements, 3: refractory and 4: steel shell) and arrangement of the heating elements (b).

A potential implementation of the heating system is shown in Figure 4. The rotating cylinder is equipped with a slip ring for transfer of electrical energy to the heating elements. The elements are covered by a thin protective

layer on the inside (exposed to the hot meal flowing through the rotary calciner). Outside the heating elements there is a refractory layer to minimize the heat loss to the surroundings. The cylinder itself is made of carbon steel, similar to a regular clinker kiln.

3. MODELLING OF THE MODIFIED SYSTEM

The electrified calciner is integrated with an existing cement kiln system in such a way that minimum disturbance of the production process is obtained, i.e. the material streams (gases and solids) in the preheater, rotary kiln and cooler are kept close to the flow rates in the regular system (cf. Figure 1).

3.1 Mass and energy balance

A mass and energy balance for steady state conditions was conducted, so that relevant temperatures, flow rates and duties in the modified system (cf. Figure 2) could be calculated and compared with the values in the regular system (cf. Figure 1). A set of altogether 176 equations (not shown here) constitutes the mass and energy balance for the kiln system.

3.2 Design basis

The design basis values are summarized in Table 2. The values are selected to cover typical process conditions in a modern precalciner cement kiln system producing 1 Mt of clinker per year.

3.3 Calculation results

Selected calculation results for both systems are shown in Table 3. The calciner exit gas flow rate is reduced from 270 to 67 t/h because the calciner fuel, the tertiary air and the kiln gas streams are no longer entering the calciner (cf. Figure 3). However, the preheater exit gas is only slightly reduced (from 316 to 306 t/h) because the kiln gas, the tertiary air and some of the vent air from the cooler has been routed to the preheater tower. Hence, the vent air is reduced from 177 to 106 t/h. Moreover, the preheater exit gas is only slightly reduced (from 446 to 399 °C), and this is also the case for the preheated meal temperature (from 700 to 658 °C). This ensures minimal impact on the kiln process and means that no modification of the preheater tower, rotary kiln or cooler is required.

The net CO_2 emissions from the kiln system is reduced from 114 to 32 t/h. This is due to the elimination of calciner fuel CO_2 generation and the capture of the CO_2 from the precalcination process. The only extra CO_2 contribution from the electrifed calciner system is coming from the electricity generation. A CO_2 footprint of 47 g/kWh (corresponding to the Norwegian energy mix in the period 2011-2015) [30] has been assumed for the electrical energy.

The net CO_2 emission reduction in the electrified calciner case is 72 % when compared to the regular coal-fired plant.

Table 2**:** Design basis values.

Parameter	Unit	Regular system	System with el-calciner
Clinker production	t/y	1 000 000	1 000 000
Operation time	h/y	7 315	7 315
Specific thermal energy cons.	MJ/kg_cli	3.40	Calculated
Calciner CO2 capture rate	-	0 %	90 %
CO2 footprint of electricity	gCO2/kWhel	47	47
Mass fraction of CaCO3 i raw meal	kg/kg	0.77	0.77
Cyclone 1 efficiency	-	94 %	94 %
Calciner thermal energy fraction	-	62 %	Calculated
Calcination degree in the calciner	-	94 %	94 %
Primary air supply in the rot. kiln	-	8 %	8 %
Purged bypass gas	-	5 %	5 %
Primary air supply in the calciner	-	5 %	5 %
O2 in the rotary kiln exit gas (dry)	vol%	3 %	3 %
O2 in the calciner exit gas (dry)	vol%	3 %	3 %
Bypass dust ratio	kg/kg_cli	0.02	0.02
False air in the rotary kiln	kg/kg_cli	0.03	0.03
False air in the calciner	kg/kg_cli	0.01	0
Specific clinker cooling air supply	Nm^3/kg_cli	2.0	2.0
Mass fraction of C in fuel	kg/kg	0.722	0.722
Mass fraction of H in fuel	kg/kg	0.040	0.040
Mass fraction of O in fuel	kg/kg	0.057	0.057
Mass fraction of S in fuel	kg/kg	0.012	0.012
Mass fraction of N in fuel	kg/kg	0.016	0.016
Mass fraction of moisture in fuel	kg/kg	0.018	0.018
Mass fraction of ash in fuel	kg/kg	0.135	0.135
Lower heating value of fuel	MJ/kg	28.0	28.0
Specific rotary kiln heat loss	MJ/kgcli	0.15	0.15
Ambient temperature	°C	20	20
Hot clinker temperature	°C	1 400	1 400
Minimum temp. diff. in HEX	°C	NA	100
Calcination temperature	°C	900	900
Meal inlet temperature	°C	50	50
Calciner fuel inlet temperature	°C	30	30
Calciner primary air inlet temp.	°C	30	30
El-to-heat efficiency	-	NA	90 %
Rotary kiln fuel inlet temperature	°C	30	30
Rotary kiln primary air inlet temp.	°C	30	30

3.4 Impacts on the cement kiln process

No negative impacts on the process, product quality or emissions are expected. This is because the mass flow rates and temperature profiles in the system are identicial to or kept very close to the values in the regular system. There are no changes at all in the cooler or in the rotary kiln and only minor changes in the preheater tower. The calciner is of course different in many respects, but the meal exiting the calciner has the same temperature and degree of calcination as in the regular system.

One may expect somewhat lower emissions of combustion related components, such as CO and VOC, as there is no longer any combustion going on in the calciner. This is a potential positive side-effect of the new system.

The following modifications to the system are required:

- a new calciner, equipped with an electrically driven heating system
- a new electrical power supply system of ~85 MW
- a new CO_2/air heat exchanger (HEX)
- a new CO_2 processing system
- a new gas duct from the kiln inlet to the preheater tower

- a new gas duct for conveying of the air into and out of the CO_2 HEX
- re-routing of the tertiary air duct

Table 3: Comparison of selected process values.

Parameter	Unit	Regular system	System with el-calciner
Secondary air	t/h	61	61
Rotary kiln exit gas	t/h	79	79
Tertiary air	t/h	114	114
Calciner exit gas	t/h	270	67
Preheater inlet gas	t/h	270	260
Preheater exit gas	t/h	316	306
Air heated in CO2 HEX	t/h	0	71
Cooler vent air	t/h	177	106
Gross raw meal feed rate	t/h	221	223
Net raw meal feed rate	t/h	207	210
Gross precalcined meal (w/ ash)	t/h	143	143
Clinker production	t/h	137	137
CO2 from raw meal decarbonation	t/h	70	71
Fuel-gen. CO2 in the rotary kiln	t/h	17	17
Fuel-gen. CO2 in the calciner	t/h	27	0
CO2 from precalcination	t/h	66	67
CO2 from precalcination captured	t/h	0	60
CO2 from precalcination emitted	t/h	66	7
CO2 from postcalcination	t/h	4	4
Net fuel-gen. CO2 in the rotary kiln	t/h	17	17
Net fuel-gen. CO2 in the calciner	t/h	27	0
CO2 from electricity production	t/h	0	4
Net CO2 emissions	t/h	114	32
Secondary air temperature	°C	881	881
Kiln gas exit temperature	°C	1 150	1 150
Tertiary air temperature	°C	684	684
Preheater gas inlet temperature	°C	900	860
Preheater exit gas temperature	°C	446	399
Raw meal exit temp. preheater	°C	700	658
Clinker temp. vent air zone	°C	97	97
N2 in the PH exit gas	vol%	65 %	78 %
CO2 in the PH exit gas	vol%	26 %	4 %
H2O in the PH exit gas	vol%	3 %	1 %
O2 in the PH exit gas	vol%	6 %	17 %
Calciner fuel energy	MW	80	0
Calciner el-to-heat energy	MW	0	76
Electrical power loss	MW	0	8
Rotary kiln fuel energy	MW	49	49
Net CO2 emission reduction	%	0 %	72 %

4. CO_2 COMPRESSION

Downstream of the kiln system, the CO_2 is compressed to 70 bar and 25 °C. Liquefaction is not included. Figure 5 shows the CO_2 processing section.

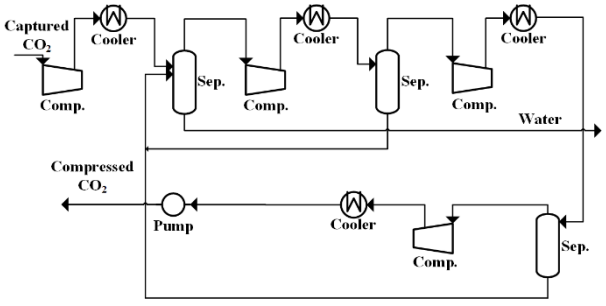

Figure 5: CO_2 compression plant.

The CO_2 entering the compression and liquefaction section has been taken as a pure stream. In reality it may contain some impurities, such as O_2 and N_2 from false air entering into the calciner along with the the raw meal. However, the concentrations are on ppm levels, so have not been included in the process calculations.

5. COMPARISON WITH POST-COMBUSTION AMINE ABSORPTION CO_2 CAPTURE

When evaluating the electrified calcination and CO_2 capture concept it is compared with CO_2 capture by amine absorption as this can be considered the most mature capture technology today [31].

A generic amine absorption plant is shown in Figure 6. The flue gas entering the absorption plant is the preheater gas from the kiln system shown in Figure 2. The CO_2 from the capture plant ("CO_2 to compressions" in Figure 6) is routed to a CO_2 processing plant as shown in Figure 5.

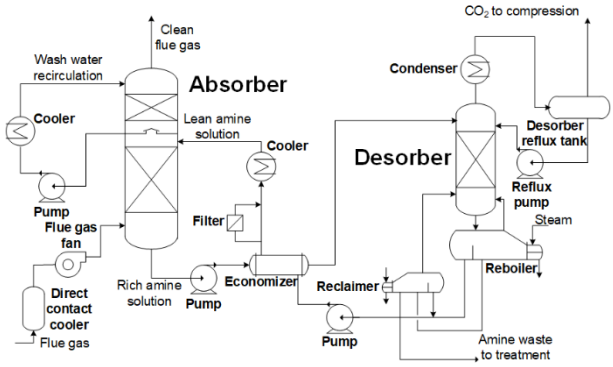

Figure 6: Amine absorption plant.

Three different scenarios are compared, as shown in Table 4. Case 1 can be seen as a "standard" post-combustion absorption process implemented to obtain around 90 % CO_2 capture. Such a process requires a significant amount of thermal energy for regeneration of the solvent (3.7 MJ/kg_{CO2} in this study). The thermal energy can be provided in different ways, for example by combustion of fuels (which would give an extra on-site CO_2 footprint), such as natural gas, but to facilitate comparison it has been assumed that this energy is provided via an electric boiler.

In Case 2, an advanced proprietary amine with a lower specific solvent regeneration energy (3.0 MJ/kg_{CO2}) is applied, and all the energy required for the regeneration is provided by waste heat available in the kiln exhaust gases (33 MW in this study) and by process integration (13 MW in this study) inside the battery limit of the capture plant (hence a partial capture case). Such waste heat utilization is possible because the solvent regeneration occurs at a relatively low temperature (~120 °C), which is a big advantage of the amine-absorption process both when it comes to energy consumption and operational costs. However, significant amounts of waste heat are only available in some cement plants.

Case 3 is the electrified calciner case, which is also a partial capture case because the CO_2 from the rotary kiln is not captured.

Table 4: Compared CO_2 capture cases.

Case	Concept	CO_2 capture	Cement plant waste heat
1	Absorption using an optimized standard MEA solvent	Full (post-comb.)	Not used
2	Absorption using an advanced proprietary amine solvent	Partial (post-comb.)	The only source of energy for solvent regeneration
3	Rotary calciner applying electric resistance heating	Partial (inte-grated)	Not used

The energy consumption in the three cases is shown in Figure 7. Both in the standard MEA case and in the electrified calciner case, the electricity consumption makes the biggest contribution. In the MEA case, this is due to the electrical power consumption required for providing energy to the reboiler in order to regenerate the solvent (cf. Figure 6).

The advantage of the waste heat scenario is very clear from the graph; the electrical energy is almost eliminated because all energy required for regeneration of the solvent is provided by waste heat. However, as mentioned, waste heat is not available in all cement plants, at least not to the same extent as in the plant used in this study. Several factors impact the waste heat availability, such as the fraction of exhaust gas utilized for drying the raw materials, the excess air levels in the combustion zones and false air inleakage in the preheater tower.

An advantage of the electrified calciner case, however, is the significant reduction of fuel energy in the calciner. For a coal-fired calciner, this means a significant reduction in fuel costs and hence operational costs of the cement kiln system.

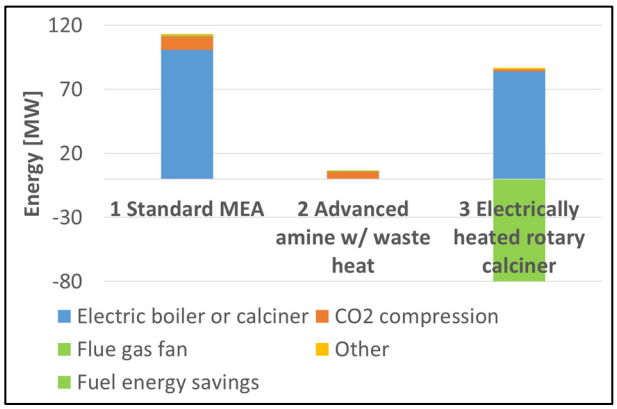

Figure 7: Electrical energy consumption and fuel energy savings in the three compared scenarios.

6. COST ESTIMATION

The new process equipment units in the electrified calciner system (cf. Figure 3) and all the required units in the CO_2 processing system were designed and sized.

With all components identified and sized, a detailed factor estimation method [32] was applied to make a cost estimate for the capital expenditure (CAPEX). This method normally has an uncertainty of ± 40% (80% confidence interval). The equipment costs are for the most part calculated using the "Aspen In-Plant Cost Estimator" v10. It was assumed that the CO_2 capture plant built is the n^{th} of a kind (NOAK; i.e. the technology is mature), hence the costs reflect that maturity level. Further cost input data, including inputs for the operational expenditure (OPEX), are given in Table 5. The annual costs are calculated based on a utility and personnel unit price list, and maintenance cost. It should be noted that the electricity cost is set as low as 0.033 EUR/kWh as the installation of transformers are included in the investment cost. The reduced coal consumption in the calciner in the el-calciner case is included in the cost calculation as a fuel saving.

Table 5: Cost calculation input data.

Parameter	Unit	Value
Operating hours	h/y	7 315
Electricity price	EUR/kWh	0.033
Coal price	EUR/t	111
Cooling water	EUR/m³	0.02
Personnel (operators)	kEUR/y	650
Maintenance (% of CAPEX)	%	4
Interest	%	7.5
Number of years for depreciation	-	25
Contingency	%	20
Cost data reference year	-	2018

The costs per mass of avoided CO_2 are illustrated in Figure 8. The advantage of the low electrical energy consumption in the waste heat scenario is evident, giving a total cost of 40 € per ton of avoided CO_2. The electrified calciner case is, however, less costly (67 €/t_{CO2}) than the amine case operating without waste heat utilization (75 €/t_{CO2}).

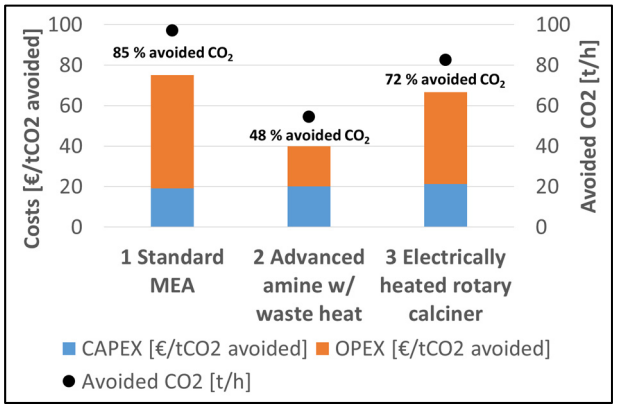

Figure 8: CO_2-specific operational costs (OPEX) and capital costs (CAPEX) and avoided CO_2 emissions.

A sensitivity analysis was also made to investigate the impact of changes in the input parameters (which may be different in the future). The details are not shown here, but the main outcome is that the strong dependence of Scenario 1 and 3 on electrical energy make them very sensitive to variations in electricity price and CO_2 footprint.

7. CONCLUSIONS

Calcination based on electric heating appears to be possible. Different energy transfer concepts may be applied, but heat transfer based on ohmic resistance seems to be a good solution when only the calciner is considered. It is possible to implement such a system in an existing kiln system without any negative impacts on the process, emissions or product quality.

In cement plants where large amounts of waste heat are available, amine-based absorption appears to be the least expensive option for reduction in CO_2 emissions. However, in systems with no such waste heat available, electrified calcination, for example in the form of electrified rotary calciners, may be a competitive alternative to post-combustion capture technology.

Acknowledgements

Gassnova is greatly acknowledged for partial funding of the project.

References

[1] Andrew, RM.: "Global CO_2 emissions from cement production, 1928–2017", Earth Syst. Sci. Data, 10, 2213–2239, 2018

[2] Wikipedia, "Calcination", Available online, https://en.wikipedia.org/wiki/Calcination

[3] Tran, H.N. and Mostaghimi, J.: "Microwave heating device for lime and calcining", patent, available online: https://patents.google.com/patent/US5525783

[4] Fall, M., Esquenazi, G., Allan, S., Shulman, H. "Rapid Limestone Calcination Using Microwave Assisted Technology", ACEEE Summer Study on Energy Efficiency in Industry, 2011.

[5] Koleini, S.M.J., Barani, K. Microwave Heating Applications in Mineral Processing, Intech, 2012.

[6] "Microwave Research and Applications", Available online: http://www.microwaveresearch.com (accessed June 2019)

[7] C-tech, "Induction heating equipment", Available online: http://www.ctechinnovation.com/qulom-advanced-induction-heating/

[8] Hwang, D.J., Ryu, J.Y., Park, J.H., Yu, Y.H., Lee, S.K., Cho, K.H., Han, C., Lee, J.D. "Calcination of mega-crystalline calcite using microwave and electric furnaces" Journal of Industrial and Engineering Chemistry, 18, pp. 1956-1963, 2012.

[9] Buttress, A.J., Jones, D.A., Kingman, S.W., "Microwave processing of cement and concrete materials - towards an industrial reality?", Cement and Concrete Research, 68, pp. 112-123, 2015. ISSN 0008-8846

[10] Wikipedia, "Plasma", Available online (accessed June 2019): https://en.wikipedia.org/wiki/Plasma_(physics)

[11] "Plasma", Available online (June 2019): https://snl.no/plasma_-_fysikk

[12] Westinghouse Plasma Corporation: "Westinghouse Plasma Torches", available online (accressed May 2018): http://www.alternrg.com/wp-content/uploads/2012/11/WPC-Plasma-Torches-Eng-Email-Feb-2012.pdf

[13] Westermoen A., "Modelling of Dynamic Arc Behaviour in a Plasma Reactor", Doctoral Theses at NTNU, 2007:38, 2007

[14] Zhukov M.F., Zasypkin I.M., 2007, "Thermal Plasma Torches", Cambridge International Science Publishing, http://www.itam.nsc.ru/upload/medialibrary/76c/plasma-heaters.pdf

[15] Nyrstar, "Resources for a changing world", available online (accessed 17 September 2019): https://www.nyrstar.com/~/media/Files/N/Nyrstar/resources-and-materials/factsheets/fact-sheet-hoyanger.pdf

[16] Jensen R., State of the Art Plasma Research at SINTEF-NTNU, available online (accressed May 2018): https://www.sintef.no/contentassets/8bfce4fab2554785973774fbb248041d/state-of-the-art-plasma-research-at-sintef-ntnu.pdf

[17] Wilhelmsson, B., Kollberg, C., Larsson, J., Eriksson, J., Eriksson, M., "CemZero – A feasibility study evaluating ways to reach sustainable cement production via the use of electricity", Project report, Cementa/Vattenfall, 2018

[18] Vincent, A., Rennie, D., Sceats, M., Gill, M., Thomson, M., "Public LEILAC Pre-FEED Summary Report", Project report, October 2016

[19] Kunii, D., Levenspiel, O., "Fluidization engineering – Second edition", Butterworth-Heinemann, USA, 1991

[20] Gao, Y., Glasser, B.J., Ierapetritou, M.G., Cuitino, A., Muzzio, F.J., Beeckman, J.W., Fassbender, N.A., Borghard, W.G., "Measurement of residence time distribution in a rotary calciner", AIChE Journal, Vol.59, No. 11), pp 4068-4076, 2013

[21] Hynynen, K., "Ultrasound Heating Technology, in Thermoradiotherapy and Thermochemotherapy: Biology, Physiology, Physics, M.H. Seegenschmiedt, P. Fessenden, and C.C. Vernon, Editors", Springer, pp. 253-277, 1995

[22] Kowalski, S.J., "Ultrasound in wet materials subjected to drying: A modeling study", International Journal of Heat and Mass Transfer, 84 ,pp. 998-1007, 2015

[23] John, O.A. et al., "Synthesis of Hydroxyapatite through Ultrasound and Calcination Techniques", IOP Conference Series: Materials Science and Engineering, 203(1), 2017.

[24] Wikipedia, "Induction heating", available online (August 2018): https://en.wikipedia.org/wiki/Induction_heating

[25] Wikipedia, "Induction welding", available online (August 2018): https://en.wikipedia.org/wiki/Induction_welding

[26] Wikipedia, "Induction furnace", available online (August 2018): https://en.wikipedia.org/wiki/Induction_furnace

[27] Elektra, "Electromagnetic induction and electric conduction in industry", Centre Francaise de l'Electricité, ISBN 2-910668-26-6

[28] Ogawa T., Takeuchi M., Kajikaw Y, "Analysis of Trends and Emerging Technologies in Water Electrolysis Research Based on a Computational Method: A Comparison with Fuel Cell Research", Sustainability, 10, 478, 2018, doi:10.3390/su10020478

[29] Schmidt, O., Gambhir, A., Staffell, I., Hawkes, A., Nelson, J., Few, S., "Future cost and performance of water electrolysis: An expert elicitation study", International Journal of Hydrogen Energy, 42, pp. 30470–30492, 2017

[30] Asplan Viak, Available online (accessed December 2017) https://www.asplanviak.no/aktuelt/2016/02/03/nordisk-stroem-blir-renere/

[31] Tokheim, L.A., Eldrup, N., Anette Mathisen, A., "Norcem CO_2 capture project: Benchmark Study – Commercial Scale Perspective - Preliminary results from WP7 Benchmark Study", International CCS Conference, Langesund, 20-21 May 2015

[32] Eldrup N.H., Mathisen A., Skagestad R., Haugen H.A, A Cost Estimation Tool for CO_2 Capture Technologies. 14th Greenhouse Gas Control Technologies Conference Melbourne 21-26 October 2018 (GHGT-14). Available online: https://ssrn.com/abstract=3366036

ENERGY AND MATERIAL MINIMIZATION DURING CO_2 CAPTURE USING A COMBINED HEAT AND MASS INTEGRATION TECHNIQUE

K.O. Yoro [1], N. Chiwaye [1], A.J. Isafiade [2], M.O. Daramola [1, *]

[1] School of Chemical and Metallurgical Engineering, Faculty of Engineering and the Built Environment, University of the Witwatersrand, Private Bag X3, Wits 2050, Johannesburg, South Africa

[2] Department of Chemical Engineering, University of Cape Town, Private Bag, Rondebosch 7701, Cape Town, South Africa

*Corresponding author e-mail: michael.daramola.wits.ac.za

Abstract

Heat and mass exchange occur concurrently during CO_2 capture. Therefore, the application of a combined heat and mass exchanger network (CHAMEN) could be a very good option to reduce energy and material consumption simultaneously during CO_2 capture. In this study, a systematic technique for the synthesis of combined heat and mass exchanger networks (CHAMENs) was introduced to concurrently minimize the use of external utilities and mass separating agents (MSA) during adsorptive CO_2 capture. The method proposed in this study is based on an innovative approach that integrates a mathematical programming technique for the heat exchanger networks (HENs) synthesis and a sequentially-based composition interval technique for mass exchanger networks (MENs) synthesis with regeneration. A combined optimization approach was used to minimize the total annualized cost of the synthesized CHAMEN. An example was solved to test the efficacy of the proposed method. The cost of mass separating agents, as well as hot and cold utilities which form the total annualized costs (TAC) for the combined heat and mass exchangers, was minimized. The total annualized cost (TAC) of the synthesized CHAMEN obtained in this study (TAC=$199800/yr) showed significant improvement over the TAC reported in the literature using other synthesis techniques. Results obtained in this study confirmed that the integration of a combined heat and mass exchanger with regeneration network is an effective way to minimize heat and mass during adsorptive CO_2 capture. The combined heat and mass exchanger networks adequately satisfied the heat and mass balance of the process with a lower total annualized cost.

Keywords: *Adsorption, CO_2 capture, Combined heat and mass exchanger network, Energy minimization, Mass separating agent, Process optimization*

1. Introduction

Most CO_2 capture techniques (e.g. absorption, adsorption and membrane separation) are material and energy-intensive in nature. So far, sorbent blending and scrubbing; the use of phase change solvents; and extra external utilities such as steam and cooling water have been proposed as ways to reduce energy consumption during CO_2 capture [1]. Although these strategies have helped in dropping down energy requirement to some extent, it has in turn increased process cost thereby rendering carbon capture an expensive technology. To ensure the economic advantage of the available CO_2 capture techniques, this study proposed the application of process synthesis techniques through the synthesis of heat exchanger networks (HENs) and mass exchanger networks (MENs) to minimize both energy and material consumption. Heat and mass exchanger network synthesis has been a major research topic in the field of process system engineering and environmental sustainability because heat and mass are very important resources in many industrial applications [1], [2]. Industrial applications like the separation of CO_2 from flue gas streams using sorbents account for high consumption of energy and other resources such as sorbents, steam and cooling water [3]. The excessive use of these important but expensive resources must be minimized to make CO_2 capture technology affordable in developing countries, especially in sub-Saharan Africa [4]. So far, It has been documented in the literature that the application of heat and mass exchanger networks or a combination of both in CO_2 capture studies could be a promising technique for integrating processes with a potential of providing meaningful improvements over the synthesis of the individual heat and mass exchanger networks [1, 5–7]. Since the use of heat and mass is typically intertwined in most CO_2 capture techniques, it is important to account for such interactions in this study. Furthermore, heat and mass exchanger network synthesis has been a key area of research that has significantly contributed to industrial energy-saving, improved plant efficiency and material minimization since the past four decades [8].

Until now, researchers have attempted the synthesis of heat and mass exchanger networks separately without combining them with a regeneration network [9-11]. Furthermore, the majority of HENs synthesis techniques reported in open literature applied pure mathematical programming approaches based on the stage-wise superstructure model proposed by Yee and Grossmann [12]. The superstructure-based SYNHEAT model allows for a large number of likely stream matches into a superstructure, while fully considering stream splitting and isothermal mixing [13], [14]. According to Furman

and Sahinidis [15], the superstructure-based method is very effective when used to determine potential networks. However, its complex non-linear formulation makes it challenging to solve with current solvers. Also, most superstructure-based formulations do not consider some important details for heat exchanger design, such as fluctuating heat transfer coefficients, pumping costs, number of baffles, tube passes, and number of shells. In addition, the formulation of Yee and Grossman [12] cannot be extended to consider the aforementioned details for heat exchanger design because its already complex combinatorial nature with increased non-linearity will not yield optimal solutions. Other reports in this field that did not apply the super-structure based approach used pinch analysis-based concepts [15].

As far as could be ascertained, most CHAMEN synthesis techniques reported so far in the literature applied mathematical programming or pinch analysis techniques separately. No methodology has effectively combined a pinch technology-based technique with a mathematical programming technique to synthesize a combined heat and mass exchanger network while considering sorbent regeneration. This study presents an overview of combined heat and mass exchanger networks synthesis (CHAMENS) in relation to energy and resource minimization while considering sorbent regeneration. It also discusses a hybrid simultaneous-sequentially based methodology to design and operate CHAMENs with a focus on applying it to reduce the high energy requirement associated with sorbent-based CO_2 capture methods. This hybrid technique is new and its application in the field of CO_2 capture has not been reported before now.

Nomenclature

A	Heat transfer area
B	Exponent in cost equation of heat exchanger
C	Unit cost for MSA/lean stream/utility
CF	Fixed cost for heat exchanger
Cp	Heat capacity
cu	Cold utility
C_{CU}	Hot utility unit cost
C_e	Heat exchanger area cost coefficient
CF_{CU}	Unit charge of cooler (fixed)
CF_e	Heat exchanger unit's fixed charge
CF_{HU}	Heater unit's fixed charge
C_{HU}	Area cost coefficient for the heater
C_{HU}	Unit cost of hot utility
C_j	Final CO_2 adsorbed by MSA
FC	Annualized capital cost
F_{CP}	Heat capacity flow rate of main stream
G_i	Mass flow rate of the rich main stream
hu	Hot utility
i	i^{th} rich stream
j	j^{th} MSA/lean stream
k	k^{th} stage in MEN
L	Mass flow rate of the MSA/lean main stream
MEN	Mass exchanger network
MSA	Mass separating agent/lean stream
N	Number of mass exchanger trays
Q	Heat load
Qcu	Heat load of cold utility
Qhu	Heat load of hot utility
R	Rich stream
TAC	Total annual cost
T_j^{LB}	Inlet temperature to MSA
T_j^{UB}	Outlet temperature from MSA
x_j^s	Supply composition of CO_2 in the MSA
x_j^t	Target composition of CO_2 in the MSA
x	Concentration of MSA/lean stream
y	Concentration of rich stream

1.1 Advances in the synthesis of CHAMENs

The recent work of Yoro et al. [1] reported an extensive review on the application of heat and mass integration techniques for energy and material minimization during CO_2 capture via HENs and MENs synthesis. The authors discussed the prospects of introducing heat and mass integration techniques via the application of individual HENs, MENs and a combined heat and mass exchanger network for energy and material saving. However, the techniques proposed in the review were not tested in any case study. Srinivas and El-Halwagi [16] were the first group of researchers to present a methodology for the synthesis of a combined heat and mass exchanger network. The researchers formulated a technique that focused on optimizing individual mass-exchange temperatures in a constant-temperature unit, which was used to simultaneously isolate a certain pollutant from a set of rich streams to a physical and reactive lean stream (mass-separating agents) while also accomplishing a specific heat transfer task in a cost-effective manner. In spite of the results obtained by Srinivas and El-Halwagi [16], their proposed technique is only effective with reactive mass exchangers without considering the annualized capital cost of the absorbers and the regenerating units.

Papalexandri and Pistikopoulos [17] suggested a hyperstructure-based mixed integer non-linear programme based mathematical model to tackle the problem of combined heat and mass integration. However, the major drawback with their methodology is that the model formulation for the hyperstructure was observed to be extremely non-linear and non-convex in nature. This is due to the introduction of many binary variables to the problem; hence, it became very difficult to get better results than the one reported by Srinivas and El-Halwagi [16]. Furthermore, Prakotpol and Srinophakun [18] developed a genetic algorithm in MATLAB to minimize energy and material consumption in a wastewater minimization problem. The researchers formulated an optimization model for both single and multiple contaminants as an MINLP. Although the proposed algorithm was useful for the synthesis problem, it had similar limitations as the hyperstructure-based MINLP model of Papalexandri and Pistikopoulos [17]. Soywiset et al. [19] presented a simultaneous technique for heat and mass exchanger network synthesis using an ASPEN process simulator. The authors applied their technique to the synthesis of HENs and MENs separately and then CHAMENs. However, they concluded that CHAMEN synthesis was not suitable for all industrial applications. This simply means that by using their proposed methodology, synthesizing HENs and MENs separately possibly offers a reduced total annualized cost than combining them in a network.

In another contribution, Isafiade and Fraser [2] suggested a methodology based on pinch technology, where the sub-HEN and sub-MEN were combined via heat and mass pinch approach to investigate the effect of mass exchange temperature on the annual operating cost and how the annualized capital cost affects CHAMENs. Further findings from the work of Isafiade and Fraser [2]

revealed that depending on the methodology used, assumptions and process considered, synthesizing a combined heat and mass exchanger network yields better results than an individual synthesis of HENs and MENs, in contrast to the claims of Soywiset et al. [19]. Furthermore, Liu et al. [20] suggested a new methodology for the simultaneous generation of CHAMENs with multi-dimensional optimization problems. The methodology was a blend of the mass pinch technology for mass exchanger network (MEN) synthesis and a quasi T-H diagram technique for the heat exchanger network (HEN) synthesis which are both sequential in nature. The authors introduced a lean by-pass stream to a combined network structure to decrease its associated costs. The authors then suggested a mathematical model and a cross-genetic algorithm annealing-based method to achieve a synchronized minimization for the total cost of the MEN and the HEN separately. However, the technique was ineffective when tested for a combined heat and mass exchanger network in a multi-period situation. Additionally, Liu et al. [21] and Velázquez-Guevara et al. [22] developed a superstructure for the synthesis of mass exchanger networks by modelling the superstructure through general disjunctive mathematical programming and then re-formulated it as a mixed integer non-linear program. The proposed superstructure allowed for mixing and splitting of process streams thereby increasing the number of possible exchangers in the superstructure. In this study, the technique introduced is quite different from the one proposed by Liu et al. [20] because here, we hybridized a simultaneous-sequential based approach to achieve an optimal CHAMEN with remarkable energy and material saving during adsorptive CO_2 capture.

In this study, it was observed that during of CO_2 capture and storage, heat and mass exchange operations are usually multi-period in nature and are also affected by heating and cooling demands as speculated by other researchers [23],[24]. As such, synthesizing a HEN and MEN as two independent processes will not yield high energy and material saving compared to combining them in a single network [25],[26]. Additionally, most synthesis methodologies reported in the past did not consider the interactions between heat and mass exchange concomitantly [27]. Another research gap identified in this study is that most of the energy conservation tasks in the area of environmental sustainability suggest the use of external utilities (e.g. cooling water, additives) to minimize energy and material usage during CO_2 capture despite its high cost. But in this study, it is proposed that combined energy and mass integration could be an effective and sustainable approach for energy and resource minimization in many energy-intensive industrial processes. Hence, the use of internal process heat and mass for resource minimization via combined heat and mass exchanger network synthesis is proposed. The process synthesis approach presented in this study is new to the field of CO_2 capture, and we envisage that if the proposed technique is fully harnessed with optimized capital cost functions during CO_2 capture operations in large point-sources (for example coal-fired power plants), the emission of CO_2 during power generation will be considerably minimized and significant amounts of energy, as well as material (sorbents) used during CO_2 capture, will be saved.

Against this background, this study was dedicated to synthesizing a combined heat and mass exchanger network with regeneration that can minimize the excessive consumption of energy and mass (material) concurrently while decreasing the levels of CO_2 emission to the atmosphere. The study introduces a new CHAMEN synthesis technique that combines both sequential and simultaneous based principles. This study also discusses multi-period formulations for the first time in a combined heat and mass exchanger network (CHAMEN) with sorbent regeneration. Finally, this study confirms whether the combination of sequential and simultaneous concepts in a single methodology for CHAMENs can yield results with better total annualized cost (TAC).

2. Synthesis of the combined heat and mass exchanger network

The major challenge observed with most synthesis techniques for combined heat and mass exchanger network (CHAMEN) lies in the combinatorial approach as well as the optimization approach between the sub-MEN and sub-HEN. To proffer solution to this challenge, Srinivas and El-Halwagi [16] proposed a MEN–HEN combination technique, in which the heat exchanged finds a pre- and post-MEN with the lean streams flowing through the MEN at fixed stream temperatures. Although this technique yielded results, it is only applicable to single-period CHAMENs where parameters are fixed and do not fluctuate. It cannot be extended to multi-period scenarios where stream temperatures, flow rates and gas composition fluctuate as seen in a typical CO_2 separation study where sorbent regeneration is paramount. As a result, this paper modified the methodology of Srinivas and El-Halwagi [16] to specifically address a CHAMEN synthesis problem with regeneration and fluctuating process parameters. The thermodynamic feasibility of the heat exchanged in this work was ensured by using a lower value of the minimum approach temperature (ΔT_{min}).

In addition, the body of knowledge in this field is rich in different approaches for the synthesis of both reactive and non-reactive CHAMENs [2],[16],[20],[28,29]. However, due to the interaction of heat and mass during adsorptive CO_2 capture, this study reports the synthesis of CHAMENs for adsorptive CO_2 capture alongside the regeneration network. As far as could be ascertained, this has not been reported before now. Furthermore, to improve on the work of Srivinas and El-Halwagi [16], this study was extended beyond optimizing just the outlet gas composition to introduce a more rigorous optimization-based method for the synthesis of CHAMENs to include the coupling of sub-networks as well as simultaneous integration, and the optimization of CHAMENs.

The following assumptions were made for the mass exchangers synthesized in this study;
1) Individual rich and lean stream have a fluctuating mass flow rates throughout the network.

2) The mass exchangers operate at non-isothermal conditions.

3) Mass exchange temperatures are generated only from the temperatures of the lean streams.

4) Equilibrium relations are assumed to be monotonic functions of the sorbent temperature and compositions as described by Henry's law.

3. Problem statement

The combined heat and mass-exchanger network (CHAMEN) synthesis problem in this study is presented as follows;

'Given are a number of rich streams 'NR' and a number of lean streams 'NS' (physical MSAs). The task is to synthesize a cost-effective network of combined heat and mass exchangers that can satisfactorily transfer a certain undesirable pollutant (CO_2) from rich flue gas streams to the MSA (in this case, the sorbent). The flow rate of each rich stream, G_i; the supply (inlet) composition, y_{si}; and the target/outlet composition, y_{ti} are known and specified in the problem. The supply and target compositions of the MSA (sorbent) during absorptive CO_2 capture are given as x_{sj} and x_{tj} respectively. In addition, hot and cold process and utility streams are available to optimize mass exchange temperatures. Important problem data for this study such as gas flow rate, concentration and temperature intervals were adapted from the previous work of Yoro [30] and extended to tackle a combined heat and mass exchanger network synthesis problem to achieve a reduced energy and material usage during adsorptive CO_2 capture.

4. Methodology

A systematic combination of both pinch technology and mathematical programming concepts is employed in this study to synthesize a CHAMEN. The step-wise procedure presented in Figure 1 was used to set the formulation for the synthesis of a combined heat and mass exchanger network (CHAMEN) in this study.

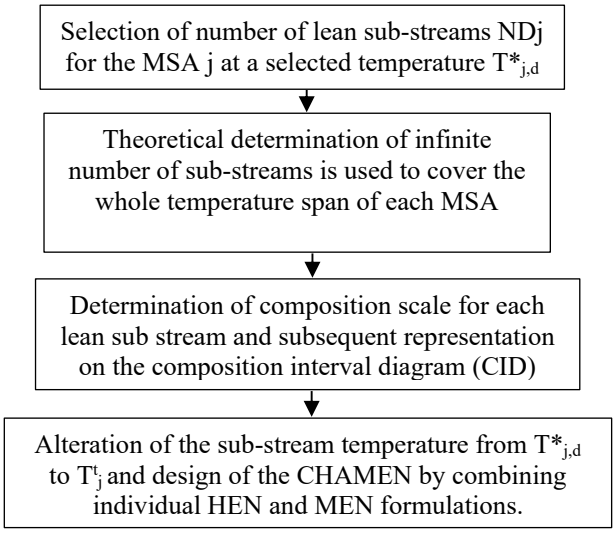

Figure 1: Methodical procedure for the formulation of CHAMENs

The adsorbent (polyaspartamide) for CO_2 capture suffices as the mass transfer agent (MSA) in this study and its cost is determined from Equation (1).

$$\textbf{Cost of MSA} = \sum_{j=1}^{N_s} C_j \sum_{dj=1}^{ND_j} L_j, dj \qquad (1)$$

Material balance around the composition interval is given by;

$$\delta_k - \delta_{k-1} + \sum_j k \sum_{dj\ through\ interval\ K} w_{j,k}^{s} = W_k^{R} \qquad (2)$$

Where k = 1, 2 …N_{int}, $L_j, dj \geq 0$, j = 1, 2… N_s

$$\sum_{dj=1}^{ND_j} L_j, dj \leq L_j^{C} \quad j = 1, 2, \ldots N_s \qquad (3)$$

Mass residual constraints for the case study considered in this paper were stated as;

$$\delta_0 = \delta_{N,int} = 0 \qquad (4)$$

$$\delta_k \geq 0, k = 1, 2 \ldots N_{int} - 1 \qquad (5)$$

Equations (1)-(5) together with the HEN-targeting equations presented by El-Halwagi [31] represent the constraints of the CHAMEN synthesis formulation.

The equilibrium relation for CO_2 scrubbing in water depends on temperature according to Equation (6) which was adapted and modified from Liu et al. [19] to suit this study;

$$y = x_1 (0.053T_1 - 14.5) \qquad (6)$$

Where y refers to the mass fraction of CO_2 in the flue gas stream, T_1 is the temperature of the water in degree Celsius and x_1 is the mass fraction of CO_2 in water after scrubbing.

An objective function was developed in this study to minimize the cost of mass separating agents (MSAs) as well as the heating and cooling utilities. The objective function discussed in this study is a linear programming formulation whose solution determines the optimal flow rate and temperature of each sub-stream as well as its heating/cooling duty. The general methodology used to synthesize the optimal CHAMEN in this study to achieve an improved total annualized cost (TAC) is presented in Figure 2.

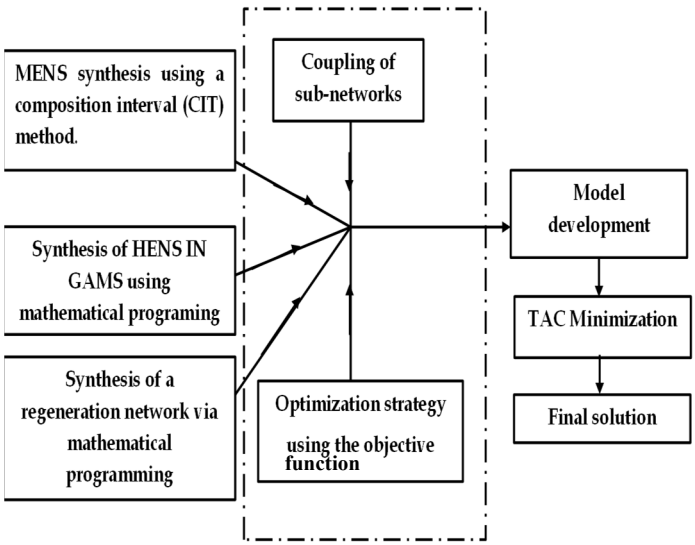

Figure 2: Methodology for the synthesis of a CHAMEN with regeneration network

5. Case study for CHAMEN synthesis

The efficacy of the methodology for synthesizing the CHAMEN with regeneration proposed in this study is tested in this section using a CO_2 adsorption case study from the work of Yoro [30]. The case study has a mass exchanger network (MEN) with mass separating agents (which is the sorbent in this case) integrated with a heat exchanger network (HEN) with the possibility of optimally regenerating the MSAs.

The task: *Adsorption of CO_2 with two MSAs and two cold and hot external utilities*

In this problem, steam and cooling water are the hot and cold utilities added to the process with the aim of heating up and cooling down the mass separating agents (MSAs) for effective adsorption of CO_2. The task is to synthesize a CHAMEN that can adequately transfer CO_2 in the waste streams to the MSA and the energy and material saved determined based on the stream data presented in Table 1-3. The physical meaning of all the symbols used in Table 1-3 and others used elsewhere in this study are already provided in the nomenclature section of this study.

Table 1**:** Waste stream data for CO_2 separation

Stream	Flow rate Gi (kg/s)	Gas Supply comp. y_i^s	Gas target comp. y_i^t
R_1	1.5	0.15	0.05

Table 2**:** Lean stream data

Stream	x_j^s	x_j^t	m_j	ε_j	C_j	T_j^{LB} (˚C)	T_j^{UB} (˚C)
S_1	0.00	0.05	0.10	0.001	0.05	35	50
S_2	0.02	0.09	0.20	0.001	0.01	48	48

Table 3**:** Cold and hot utility stream data

Stream	Supply Temp(˚C)	Target Temp (˚C)	Cost ($/kW.yr)
C_1	15	25	10
C_2	28	35	30
H_1	130	80	120
H_2	120	70	150

Two cooling utilities (cold water) and two hot utilities (steam) are available as shown in Table 3. For this case study, the specific heat capacity is fixed at 4.2 kJ·kg^{-1}·˚C^{-1} (specific heat capacity of water at room temperature) while the minimum approach temperature ΔT_{min} was assumed at 10 ˚C.

The cost of heat exchanger area (A) is expressed in Equation (7) as described by Shenoy [32];

$$\text{Area cost} = 30000 + 750A^{0.81} \quad (7)$$

The objective function for the mathematical model is presented as Equation (8) and was solved in GAMS (General algebraic modelling system). The objective function comprises of the total annual cost (TAC) of the CHAMEN presented as a combination of the costs associated with the sub-MEN and the sub-HEN. The objective function of the model gives more information on the capital costs of the coolers, heaters and the number of heat exchanger units for all process streams.

$$\text{Min} \sum_{i}\sum_{j}\sum_{k} N_{i,j,k} \cdot K_{stage} + H_Y \sum_{j} L_j \cdot C_j^l + \sum CF_{cu,v} + \sum_{v} CF_{hu,w} + \sum_{w}\sum_{u}\sum_{v}\sum_{w} CF_{u,v,w} + \sum_{v} C_{cu,v} \cdot A_{cu,v}^{Bcu,v} + \sum_{w} Chu_{,w} \cdot A_{hu,w}^{Bhu,w} + \sum_{u}\sum_{v}\sum_{w} Cv_{w,u} \cdot A_{v,w,u}^{Bv,w,u} + \sum_{v} C^{cu} \cdot q_{cu,v} + \sum_{w} C^{hu} \cdot q_{hu,w} \quad (8)$$

Hot and cold streams for the networks were determined through optimization using Equation (9).

$T_j^s < T_j^*$, $T_j^* < T_j^t$ = hot stream, j ϵ N_i

$T_j^s > T_j^*$, $T_j^* > T_j^t$ = cold stream, j ϵ N_i (9)

Equations (1)-(9) were coupled with the non-negativity constraints to form a linear program that was modelled and run in GAMS using the DICOPT solver.

Table 4**:** Composition interval diagram for the case study

Interval	Waste stream y 0.15 R1	X_1, 1 at 35 ºC	X_1, 1 at 70 ºC	Target 0.09
1	0.13			0.08
2	0.12			0.07
3	0.10		0.13	0.06
4	0.09	0.13	0.09	0.05
5	0.08	0.11	0.07	0.04
6	0.07	0.09	0.05	0.03
7	0.06	0.05	0.00	0.03
8	0.05	0.00	$S_{1,2}$	0.02
		$S_{1,1}$		S_2

Table 5: Temperature interval diagram

Interval	Hot streams $S_{1,1}$, $S_{1,1}$ T(ºC)	Target Temp(˚C)
1	35	130
2	28	120
3	25	80
4	15	70 CU_1
		CU_2

6. Regeneration

Since the example considered in this paper involves CO_2 adsorption using a solid sorbent, there is a need to consider the amounts of energy that could be saved during the regeneration of sorbents in the CHAMEN. As a result, a regeneration network was integrated into the CHAMEN in this study. The main MSA target composition during regeneration was determined from the interaction with the stripping column. A complex

mathematical problem was solved in GAMS using the DICOPT solver as ΔT_{min} changes and results obtained are presented in Table 6. The superstructure showing expected flows in the combined heat, mass exchanger with regeneration network is shown in Figure 3 while the synthesized CHAMEN alongside its regeneration is presented in Figure 4. To substantiate our claims in this study, the minimum TAC obtained in this study using the proposed technique was compared with other CHAMEN synthesis techniques procedures reported in the past and presented in Table 7. The technique proposed in this study resulted in a slightly superior value of TAC when compared to previously reported techniques as shown in Table 7. The TAC value obtained in this study is closer to that reported by Isafiade et al. [2]. However, the slight difference observed could be attributed to the fact that Isafiade et al. [2] used only a simultaneous approach without considering regeneration while this study used a combined sequential and simultaneous approach with due consideration to sorbent regeneration.

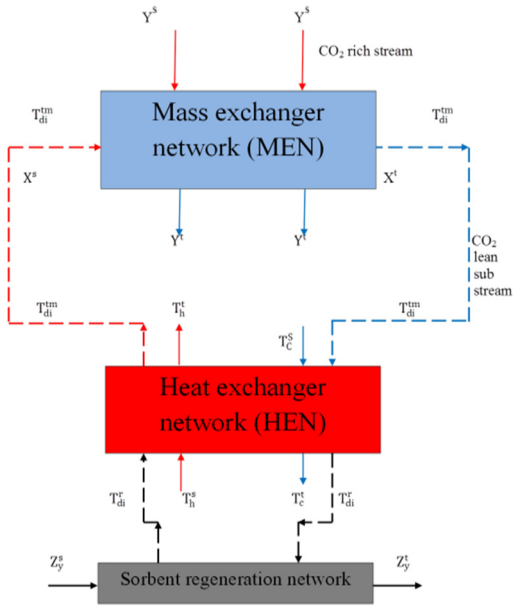

Figure 3: The CHAMEN + regeneration superstructure (Adapted from Yoro et al. [1]).

Table 6: TAC obtained at different target compositions and Δ T_{min}.

Compositions x^s	Compositions x^t	Δ T_{min} (°C)	TAC for CHAMEN ($million/yr.)
0.15	0.03	10	0.1998
0.15	0.05	13	0.2156
0.15	0.07	15	0.2800
0.15	0.10	20	0.3763

Table 7: Minimum total annualized cost compared with literature

Reference	Network type	Minimum TAC for CHAMEN ($million/yr.)
This study	CHAMENs	0.1998
Liu et al. [20]	CHAMENs	0.3402
Isafiade et al. [2]	CHAMENs	0.1973
Soywiset et al. [18]	CHAMENs	2. 6731

Table 8: Energy and material saved during CO_2 capture using different energy and material saving techniques

Technique	Energy saved (%)	Sorbent/ material saved (%)	Reference
CHAMEN + Regeneration	30	19	This study
Use of phase change solvents	40	Not reported	Shavalieva et al. [33]
Sorbent blending	17	9	Bachelor and Toochinda [34]
Amine scrubbing	31	Not reported	Pellegrini et al. [35]
Use of extra external utilities	12	0	Bougie and Iliuta [36]

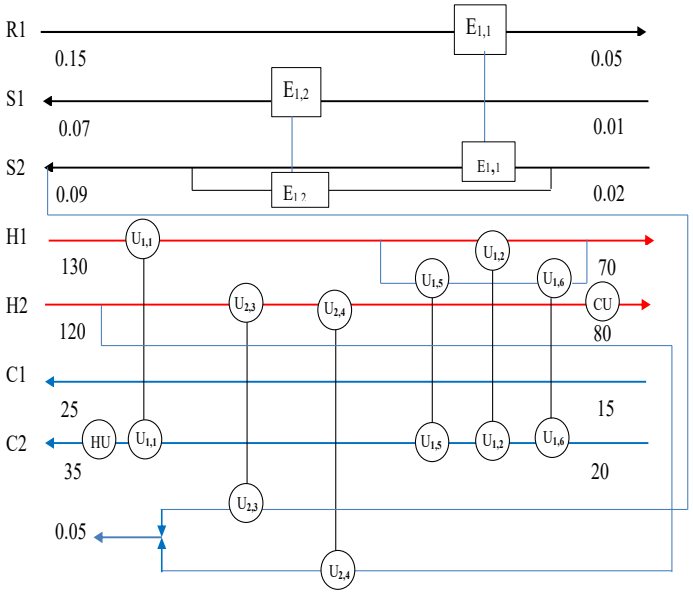

Figure 4: CHAMEN with regeneration for this case study.

7. Discussion of Results

This study attempted using the composition interval method (for MENS), with temperature interval diagram (for HENS) and linear programming to explore the possibility of synthesizing a combined heat and mass exchanger network with a provision for sorbent regeneration. The composition interval diagram presented in this work was used to ensure the thermodynamic feasibility of the mass exchanged during the CO_2 capture process while the temperature intervals catered for the heat exchanged and potential energy saving. The number of intervals represents the number of process streams (both hot and cold) considered in the capture process. The all-positive values in the composition interval diagram (CID) presented in Table 4 established that within any interval, it is thermodynamically feasible to transfer mass from the waste streams to the mass separating agents (sorbents). The solution obtained from the combined network also confirms that the lean stream (sorbent) is actively involved in the adsorption process and a by-pass stream with unequal supply and target temperature is expected. The CHAMENs further illustrates that the incorporation of by-pass streams with the combination of simultaneous and sequential-based synthesis technique yields results with significant improvements over previously reported methodologies that used just mathematical programming or sequential approach.

Another important result presented in this study is the total annualized cost (TAC) of the combined network. A lower value of TAC for the CHAMEN means better operating and capital cost for the network which also translates to higher energy savings and minimization of material in the CO_2 adsorption process. Furthermore, results on Table 6 show that as the target composition of the gas (with respect to mass exchange) and minimum approach temperature (ΔT_{min}) with respect to heat exchanged is increased, the TAC also increases. This means that operating at a lower ΔT_{min} could result in a more efficient combined heat and mass exchanger network with regeneration during CO_2 capture.

The parameters included in the objective function formulated in this study were responsible for the significant decrease in the total annualized cost and energy consumption by the resultant CHAMEN. The value of the minimum approach temperature (10 ^oC) adopted in this study impacted positively on energy penalty reduction during adsorptive CO_2 capture which subsequently improves the efficiency of the power plant. The inclusion of a sorbent regeneration network in the CHAMEN presented in this study established that process synthesis techniques can be used to tackle the high energy requirement associated with most CO_2 capture techniques.

The results in Table 7 suggest that the combined methodology introduced in this work is better in terms of the total annualized costs than some methodologies reported in the literature. This makes the combined network generated in this paper more ideal for application in CO_2 capture studies. The amount of energy and material saved during CO_2 capture reported for different energy and material saving techniques is presented in Table 8 and compared with the technique proposed in this study. According to the results in Table 8, the integration of CHAMENs with a regeneration network in a CO_2 capture problem could result in 30 and 19 % energy and material saving respectively. Other techniques that reported a slightly higher value could only account for energy without material saving. Although the use of phase change solvents as proposed by Shavalieva et al. [33] is good and results in a significantly higher energy saving (40%) as shown in Table 8, the technique cannot be extended for material saving. Amine scrubbing technique also resulted in huge energy savings during CO_2 capture, however, it cannot also account for the quantity of materials that could be saved in the process. Thus, it is evident that the integration of a CHAMEN with regeneration as proposed in this study could potentially facilitate and account for a reduction in both energy and material during CO_2 capture.

8. Conclusions

The benefit of combining heat and mass exchanger networks with a sorbent regeneration network for concurrent minimization of energy and material during CO_2 capture was investigated in this study. It was established from the results obtained in this study that combining heat and mass exchanger with a sorbent regeneration network is an effective way of concurrently minimizing energy and material consumption during CO_2 capture. Results obtained from the case study considered in this work revealed that operating the lean streams at their supply temperatures alone is not the best approach to cut operational cost and simplify CHAMEN network design. Furthermore, It has been demonstrated in this study that it is possible to combine a sequential-based approach (composition interval method) with a simultaneous-based technique (mathematical programming) to achieve optimal results for energy and material saving in a combined heat and mass exchanger network. The combinatorial approach introduced in this study gave insight into how best to combine the heat and mass exchangers with regeneration networks for energy and material minimization. Finally, the total annualized cost obtained in this study (TAC=$million 0.1998 /yr.) showed significant improvement over the TAC previously reported which also mean a significant reduction in energy requirement when compared with previously reported approaches. The CHAMEN synthesized in this study can be extended to minimize energy and material consumption in other CO_2 capture methodologies such as absorption, membrane, and cryogenic separation. Finally, it was established in this study that although other energy-saving techniques for CO_2 capture (for example amine scrubbing, sorbent blending, the use of phase change materials etc.) yielded results in terms of energy-saving, if energy and material minimization is to be accounted for concurrently, the application of a combined heat and mass exchanger network is the better option.

Acknowledgements

K.O. Yoro is thankful to the National Research Foundation of South Africa and the University of Witwatersrand for funding this research through the NRF-DST innovation doctoral scholarship (block grant

number 107867) and the WITS postgraduate merit award (WITS-PMA 2017-2019) respectively.

References

[1] K. O. Yoro, P. T. Sekoai, A. J. Isafiade, and M. O. Daramola, 'A review on heat and mass integration techniques for energy and material minimization during CO_2 capture', *International Journal of Energy and Environmental Engineering,* vol. 10, pp. 367–387, 2019.

[2] A. Isafiade and D. Fraser, 'Optimization of combined heat and mass exchanger networks using pinch technology', *Asia-Pacific Journal of Chemical Engineering*, vol. 2, no. 6, pp. 554–565, 2007.

[3] K. O. Yoro and P. T. Sekoai, 'The Potential of CO_2 Capture and Storage Technology in South Africa's Coal-Fired Thermal Power Plants', *Environments*, vol. 3, no. 3, p. 24, 2016.

[4] K. O. Yoro, M. Singo, J. L. Mulopo, and M. O. Daramola, 'Modelling and Experimental Study of the CO_2 Adsorption Behaviour of Polyaspartamide as an Adsorbent During Post-Combustion CO_2 Capture', *Energy Procedia*, vol. 114, pp. 1643–1664, 2017.

[5] M. B. Noureldin, 'Methods for heat exchanger network energy efficiency assessment and lifetime retrofit', US8150560B2, 2012.

[6] Y. L. Tan, D. K. S. Ng, D. C. Y. Foo, M. M. El-Halwagi, and Y. Samyudia, 'Heat integrated resource conservation networks without mixing prior to heat exchanger networks', *Journal of Cleaner Production*, vol. 71, pp. 128–138, 2014.

[7] F.B. Gabriel and M.M. El-Halwagi, 'Simultaneous synthesis of waste interception and material reuse networks: Problem reformulation for global optimization', *Environmental Progress*, vol. 24, no. 2, pp. 171–180, 2005.

[8] K. O. Yoro, A. J. Isafiade, and M. O. Daramola, 'Synthesis of Optimal Heat Exchanger Networks with Quantified Uncertainties and Non-isothermal Mixing', *J. Phys. Conf. Ser.,* vol. 1378, pp. 022018, 2019.

[9] O. S. Azeez, A. J. Isafiade, and D. M. Fraser, 'Supply-based superstructure synthesis of heat and mass exchange networks', *Computers & Chemical Engineering*, vol. 56, pp. 184–201, 2013.

[10] S. Ghazouani, A. Zoughaib, and S. Pelloux-Prayer, 'Simultaneous heat integrated resource allocation network targeting for total annual cost considering non-isothermal mixing', *Chemical Engineering Science*, vol. 134, pp. 385–398, 2015.

[11] A. Wechsung, A. Aspelund, T. Gundersen, and P. I. Barton, 'Synthesis of heat exchanger networks at subambient conditions with compression and expansion of process streams', *AIChE Journal*, vol. 57, no. 8, pp. 2090–2108, 2011.

[12] T. F. Yee and I. E. Grossmann, 'Simultaneous optimization models for heat integration—II. Heat exchanger network synthesis', *Computers & Chemical Engineering*, vol. 14, no. 10, pp. 1165–1184, 1990.

[13] K.F. Huang, E.M. Al-mutairi and I. A. Karimi. 'Heat exchanger network synthesis using a stage-wise superstructure with non-isothermal mixing '.*Chemical engineering science,* vol. 73, pp. 30-43, 2012.

[14] J. M. Zamora and I. E. Grossmann, 'A global MINLP optimization algorithm for the synthesis of heat exchanger networks with no stream splits', *Computers & Chemical Engineering*, vol. 22, no. 3, pp. 367–384, 1998.

[15] K. C. Furman and N. V. Sahinidis, 'A Critical Review and Annotated Bibliography for Heat Exchanger Network Synthesis in the 20th Century', *Ind. Eng. Chem. Res.*, vol. 41, no. 10, pp. 2335–2370, 2002.

[16] B. K. Srinivas and M. M. El-Halwagi, 'Synthesis of combined heat and reactive mass-exchange networks', *Chemical Engineering Science*, vol. 49, no. 13, pp. 2059–2074, 1994.

[17] K. P. Papalexandri and E. N. Pistikopoulos, 'A multiperiod MINLP model for the synthesis of flexible heat and mass exchange networks', *Computers & Chemical Engineering*, vol. 18, no. 11, pp. 1125–1139, 1994.

[18] D. Prakotpol and T. Srinophakun, 'GAPinch: genetic algorithm toolbox for water pinch technology', *Chemical Engineering and Processing: Process Intensification*, vol. 43, no. 2, pp. 203–217, 2004.

[19] S. Soywiset, T. Srinophankun, K. Turnprakiat, and W. Nuengwang, 'Simultaneous Heat and Mass Exchanger Networks with Process Simulator', *Journal of Chemical Engineering of Japan*, vol. 46, no. 2, pp. 146–157, 2013.

[20] L. Liu, J. Du, M. M. El-Halwagi, J. M. Ponce-Ortega, and P. Yao, 'A systematic approach for synthesizing combined mass and heat exchange networks', *Computers & Chemical Engineering*, vol. 53, pp. 1–13, 2013.

[21] L. Liu, J. Du, and F. Yang, 'Combined mass and heat exchange network synthesis based on stage-wise superstructure model', *Chinese Journal of Chemical Engineering*, vol. 23, no. 9, pp. 1502–1508, 2015.

[22] M. Á. Velázquez-Guevara *et al.*, 'Synthesis of mass exchange networks: A novel mathematical programming approach', *Computers & Chemical Engineering*, vol. 115, pp. 226–232, 2018.

[23] K. O. Yoro, M. K. Amosa, P. T. Sekoai, J. Mulopo, and M. O. Daramola, 'Diffusion mechanism and effect of mass transfer limitation during the adsorption of CO_2 by polyaspartamide in a packed-bed unit', *International Journal of Sustainable Engineering*, 2019. https://doi.org/10.1080/19397038.2019.1592261

[24] K. O. Yoro, M. K. Amosa, P. T. Sekoai, and M. O. Daramola, 'Modelling and experimental investigation of effects of moisture and operating parameters during the adsorption of CO_2 onto polyaspartamide', *International Journal of Coal Science & Technology*, vol. 6, pp.225-234, 2019.

[25] A. Isafiade, M. Bogataj, D. Fraser, and Z. Kravanja, 'Optimal synthesis of heat exchanger networks for multi-period operations involving single and multiple utilities', *Chemical Engineering Science*, vol. 127, pp. 175–188, 2015.

[26] K.O., Yoro, A.J., Isafiade, and M.O., Daramola, 'Sequential synthesis of mass exchanger networks for CO_2 capture'. *In: Lecture notes in engineering and computer science: proceedings of the world congress on engineering and computer science*, San Francisco, USA, vol. 2*,* pp. 503–508, 2018.

[27] K.O., Yoro, A.J., Isafiade, and M.O., Daramola, Multi-period Heat Exchanger Network Synthesis with Temperature Intervals and Uncertain Disturbances, *Chemical Engineering Transactions*, vol. 76, 1039-1044, 2019.

[28] O. S. Azeez, 'Combined heat and mass exchanger network synthesis', PhD thesis, University of Cape Town, 2016.

[29] H. Yeomans and I. E. Grossmann, 'A systematic modelling framework of superstructure optimization in process synthesis', *Computers & Chemical Engineering*, vol. 23, no. 6, pp. 709–731, 1999.

[30] K. O. Yoro, 'Numerical simulation of CO_2 adsorption behaviour of polyaspartamide adsorbent for post-combustion CO_2 capture', MSc. Thesis, University of the Witwatersrand, 2017.

[31] M. M. El-Halwagi, Sustainable Design through Process Integration: Fundamentals and Applications to Industrial Pollution Prevention, Resource Conservation, and Profitability Enhancement. Butterworth-Heinemann, 2017.

[32] U. V. Shenoy, Heat Exchanger Network Synthesis: Process Optimization by Energy and Resource Analysis. *Gulf Professional Publishing,* 1995.

[33] G. Shavalieva, S. Papadokonstantakis, P. Kazepidis, A.I. Papadopoulos, and P. Seferlis, 'Sustainability Analysis of Phase-Change Solvents for Post-Combustion CO_2 Capture', *Chemical Engineering Transactions,* vol. 76, 1045-1050, 2019.

[34] T.T.N. Bachelor, and P. Toochinda, 'Development of low-cost amine-enriched solid sorbent for CO_2 capture'. *Environmental Technology,* vol. 33, 2645-2651, 2012.

[35] L.A. Pellegrini, S. Moioli, and S. Gamba, 'Energy saving in a CO_2 capture plant by MEA scrubbing'. *Chemical Engineering Research and Design*, vol. 89, 1676–1683, 2011.

[36] F. Bougie, and M.C. Iliuta, 'CO_2 absorption in aqueous piperazine solutions: experimental study and modelling'. Journal of Chemical & Engineering Data, 56, 1547-1554, 2011.

SELECTED PAPERS FROM THE 10TH INTERNATIONAL TRONDHEIM CCS CONFERENCE

These proceedings contain selected papers from the 10th International Trondheim CCS Conference (TCCS-10), held in Trondheim, Norway, on June 17th-19th 2019.

The bi-annual Trondheim CCS Conference is a leading scientific CCS technology conference. Since its inception in 2003, the Conference has developed to become a globally important meeting place for over 400 CCS experts. The Conference typically has 150 oral presentations, five or six parallel sessions, over 100 posters and world leading keynote speakers.

SINTEF Academic Press